National Library
of Canada

Canadian Theses Service

Ottawa, Canada
K1A 0N4

Bibliothèque nationale
du Canada

Service des thèses canadiennes

NOTICE

The quality of this microform is heavily dependent upon the quality of the original thesis submitted for microfilming. Every effort has been made to ensure the highest quality of reproduction possible.

If pages are missing, contact the university which granted the degree.

Some pages may have indistinct print especially if the original pages were typed with a poor typewriter ribbon or if the university sent us an inferior photocopy.

Previously copyrighted materials (journal articles, published tests, etc.) are not filmed.

Reproduction in full or in part of this microform is governed by the Canadian Copyright Act, R.S.C. 1970, c. C-30.

AVIS

La qualité de cette microforme dépend grandement de la qualité de la thèse soumise au microfilmage. Nous avons tout fait pour assurer une qualité supérieure de reproduction.

S'il manque des pages, veuillez communiquer avec l'université qui a conféré le grade.

La qualité d'impression de certaines pages peut laisser à désirer, surtout si les pages originales ont été dactylographiées à l'aide d'un ruban usé ou si l'université nous a fait parvenir une photocopie de qualité inférieure.

Les documents qui font déjà l'objet d'un droit d'auteur (articles de revue, tests publiés, etc.) ne sont pas microfilmés.

La reproduction, même partielle, de cette microforme est soumise à la Loi canadienne sur le droit d'auteur, SRC 1970, c. C-30.

NL-339 (r. 88/04)

Canada

THE UNIVERSITY OF ALBERTA

Determination of Interatomic and Intermolecular Potential Energy Surfaces from Crossed Molecular Beam Scattering

by

©

Laurie James Danielson

A THESIS

SUBMITTED TO THE FACULTY OF GRADUATE STUDIES AND RESEARCH
IN PARTIAL FULFILMENT OF THE REQUIREMENTS FOR THE DEGREE
OF

Doctor of Philosophy

Department of Chemistry

EDMONTON, ALBERTA

Fall 1988

Permission has been granted to the National Library of Canada to microfilm this thesis and to lend or sell copies of the film.

The author (copyright owner) has reserved other publication rights, and neither the thesis nor extensive extracts from it may be printed or otherwise reproduced without his/her written permission.

L'autorisation a été accordée à la Bibliothèque nationale du Canada de microfilmer cette thèse et de prêter ou de vendre des exemplaires du film.

L'auteur (titulaire du droit d'auteur) se réserve les autres droits de publication; ni la thèse ni de longs extraits de celle-ci ne doivent être imprimés ou autrement reproduits sans son autorisation écrite.

ISBN 0-315-45697-3

23 September 1987

To Whom It May Concern:

I, Karen McLeod, give permission for the publication:

J. Chem. Phys. 87 (1) 239 (1987)

to be used as a part of Laurie Danielson's doctoral thesis.

Sincerely,

Karen McLeod

Karen McLeod

THE UNIVERSITY OF ADELAIDE

Department of Physical and Inorganic Chemistry

G.P.O., Box 498,
Adelaide,
South Australia 5001

16 December 1987

Mr Laurie Danielson,
Department of Chemistry,
University of Alberta,
Edmonton,
Alberta,
Canada, T6G-2G2.

Dear Laurie,

I give you my permission to use as part of your thesis the paper "Anisotropic Intermolecular Potentials for HeC_2H_2, HeC_2H_4, HeC_2H_6, and an Effective Spherical Potential for $HeCHF_3$ from Multi-property Fits", which has been submitted to the Journal of Chemical Physics.

Regards,

Peter Dunlop

Peter J. Dunlop

MAX-PLANCK-INSTITUT FÜR STRÖMUNGSFORSCHUNG

ABTEILUNG ATOM- UND MOLEKÜLPHYSIK

Prof. U. Buck

MPI für Strömungsforschung · Bunsenstr. 10 · D 3400 Göttingen · Postf. 2853 · Tel. (0551) 709- 2572 sid. 709-1 · Telex 96768 mpstr d · Telefax (0551) 7092704

Mr. Laurie J. Danielson
Department of Chemistry
Faculty of Science
University of Alberta
E3-43 Chemistry Building East
Edmonton, T6G 2G2
Canada

We grant permission to Mr. Laurie J. Danielson to use the manuscript entitled "The He-Ne intermolecular potential from multiproperty fits and Hartree-Fock calculations" as part of his thesis to be submitted to the Chemistry Department of the University of Alberta, Edmonton.

Göttingen, April 13, 1988

U. Buck
Prof. Dr. Udo Buck

Dr. Jens Schleusener

F. Huisken
Dr. Friedrich Huisken

UNIVERSITY OF VICTORIA
P.O. BOX 1700, VICTORIA, B.C., CANADA V8W 2Y2
TELEPHONE (604) 721-7152 TELEX 049-7222

DEPARTMENT OF CHEMISTRY

April 28, 1988

Mr. Laurie Danielson
Department of Chemistry
University of Alberta
Edmonton, Alberta
T6G 2G2

Dear Laurie:

This letter is to confirm that I have no objection to you using the paper entitled:

"The HeNe Interatomic Potential from Multiproperty Fits and Hartree-Fock Calculations by M. Keil, L.J. Danielson, V. Buck, J. Schleusener, F. Huisken and T.W. Dingle as part of your thesis presentation for your Ph.D. degree.

All the best wishes for the successful completion of your degree.

Yours sincerely,

Thomas Dingle

T.W. Dingle
Associate Professor

TWD:pr

April 22, 1988

Professor John C. Light, Editor
Journal of Chemical Physics
Department of Chemistry
5735 S. Ellis Avenue
University of Chicago
Chicago, Illinois 60637
U.S.A.

Dear Professor Light:

I, Laurie James Danielson, am currently preparing my Ph.D. thesis. It is a paper format thesis, and "for microfilming purposes, the National Library of Canada requires that students using previously copyrighted material in their theses must include, with their thesis, letters of permission from the person/s or publishing company holding the copyright. These letters must accompany the thesis when the final copies are presented to the Faculty of Graduate Studies and Research." In this regard, I request your written signed approval for use of the following materials:

1. L.J. Danielson, K.M. McLeod, and M. Keil, J. Chem. Phys. **87**, 239 (1987).
2. L.J. Danielson and M. Keil, J. Chem. Phys. **88**, 851 (1988).
3. L.J. Danielson, M. Keil, and P.J. Dunlop, J. Chem. Phys. **88**, 4218 (1988).

I will be submitting my thesis to the Faculty of Graduate Studies and Research on or before the 19 day of June (1988). I hope to hear from you soon.

Thank you for your attention in this matter.

Cordially,

Laurie Danielson

Mr. Laurie Danielson

THE JOURNAL OF CHEMICAL PHYSICS

PUBLISHED BY THE

AMERICAN INSTITUTE OF PHYSICS

J. C. LIGHT
EDITOR
D. H. LEVY
ASSOCIATE EDITOR

DEPARTMENT OF CHEMISTRY
5735 S. ELLIS AVENUE
UNIVERSITY OF CHICAGO
CHICAGO, ILLINOIS 60637

02 May 1988

FILE NO.

Mr. Laurie Danielson
Department of Chemistry
University of Alberta
Faculty of Science
E3-43 Chemistry Building East
Edmonton, CANADA T6G 2G2

Dear Mr. Danielson:

Thank you for your letter of April 22, 1988 requesting permission to reproduce material which has been submitted for publication in the Journal of Chemical Physics.

Permission to reproduce the material cited in your letter is granted provided that you have also obtained the permission of the co-authors and that acknowledement of the authors and the Journal of Chemical Physics is made.

Sincerely yours,

JCLight

J.C. Light
D.H. Levy

JCL:mj

cc: Goodwin/AIP

Danielson, McLeod, and Keil, [J. Chem. Phys. 87, 239 (1987)].

Danielson and Keil, [J. Chem. Phys. 88, 851 (1988)].

Danielson, Keil, and Dunlop, [J. Chem. Phys. 88, 4218 (1988)].

University of Alberta
Edmonton

Canada T6G 2G2

Department of Chemistry
Faculty of Science

E3-43 Chemistry Building East, Telephone (403) 432-3254

May 22, 1988

To whom it may concern;

I, Mark Keil, hereby give my permission to Laurie James Danielson to use the following papers as a part of his Ph.D. thesis:

1. L.J. Danielson, K.M. McLeod, and M. Keil, J. Chem. Phys. **87**, 239 (1987).
2. L.J. Danielson and M. Keil, J. Chem. Phys. **88**, 851 (1988).
3. M. Keil and L.J. Danielson, Can. J. Phys. **66**, 159 (1988).
4. L.J. Danielson, M. Keil, and P.J. Dunlop, J. Chem. Phys. **88**, 4218 (1988).
5. M. Keil, L.J. Danielson, U. Buck, J. Schleusener, F. Huisken, and T.W. Dingle, "The HeNe Interatomic Potential from Multirpoperty Fits and Hartree-Fock Calculations", submittted to J. Chem. Phys. (1988).

Sincerely,

Mark Keil

THE UNIVERSITY OF ALBERTA

RELEASE FORM

NAME OF AUTHOR: **Laurie James Danielson**

TITLE OF THESIS: **Determination of Interatomic and Intermolecular Potential Energy Surfaces from Crossed Molecular Beam Scattering**

DEGREE: **Doctor of Philosophy**

YEAR THIS DEGREE GRANTED: **Fall 1988**

Permission is hereby granted to THE UNIVERSITY OF ALBERTA LIBRARY to reproduce single copies of this thesis and to lend or sell such copies for private, scholarly or scientific research purposes only.

The author reserves other publication rights, and neither the thesis nor extensive extracts from it may be printed or otherwise reproduced without the author's written permission.

Laurie Danielson

Box 313
Fernie, B.C.
V0B 1M0

Date: June 13, 1988.

THE UNIVERSITY OF ALBERTA

FACULTY OF GRADUATE STUDIES AND RESEARCH

The undersigned certify that they have read, and recommend to the Faculty of Graduate Studies and Research for acceptance, a thesis entitled **Determination of Interatomic and Intermolecular Potential Energy Surfaces from Crossed Molecular Beam Scattering** submitted by **Laurie James Danielson** in partial fulfilment of the requirements for the degree **Doctor of Philosophy**.

Supervisor

E. H. Pinnington

A Kalantar

Loren Hepler

Roger Miller

External Examiner

Date: June 13, 1988.

To Deb

ABSTRACT

This thesis presents interatomic and intermolecular potential energy surfaces for interactions between He atoms and various atomic and molecular partners. Differential cross sections (DCS) for scattering of thermal energy He atoms by crossed atomic and molecular beams are measured in our laboratory. These data are included, along with other properties reported in the literature, in multiproperty fits to determine the interatomic and intermolecular potentials by adjusting parameters of assumed analytical forms with an automated nonlinear least-squares fitting algorithm.

The sensitivity of scattering cross sections and dilute gas properties to the interatomic potential energy, for low reduced-mass atom + atom van der Waals interactions, is determined directly. These results are used to develop the most fruitful miltiproperty fitting procedure for extracting reliable pair potentials. Error bounds can be estimated for the potentials thus obtained.

High resolution DCS measurements reported for HeAr, HeKr, and HeXe are used to determine interatomic potentials by simultaneously fitting the DCS's, as well as mixture viscosity (η_{mix}) and interaction second virial (B_{12}) data. Bias due to systematic and potential model errors is examined and used to estimate the accuracy of the potential energy curves obtained. The best-fit potentials are compared with the best, previously reported, potentials for these interactions. New high-resolution DCS results reported for the HeNe interaction are included along with several other properties to determine a highly accurate interatomic potential from multiproperty fits and Hartree-Fock calculations. The potential is compared to previously proposed HeNe interatomic potentials, including one obtained by direct inversion of similar high quality DCS data.

Total DCS measurements for $HeCO_2$, HeOCS, HeC_2H_2, HeC_2H_4, HeC_2H_6, and $HeCHF_3$ are reported. In addition, B_{12} and accurate limiting diffusion (D°_{12}) measurements are reported for the hydrocarbon interactions. Damping of the DCS's is discussed in relation to the anisotropy of the molecular partner. The $HeCO_2$ results are shown to be consistent with recent partially resolved inelastic DCS measurements. Anisotropic intermolecular potentials are determined for HeOCS from the DCS, and for HeC_2H_2, HeC_2H_4, and HeC_2H_6 from multi-property fits within the infinite-order sudden approximation (IOSA). An effective spherical potential is determined for the $HeCHF_3$ interaction.

Acknowledgements

I would like to take this opportunity to thank all of those people who helped make this thesis a reality. Above all, I want to express by deepest thanks to my wife Deb, who has put up with the less than pleasant lifestyle offered by a graduate student for more than six years now. Throughout that time however, she has maintained a constant level of encouragement and enthusiasm for my work. In fact, she helped collect a majority of the data presented in this thesis. For her many sacrifices along the way, I dedicate this thesis to her.

I would like to thank my supervisor, Mark Keil, for his patience and guidance over the past few years. We have worked closely over most of this time, constructing the apparatus and collecting the data. As with any close interaction, there have been "rocky roads" along the way. Nonetheless, I am grateful to, and respect Mark for his tireless efforts in both the experimental and theoretical aspects of the work presented in this thesis.

It is gratifying to recognize the efforts of Mike Vatter who, in the short time that he was here, aided in the construction of the apparatus. Karen McLeod, who worked with us for a while and helped construct parts of the apparatus, aided in the data collection, and in the programming for the data reduction. I am glad that we had the opportunity to get to know one another, to work together, and I thank them for their contributions to this work.

I would also like to express my thanks to the late Dr. F. Birss for his sincere friendship and stimulating discussions of many aspects of this work. His help with the second virial program, used in the data reduction, was essential to my understanding of it. We not only shared the same birthdate, but also a camaraderie that is not often found in this busy world. I shall always remember him, and thank him for his participation in my life here at the University of Alberta.

There have been three undergraduate students who have helped, in many different capacities, bring about this thesis. They are Donald Stanley, Kevin Charter and Gary Samek and I thank them for their hard work and participation in this project. I am very grateful to everyone in the chemistry machine shop and the electronics shop. They have always managed to help out when they were needed and I thank them all for their major contributions to the apparatus and for their friendship over the past few years. In his capacity as the senior electronics engineer for the chemistry department, Rudy Kenwell worked on many of the necessary electronic components for the apparatus, and I am glad to acknowledge his participation in this work.

Looking back over the years, this thesis would not have been possible without the encouragement and support given to me by my late parents. I will never forget the many things that they have done for me and with deep respect I thank them. In many ways this is not my thesis, but theirs in that it is the realization of their hopes and dreams for me. Wherever they are, I hope that they have found peace. I am deeply grateful to Vic Loewen and his family for their kindness and generosity when I needed it most. As my highschool chemistry teacher and as my friend, Vic was a major source of encouragement for me after the tragic loss of my parents. For all of the things that he and his family have done for me, I am eternally thankful.

I would also like to thank a very special lady for her support and encouragement over the past many years. That is, my dad's mother, my grandmother, "Grandma Leech". Thanks grandma for always being there and always having an encouraging word when things looked dark and gloomy.

Finally, I am grateful to the University of Alberta and to my supervisor for their financial support over the past three years.

TABLE OF CONTENTS

Chapter Page

1. **Introduction** 1
  - 1.1 General 1
  - 1.2 Multiproperty Fitting 9
  - 1.3 Theoretical Background 11
    - 1.3.A. Classical Mechanics of Scattering 11
    - 1.3.B. Quantum Mechanics of Scattering 13
      - 1.3.B.1. Atom + Atom Scattering 13
      - 1.3.B.2. Atom + Molecule Scattering 17
  - References 22
2. **Interatomic Potentials for HeAr, HeKr, and HeXe From Multiproperty Fits** 29
  - 2.1. Introduction 29
  - 2.2. Experimental 31
    - 2.2.A. Beam Sources and Characterizations 31
    - 2.2.B. Scattering Chamber and Detector 36
    - 2.2.C. Data Acquisition and Experimental Results 38
  - 2.3. Calculations and Simultaneous Fitting 42
    - 2.3.A. Differential Cross Sections 42
    - 2.3.B. Transport Properties 45
    - 2.3.C. Interaction Second Virial Coefficients 47
    - 2.3.D. Absolute Integral Cross Sections 47
    - 2.3.E. Multiproperty Fitting 48
  - 2.4. Dilute Gas Data Selection 51
    - 2.4.A. Mixture Viscosities 51

Table of Contents (continued)

Chapter Page

2.4.B. Interaction Second Virials 53

2.5. Interatomic Potential Parameterizations 54

2.6. Results and Discussion 56

2.6.A. Fitted Interatomic Potentials 56

2.6.B. Fitted Properties 60

2.6.C. Properties Excluded from the Fits 63

2.6.C.1. Diffusion 68

2.6.C.2. Thermal Diffusion 69

2.6.C.3. Thermal Conductivity 69

2.6.C.4. Integral Cross Sections 69

2.6.D. Error Bounds for the Fitted Potentials 70

2.6.D.1. Systematic Errors 70

2.6.D.2. Model Bias and Potential Error Bounds 74

2.6.D.3. Comparison to Previous Best-Fit Potentials 77

2.7. Summary 80

Acknowledgements 81

Appendix A2. Influence of Data Included in the Multiproperty Fits 82

References 83

3. **The HeNe Interatomic Potential From Multiproperty Fits and Hartree-Fock Calculations** 90

3.1. Introduction 90

3.2. Experimental 93

3.2.A. Alberta Scattering Apparatus 93

Table of Contents (continued)

Chapter Page

3.2.B. Göttingen Scattering Apparatus 99

3.3. Hartree-Fock SCF Potential Calculations 101

3.4. Analysis 104

3.4.A. Interatomic Potential Parameterizations 104

3.4.B. Calculations of the Fitted Properties 106

3.4.C. Multiproperty Fitting 108

3.5. Data Selection 110

3.5.A. Differential Cross Sections 110

3.5.B. Integral Cross Sections 110

3.5.C. Dilute-Gas Properties 111

3.6. Results and Discussion 114

3.6.A. Fitted Properties 114

3.6.B. Fitted Interatomic Potentials 123

3.6.C. Properties Excluded From the Fits 125

3.6.C.1. Diffusion 125

3.6.C.2. Thermal Diffusion 127

3.6.C.3. Thermal Conductivity 127

3.6.D. Comparison to Literature Potentials 129

3.6.D.1. Numerical Potentials 129

3.6.D.2. Model Potentials 131

3.6.D.3. Fitted Potentials 131

3.7. Summary 134

Acknowledgements 136

Table of Contents (continued)

Chapter Page

References 137

4. **Sensitivity of Experimental Measurements in Fitting Interatomic Potential Energy Curves** 142

4.1. Introduction 142

4.2. Calculations 144

4.3. Results 148

4.3.A. Differential Cross Sections 148

4.3.B. Integral Cross Sections 150

4.3.C. Transport Properties 152

4.3.D. Interaction Virial Coefficients 154

4.4. Multiproperty Fitting Procedure 157

Acknowledgements 159

References 160

5. **Damping of Total Differential Cross Sections: Observations and Empirical Anisotropic Potentials for HeC_2H_2 and HeOCS** 162

5.1. Introduction 162

5.2. Experimental 165

5.2.A. Apparatus 165

5.2.B. Data Acquisition 169

5.3 Analysis 173

5.3.A. Scattering Calculations 173

5.3.B. Intermolecular Potentials 174

5.4. Results and Discussion 177

5.4.A. Data Reliability and Sensitivity 177

Table of Contents (continued)

Chapter Page

5.4.B. Diffraction Oscillations 179

5.4.C. Potential Energy Surfaces 180

5.5. Summary 189

Acknowledgements 190

References 191

6. **Anisotropic Intermolecular Potentials For HeC_2H_2, HeC_2H_4, and HeC_2H_6, and an Effective Spherical Potential for $HeCHF_3$ From Multiproperty Fits** 196

6.1. Introduction 196

6.2. Experimental 198

6.2.A. Crossed Beams Apparatus 198

6.2.B. Dilute-Gas Measurements 198

6.2.B.1. Diffusion 198

6.2.B.2 Second Virial Coefficients 201

6.3. Analysis 206

6.3.A. Intermolecular Potential Parameterizations 206

6.3.B. Calculations 208

6.3.C. Multiproperty Fitting 209

6.4. Results and Discussion 211

6.4.A. Total Differential Cross Sections 211

6.4.B. Dilute-Gas Data 215

6.4.C. Potential Energy Surfaces 218

6.4.D. Spherical Limit Potentials 222

6.5. Summary 224

Table of Contents (continued)

Chapter Page

Acknowledgements 225

References 226

7. **General Discussion** 230

References 237

APPENDIX A: **Experimental Details** 239

A.1. General 239

A.1.A. Design Considerations 239

A.1.B. Apparatus Description 245

A.2. Beam Nozzle and Skimmer Assemblies 249

A.2.A. Nozzle Assembly 249

A.2.B. Skimmer Manufacture and Mounting 251

A.3. Beam Characterizations 254

A.3.A. Mass Spectrometer Calibration 266

A.4. Scattering Chamber and Detector 278

A.4.A. The Bolometer Detector 279

A.4.B. Apparatus Angular Resolution 288

A.5. Experimental Procedure 291

References 297

APPENDIX B: **Experimental Data not yet Published** 299

References 303

LIST OF TABLES

Table Description Page

2-1. Beam Operating Conditions (He, Ar, Kr, and Xe) 35

2-2. Experimental Differential Cross Section Measurements (HeAr, HeKr, and HeXe) 39

2-3. Calculational Parameters 43

2-4. Assigned Error Bars for Dilute Gas Data (HeAr, HeKr, and HeXe) 52

2-5. Best-Fit Potential Parameters and Fitting Quality (HeAr, HeKr, and HeXe) 58

2-6. Fitting Quality for Mixture Diffusion (HeAr, HeKr, and HeXe) 66

2-7. Fitting Quality for Mixture Thermal Diffusion (HeAr, HeKr, and HeXe) 67

2-8. Error Bounds for the HeRg Potentials 76

2-9. Comparison Between Interatomic Potentials (HeAr, HeKr, and HeXe) 78

2-10. Effect of Data Sets used in Determining the HeXe Interatomic Potential 83

3-1. Beam Operating Conditions (He, ^{20}Ne, and ^{22}Ne) 94

3-2. Experimental Differential Cross Section Measurements (Alberta HeNe, Göttingen HeNe) 95

3-3. Summary of Hartree-Fock SCF Calculations on the HeNe Potential 103

3-4. Best-Fit Interatomic Potential Parameters (HeNe) 115

3-5. Interatomic Potentials and Fitting Qualities for HeNe 116

3-6. Fitting Qualities for Properties Excluded from the HFD1 Fits (HeNe) 126

4-1. Modification Types Characterized 146

5-1. Beam Operating Conditions (He, Ar, C_2H_2, CO_2, OCS) 167

List of Tables (continued)

Table Description Page

5-2. Intermolecular Potential Parameters ($HeCO_2$, HeC_2H_2, and HeOCS) 178

6-1. Beam Operating Conditions for DCS Measurements (He, C_2H_2, C_2H_4, C_2H_6, and CHF_3) 199

6-2. Experimental Total Differential Cross Section Measurements (HeC_2H_2, HeC_2H_4, HeC_2H_6, and $HeCHF_3$) 200

6-3. Least-Squares Coefficients for Eqn. (6-2) 202

6-4. Limiting Diffusion Coefficients (HeC_2H_2, HeC_2H_4, HeC_2H_6, and $HeCHF_3$) 203

6-5. Experimental Excess and Cross-Term Virial Coefficients (HeC_2H_4 and HeC_2H_6) 205

6-6. Best-Fit HFD Anisotropic Intermolecular Potential Parameters and Fitting Quality (HeC_2H_2, HeC_2H_4, and HeC_2H_6) 213

6-7. Spherical Limit Potential Parameters and Fitting Quality (HeC_2H_2, HeC_2H_4, HeC_2H_6, and $HeCHF_3$) 214

A-1. Optimized Beam Conditions (He, Ne, Ar, Kr, Xe, CO_2, OCS, C_2H_2, C_2H_4, C_2H_6, and CHF_3) 255

B-1. Measured DCS data for $HeCO_2$ and HeOCS 300

LIST OF FIGURES

Figure Page

2.1 Top View of Apparatus 32

2.2 Side View of Apparatus 33

2.3 Measured DCS's for HeAr, HeKr and HeXe 41

2.4 Best-Fit Interatomic Potentials for HeAr, HeKr and HeXe 57

2.5 Interaction Viscosity Data for HeAr, HeKr and HeXe 61

2.6 Interaction Second Virial Data for HeAr, HeKr and HeXe 62

2.7 Interaction Diffusion Data for HeAr, HeKr and HeXe 64

2.8 Equimolar Thermal Diffusion Data for HeAr, HeKr and HeXe 65

2.9 Integral Cross Section Data for HeAr, HeKr and HeXe 71

2.10 Error Bounds for the Fitted HeAr, HeKr and HeXe Interatomic Potentials 73

3.1 Differential Cross Sections for HeNe 98

3.2 HeNe Interatomic Potentials 117

3.3 Integral Cross Sections for HeNe 118

3.4 Limiting Diffusion Coefficients for HeNe 119

3.5 Interaction Viscosity Coefficients for HeNe 120

3.6 Interaction Second Virial Coefficients for HeNe 121

3.7 Equimolar Thermal Diffusion Data for HeNe 128

4.1 The Standard Model Potential for the Modifications 145

4.2 Differential Cross Sections Calculated from the Standard Potential and Modifications to it 149

4.3 Integral Cross Sections Calculated from the Standard Potential and Modifications to it 151

4.4 Mixture Transport Properties from the Model Potential 153

4.5 Interaction Second Virial Coefficients from the Model Potential 155

List of Figures (continued)

Figure Page

5.1 Schematic Diagram of the Apparatus 166

5.2 Differential Cross Sections for HeAr, HeC_2H_2, $HeCO_2$, and HeOCS 171

5.3 Anisotropic HFD Intermolecular Potential for HeC_2H_2 181

5.4 Anisotropic HFD Intermolecular Potential for HeOCS 182

5.5 Potential Energy Contour Plot of the HeC_2H_2 Potential 183

5.6 Potential Energy Contour Plot of the HeOCS Potential 184

6.1 Total Differential Cross Sections for $HeCHF_3$, HeC_2H_2 HeC_2H_4, and HeC_2H_6 212

6.2 Limiting Diffusion Coefficients for $HeCHF_3$, HeC_2H_2 HeC_2H_4, and HeC_2H_6 216

6.3 Interaction Virial Coefficients for HeC_2H_4 and HeC_2H_6 217

6.4 Anisotropic HFD Intermolecular Potentials for HeC_2H_2, HeC_2H_4, and HeC_2H_6 219

6.5 Spherical Limit HFD Potentials for HeC_2H_2, HeC_2H_4, HeC_2H_6, and $HeCHF_3$ 220

A.1 Side View of the Nozzle Skimmer Assembly 250

A.2 Flow Scans for He and Ar 258

A.3 Nozzle-Skimmer Scans for He and Ar 261

A.4 Velocity Distributions for Ar 263

A.5 Angular Profiles for He and Ar Beams 265

A.6 Mass Spectrometer Calibration With SF_6 270

A.7 Mass Spectrometer Calibration With the Rare Gases 271

A.8 Mass Spectrum for OCS (m/e ~ 9 amu to m/e ~ 30 amu) 273

A.9 Mass Spectrum for OCS (m/e ~ 24 amu to m/e ~ 62 amu) 274

List of Figures (continued)

Figure Page

A.10 Flight Time for the OCS Beam 276

A.11 Velocity Breadth of the OCS Beam 277

A.12 HeNe Differential Cross Section Measurements 287

A.13 Angular Resolution of the Apparatus 289

B.1 Differential Cross Section Measurements for $HeCO_2$ and HeOCS ... 302

CHAPTER 1

Introduction

1.1. GENERAL

Knowledge of the intermolecular potential is of fundamental importance for understanding the properties of gases, liquids, and solids.[1] In order to be of use, however, one must be able to determine the potential from the properties. For this reason, there has been much effort devoted, both experimentally and theoretically, over the past 60 years to the determination of accurate intermolecular potentials.[1-10] In this thesis, we have studied the interaction of thermal energy He atoms with other rare gas atoms (Ne, Ar, Kr, and Xe) and with several linear, or near linear, molecules (CO_2, OCS, C_2H_2, C_2H_4, and C_2H_6).

It has been recognized for a long time that the forces between two closed shell atoms can be represented by a function depending only upon their relative separation.[1,5] The function is composed of a steeply rising repulsive part at short range and an attractive force at long range. These two extremes are joined by the well region, which has a single minimum. The short range behaviour can be explained by the overlap of electron clouds. The Pauli exclusion principle prohibits some electrons from occupying the overlap region.[1] Consequently, the positively charged nuclei are incompletely shielded and exert a strong repulsive force on one another. The long range attraction is more difficult to explain. For spherically symmetric atoms, the only contribution to the long range attraction is the London dispersion force.[1] Since the electrons of an atom are in continuous motion around the nucleus, at any instant the atom will possess an instantaneous electric dipole.[1] This dipole may induce an instantaneous dipole in a second atom. The interaction of the instantaneous dipole with the induced instantaneous dipole produces an attractive energy called the dispersion or van der Waals energy.[1]

For an S-state atom interacting with a Σ-state molecule, the intermolecular potential depends not only on the relative separation, but also upon the relative orientation,[1] and internal coordinates of the molecule. The long range energy may have additional terms depending on the properties of the molecule, and also on its relative orientation. If the molecule possesses a permanent dipole moment, for example, there will be an induction contribution to the long range energy. The permanent dipole will induce a dipole in the atom and this dipole-induced dipole interaction will be attractive (called the induction energy).[1] As in the previous case, there will also be a dispersion energy, which is the only contribution present in all molecular interactions and is usually the largest contribution to the long range energy.[1]

Calculation of intermolecular potentials from *ab initio* calculations has not, as of yet (except for the simplest of systems), become practical for most interactions. For many systems, however, accurate calculations of the long range part of the potential are available.[11,12,13] The short range part of the potential can be obtained from self-consistent field (SCF)[7,14] calculations, which are difficult to perform for most systems and are therefore not available for very many interactions. A simple statistical method has been developed[15] that appears capable of giving reasonably reliable repulsive potentials. Consequently, an approach to determine intermolecular potentials has been developed that is based on experimentally measurable quantities. An analytical form is assumed for the intermolecular potential and the measured quantities are calculated using this potential. The parameters defining the model potential are then adjusted to provide the best possible agreement between the calculated and the measured data. The choice of the analytical function and the quality of the experimental data determine the usefulness of the intermolecular potential extracted.[1] A second, more appealing, technique to obtain intermolecular potentials is the direct inversion of the measured data.[16,17]

Direct inversion methods are not easy to apply to most systems however, and consequently the former method remains the most popular.

The choice of an analytical form for the intermolecular potential is not an easy one.[6] One need only review the HeAr system[6,18–21] to gain an appreciation for this point. Ideally, one would like to choose a potential that is soundly based on the theory of intermolecular forces. It must be realistic at short and long ranges and readily accomodate theoretical short range replusions and long range attractions, when these are available.[6] This, however, is true of many of the existing analytical forms.[6] The Hartree-Fock plus damped dispersion (HFD) potential form[19(c)] has shown considerable promise as the analytical potential of choice,[6] because it is physically based[19(c)] and exhibits realistic short and long range behaviours.

Assuming we can choose a good analytical form for the intermolecular potential,[6] the question arises as to what physically measurable properties could provide valuable information on the intermolecular forces. This discussion will be limited to those properties which have proven to be the most useful for this purpose.[1,3,22] The theory of equilibrium statistical mechanics leads to the virial expansion for the equation of state for a gas.[1] For an infinitely dilute gas, the virial expansion yields the ideal gas equation. Consequently, the higher order terms represent the effect of intermolecular interactions on the pressure of a gas. The second virial coefficient, B, is a direct measure of the effect of pairs of molecules on the pressure of the gas.[1,5] The second virial coefficient is therefore related to the intermolecular potential via equilibrium statistical mechanics.[23] Second virial coefficients have been calculated directly from PVT data for many gases and gas mixtures over a wide range of temperatures.[24]

Transport properties of dilute gases involve the transport of momentum (viscosity; η), kinetic energy (thermal conductivity; λ), and mass (diffusion;

D) under the influence of a gradient of velocity, temperature, and concentration respectively.[1] Thermal diffusion (α_T) involves the transport of mass along a temperature gradient.[1] The ease with which this motion occurs depends on the scattering of molecules by others in the gas. For sufficiently dilute gases, this scattering results from collisions between pairs of molecules. The transport properties are therefore determined by the intermolecular pair potential through the kinetic theory of dilute gases[1] and the Chapman-Enskog theory.[1] Of the transport properties, the viscosity has proved the easiest to measure accurately.[1,25] The remaining transport properties are, for the most part, difficult to measure accurately.[1] Recently, accurate diffusion coefficients near room temperature have been measured by Dunlop and co-workers for several systems.[26] Results of these measurements have been useful in the calculation of accurate intermolecular potentials.[26(b),27]

It has been over 70 years since the pioneering work of Dunoyer[28] and Stern[29] demonstrated the usefulness of atomic and molecular beams. The application of these techniques to gas kinetics has lead to a wealth of information on intermolecular forces.[1-10] With the production of supersonic nozzle beams[4] and good vacuum conditions, molecular beam experiments currently provide the most direct and detailed information for studying atom-atom and atom-molecule van der Waals interactions.[1,2,6,7,9,10,22,30,31] One can prepare the atoms or molecules of a beam, in the ideal case, with a specific set of properties (velocities and in some cases selected quantum states). The beams of atoms or molecules are then allowed to intersect under conditions ($P_{scat} \lesssim 10^{-6}$ torr) whereby only single collisions result between them. In contrast, the dilute-gas data discussed above may not be as sensitive to the pair potential since the observed quantities are averages over many collision events. Also, for crossed beam scattering, the observed scattering patterns show a number of interference effects due to the presence of both attractive and repulsive forces (see Chapter 2). The position, spacing, and amplitude of these interferences provides detailed information on the repulsive and attractive branches of the intermolecular potential (see Sec. 1.3). The observed quantities for the dilute-gas data are smooth and featureless (see Chapter 2) and therefore contain less detailed information on the pair potential. Consequently, studying the scattered atoms or molecules from crossed beam interactions in the framework of the dynamics and the Schrödinger equation for the system yields direct information on the pair potential.[1-3]

Measuring the number of particles scattered out of one of the beams by the other beam, into a particular angular direction, leads to a plot of the scattered intensity versus the scattering angle. Such a curve is called a differential cross section (DCS). Measuring the total amount of scattering in all directions versus the incident beam energy results in the integral cross section (ICS). This measurement is usually done by monitoring the loss of intensity (attenuation) of the incident beam due to the crossed beam for different incident beam energies.

The most detailed beam scattering data are provided by rotationally inelastic state-to-state DCS measurements,[32-34] or by DCS measurements of incompletely resolved rotational inelasticities.[35] Total DCS measurements, which do not resolve rotationally inelastic scattering from elastic scattering, are also very useful in extracting intermolecular potentials.[1,6,7,21,22,26(b),36-38] ICS's provide details on the pair interactions primarily for the potential well region.[22(b),39] DCS experiments yield information for broad ranges of the potential energy surfaces beyond their absolute minima.

The development of molecular beam electric resonance[40] (MBER) marked the begining of spectroscopic applications of molecular beams.[41(a)] This technique is used to characterize van der Waals complexes whose molecular partners possess permanent dipole[42,43] or quadrupole[44,45] moments. These experiments yield spectroscopic precision for bound states of van der Waals molecules in the region of their equilibrium configurations. Rotational inelastic cross sections studied with microwave spectroscopy have yielded valuable information on intermolecular pair potentials.[46] Ultraviolet and infrared spectroscopy on van der Waals dimers[47] have provided detailed information on their bound states. This information has proven to be a stringent test for pair potentials for these systems. Infrared photodissociation of van der Waals molecules also provides useful information about the equilibrium geometry of the molecules.[48] Collision broadening and the shifting of atomic spectral lines is an important process which is strongly related to the interaction pair potential.[49]

Another source of information on intermolecular forces comes from studying condensed phases, although this work is plagued by the problem of many-body forces. In particular, the detailed experimental[50] and theoretical[51] work for scattering of atoms by solid surfaces may become a discriminating test for pair potentials. The atom-surface potential is usually obtained by summing the pair interactions over the solid (i.e., the pair potential) and then adding a non-additive three-body correction term. The non-additive Axilrod-Teller triple-dipole term may not be well known[51(d)] however and therefore the inablility of the pair potential to generate the correct atom-surface potential cannot yet be used to discriminate between pair potentials. Consequently, the use of these data in determining accurate pair potentials is somewhat controversial at present.

The solid-state has traditionally played an important role in efforts to determine intermolecular forces.[1] The experimental data for the lattice properties of solid argon, for example, played a vital role in the development of pair potentials.[1,52] In order for these properties to be of use in the refinement of pair potentials, more realistic models, accounting for the many-body interactions, are necessary. The non-additive terms (correction terms to the pairwise sum over the surface) may be rather large for molecule systems[53] and therefore must be dealt with in order to accurately calculate solid-state properties. In this framework, studies of intermolecular forces from the solid-state for more complex molecules should provide a sensitive probe of the anisotropy of the molecular interactions,[54] since molecules are essentially fixed in specific relative orientations in the solid state. The accurate prediction of this behaviour, therefore, should be a sensitive test of the orientation dependence of intermolecular forces.

The liquid state has not proven to be a very useful source of information, to date, on intermolecular forces.[1] This is largely due to the complicated connection, via statistical mechanics, between molecular interactions and the structrue and properties of liquids.[1] This will probably remain the case until more suitable theories dealing with the many-body effects in the liquid state become available. The importance of the liquid state in determining or refining intermolecular pair potentials has nevertheless been recognized for a long time.[55] Measurements of the structural and thermodynamic data for the liquified inert gases have been made over wide temperature ranges.[56] These data, particularly those for argon, were used with simple model potentials assuming the validity of pairwise additivity, which has been shown to be invalid for liquid systems.[57] In recent years, there has been considerable interest in simple molecular fluids[58] and in simple liquid mixtures.[59] Thus the accurate prediction of the properties of the liquid state from intermolecular pair potentials may soon be possible.

This thesis presents interatomic and intermolecular potential energy surfaces for several systems. The DCS measurements, conducted in our laboratory, are supplemented by additional data from the literature (see Sec. 1.2) to extract these potentials, by adjusting parameters of an assumed analytical form.

Chapter 2 presents the apparatus and the results for HeAr, HeKr, and HeXe, fulfilling Aziz' call for high quality DCS measurements for these systems.[6] The HeNe system is the subject of Chapter 3, and provides a comparison between direct inversion techniques and multiproperty fitting techniques which adjust parameters of assumed mathematical forms to simultaneously fit several properties, and determine the interatomic potential. The sensitivity of the various properties, used in the two preceeding chapters, to the interatomic potential is examined in Chapter 4. Chapter 5 presents a preliminary study of the HeC_2H_2 and HeOCS systems, both of which were expected to be highly anisotropic based on their molecular lengths. It also demonstrates the consistency between our $HeCO_2$ results and partially resolved inelastic DCS measurements for this system. The following chapter presents intermolecular potential energy surfaces for HeC_2H_2, HeC_2H_4, HeC_2H_6, and $HeCHF_3$. These systems allow one to study the effect of molecular π bonds on the scattering cross sections compared to scattering data from open shell atoms with these same molecular partners. They also demonstrate the ineffectiveness of terminal hydrogens in extending the overall molecular length. Finally, a general discussion of all of this work is given in Chapter 7. Appendix A provides more detailed information about the apparatus, and Appendix B presents some, as of yet, unpublished total DCS data for $HeCO_2$ and HeOCS.

Section 1.2 of this chapter comments on the need for multiproperty fitting to extract accurate interatomic and intermolecular potentials. The last section of this chapter presents the theoretical connection between our measured total DCS's and the intermolecular pair potential.

1.2. MULTIPROPERTY FITTING

As discussed in Chapter 4, not all of the above mentioned properties provide information on the entire intermolecular potential. In particular, for thermal energy He atoms interacting with other rare gas atoms, DCS measurements are sensitive to the position of the attractive well and weakly repulsive wall up to ~ 20 meV, and are independently sensitive to the attractive well depth. The transports (viscosity, diffusion, thermal diffusion, thermal conductivity) and virials are sensitive to the repulsive wall up to ~ 100 meV, but not at all to the position of the attractive well and therefore complement the DCS measurements. Low temperature virial measurements are sensitive to the attractive well and outer bowl of the attractive well region. The ICS data can provide a stringent test of the attractive well region, and its outer bowl, commensurate with the reliability of its absolute calibration. From this study, one can see that there is a need to use a lot of experimental data to determine an accurate interatomic potential.[22,36,37(b)]

It is generally impossible to obtain an accurate intermolecular potential by fitting its parameters to only one property. Potentials determined in this way generally fail to reproduce the remaining properties within their experimental errors[22(a)] (see Appendix A2 at the end of Chapter 2). This has been demonstrated by the work of Pack et al. for SF_6 containing systems[36(a),36(b)] and Xe containing systems.[36(c)] It has also been commented on in Aziz' detailed review[6] on the rare gases. Consequently, one tries to use a number of properties which, in total, provide sensitivity to a wide range of the intermolecular pair potential.

The best-fit potentials reported in this thesis (with the exception of those in Chapter 5 and Chapter 6) were obtained by simultaneously fitting our measured DCS's, and literature mixture viscosities, and interaction second virials as a minimum data set. Sometimes ICS's and diffusions were also included in the fitting procedure. For the He + hydrocarbon data presented in Chapter 6, the interaction second virial and diffusion data were used along with our measured DCS's, to determine anisotropic intermolecular potential energy surfaces, as these were the only data available for these systems. The DCS constrains the position and depth of the attractive well, whereupon the virials and ICS's sensitively determine the outer bowl of the attractive well. The transports and virials together serve to fix the repulsive wall, once the attractive well position is established.

Multiproperty fitting will be discussed in more detail in Sec. 2.3.E and in Chapter 4.

1.3. THEORETICAL BACKGROUND

In order to understand how an accurate interatomic potential can be extracted from measured total DCS data, one must understand the theoretical connection of the interatomic potential to the DCS. In the following sections, the classical and quantal descriptions of scattering will be presented in a simplified manner. These sections are intended as a reference for the rather complex data reduction used for the results presented in this thesis. The simplest situation to examine theoretically is the elastic collision between a pair of particles interacting in a central-force field with a spherically symmetrical potential V(r). Separating the center-of-mass motion from the relative motion reduces the laboratory frame two-body problem to a one-body problem in the center-of-mass frame with reduced mass $\mu = \frac{m_1 m_2}{m_1 + m_2}$ and constant center-of-mass velocity.[1,60]

1.3.A. Classical Mechanics of Scattering

Considering the conservation of both energy and momentum in the above system leads to the following first-order differential equations,[1]

$$\frac{dr}{dt} = \pm \left[\frac{2}{\mu} \left\{ E - \frac{1}{2}\mu v^2 \frac{b^2}{r^2} - V(r) \right\} \right]^{1/2}, \qquad (1-1)$$

and,

$$\frac{d\theta}{dt} = \frac{L}{\mu r^2}, \qquad (1-2)$$

where E is the total energy, v is the initial relative velocity, b is the impact parameter which is the distance of closest approach in the absence of the potential V(r), θ is the orientation angle, and L is the angular momentum. The last two terms in Eq. (1-1) are generally grouped together in an effective potential U(L,r) $= \frac{1}{2}\mu v^2 \frac{b^2}{r^2} + V(r) = \frac{L^2}{2\mu r^2} + V(r)$, where the first term is the centrifugal potential energy.

Ultimately, we would like to know what the angle of deflection as a function of the impact parameter looks like, as this describes the scattering process. Combining Eqs. (1-1) and (1-2) gives,

$$\frac{\mathrm{d}\theta}{\mathrm{dr}} = \frac{\mathrm{d}\theta}{\mathrm{dt}}\frac{\mathrm{dt}}{\mathrm{dr}} = \pm\frac{L}{\mu \mathrm{r}^2}\left[\frac{2}{\mu}\left\{\mathrm{E} - \frac{1}{2}\mu v^2\frac{\mathrm{b}^2}{\mathrm{r}^2} - \mathrm{V(r)}\right\}\right]^{-1/2}, \qquad (1-3)$$

integrating and taking the asymptotic values of $\mathrm{E}(= \frac{1}{2}\mu v^2)$ and $\mathrm{L}(= \mu \mathrm{b}v)$, we have,

$$\chi(\mathrm{b}, v) = \pi - 2\mathrm{b}\int_{\mathrm{r}_0}^{\infty}\frac{\mathrm{dr}/\mathrm{r}^2}{\left\{1 - [\mathrm{b}^2/\mathrm{r}^2] - \left[\mathrm{V(r)}/\frac{1}{2}\mu v^2\right]\right\}^{1/2}}, \qquad (1-4)$$

where χ is the angle of deflection. This variation of χ with the impact parameter is called the classical deflection function. The classical turning point, r_0, is the distance of closest approach in the presence of the interaction potential, and is obtained by setting $\frac{\mathrm{dr}}{\mathrm{dt}} = 0$ in Eq. (1-1). The classical deflection function can describe the trajectories of scattered particles in terms of their impact parameter and collision energy. In particular, for potentials having both attractive and repulsive branches, collisions leading to large positive χ values can be attributed to the repulsive part of the interatomic potential for small impact parameters (or low values of L). As the impact parameter increases, the deflection χ decreases until at some point there is no net deflection. At still larger values of the impact parameter, χ passes through a minimum (called the rainbow angle, χ_{r}) and converges to zero as b goes to infinity.[1]

The definition of the differential cross-section $\sigma(\chi, \mathrm{E})$ is given by,[1]

$$\sigma(\chi, \mathrm{E}) = \frac{[\text{Number of scattered particles/unit time}]\text{/unit solid angle}}{[\text{Number of incident particles/unit time}]\text{/unit area.}} \qquad (1-5)$$

All scattering into a solid angle $\mathrm{d}\Omega$, projected by an angle $\mathrm{d}\chi$ centered on χ, comes from an annular area of $2\pi b db$.[1] Since $d\Omega = 2\pi \sin\chi d\chi$, we have,

$$\sigma(|\chi|, E) = \left|\frac{2\pi b I_0 db / 2\pi \sin\chi d\chi}{I_0}\right| = \left|\frac{b}{\sin\chi (d\chi/db)}\right| , \qquad (1-6)$$

where I_0 is the incident flux ([particles/unit time]/unit area). The integral cross-section, Q(E), is a measure of all the scattering irrespective of angle, and is simply the integral of $\sigma(\chi, E)$ over all solid angles,[1]

$$Q(E) = \int \sigma(\chi, E) d\Omega = \int_0^{\pi} \sigma(\chi, E) 2\pi \sin\chi d\chi \, . \qquad (1-7)$$

The classical DCS becomes singular on two occasions; (i) the glory effect arises when $\sin\chi \rightarrow 0$ and (ii) the rainbow angle occurs when $d\chi/db = 0$. As long as $|\chi| < \chi_r$, there are three impact parameters which lead to the same value of $|\chi|$ for the same collision energy. Since experimentally one cannot distinguish the sign of χ, these three impact parameters will lead, in a quantum description of the scattering, to interference in the observed DCS. Although the classical description provides useful insights into the qualitative features of the DCS, it cannot be used to account for the DCS's observed for systems as quantum as the He containing systems discussed in this thesis.

1.3.B. Quantum Mechanics of Scattering

1.3.B.1. Atom + Atom Scattering

For the systems considered in this thesis, a classical description of the scattering fails to explain the observed DCS's, since the potential energy changes significantly over the de Broglie wavelength (~ 0.6 Å, calculated from the de Broglie hypothesis for He with a velocity of 1775 m/sec). The breakdown of the classical description is a manifestation of the uncertainty principle in that both the impact parameter, b, and the deflection angle, χ, cannot be simultaneously well defined. Therefore, we will outline the basics of a quantum mechanical description of scattering in the next few paragraphs. As in the classical description above, we shall consider the scattering in the center-of-mass frame. It is worth noting, that simple Fraunhoffer diffraction theory can predict the position of the oscillations, observed in atom + atom scattering, reasonably well for low angle oscillations (see Appendix A, Sec. A.1.A).

A full quantum treatment of elastic scattering for a spherically symmetric potential describes the system in terms of a wave function $\Psi(\mathbf{r})$ which depends only on the relative position $\mathbf{r}$ of the particle.[1] The Schrödinger equation is given by,

$$\left(-\frac{\hbar^2}{2\mu}\nabla^2 + V(r)\right)\Psi(\mathbf{r}) = E\Psi(\mathbf{r}) \qquad (1-8)$$

where $\nabla^2 = \frac{1}{r^2}\frac{\partial}{\partial r}\left(r^2\frac{\partial}{\partial r}\right) - \frac{\hat{L}^2}{r^2\hbar^2}$, with $\hat{L}^2$ the angular momentum operator. The boundary conditions of $\Psi(\mathbf{r})$ require;

$$\Psi(\mathbf{r}) = 0 \ , \qquad r \rightarrow 0 \ , \qquad (1-9)$$

$$\Psi(\mathbf{r}) = \Psi^0(\mathbf{r}) + \frac{f(\theta)e^{ikr}}{r} \ , \qquad r \rightarrow \infty \qquad (1-10)$$

where $\Psi^0(\mathbf{r})$ is the wavefunction in the absence of $V(r)$, $f(\theta)$ is the scattering amplitude, and $\mathbf{k}$ is the wavevector.[1] The magnitude of $\mathbf{k}$ is known as the wavenumber and corresponds to the particle momentum,

$$k = \frac{(2\mu E)^{1/2}}{\hbar} \ . \qquad (1-11)$$

The intensity of a wave with eigenfunction Ψ is Ψ^2 and the flux is $\Psi^2 v$, where v is the wave velocity. The incident flux is therefore just v since $|\Psi^0(\mathbf{r})|^2 = 1$, i.e., $\Psi^0(\mathbf{r})$ is normalized. Similarly, the scattered flux is given by $|\frac{f(\theta)}{r}|^2 v$. As in the classical description given earlier, the area of the annular region leading to scattering is $2\pi r^2\sin\theta d\theta$ which has been scattered into a solid angle of $2\pi\sin\theta d\theta$. Recalling the definition of the differential cross-section (Eq. 1-5) leads to the following expression for the quantal differential cross-section,

$$\sigma(\theta,E) = |f^k(\theta)|^2 \ , \qquad (1-12)$$

where the superscript k on the scattering amplitude, $f(\theta)$, indicates that it depends on the energy. It follows from the definition of the integral cross-section that,

$$Q(E) = \int \sigma(\theta,E)d\Omega = \int_0^\pi 2\pi|f^k(\theta)|^2\sin\theta d\theta \ . \qquad (1-13)$$

The entire objective of the quantum mechanical treatment of scattering is therefore to determine $|f^k(\theta)|$, just as in the classical description it was to find the deflection function $\chi(b)$. In other words, the Schrödinger equation must be solved for $\Psi(\mathbf{r})$.[1]

Multiplying the wave equation (Eq. 1-8) by $\frac{2\mu}{\hbar^2}$ gives,

$$(\nabla^2 + k^2 - u(r))\Psi(\mathbf{r}) = 0 \ . \qquad (1-14)$$

where $u(r) = V(r)\frac{2\mu}{\hbar^2}$. Expanding the wave equation in terms of partial waves, each of which corresponds to a particular angular momentum state of the system gives,

$$\Psi(\mathbf{r}) = \frac{1}{r}\sum_{\ell=0}^{\infty} C_\ell \psi_\ell(r) P_\ell(\cos\theta) \qquad (1-15)$$

where C_ℓ are the amplitudes of the partial waves $\psi_\ell(r)$, $P_\ell(\cos\theta)$ are the Legendre polynomials,[1] and ℓ is the angular momentum quantum number. Substituting Eq. (1-15) into Eq. (1-14) leads to a set of equations,

$$\left(\frac{d^2}{dr^2} + k^2 - u_\ell(r)\right)\psi_\ell(r) = 0 \qquad (1-16)$$

where $u_\ell(r) = u(r) + \frac{\ell(\ell+1)}{r^2}$.

Equation (1-16) is called the partial wave equation and can be solved as follows. Providing $ru(r) \rightarrow 0$ as $r \rightarrow \infty$ the solution of the partial wave equation for each partial wave is given by,[1]

$$\psi_\ell(r) \cong \sin(kr + \delta_\ell) \qquad (1-17)$$

where δ_ℓ is the relative phase of the incoming and outgoing parts of $\psi_\ell(r)$. If $u(r) = 0$, then the partial wave equation has the following solutions[1]

$$\psi_\ell^0(r) \cong \sin(kr - \ell\pi/2) \qquad (1-18)$$

where $-\ell\pi/2$ is δ_ℓ^0, the phase term due solely to the centrifugal contribution $\frac{\ell(\ell+1)}{r^2}$. The phase shift caused by the potential is therefore,

$$\eta_\ell = \delta_\ell - \delta_\ell^0 = \delta_\ell + \ell\pi/2. \qquad (1-19)$$

Asymptotically then,

$$\psi_\ell(r) \cong \sin(kr + \eta_\ell - \ell\pi/2). \qquad (1-20)$$

The coefficients C_ℓ in Eq. (1-15) may be determined from the normalization condition for $\Psi(\mathbf{r})$, $\int \Psi\Psi^* dr = 1$, and from the orthogonality of the Legendre polynomials. This leads to

$$f^k(\theta) = \frac{1}{2ik} \sum_{\ell=0}^{\infty} (2\ell + 1) \left(e^{2i\eta_\ell} - 1\right) P_\ell(\cos\theta) \ , \qquad (1-21)$$

and also from the orthogonality of Legendre polynomials,

$$Q(E) = \frac{4\pi}{k^2} \sum_{\ell=0}^{\infty} (2\ell + 1)\sin^2\eta_\ell \ . \qquad (1-22)$$

In the quantum mechanical treatment, we can see that the phase shift, η_ℓ, plays a very major role.

The determination of the scattering phase shifts can be made by comparing the asymptotic behaviour of the radial wavefunctions (the $u_\ell(r)$ satisfying Eq. 1-16), with the corresponding $V(r) = 0$ solutions. The $u_\ell(r)$ can be obtained by direct numerical integration of Eq. (1-16). The phase shifts may also be obtained from the JWKB approximation,[1,4,61] although at low ℓ values they are not sufficiently accurate for the systems studied in this thesis. This then completes the link between the interatomic potential and the DCS in the forward sense.

The computational procedure for obtaining DCS's is thus quite straightforward. For an assumed interatomic potential, the Schrödinger equation (Eq. 1-16) is numerically integrated for each ℓ to obtain the partial wave phase shifts. These are then used to obtain the DCS by direct substitution into Eq. (1-21), as per Eq. (1-12). This DCS, calculated in the center-of-mass frame, is transformed to the laboratory frame and compared with the measured DCS. Prior to this comparison, the calculated DCS must be averaged over the apparatus angular resolution and the relative velocity distributions of the beams. The comparison between the calculated and measured DCS's is optimized by adjusting parameters of the assumed mathematical form (for the HFD potential these parameters are: the repulsive wall, α; the minimum position, r_m; and the long range, C_8).

1.3.B.2. Atom + Molecule Scattering

For the scattering of an S-state atom by a Σ-state molecule, we have used the infinite-order sudden approximation (IOSA) which has been described in detail elsewhere.[1,62,63] We have also assumed that the molecule is a rigid rotor leading to the following Schrödinger equation,

$$\left(-\frac{\hbar^2}{2\mu_{12}r}\frac{\partial^2}{\partial r^2}r + \frac{L^2}{2\mu_{12}r^2} + \frac{J^2}{2I} + V(r,\gamma)\right)\Psi(r,\gamma) = E\Psi(r,\gamma) \qquad (1-23)$$

where μ_{12} and **L** are the reduced mass and orbital angular momentum, respectively, of the atom relative to the molecule.[37(b)] The total angular momentum **J** is the sum of the molecular angular momentum J and the orbital angular momentum **L**; $\mathbf{J} = J + \mathbf{L}$. The moment of inertia of the rigid rotor is **I** and V(r,γ) is the intermolecular potential where γ is the angle between the molecular axis and the relative separation vector **r**.

In the IOSA, one makes both the centrifugal sudden (CS)[1,62]

$$\mathbf{L}^2 = \hbar^2 \bar{\ell}(\bar{\ell} + 1) \qquad (1-24)$$

and energy sudden (ES)[1,62]

$$J^2 = \hbar^2 \bar{j}(\bar{j} + 1) \qquad (1-25)$$

approximations. That is, one replaces the angular momentum operators by their eigenvalue forms. The CS approximation assumes that the relative kinetic energy is so large that the precise value of the centrifigal potential is not important. This allows one to replace ℓ by some average value $\bar{\ell}$ usually chosen as the initial value of ℓ, ℓ_0. The ES approximation has the effect of replacing all of the wavenumbers k by a single average value $\bar{k}$. These two approximations used together remove the operators, from Eq. (1-23), which depend on the angle γ. Therefore, Eq. (1-23) depends on γ only parametrically through V(r, γ).[62] This results in the single uncoupled ordinary differential equation,

$$\left[\frac{d^2}{dr^2} + \bar{k}^2 - \frac{\bar{\ell}(\bar{\ell}+1)}{r^2} - \frac{2\mu_{12}}{\hbar^2} V(r,\gamma)\right] g_{\bar{\ell}}^{\bar{k}}(r,\gamma) = 0 \ , \qquad (1-26)$$

with

$$\bar{k}^2 = \frac{2\mu_{12}}{\hbar^2}\left(E - \frac{\hbar^2 \bar{j}(\bar{j}+1)}{2I}\right) \qquad (1-27)$$

a measure of the incident relative kinetic energy. One should notice the similarity between Eqs. (1-26) and (1-16).

Equation (1-26) must be solved for the radial wavefunctions $g_\ell^{\bar{k}}(r,\gamma)$, subject to the boundary conditions,

$$g_\ell^{\bar{k}}(r,\gamma) = 0 \ , \qquad r \rightarrow 0 \ , \tag{1 – 28}$$

and

$$g_\ell^{\bar{k}}(r,\gamma) = \bar{k}^{(-1/2)} \left\{ e^{-i(\bar{k}r - \ell\pi/2)} - e^{-[(\bar{k}r - \ell\pi/2 + 2i\eta_\ell^{\bar{k}}(\gamma)]} \right\} \ , \qquad r \rightarrow \infty \ . \tag{1 – 29}$$

These conditions lead to an expression for the scattering amplitude for a fixed orientation angle γ as,[62]

$$f^{\bar{k}}(\gamma|\theta) = \frac{i}{2\bar{k}} \sum_{\ell=0}^{\infty} (2\ell+1) \left[1 - e^{2i\eta_\ell^{\bar{k}}(\gamma)} \right] P_\ell(\cos\theta) \tag{1 – 30}$$

where $\eta_\ell^{\bar{k}}(\gamma)$ is the phase shift for a fixed orientation angle γ. As in the previous case, the problem has been reduced to one of finding the scattering phase shifts for each γ. As shown by Keil and Parker,[37(b)] the DCS out of a rotational state j is independent of j. The total DCS is therefore given by the weighted orientation average,[62(b)]

$$\sigma(\theta) = \frac{1}{2} \int_{-1}^{1} \sigma(\gamma,\theta) d(\cos\gamma) \tag{1 – 31}$$

where

$$\sigma(\gamma,\theta) = |f^{\bar{k}}(\gamma|\theta)|^2 \ . \tag{1 – 32}$$

Similarly, the integral cross section is given by,

$$Q = \frac{1}{2} \int_{-1}^{1} Q(\gamma) d(\cos\gamma) \tag{1 – 33}$$

where

$$Q(\gamma) = \frac{4\pi}{k^2} \sum_{\ell=0}^{\infty} (2\ell + 1) \sin^2 \eta_\ell^{\bar{k}}(\gamma) \,. \qquad (1-34)$$

As in the atom + atom case, the connection between the intermolecular potential and the DCS is quite straightforward. One simply calculates the cross section for fixed γ, using the simple formulas given above, and then averages over γ.

The IOSA is expected to be valid whenever the relative kinetic energy is large, (i) compared to the rotational energy level spacing of the molecule (the ES approximation), and (ii) compared to the differences in the centrifugal potentials (the CS approximation).[62(b)] In other words, for the IOSA to be valid under point (ii), rotational transitions of the molecule should be dominated by small values of the orbital angular momentum. For the atom + molecule systems presented in this thesis, the relative kinetic energy is ~ 70 meV whereas the rotational energy spacing of the molecules ranges from ~ 1 meV for OCS to ~ 6 meV for C_2H_4. The relative kinetic energy is also ~ 20 times greater than the well depths of the atom + molecule interactions studied herein. The ES approximation therefore appears reasonable for the systems studied in this thesis, being worst for the C_2H_4 interaction.[26(b)] The CS approximation is a good one when the collisions are dominated by the short-range part of the potential.[1] The validity of the CS approximation increases with the relative kinetic energy. Generally, as long as the relative kinetic energy is large compared to the well depth, the CS approximation will be valid.[1] Consequently, for the systems presented in this work, one would expect the CS approximation to be a reasonable one also.

The IOSA has been compared favorably with close-coupling or coupled states calculations for thermal energy HeHF,[64] HeH_2,[65] HeCO,[66] $HeCO_2$,[62(b),62(d)] and HeN_2[67] interactions. In the case of HF and H_2, the rotational energy spacings are ~ 9 meV and ~ 28 meV respectively. The HF spacings are similar to our

C_2H_2 and C_2H_4 beams, while the H_2 spacings are large compared to our molecular systems. Our use of the IOSA therefore appears quite reasonable.

References

1. G.C. Maitland, M. Rigby, E.B. Smith, and W.A. Wakeham, *Intermolecular Forces: Their Origin and Determination* (Clarendon, Oxford, 1981).
2. (a) *Atom-Molecule Collision Theory: A Guide for the Experimentalist*, edited by R.B. Bernstein (Plenum, New York, 1979); (b) R.B. Bernstein, *Chemical Dynamics via Molecular Beam and Laser Techniques* (Clarendon, Oxford, 1982).
3. Adv. Chem. Phys. **12**, *Intermolecular Forces*, edited by J.O. Hirschfelder (Interscience, New York, 1967).
4. Adv. Chem. Phys. **10**, *Molecular Beams*, edited by J. Ross (Interscience, New York, 1966), particularly chapters 2, 3, 8 and 9.
5. J.O. Hirschfelder, G.F. Curtiss, and R.B. Bird, *Molecular Theory of Gases and Liquids* (Wiley, New York, 1954).
6. R.A. Aziz, in *Inert Gases: Springer Series in Chemical Physics*, edited by M. Klein (Springer, Berlin, 1984); Vol. **34**.
7. G. Scoles, Annu. Rev. Phys. Chem. **31**, 81 (1980).
8. U. Buck in Adv. Chem. Phys., edited by K.P. Lawley (Interscience, New York, 1975); Vol. **30**.
9. M. Faubel, Adv. Atomic Mol. Phys. **19**, 345 (1983).
10. *Van der Waals Molecules*, Faraday Disc. Chem. Soc. **73** (1982).
11. (a) R.E. Johnson, S.T. Epstein, and W.J. Meath, J. Chem. Phys. **47**, 1271 (1967); (b) G.F. Thomas and W.J. Meath, Mol. Phys. **34**, 113 (1977); (c) G.D. Zeiss and W.J. Meath, Mol. Phys. **33**, 1155 (1977); (d) D.J. Margoliash and W.J. Meath, J. Chem. Phys. **68**, 1426 (1978); (e) B.L. Jhanwar and W.J. Meath, Mol. Phys. **41**, 1061 (1980); (f) A. Kumar and W.J. Meath,

Chem. Phys. **91**, 411 (1984); (g) A. Kumar and W.J. Meath, Mol. Phys. **54**, 823 (1985).

12. (a) K.T. Tang, J.M. Norbeck, and P.R. Certain, J. Chem. Phys. **64**, 3063 (1976); (b) J.M. Standard and P.R. Certain, J. Chem. Phys. **83**, 3002 (1985).
13. R.T Pack, J. Chem. Phys. **64**, 1659 (1976).
14. I.N. Levine, *Quantum Chemistry* (Allyn and Bacon, Inc., Toronto, Ontario, 1983), Chapter 11.
15. (a) V.I. Gaydaenko and V.K. Nikulin, Chem. Phys. Lett. **7**, 360 (1970); (b) R.G. Gordon and Y.S. Kim, J. Chem. Phys. **56**, 3122 (1972).
16. U. Buck, Rev. Mod. Phys. **46**, 369 (1974).
17. G.C. Maitland and W.A. Wakeham, Mol. Phys. **35**, 1429; 1443 (1978).
18. C.H. Chen, P.E. Siska, and Y.T. Lee, J. Chem. Phys. **59**, 601 (1973).
19. (a) K.M. Smith, A.M. Rulis, G. Scoles, R.A. Aziz, and G. Duquette, J. Chem. Phys. **63**, 2250 (1975); (b) K.M. Smith, A.M. Rulis, G. Scoles, R.A. Aziz, and V. Nain, J. Chem. Phys. **67**, 152 (1977); (c) R. Ahlrichs, R. Penco, and G. Scoles, Chem. Phys. **19**, 119 (1977).
20. M. Keil, J.T. Slankas, and A. Kuppermann, J. Chem. Phys. **70**, 482 (1979).
21. R.A. Aziz, P.W. Riley, U. Buck, G. Maneke, J. Schleusener, G. Scoles, and U. Valbusa, J. Chem. Phys. **71**, 2637 (1979).
22. (a) L.J. Danielson and M. Keil, J. Chem. Phys. **88**, 851 (1988); (b) M. Keil and L.J. Danielson, Can. J. Phys. **66**, 159 (1988).
23. D.A. McQuarrie, *Statistical Mechanics* (Harper and Row, New York, 1976).
24. J.H. Dymond and E.B. Smith, *The Virial Coefficients of Pure Gases and Mixtures* (Clarendon, Oxford, 1980).
25. (a) G.C. Maitland and E.B. Smith, J. Chem. Eng. Data **17**, 150 (1972); (b) R.A. Dawe and E.B. Smith, J. Chem. Phys. **52**, 693 (1970); (c) J.

Kestin, S.T. Ro, and W.A. Wakeham, J. Chem. Phys. **56**, 4119 (1972); (d) J. Kestin, R. Paul, A.A. Clifford, and W.A. Wakeham, Physica **100A**, 349 (1980); (e) J. Kestin, H.E. Khalifa, S.T. Ro, and W.A. Wakeham, Physica **88A**, 242 (1978).

26. (a) P.S. Arora, H.L. Robjohns, and P.J. Dunlop, Physica **95A**, 561 (1979); (b) L.J. Danielson, M. Keil, and P.J. Dunlop, J. Chem. Phys. **88**, 4218 (1988).
27. M. Keil, L.J. Danielson, U. Buck, J. Schleusener, F. Huisken, and T.W. Dingle, in preparation for submission to J. Chem. Phys.
28. L. Dunoyer, Comptes Rendus **152**, 594 (1911).
29. O. Stern, Z. für Physik **39**, 751 (1926).
30. L. Eno and H. Rabitz, J. Chem. Phys. **74**, 3859 (1981).
31. (a) R.B. Gerber, M. Shapiro, U. Buck, and J. Schleusener, Phys. Rev. Lett. **41**, 236 (1978); (b) R.B. Gerber, V. Buch, and U. Buck, J. Chem. Phys. **72**, 3596 (1980).
32. U. Buck, H. Meyer, and R.J. LeRoy, J. Chem. Phys. **80**, 5589 (1984).
33. U. Hefter, G. Ziegler, A. Mattheus, A. Fischer, and K. Bergmann, J. Chem. Phys. **85**, 286 (1986); A. Mattheus, A. Fischer, G. Zeigler, E. Gottwald, and K. Bergmann, Phys. Rev. Lett. **56**, 712 (1986).
34. M. Faubel, K.H. Kohl, J.P. Toennies, and F.A. Gianturco, J. Chem. Phys. **78**, 5629 (1983).
35. (a) U. Buck, H. Meyer, M. Tolle, and R. Schinke, Chem. Phys. **104**, 345 (1986); (b) U. Buck, D. Otten, R. Schinke, and D. Poppe, J. Chem. Phys. **82**, 202 (1985).
36. (a) R.T Pack, J.J. Valentini, and J.B. Cross, J. Chem. Phys. **77**, 5486 (1982); (b) R.T Pack, E. Piper, G.A. Pfeffer, and J.P. Toennies, J. Chem.

Phys. **80**, 4940 (1984); (c) R.T Pack, J.J. Valentini, C.H. Becker, R.J. Buss, and Y.T. Lee, J. Chem. Phys. **77**, 5475 (1982).

37. (a) G.A. Parker, M. Keil, and A. Kuppermann, J. Chem. Phys. **78**, 1145 (1983); (b) M. Keil and G.A. Parker, J. Chem. Phys. **82**, 1947 (1985).
38. L. Beneventi, P. Casavecchia, and G.G. Volpi, J. Chem. Phys. **85**, 7011 (1986).
39. (a) F. Pirani and F. Vecchiocattivi, J. Chem. Phys. **66**, 372 (1977); (b) R. Düren, R. Helbing, and H. Pauly, Z. für Physik, **188**, 468 (1965); (c) R.W. Landorf and C.R. Mueller, J. Chem. Phys. **45**, 240 (1966); (d) M.G. Dondi, G. Scoles, and F. Torello, J. Chem. Phys. **51**, 392 (1969); (e) R.S. Grace, D.L. Johnson, and J.G. Skofronick, J. Chem. Phys. **67**, 2443 (1977).
40. H.K. Hughes, Phys. Rev. **72**, 614 (1947).
41. (a) R.E. Miller, Ph.D. Thesis, Waterloo, Ontario, 1980; (b) G. Fischer, R.E. Miller, P.F. Vohralik, and R.O. Watts, J. Chem. Phys. **83**, 1471 (1985); (c) R.E. Miller, P.F. Vohralik, and R.O. Watts, J. Chem. Phys. **80**, 5453 (1984); (d) F. Huisken, H. Meyer, C. Lauenstein, R. Sroka, and U. Buck, J. Chem. Phys. **84**, 1042 (1986).
42. S.J. Harris, K.C. Janda, S.E. Novick, and W. Klemperer, J. Chem. Phys. **63**, 881 (1975).
43. E.J. Campbell, A.C. Legon, and W.H. Flygare, J. Chem. Phys. **78**, 3494 (1983).
44. J.M. Steed, T.A. Dixon, and W. Klemperer, J. Chem. Phys. **70**, 4095 (1979).
45. R.L. DeLeon and J.S. Muenter, J. Chem. Phys. **72**, 6020 (1980).
46. (a) L.H. Scharpen, J.S. Muenter, and V.W. Laurie, J. Chem. Phys. **53**, 2513 (1970); (b) A. Picard-Bersellini and B.J. Whitaker, J. Mol. Struct. **115**, 347 (1984); (c) M. Broquier, A. Picard- Bersellini, and B.J. Whitaker, J. Chem. Phys. **84**, 2104 (1986).

47. (a) Y. Tanaka and K. Yoshino, J. Chem. Phys. **57**, 2964 (1972); (b) A.R.W. McKellar and H.L. Welsh, Can. J. Phys. **52**, 1082 (1974) and **50**, 1458 (1972).

48. C.M. Western, M.P. Casassa, and K.C. Janda, J. Chem. Phys. **80**, 4781 (1984).

49. (a) A. Bielski, W. Dokurno, J. Szudy, and J. Wolnikowski, Physica **101C**, 113 (1980); (b) M.L. Mandich and G.W. Flynn, J. Chem. Phys. **73**, 3679 (1980).

50. (a) T.H. Ellis, S. Iannota, G. Scoles, and U. Valbusa, Phys. Rev. **B 24**, 2307 (1981); (b) T.H. Ellis, G. Scoles, and U. Valbusa, Chem. Phys. Lett. **94**, 247 (1983); (c) T.H. Ellis, G. Scoles, and U. Valbusa, Surf. Sci. **118**, L251 (1982); (d) G. Bracco, P. Cantini, A. Glachant, and R. Tatarek, Surf. Sci. **125**, L81 (1983); (e) G. Bracco, P. Cantini, E. Cavanna, R. Tatarek, and A. Glachant, Surf. Sci. **136**, 169 (1984); (f) J.Z. Larese, W.Y. Leung, D.R. Frankl, N. Holter, S. Chung, and M.W. Cole, Phys. Rev. Lett. **54**, 2533 (1985); (g) J.C. Ruiz, Ph.D. Thesis, University of Waterloo (1987); (h) S.J. Sibener, private communication.

51. (a) J.M. Hutson and C. Schwartz, J. Chem. Phys. **79**, 5179 (1983); (b) H. Jónsson, J.H. Weare, T.H. Ellis, G. Scoles, and U. Valbusa, Phys. Rev. **B 30**, 4203 (1984); (c) T.H. Ellis, G. Scoles, U. Valbusa, H. Jónsson, and Weare, Surf. Sci. **155**, 499 (1985); (d) H. Jónsson and J.H. Weare, Farad. Disc. Chem. Soc. **80**, 29 (1985); (e) S. Chung, N. Holter, and M.W. Cole, Phys. Rev. **B 31**, 6660 (1985).

52. J.A. Barker and A. Pompe, Aust. J. Chem. **21**, 1683 (1968).

53. P.A. Monson and M. Rigby, Mol. Phys. **39**, 1163 (1980).

54. J.C. Raich and N.S. Gillis, J. Chem. Phys. **66**, 846 (1977).

55. (a) J.A. Barker and D. Henderson, Rev. Mod. Phys. **48**, 587 (1976); (b) J.P. Hansen and I.R. McDonald, *Theory of Simple Liquids* (Academic Press, London, 1969).

56. (a) W.B. Street and L.A.K. Stavely, J. Chem. Phys. **50**, 2302 (1969); (b) R.K. Crawford and W.B. Daniels, J. Chem. Phys. **50**, 3171 (1969).

57. J.A. Barker, R.A. Fisher, and R.O. Watts, Mol. Phys. **21**, 657 (1971).

58. (a) W.B. Street and K.E. Gubbins, Ann. Rev. Phys. Chem. **28**, 373 (1977); (b) D. Chandler, Ann. Rev. Phys. Chem. **29**, 441 (1978).

59. J.K. Lee, D. Henderson, and J.A. Barker, Mol. Phys. **29**, 429 (1975).

60. H. Goldstein, *Classical Mechanics* 2nd ed. (Addison-Wesley Publishing Co., Don Mills, Ontario, 1980).

61. L.I. Schiff, *Quantum Mechanics* (McGraw-Hill, New York, 1968), Chapters 5 and 9.

62. (a) R.T Pack, J. Chem. Phys. **60**, 633 (1974); (b) G.A. Parker and R.T Pack, J. Chem. Phys. **68**, 1585 (1978); (c) T.P. Tsein, G.A. Parker, and R.T Pack, J. Chem. Phys. **59**, 5373 (1973); (d) R.T Pack, J. Chem. Phys. **66**, 1557 (1977).

63. P. McGuire and D.J. Kouri, J. Chem. Phys. **60**, 2488 (1974).

64. (a) F. Battaglia, F.A. Gianturco, and A. Palma, J. Chem. Phys. **80**, 4997 (1984); (b) C.V. Boughton, R.E. Miller, P.F. Vohralik, and R.O. Watts, Mol. Phys. **58**, 827 (1986).

65. (a) J.M. Bowman and S.C. Leasure, J. Chem. Phys. **66**, 288 and 4724 (1977); (b) S.C. Leasure and J.M. Bowman, Chem. Phys. Lett. **48**, 179 (1977); (c) G. Pfeffer and D. Secrest, J. Chem. Phys. **67**, 1394 (1977).

66. (a) R. Goldflam, S. Green, and D.J. Kouri, J. Chem. Phys. **67**, 4149 (1977); (b) V. Khare, D.E. Fitz, and D.J. Kouri, J. Chem. Phys. **73**, 2802 (1980).

67. M. Faubel, K.H. Kohl, and J.P. Toennies, Faraday Discuss. Chem. Soc. **73**, 205 (1982).

CHAPTER 2

Interatomic Potentials for HeAr, HeKr, and HeXe from Multiproperty Fits†

2.1. INTRODUCTION

The importance and interest in accurate interatomic potentials can easily be garnered from the large number of recent articles and reviews on this topic.[1–9] In a recent review, Aziz[1] has detailed the current state of our knowledge for the rare-gas two-body interatomic potentials. He concludes that the HeAr interaction is one of the best characterized of the rare-gas mixtures largely because of high-resolution differential cross section (DCS) measurements.[5]

In this work, we report new high-resolution DCS measurements for HeAr, HeKr, and HeXe elastic scattering. The HeAr results confirm the reliability of the previous potential,[1,5] and establish the validity and accuracy of the present work. The HeKr and HeXe studies fulfill Aziz' call for high quality DCS measurements for these systems. The potentials obtained are valuable in providing accurately determined spherical reference systems to which nonspherical atom-molecule interactions may be compared.[10–14] They are also of particular importance in understanding the detailed experimental[15] and theoretical[16] work for scattering of atoms by rare-gas overlayers grown on graphite and metal surfaces. Finally, we remark that reliable interatomic potentials can facilitate dynamical understanding of van der Waals bond exchange in collisions between rare gas atoms and molecules.[17]

In Sec. 2.2 of this paper, we provide a detailed description of the scattering apparatus newly constructed at Alberta, supplementing an earlier cursory description.[10] The calculations used to reproduce DCS, transport, virial and integral cross section (ICS) data for comparison to the present measurements and literature values are discussed in Sec. 2.3, along with simultaneous fitting procedures. In Sec. 2.4 we discuss the selection of dilute gas data from the large body of available literature, and assess error bars for the data used. Interatomic potential parameterizations used for the fits are detailed in Sec. 2.5. The results are presented and discussed in Sec. 2.6 along with an extensive error analysis applied to the interatomic potential energy curves determined. Finally, we summarize our results in Sec. 2.7. An Appendix (A2) illustrates how the extracted potentials can depend on the input data.

---

† A version of this chapter has been published. L.J. Danielson and M. Keil, J. Chem. Phys. 88, 851 (1988).

2.2. EXPERIMENTAL

An earlier paper[10] presented an outline of the apparatus which will be discussed in more detail here. As the top-view schematic in Fig. 2.1 illustrates, the apparatus features two supersonic beam sources (S_1 and S_2) intersecting at 90°, and an in-plane rotatable liquid helium-cooled bolometer detector (B). Also shown is a non-rotatable mass spectrometer used for beam optimization and monitoring. These components are bolted to the central scattering chamber in pre-aligned locations. Bolometer detectors are not commonly used for high-resolution DCS measurements,[18] so we present a detailed side view of the beam source and scattering detector regions in Fig. 2.2.

2.2.A. Beam Sources and Characterizations

The molecular beams are generated in separate source chambers pumped by Varian VHS-400 diffusion pumps (DP_1 and DP_2 in Fig. 2.1, each 8000 ℓ/s), backed independently by Leybold-Heraeus S160C mechanical pumps (40 ℓ/s), which maintain the pressure between 10^{-3} and 10^{-4} torr with gases flowing. The gases inlet to the apparatus are regulated by mass-flow controllers (Tylan), and are expanded through Pt apertures (Pellco; Nz in Fig. 2.2) sealed by nuts nestling in nozzle alignment cones (Aℓ). The nozzles may be heated (H) to repress dimer formation and are mounted on movable stages for alignment. Minor optimizations in alignment, and the nozzle-skimmer distance, may be effected with external controls. The beams emerge into the scattering chamber through home-made, Gentry-type skimmers (Sk), whereupon they may be flagged (Fℓ), and modulated by tuning-fork choppers (Ch). Scattering measurements are made by flagging and chopping the secondary beam. Final collimation occurs 15 mm before the scattering centre (SC) without an intervening stage of differential pumping.

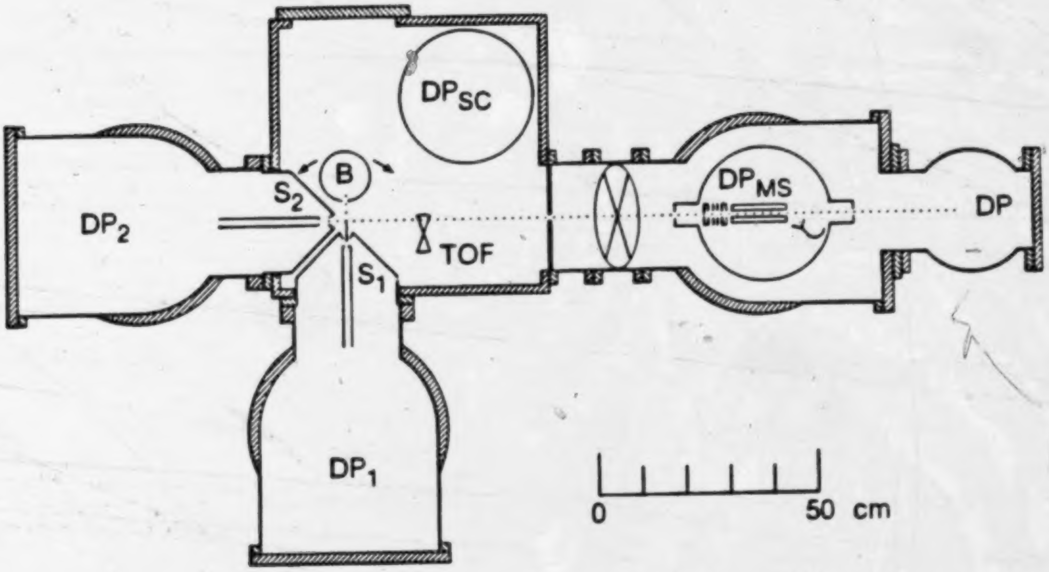

Figure 2.1

Schematic view of the apparatus (from above). All dimensions are to scale except for the apertures. S_1,S_2 – beam sources; DP$_1$,DP$_2$ – source chamber diffusion pumps; DP$_{SC}$ – scattering chamber diffusion pump; DP$_{MS}$,DP – mass spectrometer and beam dump diffusion pumps; B – rotatable bolometer detector; TOF – time-of- flight chopper for beam characterization.

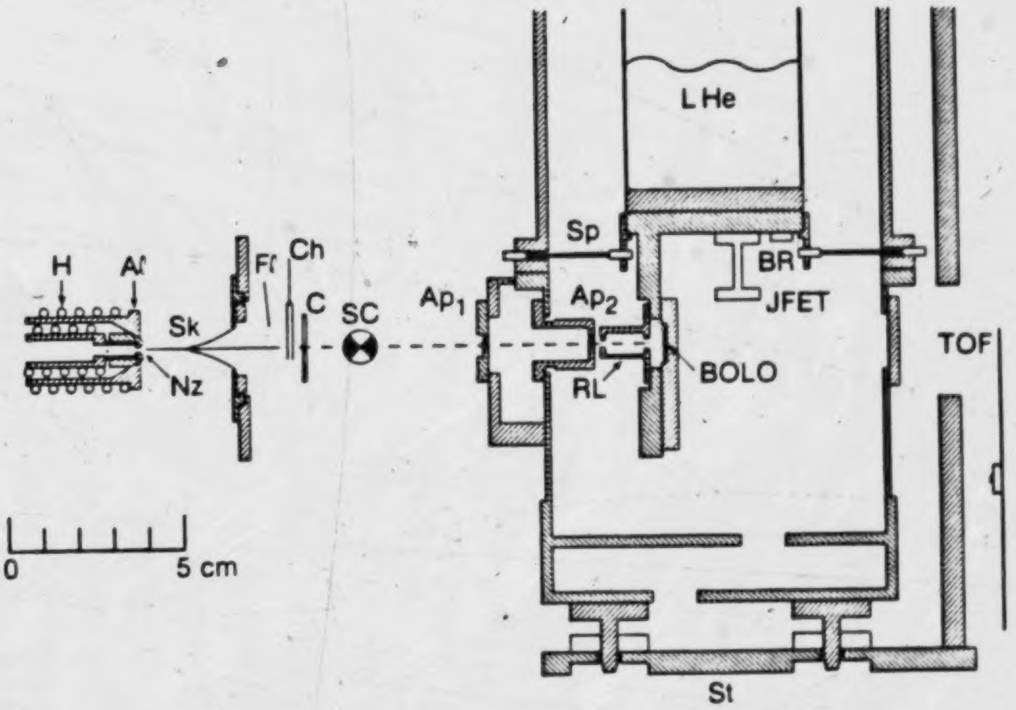

Figure 2.2

Side view of the apparatus, with the bolometer positioned opposite the secondary beam. All dimensions are drawn to scale. Nz – nozzle; Sk – skimmer; $A\ell$ – alignment cone; H – heaters; $F\ell$ – beam flag; Ch – tuning fork chopper; C – beam collimator; SC – scattering centre; Ap_1,Ap_2 – LN_2-cooled detector collimators; RL – LHe-cooled radiation-limiting apertures; BOLO – commposite Ge bolometer; JFET – pre-amplifier; BR – bias resistor; Sp,St – stiffening spokes and strut; TOF – time-of-flight chopper used when the bolometer is rotated clear of the secondary beam path.

The molecular beams were characterized using the mass spectrometer detector (Extrel 041-1 ionizer, EAI 200 quadrupole mass filter, and Gallileo 4770 channeltron). Beam intensities and velocity distributions were measured as functions of nozzle size, nozzle-skimmer distance, and mass flow. Our beam operating characteristics are collected in Table 2-1. The He beam, generated at high pressure and with a small nozzle, was characterized by temporarily moving the TOF chopper and the mass spectrometer detector opposite the S_1 source in Figure 2.1. For the heavier rare gases, we used gentler expansion conditions than typically found in the literature.[5,8] This lowered the fraction of observed dimers without degrading the velocity distributions at all. In all cases, the gas purity was 99.995% (He and Ar from Linde; Kr and Xe from Cryogenic Rare Gases).

Beam velocities and their distributions were measured with a TOF chopper calibrated using the method of Cross et al.[19] Signals were accumulated by a LeCroy 9400 digital averaging oscilloscope functioning as a multi-channel analyzer. Ion flight times were determined using SF_n^+ fragments from an SF_6 beam, while the flight distance and trigger error were determined by using highly-expanded He and Ar beams. This calibration procedure was checked with Ne and Kr beams, and was found to be precise to ±0.2%. The TOF chopper has slots in two of its four blades and holes in the other two for shutter widths down to 4 μsec. Even this narrow shutter function broadened the observed He velocity distribution prohibiting accurate measurements; therefore its value was obtained from Ref. 20 using our nozzle conditions. The exact value for the He velocity distribution does not affect the scattering calculations significantly as long as the most probable velocity is known accurately, since most of the apparatus averaging is due to angular resolution.[21]

Table 2-1. Beam Operating Conditions

	Primary Beam	Secondary Beams		
Gas	He	Ar	Kr[a]	Xe[a]
Temperature (K)	302	302	513	734
Nozzle diameter (mm)	0.050	0.30	0.30	0.30
Flow (atm.cm^3/sec)	13.0	8.3	1.7	1.7
Nozzle pressure (atm)	14.9	0.57	0.25	0.35
Nozzle-skimmer distance (mm)	9.5	15	11	12
Skimmer diameter (mm)	0.53	0.50	0.50	0.50
Most probable velocity (km/sec)	1.771	0.561	0.505	0.482
Velocity FWHM ($\Delta v/v_{mp}$)	0.04	0.072	0.087	0.095
Collision Energy (E_{mp},meV)	—	64.9	66.9	68.9
Collimator diameter (mm)	0.79	0.97	0.97	0.97
Nozzle-Scat. centre (mm)	58	63	59	60
Angular divergence (deg)[b]	1.0	1.2	1.3	1.2
Length of Scat. volume (mm)[b]	—	1.3	1.3	1.3
Attenuation of He beam (%)	—	0.25	0.19	0.19
Dimer/Monomer Signal Ratio[c]	—	0.004	0.0005	0.0003
Maximum detection angle (deg)[b,d]	—	52	68	75

[a] These beams operated slightly below their optimum mass flow to lower gas consumption.

[b] Calculated.

[c] We estimate that the dimer/monomer intensity ratio is $\lesssim$ 1.5% for the Ar, Kr and Xe beams, allowing for mass filter transmission, isotope distributions, and dimer fragmentation.[58]

[d] For the bolometer to detect scattered He only.

2.2.B. Scattering Chamber and Detector

The scattering chamber is pumped by an unbaffled Varian VHS-10 diffusion pump (DP_{SC} in Fig. 2.1; 5000 ℓ/s) backed by a Leybold-Heraeus D8A mechanical pump. Scattering chamber pressures of 2×10^{-6} torr and primary beam attenuations below 1% ensure the necessary single-collision conditions.

The scattering chamber was constructed so that all components relevant to the alignment of beams and detectors fit precisely into machined edges or dowels. Each piece can then be returned easily and reproducibly to its correct position after disassembly. The initial apparatus alignment was performed using the diffraction pattern from a HeNe laser to adjust all relevant alignment edges, which were subsequently fixed into place. This construction philosophy greatly facilitated the extensive beam characterizations conducted.

The detector is rotated about the scattering centre on a 47 cm diameter flange with an angular scale that may be positioned and read to $\pm 0.02°$ Scattered He atoms are detected by a windowless composite Ge bolometer (Infrared Laboratories; BOLO) operated at 1.5 K by pumping on a liquid helium reservoir. Scattered beam collimation is provided by two LN_2-cooled apertures (Ap_1 and Ap_2), with subsequent LHe-cooled apertures (RL) serving only to limit background thermal radiation. The bolometer detector's sapphire heat absorber is large enough (9 mm high and 3 mm wide) to intercept all particles passing through the collimating apertures. Signals produced are pre-amplified by a cooled JFET and are further amplified outside the vacuum (Infrared Laboratories LN-6C). The bolometer's noise equivalent power is specified as $10^{-14} W/\sqrt{Hz}$; in fact, signals at this limit have been measured successfully at our chopping frequency of 25.9 Hz. This detection limit corresponds to a scattered He flux of $\sim 10^6$ atoms/sec, or partial pressures of $\sim 10^{-13}$ torr.

The scattering detector collimating apertures are positioned 33.4 mm and 66.7 mm from the scattering centre and have diameters of 0.64 mm and 0.67 mm, respectively. The bolometer viewing cone then has a calculated diameter of 1.95 mm at the scattering centre, ensuring that the detector views the entire scattering volume regardless of scattering angle (Table 2-1).

The overall apparatus angular resolution may be estimated by considering the maximum possible deflection angle that a He atom may suffer and still be detected when the bolometer is positioned directly opposite the He beam. Taking the He nozzle as a point source, this angle is calculated to be $\sim 1.25°$. This crude calculation does not account for the angular resolution of the crossed beam or the finite size of the detector and its angular viewing cone. Since we cannot measure these instrumental inputs accurately enough to do a proper forward simulation for the overall angular resolution of the apparatus, we have adopted an alternative method for determining this quantity (see Sec. 2.6.A). We will also show (Sec. 2.6.D) that our somewhat imprecise characterization of this quantity does not affect the resulting interatomic potentials.

The bolometer apertures must deliberately be misaligned at room temperature to allow for thermal contraction of the LN_2 radiation shield and inner LHe dewar. This contraction was measured with a travelling telescope, and was reproducible to ±0.05 mm provided the bolometer dewar assembly was prevented from moving laterally. The required rigidity was achieved by pegging the LN_2 radiation shield to a room-temperature support strut (St) with Vespel standoffs. The LHe dewar was then bolted to the radiation shield with spring-loaded fibreglass spokes. The entire structure is quite rigid and free of mechanical vibration, a very important consideration for bolometers operating at such low signal levels.

A further consideration in using the bolometer detector is its insensitivity to the source of the impinging energy. The bolometer is unable to distinguish scattered He beam signal from modulated thermal radiation or modulated secondary beam signal. Thermal radiation is eliminated by carefully masking the tuning fork chopper behind the secondary beam collimator using black tape. Secondary beam scattering can be eliminated kinematically, but only for well velocity- and angularly-collimated beams. Though the bolometer can physically be positioned between −12° and +102° (the secondary beam being detected at +90°), the angular range uncontaminated by scattered secondary particles is limited to $\lesssim 52°$ for the worst-case HeAr experiment (see Table 2-1).

2.2.C. Data Acquisition and Experimental Results

The computer-controlled data acquisition has been described previously.[10] Phase-sensitive lock-in and background subtraction techniques with periodic reference normalization are used to extract signals proportional to the intensity of the scattered He atoms.

The zero position of the angular scattering scale was determined by ensuring scattering symmetry on either side of the He beam for oscillations of the HeAr DCS, including kinematic transformations but without reference to its interatomic potential. This angle scale correction has been reproducible to ±0.02° over several months. The data are shifted by this measurement and its error is convoluted with the measured uncertainty (one standard deviation) in each data point. Since the error bars are themselves rather noisy, they are 5-point smoothed to avoid undue weighting of data with fortuitously small uncertainties. The intense low-angle scattering signals are not unduly weighted either; we assign their errors as the statistical error or 3%, whichever is greater. Data are reported no closer than 4° to the primary beam, since its intense wings degrade the bolometer response below ~ 3.5°. Our experimental DCS measurements are presented in Table 2-2 and in Fig. 2.3 for HeAr, HeKr and HeXe.

Table 2-2. Experimental Differential Cross Section Measurements[a]

	HeAr		HeKr		HeXe	
$\theta(^\circ)^b$	$I(\theta)$	$\Delta I(\theta)\%$	$I(\theta)$	$\Delta I(\theta)\%$	$I(\theta)$	$\Delta I(\theta)\%$
−10.56	65.16	8.9				
−10.06	99.32	8.4	91.75	8.5		
−9.56	129.18	6.9	149.75	7.4	60.40	5.6
−9.06	147.27	4.4	196.20	6.4	104.61	4.5
−8.56	139.08	3.0	212.91	5.3	143.91	3.5
−8.06	108.43	3.0	188.81	4.6	163.50	3.1
−7.56	76.01	3.6	139.23	4.8	158.61	3.7
−7.06	66.49	4.0	102.62	5.6	115.62	4.4
−6.56	112.28	3.5	124.66	6.1	103.14	4.5
−6.06	223.51	3.0	228.36	5.6	130.85	4.5
−5.56	402.14	3.0	451.65	4.3	239.13	4.5
−5.06	654.28	3.0	757.20	3.4	469.08	3.9
−4.56	922.48	3.0	1089.59	3.5	735.08	3.0
−4.06	1232.82	3.0	1505.47	4.1	1057.48	3.0
4.44	1093.72	3.0	1240.03	3.7	803.35	3.4
4.94	790.10	3.0	847.95	4.4	500.00[c]	3.7
5.44	500.00[c]	3.3	500.00[c]	5.6	271.75	3.8
5.94	283.22	3.7	261.67	6.2	159.62	4.0
6.44	139.11	3.8	159.32	6.2	141.15	3.9
6.94	100.25	4.3	165.49	6.2	185.75	3.7
7.44	128.83	4.8	229.60	5.7	219.16	4.0
7.94	174.94	3.8	277.39	4.4	211.36	4.8
8.44	211.31	3.0	277.76	3.3	162.38	5.9
8.94	209.05	3.0	229.56	3.2	99.63	6.9
9.44	162.50	3.0	145.81	3.9	48.50	7.7
9.94	114.35	3.8	82.90	5.4	29.20	8.1
10.44	61.03	6.2	40.05	7.3	39.72	7.5
10.94	30.82	8.4	40.85	7.6	63.73	6.6
11.44	30.43	9.8	65.48	6.5	73.44	6.6
11.94	46.34	9.0	91.71	6.1	73.86	6.5
12.44	62.97	6.1	102.50	6.4	59.76	6.2
12.94	80.34	3.7	91.05	7.2	43.19	7.5
13.44	78.46	3.3	71.51	8.3	25.18	10.7
13.94	65.23	3.3	57.42	8.8	20.57	13.1
14.44	51.99	3.2	33.97	8.0	28.71	13.2
14.94	35.29	4.1	29.84	6.3	34.03	12.7
15.44	25.39	7.0	34.44	5.0	38.45	11.7
15.94	26.95	10.8	41.35	4.0	36.44	9.5
16.44	31.37	11.8	50.51	4.0	37.68	8.4
16.94	40.70	9.0	54.29	5.7	30.28	9.6
17.44	45.71	6.4	46.40	6.7	25.09	10.4
17.94	45.81	6.2	38.61	5.3	24.47	9.9
18.44	39.40	6.9	33.90	4.4	23.66	10.8

··· continued on the next page ···

Table 2-2 continued ···

	HeAr		HeKr		HeXe	
$\theta(^\circ)^b$	$I(\theta)$	$\Delta I(\theta)\%$	$I(\theta)$	$\Delta I(\theta)\%$	$I(\theta)$	$\Delta I(\theta)\%$
18.94	34.67	8.2	28.27	7.5	25.64	13.6
19.44	27.46	10.2	26.76	13.1	29.85	16.2
19.94	25.12	11.9	28.80	15.9	28.24	16.9
20.44	26.50	11.3	36.92	14.0	25.66	15.4
21.44	32.22	8.9	41.50	11.3	20.02	12.9
22.44	30.35	6.6	28.33	12.0	19.79	11.3
23.44	28.68	5.3	24.84	14.4	22.33	12.2
24.44	25.26	4.8	25.98	16.0	20.73	16.1
25.44	26.50	5.6	29.47	16.9	17.98	20.5
26.44	26.46	7.7	25.33	15.3	17.55	21.2
27.44	24.87	10.2	25.12	12.5	21.58	18.6
28.44	24.51	12.9	23.54	12.9	16.00	18.3
29.44	21.17	14.4	23.94	14.3	16.23	19.9
30.44	25.07	13.0	25.37	13.6	17.53	18.9
32.94	20.77	10.8	21.92	12.4	17.56	17.2
35.44	21.42	11.0	19.79	11.8	16.62	17.3
37.94	18.03	11.7	19.74	11.4	16.10	16.9
40.44	18.92	10.7	18.30	12.1	15.51	16.1
42.94	19.63	9.0	21.81	13.7	12.60	15.8
45.44	18.77	8.1	17.21	14.6	13.40	15.6

[a] Experimental DCS measurements are in arbitrary units; percentage error bars represent one standard deviation.

[b] Nominal scattering angles, which should be decreased by 0.016° for HeAr, and increased by 0.004° and 0.010° for HeKr and HeXe, respectively.

[c] Reference angle used for periodic normalization.

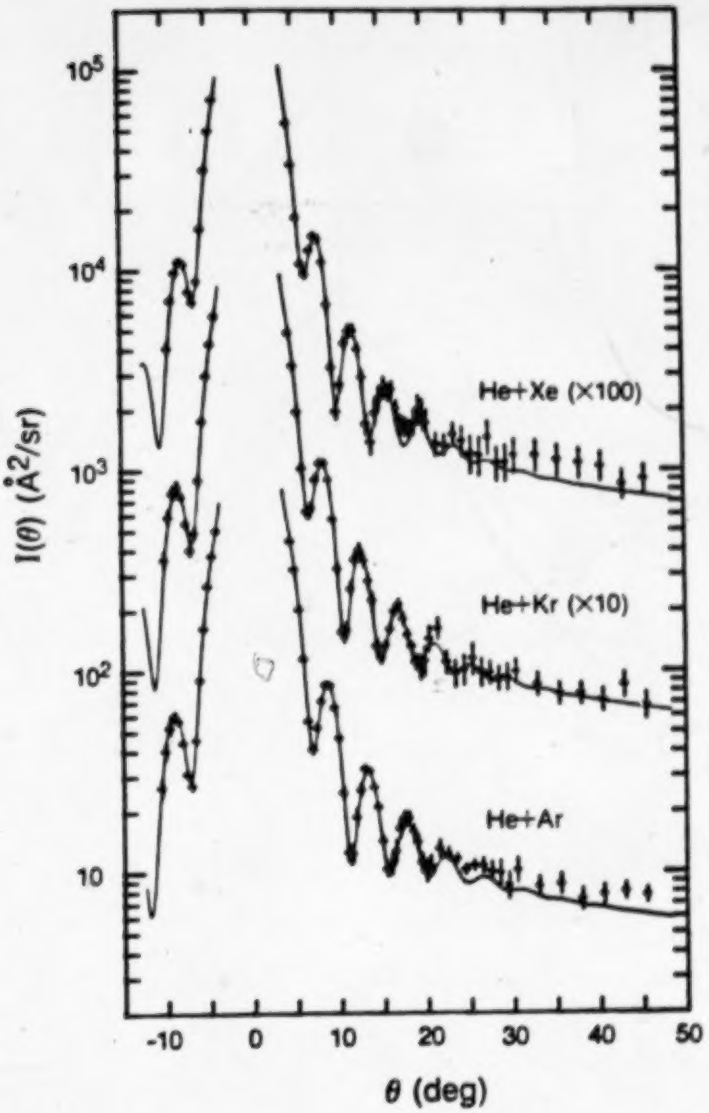

Figure 2.3

Measured differential cross section scattering data for HeAr, HeKr and HeXe. The ordinate scale in $\text{Å}^2/\text{sr}$ is generated in calculating the DCS, and multiplied as shown. The vertical height of the error bars portray the signal measurement error (1σ) convoluted with the angular scale uncertainty of ±0.02°. The calculated curves are generated from the fitted HFD interatomic potentials as discussed in Sec. 2.5.

2.3. CALCULATIONS AND SIMULTANEOUS FITTING

For the atom-atom systems being considered, dynamical approximations need not degrade the accuracy with which various properties may be calculated, unlike typical atom-molecule systems.[11,14,22] Our calculational parameters, collected in Table 2-3, are chosen to ensure dynamical errors smaller than any reported experimental precision.

2.3.A. Differential Cross Sections

For a given interatomic potential, the DCS is calculated for scattering angles in the centre-of-mass reference frame using the partial wave expansion. Exact quantum mechanical (EQM) phase shifts are generated by direct numerical integration of the radial Schrödinger equation for each orbital angular momentum ℓ. For sufficiently large ℓ ($\gtrsim 45$ for HeAr), the semiclassical WKB phase shifts accurately reproduce the EQM phase shifts and are therefore used instead. They are generated by convergent Gauss-Mehler quadrature,[23] using ℓ up to ~ 200 for HeAr.

Calculated DCS's are transformed to and convoluted in the laboratory reference frame using a number of Newton diagrams and collision energies chosen to reflect the beam velocity spreads and the beam and detector angular profiles. The overall effective apparatus angular resolution is $1.67° \pm 0.02°$ (see Sec. 2.6.A). This effective angular resolution, consistent with the detector viewing angle when convoluted with the primary beam angular distribution and scattering volume, has been reproduced many times with independent HeAr DCS measurements.

The bolometer detector responds to the total energy flux at the beam modulation frequency used. Scattered atoms may contribute their adsorption energy and their kinetic energy upon thermal accomodation with the 1.5 K surface of the bolometer. For scattering angles $\theta > 0°$, He atoms are travelling faster than

Table 2-3. Calculational Parameters

Phase shifts:	
Numerov propagator step size, for DCS:	$(3 + 3k)^{-1}$ Å
for transports:	$(10 + 3k)^{-1}$ Å
Numerov propagator starting point potential energy, for DCS:	500 meV
for transports:	200 meV
Phase shift convergence, EQM phases:	0.002 rad
WKB phases, $E < 100$ meV:	0.005 rad
WKB phases, $E > 100$ meV:	0.020 rad
Partial wave summation, truncation:	0.0002 rad
$\lvert \mathrm{EQM}_\eta - \mathrm{WKB}_\eta \rvert$, for dropping EQM:	0.002 rad
$\lvert \mathrm{WKB}_\eta - \mathrm{JB}_\eta \rvert$, for dropping WKB, $E > 100$ meV:	0.002 rad
Differential cross sections:[a]	
Number of collision energies:	4
Collision energy range:	59-71 meV
Number of Newton diagrams:	16
Angular grid:	0.25°
Transport properties:[b]	
Temperature range:	70-1800 K
Number of Gauss-Laguerre points for collision integrals:	16
Collision energy range:	0.5-8000 meV
Number of collision energies:	80
Energy grid factor, oscillatory region (< 2.0 meV):	1.044
monotonic region (> 2.0 meV):	1.19
Chapman-Cowling approximation orders, viscosity:	2
thermal conductivity:	2
diffusion:	4
thermal diffusion:	3
Pure-gas potential parameters, HeHe[c]: $\sigma = 2.6385$Å;	$\epsilon = 0.931$ meV
ArAr[d]: $\sigma = 3.477$Å;	$\epsilon = 14.22$ meV
KrKr[d]: $\sigma = 3.580$Å;	$\epsilon = 17.17$ meV
XeXe[d]: $\sigma = 3.835$Å;	$\epsilon = 23.97$ meV
Interaction Second Virial Coefficients:[e]	
Temperature range:	70-1800 K
Simpson's rule and Wigner-Kirkwood convergence:	0.01 cm^3/mole
Maximum Wigner-Kirkwood expansion order:	3
Min. potential energy for analytical short-range integration:	$70k_BT$
Min. distance for analytical long-range integration:	10 Å

··· continued on the next page ···

Table 2-3 continued ···

Absolute Integral Cross Sections:[b]	
Primary beam velocity FWHM ($\Delta v/v_{mp}$):[f]	0.03
Target gas temperature:[f]	85;298 K
Absolute calibration error:[f]	±3%
Number of primary beam velocities:	6
Number of Gauss-Hermite target gas velocities:	4-6

---

[a] DCS calculational precision of $\lesssim 0.1\%$.

[b] Generalized cross section calculational precision of $\lesssim 0.03\%$ except at very sharp bound-state resonances; collision integral precision of $\lesssim 0.05\%$ above 100 K.

[c] $HFDHe_2$, Ref. 28.

[d] Ref. 2, Appendix 10. Using the more accurate ArAr pair potential with σ=3.350Å; ϵ=12.19 meV has no significant influence upon the calculated mixture properties.

[e] Virials calculational precision of ~ 0.01 cm^3/mole.

[f] Refs. 33,34.

the incident beam and are detected more efficiently than He atoms scattered with $\theta < 0°$. This kinematic correction is slightly diminished by the adsorption energy of He atoms on the bolometer which we have estimated as 11 meV.[24] These effects have been considered in the centre-of-mass to lab transformation outlined above. Only He atoms are detected in the present experiments since the heavier partner is kinematically constrained close to the secondary beam direction.

2.3.B. Transport Properties

Generalized integral cross sections are calculated to the fourth moment in scattering angle[25] using the partial wave expansion and phase shifts obtained as for the DCS calculations above. WKB phase shifts are used only well above the three turning-point regime, and only when agreeing well with the EQM calculations. For high angular momenta, Jeffreys-Born phase shifts[26] are calculated analytically, and substituted for WKB phases where sufficiently accurate (Table 2-3). Boltzmann integrations over the collision energy up to seventh moment are performed by Gauss-Laguerre quadrature to obtain the unlike-particle interaction collision integrals up to $\Omega_{ij}^{(4,7)}(T)$. This procedure is repeated each time any interaction potential parameter is altered.

High-order Chapman-Cowling expressions require evaluation not only of interaction collision integrals like $\Omega_{ij}^{(1,7)}(T)$ and $\Omega_{ij}^{(4,4)}(T)$, but also of some pure-gas collision integrals. These are obtained by using tables of reduced collision integrals and suitable parameters for the pure-gas (Ar, Kr,and Xe) potentials. The $\Omega_{jj}^{(2,2)}$, $\Omega_{jj}^{(2,3)}$ and $\Omega_{jj}^{(2,4)}$ are generated from Table A2.12 of Ref. 2. Similarly, the $\Omega_{jj}^{(2,5)}$, $\Omega_{jj}^{(2,6)}$ and $\Omega_{jj}^{(4,4)}$, used for fourth-order diffusions and third-order thermal diffusions, are generated from Table I-M of Ref. 27. This procedure was not reliable for He however, due to quantum interference and symmetry effects. For this case, all the required $\Omega_{ii}^{(n,s)}(T)$ are calculated once, as for the unlike-particle collision integrals above, directly from a reliable potential [HFDHe$_2$ of Ref. 28].

Calculations of the mixture viscosity and thermal conductivity require the pure-gas collision integrals even in the first-order Chapman-Cowling approximation, unlike diffusion. To ensure accurate reproduction of the measured pure-gas viscosity and thermal conductivity, which cannot be influenced by the interaction potential, we calculated the $\Omega_{ii}^{(2,2)}(T)$ and $\Omega_{jj}^{(2,2)}(T)$ collision integrals from the measured pure-gas properties using second-order Chapman-Cowling calculations [Eqns. A5.2(.7) and (.14) of Ref. 2]. In this manner, the pure-gas potentials affect calculated mixture quantities only to second-order (first-order for thermal diffusions). Finally, the mixture diffusion calculations, at 1 atm pressure, require evaluation of the number density. These are calculated using the virial equation of state (with the second virials obtained from Table A2.24 of Ref. 2 and from the explicit interaction calculations outlined below), but are unimportant for the relatively high temperatures considered here ($T \gtrsim 100$ K).

Second-order Chapman-Cowling viscosity and thermal conductivity mixture calculations are based on the equations in Appendix A5.2 of Ref. 2, and appear to be converged to $\lesssim 0.2\%$ and $\lesssim 0.5\%$ respectively. Fourth-order diffusions and third-order thermal diffusions are calculated using Mason's equations[29] and are identical to literature values of similar precision.[30] They appear to be converged within $\lesssim 0.05\%$ and $\lesssim 0.5\%$ respectively. All of the transport properties are thus calculated more accurately than present experimental techniques can measure them.

We choose to compare the calculated transport properties to the reported experimental mixture quantities, since these are the data actually measured. Nevertheless, interaction quantities for viscosity, thermal conductivity, and diffusion, can be useful for presentation and for judging consistency among different author's results (Sec. 2.6). These interaction quantities are determined by adjusting them to obtain the best possible reproduction of the measured mixture properties using the Chapman-Cowling approximation orders listed in Table 2-3, and our calculated collision integrals at each temperature. For thermal diffusion data, we employed the nearly linear dependence of α_T^{-1} with mole fraction[31] in order to display and compare $\alpha_T(T)$ for equimolar mixtures. We emphasize that these interaction quantities are not used anywhere in determining our best-fit potential parameters.

2.3.C. Interaction Second Virial Coefficients

The interaction quantity B_{12} is calculated from an assumed potential using the semiclassical Wigner-Kirkwood expansion with up to third-order quantum corrections.[32] The second and third quantum corrections amount to < 0.06 cm^3/mole at the lowest temperatures, diminishing rapidly to negligible values above $\sim$ 150 K. The first quantum correction is retained at all temperatures. Simpson's rule is used to integrate all four of the semi classical expansion terms. A step size of 0.01 Å ensures convergence of the integrands to 0.01 cm^3/mole for intermediate distances. The short- and long-range contributions are integrated analytically.[2] Test calculations for HeHe show good agreement with EQM calculations for temperatures above $\sim$ 50 K.[32(a)]

2.3.D. Absolute Integral Cross Sections

The integral cross sections (ICS) calculated for generating the collision integrals as in Sec. 2.3.B above are also used to obtain the absolute ICS as a function of centre-of-mass collision velocity. For comparison to experimental measurements,[33] these are expressed instead as a function of the primary beam velocity, after Boltzmann averaging over the target gas thermal motions.[34,35] Primary beam averaging is also included. No corrections are made for insufficient angular resolving power,[36] since DCS's at the low collision energies used[33] are not too sharply forward-peaked. Since the ICS data are placed on an absolute scale with uncertainties of ±3%,[34] the experimental measurements as a whole may be scaled to the calculated cross sections only within this calibration error.

2.3.E. Multiproperty Fitting

Parameters of assumed interatomic potential forms are fitted to the experimental data by an automated non-linear least-squares fitting program.[37] The least-squares functional to be minimized is given by the dimensionless quantity

$$\delta = \left[\sum_{j=1}^{N} w_j \delta_j^2 \Big/ \sum_{j=1}^{N} w_j \right]^{1/2} , \qquad (2-1)$$

where the δ_j are the corresponding quantities for each of N properties being fit,

$$\delta_j = \left[\frac{1}{n_j} \sum_{i=1}^{n_j} \left(\frac{S_{ij}^{calc} - S_{ij}^{exp}}{\Delta S_{ij}^{exp}} \right)^2 \right]^{1/2} . \qquad (2-2)$$

Here, S_{ij}^{calc} is the calculated value of property j at point i, S_{ij}^{exp} is the corresponding experimental measurment, and ΔS_{ij}^{exp} its absolute error.

Each property being fit is weighted, as a class of data, by the w_j in Eqn. (2-1) independently of the number of experimental measurements n_j for that property. This weighting scheme was chosen to avoid excessive weight being given to any particular property merely because of repetitive measurements (for example, many mixture viscosities at one temperature, or many closely-spaced DCS measurements).

The best-fit potentials reported in this work are all obtained by simultaneously fitting the DCS, mixture viscosity, and interaction second virial data only. For some cases, trial potentials were obtained (Sec. 2.6.E) by including the mixture diffusion and mixture thermal diffusion data also. Guided by the results of a recent paper,[38] each of these properties is assigned a weighting factor w_j commensurate with features of the interatomic potential sensitively probed by that property.

Briefly, the present DCS measurements are sensitive to the position of the attractive well and weakly repulsive wall up to ~ 20 meV, and are independently sensitive to the attractive well depth. The transports and virials are sensitive to the repulsive wall up to ~ 100 meV, but not at all to the position of the attractive well, and therefore complement the DCS measurements. Transports and virials are insensitive to any feature of the attractive well except at low temperature. Such measurements, for sufficiently low temperatures, are available only for the virials. The DCS therefore constrains the position and depth of the attractive well, whereupon the virials sensitively determine the outer bowl of the attractive well. The transports and virials together serve to fix the repulsive wall, once the attractive well position is established. The ICS data can provide a stringent test of the attractive well region, and its outer bowl, commensurate with the reliability of the absolute calibration. This caveat is necessitated by the lack of orbiting structure in the observed ICS data.[33]

Since the transport and virial properties as a whole probe as much of the interatomic potential as does the DCS, the sum of the transport and virial weights is set equal to the DCS weight, and each of the transport properties is weighted equally with the virials. Whenever used, the ICS data are weighted half as heavily as the DCS mesurements.

Multiproperty fitting cannot properly be accomplished by minimizing standard deviations, since these quantities depend on the magnitude of different physical properties. Percentage standard deviations can also be difficult to interpret[1] since they would not account properly for different proportional errors in individual measurements of the same property. These quantities are also not particularly useful for comparing the ability of any given interatomic potential to reproduce the experimental measurements. The dimensionless quantity δ [Eqns. (2-1) and (2-2)] overcomes these defects: a good fit to any particular property j is indicated simply by $\delta_j < 1$ in Eqn. (2-2). The overall fitting quality δ is independent of any arbitrary normalization and properly weights each data point according to its error bar (and its sensitivity to the interatomic potential). Resulting values for δ lower than unity correspond, on average, to fitting all the data within their respective error bars.

Each non-linear parameter iteration cycle (for 3 potential parameters) required ~ 5 min on the Alberta Amdahl 5870 computer. Full convergence of all parameters was always obtained in 2-4 iterations using the Aziz parameters[1] as starting values.

2.4. DILUTE GAS DATA SELECTION

In fitting interatomic potentials to data gathered from diverse sources, it is necessary to establish objective evaluations of the input experimental data, and their error bars. The data of each individual author should be internally consistent with error bars at least overlapping each other. Where several authors have measured the same property, the respective data sets must also be consistent, allowing a smooth curve to be drawn through all of the data, unless there is some objective reason for rejecting particular literature values. In order to avoid biasing the interatomic potential fit to the data, it is crucial that each author give appropriate representations of their *accuracy, not their precision.* This is a particularly troublesome point for the available diffusion data, and to a lesser extent for thermal diffusion data (Sec. 2.6.C; there are only a few HeAr thermal conductivity measurements available). Fortunately, results from recent papers[8,11(b),38] show that data sets including DCS measurements and the two remaining dilute gas properties – viscosities and virials – should result in reliable interatomic potentials when subjected to simultaneous fitting. Error bars used for our analysis are obtained as discussed below, and are presented in Table 2-4.

2.4.A. Mixture Viscosities

The error bars used for Gough et al.[39(a)] are those estimated by the authors. For Maitland and Smith's[39(b)] data, we again use the authors' error bars, based on their own repeated measurements. Error bars for Kestin et al.[39(c),39(d)] are larger than given by the authors, reflecting the smoothness of deviation plots reported in a recent paper.[40] All of these authors' pure-gas viscosities, measured concurrently with their mixture properties, are used as outlined in Sec 2.3.B.

Table 2-4. Assigned Error Bars for Dilute Gas Data[a]

Interaction	Property	Data	Temperature (K)	Error[b]
HeAr	η_{mix}	Gough et al.[39(a)]	120-320	1.7-1.0
	η_{mix}	Kalelkar & Kestin[39(c)]	298-993	0.5-1.0
	η_{mix}	Maitland & Smith[39(b)]	295-1533	1.5
	B_{12}	Knobler et al.[42(a)]	90	2.3
	B_{12}	Brewer & co-workers[42(b),(c)]	123-323	0.85
	B_{12}	Blancett et al.[42(d)]	223-323	1.5
	B_{12}	Kalfoglou & Miller[42(e)]	303-773	0.60
HeKr	η_{mix}	Kalelkar & Kestin[39(c)]	298-993	0.5-1.0
	B_{12}	Kate & Robinson[42(f)]	90-115	1.0
	B_{12}	Brewer[42(c)]	148-323	2.0-1.15
	B_{12}	Dillard et al.[42(g)]	223-323	0.30
HeXe	η_{mix}	Kestin et al.[39(d)]	298-778	0.5-1.0
	B_{12}	Kate & Robinson[42(f)]	120-155	2.0-1.0
	B_{12}	Brewer[42(c)]	173-323	5.0-1.35

[a] Diffusion, thermal diffusion, and thermal conductivity discussed in Sec. 2.6.

[b] Units are % η_{mix}^{exp} and cm^3/mole for viscosities and virials, respectively.

2.4.B. Interaction Second Virials

Interaction second virial coefficients B_{12} can be obtained from mixture or excess measurements, with a knowledge of the pure-gas virial coefficients. We have therefore re-calculated the B_{12}^{exp} and their error bars, using the accurate and consistent National Bureau of Standards compilation[41] of pure-gas virials, for the data of Knobler et al.,[42(a)] Brewer and Vaughn,[42(b)] and Brewer.[42(c)] The re-derived B_{12}^{exp} values are within ±1.0 cm^3/mole of the authors' reported values, with the exception of Knobler et al.[42(a)] This procedure was not necessary for the data of Blancett et al.[42(d)] or Kalfoglou and Miller[42(e)] because these authors concurrently measured the pure-gas virials. The data of Blancett et al. were assigned error bars larger than the experimental precision reported by the authors.[42(d)] Kalfoglou and Miller do not report errors for their pure-gas virials. We therefore assigned error bars to their data by propagating the pure-gas errors[43] with their mixture measurement errors. The errors assigned to Knobler et al. and Brewer et al. were obtained similarly. Kate and Robinson[42(f)] determined their errors in a detailed analysis, and were adjusted only for the lowest-temperature HeXe measurement to be consistent with Kate's thesis.[44] Error bars of Dillard et al.[42(g)] are those reported by the authors.

2.5. INTERATOMIC POTENTIAL PARAMETERIZATIONS

Two types of parameterizations are used to generate the best-fit interatomic potentials presented in this paper. First, the "Hartree-Fock plus damped Dispersion" (HFD) potential form is appealing because of its apparent physical reasonableness.[6(b)] Second, the Morse-Spline-van der Waals (MSV) potential form is quite flexible,[45] and provides an important check for the uniqueness and accuracy of the fitted potentials.

We use the HFD parameterization given by[6(b),10]:

$$\begin{aligned}
V_{HFD}(r) &= V_{HF}(r) + F(r)V_D(r) \,, \\
V_{HF}(r) &= A\exp(-\alpha r) \,, \\
V_D(r) &= -\sum_{n=0}^{4} C_{2n+6} r^{-(2n+6)} \,, \qquad (2-3)\\
F(r) &= \exp\left[-\left(Dr_m r^{-1} - 1\right)^2\right] \,, \quad r \le Dr_m \,, \\
F(r) &= 1 \,, \quad r \ge Dr_m .
\end{aligned}$$

For fitting purposes, we regard only r_m, α and C_8 as adjustable parameters. In some preliminary fits (not the best-fit potentials), C_6 was adjusted instead of C_8. The damping parameter D is held fixed at 1.28.[6(b)] Requiring the potential minimum position to occur at the r_m parameter value then fixes A in terms of α and r_m:

$$A = \alpha^{-1}\exp(\alpha r_m)\left[F'(r_m)V_D(r_m) + F(r_m)V_D'(r_m)\right] \,, \qquad (2-4)$$

whereupon the well depth ϵ is:

$$\epsilon = -\left[V_{HF}(r_m) + F(r_m)V_D(r_m)\right] . \qquad (2-5)$$

When held fixed, the C_6 coefficient is that of Kumar and Meath.[46] In the preliminary studies, where C_8 is held fixed, it and C_{10} are taken as the mean of Standard and Certain's bounds[47(a)] with $C_{12} = C_{14} = 0$. When C_8 is adjusted to fit the data, C_{10}, C_{12} and C_{14} are calculated from the recursion relations of Douketis et al.[48] Thus, the best-fit HFD potentials are obtained with three adjustable parameters (preliminary two-parameter fits are discussed in Sec. 2.6.A).

The MSV parameterization is given by[22,45]:

$$\begin{aligned} V_M(r) &= \epsilon\left\{\exp\left[2\beta\left(1-\frac{r}{r_m}\right)\right] - 2\exp\left[\beta\left(1-\frac{r}{r_m}\right)\right]\right\} , \quad r \le r_1 , \\ V_S(r) &= b_1 + (r-r_1)\{b_2 + (r-r_2) \\ &\quad \times [b_3 + (r-r_1)b_4]\} , \quad r_1 \le r \le r_2 , \qquad (2-6) \\ V_V(r) &= -C_6 r^{-6} - C_8 r^{-8} , \quad r \ge r_2 . \end{aligned}$$

For this parameterization, we treat r_m, ϵ and β as adjustable parameters. The cubic spline coefficients are all fixed by smoothness conditions at the joining points. The r_1 joining point is chosen to occur at the Morse inflection point $r_1 = r_m\left(1 + \beta^{-1}\log_e 2\right)$, while $r_2 = 1.6r_m$. The C_6 coefficient is held fixed at Kumar and Meath's[46] value and the C_8 coefficient is fixed at the mean of Standard and Certain's[47(a)] bounds. Thus, the MSV potential fits are also performed with three adjustable parameters.

2.6. RESULTS AND DISCUSSION

2.6.A. Fitted Interatomic Potentials

The best-fit interatomic potentials for HeAr, HeKr, and HeXe are presented in Fig. 2.4. The corresponding potential parameters are collected in Table 2-5, along with the fitting quality δ. As discussed in Sec. 2.5, these potentials are obtained by simultaneously fitting the DCS, mixture viscosity, and interaction second virial data. Each fit optimized the r_m, α and C_8 parameters (HFD form) or the r_m, ϵ and β parameters (MSV form). It is encouraging to note that there is little to distinguish between the best-fit HFD and MSV potentials in their ability to reproduce the experimental data (Table 2-5). Despite mathematical forms that are quite different (except in the asymptotic region which is known to be correct), the potentials themselves are essentially identical (Fig. 2.4). These results strongly suggest that the potentials obtained here are largely independent of the parameterizations chosen to represent them. We will discuss errors introduced into the potential by its parameterization in Sec. 2.6.D.

Initial calculations for HeAr also allowed the effective overall apparatus angular resolution to be fitted to the DCS data, simultaneously with the potential parameters. The optimized angular resolution parameter for the HFD and MSV parameterizations was 1.69° and 1.67° respectively. This calibration is, therefore, independent of the assumed interatomic potential, and thus reliably estimates an apparatus characteristic that would otherwise be very difficult to determine for our apparatus.[18] The potentials determined do not depend significantly on this calibration procedure as shown in Sec. 2.6.D.

Our first attempts to fit the HFD potential allowed optimization of only the r_m and α parameters. Though these fits reproduced the DCS and mixture viscosity data quite well, they failed to reproduce the virials ($\delta_B = 1.25$,

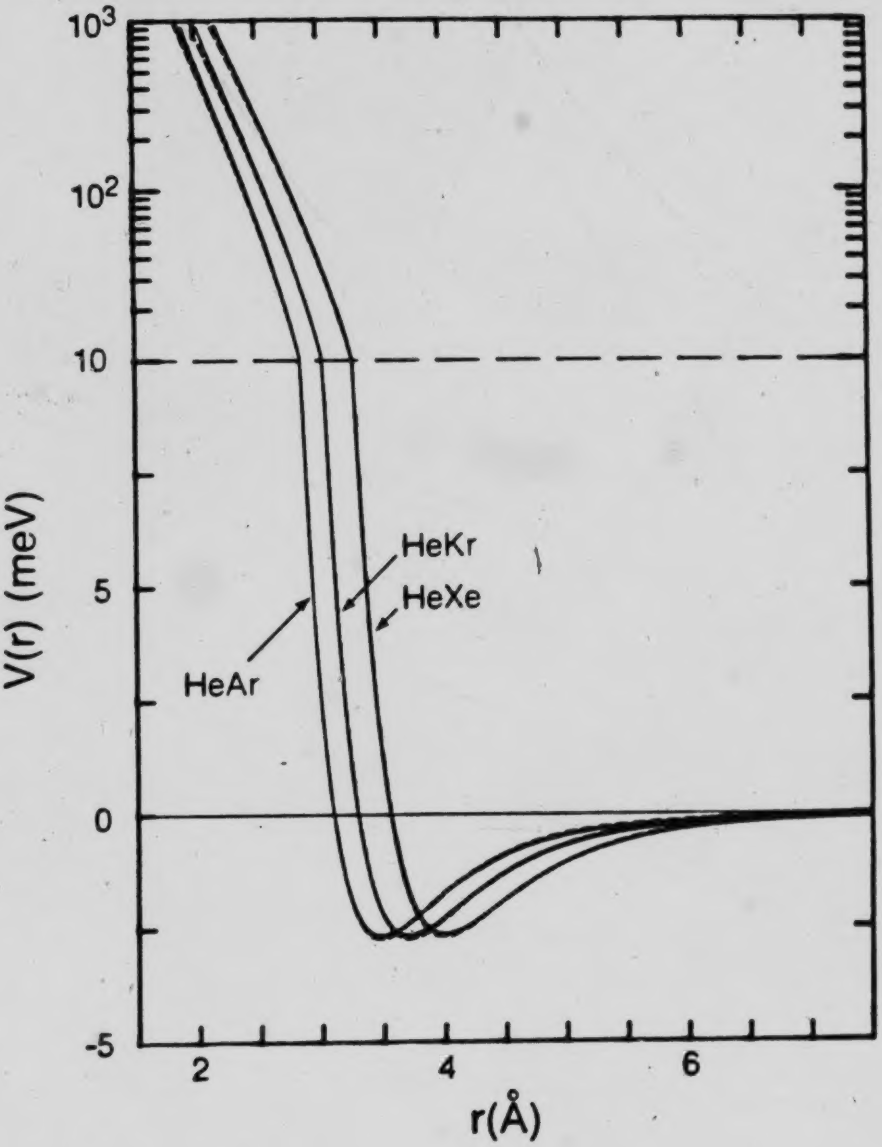

Figure 2.4

Best-fit interatomic potentials for HeAr, HeKr and HeXe. The solid curves are generated from the HFD potential form [Eqn. (2-3)] and the almost indistinguishable dashed curves from the MSV potential form [Eqn. (2-6)].

Table 2-5. **Best-Fit Potential Parameters and Fitting Quality**

	HFD[a]				MSV[b]		
	HeAr	HeKr	HeXe		HeAr	HeKr	HeXe
r_m(Å)[c]	3.482	3.702	3.997	r_m(Å)[c]	3.483	3.707	3.996
σ(Å)[d]	3.107	3.299	3.565	σ(Å)[d]	3.111	3.303	3.564
ϵ(meV)[d]	2.591	2.667	2.635	ϵ(meV)[c]	2.669	2.735	2.685
α(Å^{-1})[c]	3.987	3.682	3.422	β[c]	6.488	6.372	6.422
A(keV)[d]	2.663	2.527	2.953				
C_6(eV-Å^6)[e,f]	5.700	8.007	11.68	C_6(eV-Å^6)[e,f]	5.700	8.007	11.68
C_8(eV-Å^8)[c]	25.9	48.6	93.6	C_8(eV-Å^8)[e,g]	26.3	42.6	79.2
δ_{DCS}	1.099	0.774	0.970	δ_{DCS}	0.983	0.756	0.996
δ_η	0.378	0.541	0.470	δ_η	0.426	0.660	0.545
δ_B	0.907	0.797	1.135	δ_B	0.972	0.828	1.216
$\delta_{\mathrm{overall}}$[h]	0.920	0.729	0.920	$\delta_{\mathrm{overall}}$[h]	0.875	0.752	0.970

[a] Preferred potential, Eqn. (2-3); D=1.28, with C_n determined by recursion[48] for $n \geq 10$.

[b] Eqn. (2-6).

[c] Fitted to the data.

[d] Derived from the fitted parameters.

[e] Held fixed.

[f] Ref. 46.

[g] Ref. 47.

[h] Eqn. (2-1) with $w_{DCS}=1.00$; $w_\eta=w_B=0.50$.

1.06 and 1.67 for HeAr, HeKr and HeXe respectively), which are most sensitive to the outer bowl of the attractive well.[38] In the HFD formulation, the dispersion damping parameter D appears to be the obvious candidate for improving this region of the potential, but D actually influences damping only for distances much shorter than the attractive minimum. The resulting best-fit potentials for this case are the same as those for the r_m and α parameter optimizations above. Therefore, only the dispersion parameters are available for improving the fit to the low-temperature virials. Initially we tried some fits regarding r_m, α and C_6 as adjustable parameters. The fitted potentials then reproduced all the data very well, including the low-temperature virials. Unfortunately, these fits required C_6 values too large when compared to recent calculations estimated to be reliable to ±1%,[46] and would yield asymptotic potentials too attractive by 10% for HeAr and HeKr, and by 20% for HeXe.

The C_8 coefficients recently reported for these systems have error bounds of ±20-25%.[47(a)] The input data used to generate these bounds may have additional errors of up to 40% for Xe.[47(a)] For potential models utilizing the damped dispersion series (such as HFD, but not MSV), such errors can substantially distort the attractive well[49] and even the weakly repulsive wall (see also the Appendix A2). Allowing the C_8 coefficient to be fitted to the data ensures that the attractive well region of the HFD potential obtained will be determined by the DCS and virial data, rather than by C_8 coefficients which may be incorrect. By fitting the C_8 parameter instead of C_6, the correct asymptotic behaviour of the potential can still be ensured. The C_8 fits are almost as good as the C_6 fits and the potentials obtained are virtually indistinguishable. The fitted C_8 coefficients, and the C_{10} values derived from them by recursion,[48] lie within Standard and Certain's[47(a)] bounds for all three systems, except for the C_{10} value of HeXe which is 11% larger than Standard and Certain's upper bound. It is for this system however, that their values may be in error by more than their bounds would suggest.[47(a)] Pack et al.[8] have encountered similar difficulties with the earlier bounds of Tang, Norbeck and Certain[47(b)] for Xe-containing systems. Watanabe et al.[50] also found it necessary to optimize dispersion coefficients within these earlier bounds. We emphasize here that none of these problems arise for the MSV parameterization, since the outer attractive bowl is influenced by the β parameter instead, and the dispersion coefficients influence the potential for regions not probed by any of the data.

From the above discussion, it is clear that for either potential form, three parameters must be adjusted for the simultaneous fits to reproduce all of the experimental data. Under these conditions, both potentials are effectively identical. We nevertheless prefer the HFD results because the MSV potential yields repulsive walls that become too soft at very high energies (though beyond the range sampled by the data considered).

2.6.B. Fitted Properties

The DCS's calculated from the best-fit HFD potentials have already been shown in Fig. 2.3. Figures 2.5 and 2.6 show corresponding calculations for viscosities and second virial coefficients, respectively. In all cases, the best-fit MSV curves are almost indistinguishable from our HFD ones and are not plotted. It is apparent from these figures and the fitting quality for each property (Table 2-5) that the potentials faithfully reproduce all of the data used to construct them. There are no discernible systematic deviations for any of the viscosity measurements, and there are only minor deviations at large scattering angles for HeAr and HeXe, and for the high-temperature HeAr and low-temperature HeXe virials.

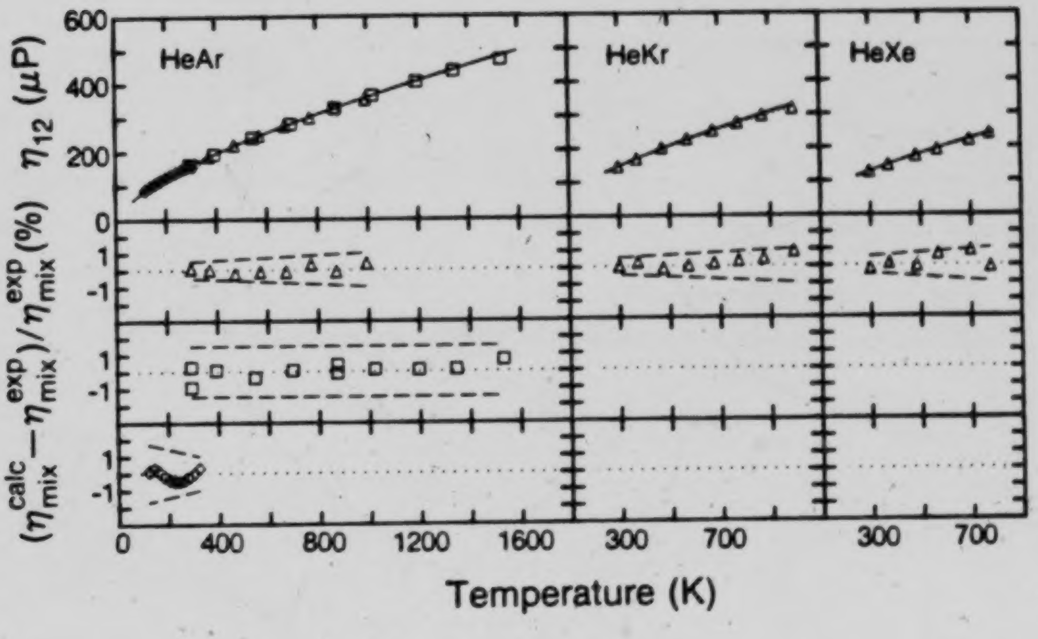

Figure 2.5

The upper frames show interaction viscosity data from experiment (symbols) and from the best-fit HFD potentials (solid curves). Lower frames detail deviations of calculated from measured viscosities for near-equimolar mixtures. Dashed lines depict the error bounds of Table 2-4. Symbols used are: △, Kestin et al.;[39(c),39(d)] □, Maitland and Smith[39(b)] (HeAr only); ◇ , Gough et al.[39(a)] (HeAr only). In all cases, the best-fit MSV potentials yield curves indistinguishable from our HFD ones; the HFD potentials of Aziz et al.[5] (HeAr) and Smith et al.[7] (HeKr, HeXe) yield the (barely distinguishable) dotted lines.

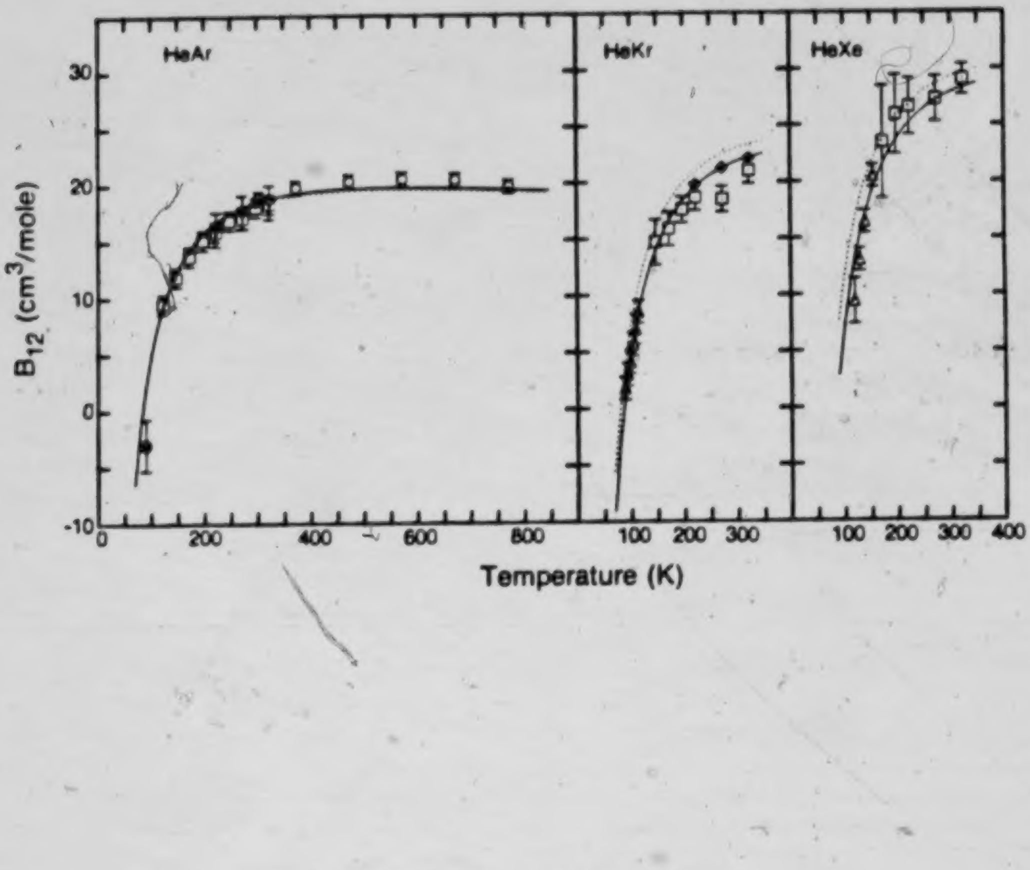

Figure 2.6

Interaction second virial data from experiment (symbols) and from the best-fit HFD potentials (solid curves). Error bars are those of Table 2-4. Symbols used are: ●, Knobler et al.[42(a)] (HeAr only); □, Brewer and co-workers;[42(b),42(c)] ▽, Blancett et al.[42(d)] (HeAr only); ⬡ , Kalfoglou and Miller[42(e)] (HeAr only); △, Kate and Robinson[42(f)] (HeKr and HeXe only); ◇, Dillard et al.[42(g)] (HeKr only). Best-fit MSV results are indistinguishable and are not shown; dotted curves as in Fig. 2.5.

These deviations cannot however, be reduced for any one or two properties without systematically degrading the fitting quality for the remaining properties.[8,11(b),38]

We find a high degree of compatibility in the data sets that we have used. In particular, the fitting qualities for each property are roughly comparable, demonstrating the consistency of the DCS, viscosity and virial data sets, and their error bars. Furthermore, we have found that fitting the DCS measurments alone do not yield substantially better fitting qualities: the DCS fits are not being distorted by any incompatibility with either the mixture viscosity or virial data. Similar statements may be made for the other two properties. Nevertheless, it is evident that the low-temperature virials (Sec. 2.4.B) could be reproduced only by simultaneously fitting all three properties at once. These experiences are similar to those of Pack et al.[8,11(b)]

2.6.C. Properties Excluded from the Fits

Figures 2.7 and 2.8 compare predictions calculated from our best-fit HFD potentials to the interaction diffusion and equimolar thermal diffusion measurements available to us.[51,52] The MSV results again are indistinguishable from the HFD ones shown. Deviation plots for several authors' mixture diffusion measurements are shown in the lower part of Fig. 2.7. Fitting qualities for each authors' data are collected in Tables 2-6 and 2-7 for diffusion and thermal diffusion measurements, respectively. In constructing these tables, we use the error bars claimed by the respective authors, except for the diffusion data of Dubro and Weissman,[51(b)] Wahby et al.,[51(i)] and Dunlop and co-workers.[51(d)–51(f)] In the first case, the mole fraction is not given, and so the error introduced by its uncertainty is convoluted with their measurement errors. For the results of Wahby et al.,[51(i)] we calculate diffusion ratios for direct comparison to their measurements, while convoluting the effects of temperature uncertainties with their statistical errors. For the data of

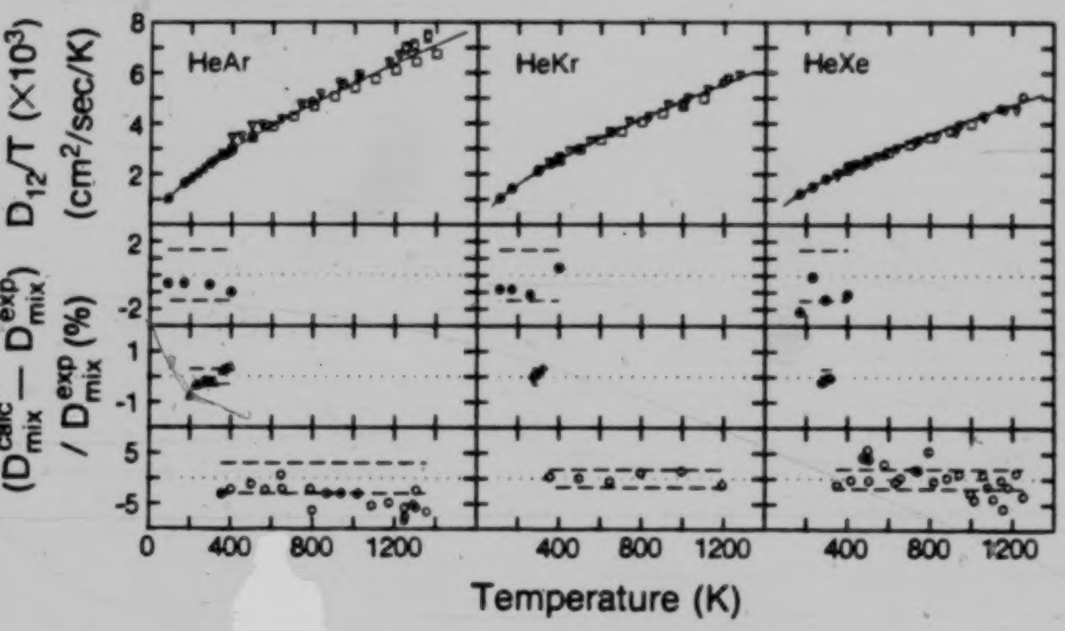

Figure 2.7

The upper frames show interaction diffusion data from representative experiments (symbols) and from the best-fit HFD potentials (solid curves). The diffusions have been divided by the temperature for clarity of display. Lower frames detail deviations of calculated from measured mixture diffusions for three authors. Dashed lines depict error bounds claimed by these authors. Symbols used are: ●, van Heijningen et al.;[51(a)] △, Trengove et al.[30] (HeAr only); ○, Taylor et al.;[51(j)–51(l)] ◇, Arora et al.;[51(e),51(f)] ▽, Zwakhals et al.;[51(g),51(h)] □, Hogervorst.[51(c)]

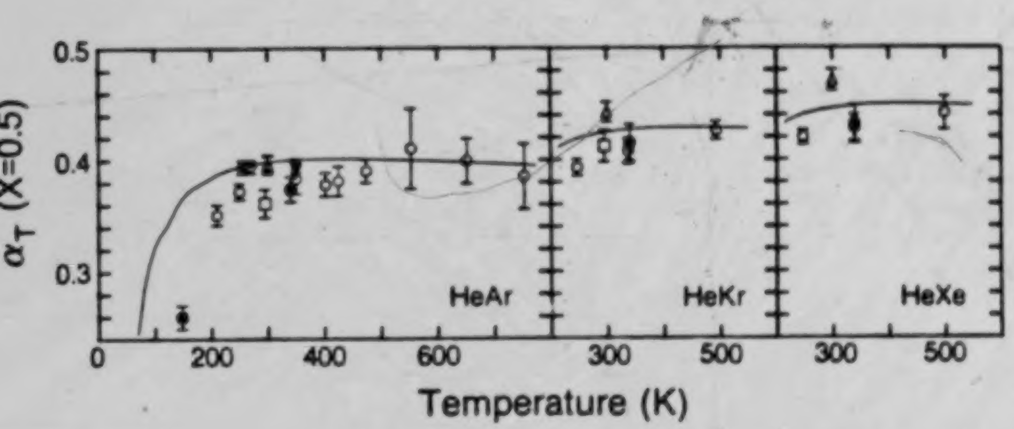

Figure 2.8

Equimolar thermal diffusion data from experiment (symbols) and from the best-fit HFD potentials (solid curves). Error bars are those claimed by the authors. Symbols used are: ●, Santamaría et al.[52(b),52(c)] and Savirón et al.;[52(a)] ○, Taylor;[52(e)] ◇, Trengove and Dunlop[31] (HeAr only); △, Trengove et al.;[52(f),52(g)] □, Timov and Suetin[52(d)] (HeAr and HeKr only); ✡, Trengove et al.[30] (HeAr only).

Table 2-6. Fitting Quality for Mixture Diffusion[a]

Interaction	Data	Temperature (K)	Error(%)[b]	δ_D[c]
HeAr	Van Heijningen et al.[51(a)]	90-400	1.5	0.438
	Dubro and Weissman[51(b)]	305-335	3.8	0.500
	Hogervorst[51(c)]	300-1400	0.75	4.183
	Yabsley and Dunlop[51(d)]	300	0.30	1.190
	Arora et al.[51(e)]	275-323	0.30	0.620
	Arora and Dunlop[51(f)]	300,323	0.30	0.481
	Zwakhals and Reus[51(g)]	298-1272	1.0	6.750
	Wahby et al.[51(i)]	237-419	0.3-0.4	1.127
	Taylor and Cain[51(j)]	358-1357	3.0	1.518
	Trengove et al.[30]	200-400	0.30	1.102
	all authors combined	—	—	3.515
HeKr	Van Heijningen et al.[51(a)]	112-400	1.5	0.564
	Hogervorst[51(c)]	300-1100	0.75	4.043
	Cain and Taylor[51(l)]	358-1194	1.75	0.550
	Arora et al.[51(e)]	275-323	0.30	0.543
	Reus et al.[51(h)]	307-1274	1.0	1.759
	Wahby et al.[51(i)]	237-419	0.3-0.5	1.174
	all authors combined	—	—	2.198
HeXe	Van Heijningen et al.[51(a)]	169-400	1.5	0.935
	Hogervorst[51(c)]	300-1000	0.75	3.763
	Arora et al.[51(e)]	275-323	0.30	0.340
	Zwakhals and Reus[51(g)]	297-1270	1.5-3.4	2.792
	Wahby et al.[51(i)]	237-419	0.3-0.4	1.459
	Taylor and Cain[51(k)]	351-1252	1.95	1.492
	all authors combined	—	—	2.231

[a] Diffusion ratios for the data of Ref. 51(i)

[b] Precision claimed by authors except for Refs. 51(b), 51(d)-51(f), and 51(i) [see Sec. 2.6.C].

[c] Eqn. (2-2).

Table 2-7. Fitting Quality for Mixture Thermal Diffusion

Interaction	Data	Temperature (K)	Error(%)[a]	$\delta_{\sigma T}$[b]
HeAr	Van Savirón et al.[52(a)]	340	3.0	2.516
	Santamaría et al.[52(b)]	148	4.0	10.309
	Timov and Suetin[52(d)]	295	3.5	2.962
	Taylor[52(e)]	210-753	2.0-7.6	1.966
	Trengove et al.[52(f)]	300	2.0	0.595
	Trengove et al.[52(g)]	300	2.0	0.515
	Trengove and Dunlop[31]	255,271	1.5	0.601
	Trengove et al.[30]	350	1.5	1.238
	all authors combined	—	—	3.317
HeKr	Timov and Suetin[52(d)]	295	3.5	2.287
	Taylor[52(e)]	247-493	1.9-2.8	2.737
	Trengove et al.[52(f)]	300	2.0	1.861
	Santamaría et al.[52(c)]	340	4-8	0.663
	all authors combined	—	—	2.401
HeXe	Taylor[52(e)]	247-499	1.6-3.4	3.067
	Trengove et al.[52(f)]	300	2.0	2.407
	Santamaría et al.[52(c)]	340	4.0	1.208
	all authors combined	—	—	2.822

[a] Precision claimed by authors; see Sec. 2.6.C.

[b] Eqn. (2-2).

Refs. 51(d)-51(f), the errors were assigned after extensive discussion with P. J. Dunlop. Errors quoted for thermal diffusions in Table 2-7 are those claimed by the authors in all cases.

It is apparent from the large overall fitting qualities appearing in Tables 2-6 and 2-7 that most of the diffusion and thermal diffusion data sets are incompatible with the data sets that were used in constructing the present interatomic potentials. Consistently good agreement is found only for the diffusion data of van Heijningen et al.,[51(a)] and Arora et al.,[51(e)] and the diffusion ratios of Wahby et al.[51(i)]

2.6.C.1. Diffusion

Several authors' data, particularly those of Zwakhals and Reus,[51(g)] exhibit unacceptably large fitting qualities δ because the apparent randomness in their data exceeds the precision they claim to achieve. This point is demonstrated with particular clarity for the Taylor and Cain HeXe diffusions[51(k)] appearing in the deviation plots of Fig. 2.7. These data sets are not consistent enough within themselves to be reproduced by any interatomic potential within the precision claimed.

The high-temperature diffusions of Hogervorst[51(c)] show systematic deviations from the predictions. Since these data probe the repulsive wall, it is apparent that they are incompatible with both the viscosity and virial data, and with the Taylor et al.[51(j)–51(l)] and Zwakhals and Reus data.[51(g),51(h)]

Dunlop and co-workers[30,51(d)–51(f)] measured diffusions in the temperature range of 275-323 K which are accurately reproduced by the present HeAr, HeKr and HeXe potentials. Their HeAr data[30] beyond this range exhibit a temperature trend suggesting that our fitted HFD hard wall is not steep enough. Nevertheless, including this data in trial simultaneous fits of the HeAr potential does not improve reproduction of their additional[30] data at all. Precisely where agreement is worst – at 400 K – the authors have recently changed their HeAr data by twice the claimed accuracy of ±0.3%.[30] We believe that their data beyond the 275-323 K temperature range should more realistically be assigned errors of ±0.5%, which still makes it among the best available for diffusion measurements. We caution that using unrealistically optimistic error bars could systematically bias the interatomic potentials extracted.

2.6.C.2. Thermal Diffusion

Thermal diffusion measurements appear to suffer from the same lack of consistency as diffusions. It is evident from Fig. 2.8 that there is no potential capable of reproducing all the data, for any of the rare gas pairs, given the accuracies stated by the authors. Much of the thermal diffusion data is also incompatible with the viscosity and virial measurements. Again, we are forced to conclude that the error bars claimed are unrealistically optimistic.

2.6.C.3. Thermal Conductivity

Thermal conductivity data are available only for HeAr at room temperature,[53] to the best of our knowledge. These results provide information similar to the viscosity, but are more difficult to measure. Despite claimed accuracy of ±0.2%, a second-order Chapman-Cowling inversion of the mixture data shows deviations of up to 1%, and these data were not considered further.

2.6.C.4. Integral Cross Sections

Finally, we should consider scattering measurements of the ICS as a function of velocity.[33,54] The most recent and reliable[55] of these data provide absolute ICS's for velocities from 0.8-2.3 km/sec,[33] where they are monotonically decreasing. Such data provide constraints for measures of the attractive well "size" (such as $\epsilon . r_m^6$), and could therefore provide useful corroboration for our fitted attractive well depths. These data are also particularly sensitive to the outer bowl of the attractive well.[38]

The best-fit HFD potentials are used to calculate ICS's for comparison with the data of Pirani and Vecchiocattivi.[33,34] The calculated ICS curves are shown in Fig. 2.9, where agreement with the HeAr and HeKr ICS data is seen to be excellent, while the calculated HeXe ICS is slightly lower than the measurements. The latter discrepancy can be removed completely by minor adjustments to the outer bowl of the attractive well as detailed in the Appendix A2.

2.6.D. Error Bounds for the Fitted Potentials

We now address the important question of the reliability of the fitted interatomic potentials, and compare them to the best potentials previously obtained.[1,5,7,50,56] We examine in detail the influence of possible systematic errors on the potential, as well as the bias attributable to choosing particular representations for the interatomic potential parameterization. The latter analysis leads us to propose error bounds for the potential itself, rather than for the fitted potential parameters.

2.6.D.1. Systematic Errors

The DCS fits presented in Fig. 2.3 show calculated curves systematically lower than the HeAr and HeXe experimental measurements. This could be due, in part, to errors made in the He adsorption energy on the bolometer (Sec. 2.3.A), for which the worst case is HeAr. Also for HeAr, the use of a crude ArAr pair potential (Table 2-3) could adversely affect our calculated mixture viscosities. A third possible systematic error is our instrumental angular resolution calibration, as discussed in Sec. 2.6.A. Finally, it is possible that inclusion of diffusion and

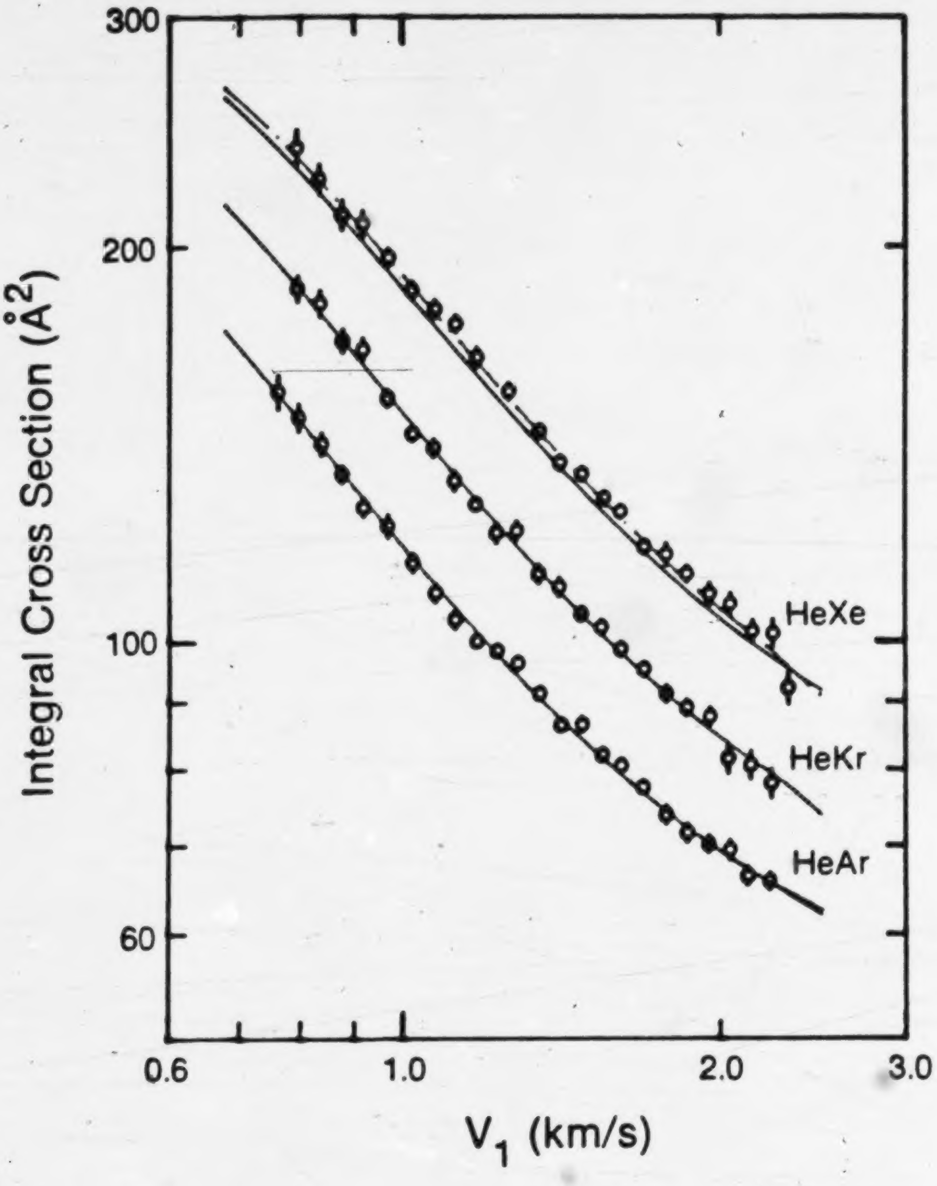

Figure 2.9

Integral cross section data as a function of primary beam velocity from experiment[33,34] (symbols) and from the best fit HFD potentials (solid curves). The error bars depict the uncertainties for each single point; the absolute calibration error of ±3%[34] is accomodated by allowing the entire set of experimental data to be adjusted by up to this ammount. Actual adjustments were +0.7%, −1.5%, and −3.0% for HeAr, HeKr and HeXe respectively. The dash-dotted curves, perceptable only for HeXe, are calculated from potentials obtained by including the Arora et al. diffusion data[51(e)] and the ICS data in the multiproperty fits (see Appendix A2).

thermal diffusion data (most extensive for HeAr), with error bars assigned as outlined in Sec. 2.4, could change the fitted interatomic potential. For the latter possibility, we assign error bars of ±0.3% for all the data of Dunlop and co-workers;[51(d)–51(f)] ±18% for the Zwakhals and Reus diffusion[51(g)] at their lowest temperature and ±10% elsewhere; ±3% to ±6% for Taylor and Cain's data[51(j)] and ±1% to ±6% for Hogervorst[51(c)] (the latter authors' errors are smaller tor their lower-temperature measurements). The remaining diffusion data[51] are used with error bars as claimed by the authors. All the thermal diffusion data[52] are assigned error bars of ±5% or the authors' stated errors, whichever is larger. The datum of Santamaría et al.[52(b)] at 148 K is dropped from the data set entirely. The assigned errors were those minimally required to ensure consistency between different authors as discussed in Sec. 2.4, without reference to our best-fit HFD potentials.

Trial simultaneous fits were then conducted for each of the four possible systematic errors outlined above. Completely neglecting the He adsorption energy on the bolometer results in an attractive well deeper by 0.027 meV; using a better ArAr pair potential gives the same well depth as the best-fit HFD potential. Including the diffusion and thermal diffusion data, along with the DCS, viscosity and virial data, gives a well shallower by 0.011 meV. Restricting the added diffusion and thermal diffusion to the precise data of Dunlop and co-workers[30,31,45(d)–45(f),52(f),52(g)] makes the well shallower by 0.009 meV. In all these cases, only the well depth is affected at all; the well and wall positions are entirely unaffected. These potentials, along with the original best-fit HFD and MSV potentials, are all plotted in Fig. 2.10 and compared with the HeAr potential of Ref. 5. It can be seen that the influence of these systematic errors is very small and indeed, is exceeded when the data are analyzed with the MSV potential (0.078 meV deeper).

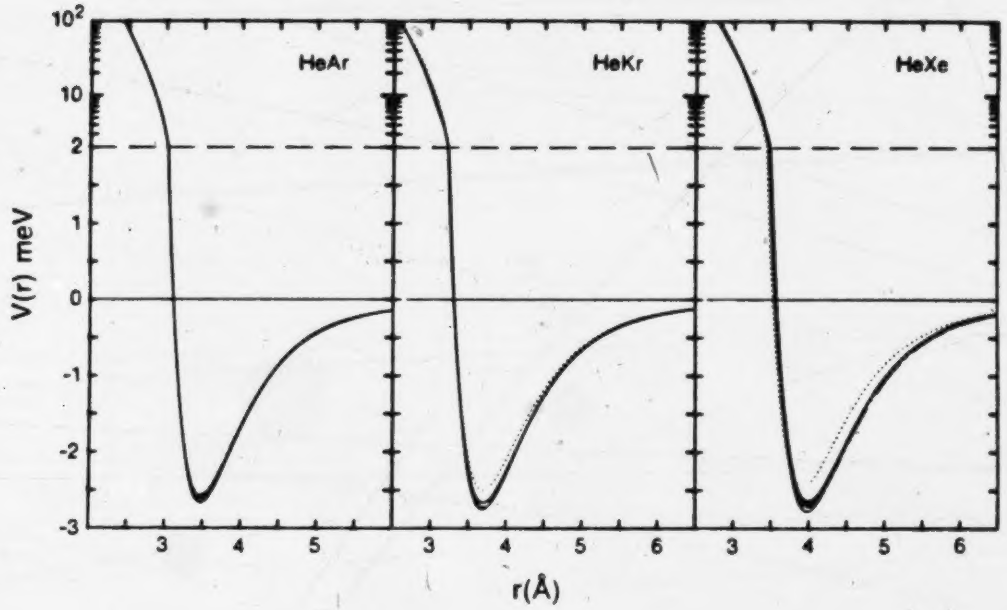

Figure 2.10

Error bounds for the fitted HeAr, HeKr and HeXe interatomic potentials are given by the regions between the solid curves. In considering systematic errors, we plot 5 curves for HeAr; we plot 6 HeKr and 4 HeXe potential energy curves for potential model bias considerations. Dotted curves are the HFD potentials of Smith et al.[7] (HeKr and HeXe). Indistinguishable from the solid curves shown are the Aziz et. al. HFD potential for HeAr[5] and the Watanabe et al. $U_b(D,K)$ potential for HeKr[50] (XC-2 of Aziz[1]); the Smith et al. MS potential for HeXe[7] (not shown) lies between the repulsive wall and the attractive well of the dotted curve and the long-range region of the solid curves. Dash-dotted curves, perceptable only for the outer bowl of the HeXe potential well, are the potentials obtained as in Fig. 2.9.

Finally, setting the apparatus angular resolution at our calculated (but highly approximate, see Secs. 2.2.B and 2.3.A) value of 1.25° results in a perceptible deepening of the attractive well (0.160 meV) but with unacceptable reproduction of the DCS oscillatory amplitudes ($\delta_{\mathrm{DCS}} = 1.970$). In fact, statistical analysis of the fitted resolution parameter gives a 95% confidence limit of ±0.02°; setting it to the upper limit results in an attractive well shallower by 0.035 meV. It is thus clear that none of the systematic errors considered have any significant influence upon the fitted HeAr potential. Since each of the four possibilities considered are worst for the HeAr case, we conclude that our fitted potentials are free of bias due to systematic errors in our experimental measurements or data analysis. A more extensive discussion of bias due to errors in other data sets appears in the Appendix A2.

2.6.D.2. Model Bias and Potential Error Bounds

When fitting parameters of assumed mathematical forms to experimental data, the interatomic potentials obtained accurately represent the true interatomic potential only to the extent that the mathematical form can reproduce the (unknown) true potential. This of course has been the incentive for direct inversion, which has yielded model-independent potentials from very extensive DCS measurements for HeNe[57] and for transport properties.[58] Such procedures have not been applied for inverting several properties simultaneously, and one is left with numerically tabulated potentials requiring interpolation or choosing between them for the weakly repulsive wall of the potential.

Our approach instead is to fit the data using the HFD and MSV potential forms. Both are physically reasonable, but parameterize the repulsive wall and attractive well regions very differently. Therefore, they will give similar values for the potential energy curve only to the extent that they are constrained by the sensitivity, consistency, and accuracy of the properties to which they are fit. In addition, we also subject the HeKr and HeXe DCS, viscosity and virial data to simultaneous fits with some of the modified potential forms described in a recent paper.[38] In these fits, we optimized all of the usual three HFD parameters (r_m, α and C_8), and one modification parameter (wall position, well depth, well position, and curve position for HeKr; wall position and well depth for HeXe) for simultaneous four-parameter fits. These modified potentials in principle could allow selected features of the interatomic potential to change totally independently of the HFD mathematical form.

The results for all of these fits are presented in Fig. 2.10. Despite arbitrary flexibility for the well depth and repulsive wall position, the fitted potentials all lie within a very narrow band of each other. We can use these bands to *assign error bounds to the potential itself, rather than to the potential parameters.* Estimates for these error bounds are collected in Table 2-8. To the best of our knowledge, this work presents the first such evaluation.

It is interesting to note that the ±0.015Å error bound on the repulsive wall position corresponds to a ±1% error in diffusion measurements near room temperature (±0.5% for the other transport properties).[38] Since the present error bounds were determined by using only the DCS, viscosity and virial data, it is possible that including the accurate (±0.3%) Arora et al. diffusion data[51(e)] in the multiproperty fits could further tighten the error bounds. We have resisted doing so however, believing that successfully *predicting* the accurate diffusion measurements would strengthen our confidence that the error bounds give the accuracy of the potentials we have determined, and not just their precision. Nevertheless, our potentials are not free of any defects due to possible *systematic* errors in the data analyzed (see Appendix A2).

Table 2-8. Error Bounds for the HeRg potentials[a]

Potential region (feature)	Value[b] HeAr	 HeKr	 HeXe	Error bounds[c,d]
Attractive well depth	2.59 meV	2.67 meV	2.64 meV	±3%
Attractive minimum position	3.482Å	3.702Å	3.997Å	±0.03Å
Zero crossing of the potential	3.107Å	3.299Å	3.565Å	±0.015Å
Position of the wall at 10 meV	2.858Å	3.035Å	3.278Å	±0.015Å
at 100 meV	2.433Å	2.573Å	2.778Å	±0.03Å
at 1000 meV[e]	1.91Å	2.00Å	2.16Å	±0.1Å

[a] Error bounds *apply to the potential and not its parameters*; see Sec. 2.6.D.

[b] Three-parameter best-fit HFD potentials; parameters in Table 2-5.

[c] Taken from the full range of potentials plotted in Fig. 2.10, and multiplied by 1.5 to accomodate more exhaustive potential modifications.

[d] Interatomic distances could also be slightly biased by collision velocity errors which are estimated as ±0.2% (Sec. 2.2.A).

[e] Extrapolated; not sensitive to properties being fit.

2.6.D.3. Comparison to Previous Best-fit Potentials

In addition to illustrating the error bounds for our HeKr and HeXe potentials, Fig. 2.10 also displays the HFD potentials previously proposed by Aziz et al.[5] for HeAr and by Smith et al.[7] for HeKr and HeXe. An extensive comparison with literature potentials has been carried out recently by Aziz[1] and we will therefore deal only with the best of those potentials. In this respect, we will discuss all of the interatomic potentials proposed by Smith et al.[7] and by Watanabe et al.[50] for these interactions (see Table 2-9). We will also briefly discuss the Maitland and Wakeham semi-inversion potentials.[56]

The HeAr potential of Aziz et al.[5] is essentially identical to the one that we have determined (Fig. 2.10). These two potentials reproduce our DCS measurements and the viscosity, virial, ICS and Arora et al.[51(e)] diffusion data equally well. It is apparent therefore, that the present HeAr results are consistent with three independent high-resolution DCS measurements.[5,9,18]

The Smith et al. HFD potentials[7] do not reproduce the virial data at low temperatures for HeXe nor at any temperature for HeKr, nor do they reproduce the ICS data. These deficiencies are caused by a potential well that is too shallow for HeKr, and by a well that is both too shallow and too narrow for HeXe. These potentials also fail to reproduce the accurate Arora et al.[51(e)] diffusion data owing to a repulsive wall that is too steep. Nevertheless, it is interesting to note that our DCS data alone do not discriminate against the Smith et al.[7] potentials. Indeed, we are impressed with their high quality, even though they were obtained from DCS measurements of rather lower resolution and signal-to-noise than the present results.

The Smith et al. MS potentials[7] do not reproduce the position of the DCS oscillations for HeAr and HeKr owing to r_m values which are too small.

Table 2-9. Comparison Between Interatomic Potentials

	HeAr				HeKr				HeXe		
	HFD[a]	HFD[b]	MS[c]	XC[d]	HFD[a]	HFD[c]	MS[c]	XC[d]	HFD[a]	HFD[c]	MS[c]
r_m(Å)	3.482	3.48	3.43	3.454	3.702	3.70	3.64	3.688	3.997	3.93	3.98
σ(Å)	3.107	3.104	3.07	3.081	3.299	3.31	3.25	3.291	3.565	3.53	3.56
ϵ(meV)	2.59	2.57	2.53	2.543	2.667	2.51	2.62	2.661	2.635	2.45	2.36
r(V=100 meV;Å)	2.433	2.43	2.45	2.402	2.573	2.61	2.61	2.580	2.778	2.82	2.81
δ_{DCS}	1.099	1.133	1.711	1.346	0.774	0.806	1.466	0.837	0.970	1.035	0.925
δ_η	0.378	0.456	0.513	0.950	0.541	0.752	0.412	0.464	0.470	0.339	0.307
δ_B	0.907	0.928	0.874	1.215	0.797	2.861	0.965	0.783	1.135	2.563	1.750
δ_D^e	0.620	0.695	0.666	7.079	0.543	4.734	0.678	0.384	0.340	2.217	1.548
δ_{ICS}	0.970	1.013	0.970	0.946	0.826	2.622	1.055	0.824	1.741	8.330	5.352
$\delta_{overall}$[f]	0.923	0.962	1.247	2.811	0.734	2.406	1.136	0.739	1.095	3.982	2.605

[a] Present work.
[b] Ref.5 as confirmed in Ref. 1.
[c] Ref. 7.
[d] Ref. 50, as selected in Ref. 1.
[e] Using only data of Ref. 51(e) with error bars of ±0.3%.
[f] Eqn. (2-1) with $w_{DCS}=1.00$; $w_\eta=w_B=w_D=0.33$; $w_{ICS}=0.50$.

These potentials do however, reproduce the viscosity, virial, and Arora et al.[51(e)] diffusion data very well. Conversely, the HeXe MS potential[7] reproduces the DCS measurements and the viscosity data very well, but does not reproduce the low-temperature virial data of Kate et al.,[42(f)] the ICS data, or the diffusion data of Arora et al.[51(e)]

The preferred Watanabe et al.[50] XC potential for HeAr [their U_b(B,B)] does not reproduce the DCS measurements, the viscosity, or the virial data very well. In addition, it completely fails to reproduce the Arora et al.[51(e)] diffusion data. This HeAr XC potential is but one of four constructed from fits to different sets of virial measurements. We remark that we found no inconsistency between these virial data sets such as the ones encountered by Watanabe et al.[50] For HeKr, Watanabe et al.[50] were unable to state a strong preference for any of their four proposed XC potentials. Nevertheless, one of them [their U_b(D,K)] is indistinguishable from our best-fit HFD potential, and was selected by Aziz[1] based on its predictions of the viscosity data. Our analysis confirms that this XC-2 potential is indeed a reliable characterization for the HeKr interaction. The above discussion also suggests that despite some inconsistencies noted earlier,[50] the XC potential form may provide a framework at least as good as the HFD one used here, as long as the data sets considered are consistent and reliable. This can best be ensured by using the multiproperty fitting procedure.

Finally, a word about the Maitland and Wakeham[55] MS potentials. These are numerical potentials derived from transport data, and subsequently reexpressed in terms of the MS potential function. Unfortunately, the inversion procedure sometimes yields unphysical "kinks" in the repulsive wall, most notably for the ArKr and ArXe interactions. Moreover, the attractive well region parameters for He-containing systems can be obtained only by extrapolation.[56]

2.7. SUMMARY

Differential cross sections for scattering of a thermal-energy He beam by crossed beams of Ar, Kr, and Xe have been re-measured with a high-resolution scattering apparatus. These data, along with mixture viscosity and interaction second virial data, are used to determine HeAr, HeKr and HeXe interatomic potentials. The potentials reproduce the above properties faithfully and consistently, and predict diffusion and thermal diffusion more accurately than current measurements allow.

Systematic errors and model bias are investigated for the fitted potentials, and provide estimates for the potential energy curves independent from the parameters used to describe them. The HeXe potential obtained has a deeper and wider attractive well than the previously proposed potential.[7] The HeAr potential is almost indistinguishable from its predecessor,[5] while the HeKr potential is slightly deeper than the Smith et al.[7] HFD potential and is indistinguishable from one of the Watanabe et al.[50] XC potentials. The attractive well depths are 2.59 meV, 2.67 meV and 2.64 meV for HeAr, HeKr and HeXe respectively, determined to ±3%.

Acknowledgements

This project was facilitated by the dedicated technical support of the Chemistry, Physics, and Technical Services Machine Shops and the Chemistry Electronics Shop. We are particularly indebted to Messrs. E. Young and H. Hofmann of the former shop. We thank Karen McLeod and Deb Danielson for their assistance in collecting the experimental data, as well as Kevin Charter and Gary Samek for their assistance with the apparatus. We have benefitted from fruitful discussions with G. Scoles (Princeton), P. J. Dunlop (Adelaide), R. A. Aziz (Waterloo), F. Vecchiocattivi (Perugia), W. J. Meath (Western Ontario), R. T Pack (Los Alamos), and R. L. Robinson (Oklahoma State), for which we are grateful. This research was supported by grants from the Natural Sciences and Engineering Research Council (Canada) and from the Research Corporation. Acknowledgement is also made to the donors of The Petroleum Research Fund, administered by the American Chemical Society, for partial support of this research.

APPENDIX A2

Influence of Data Included in the Multiproperty Fits

The error bounds for the best-fit potentials contained in Table 2-8 assume that the viscosity and virial data used in their determination have no systematic errors. Here we examine how these error bounds are affected by alternative data sets for the particularly important HeXe interatomic potential. Since the viscosity and Arora et al.[51(e)] diffusion data have similar sensitivities to the repulsive wall, and the virial and ICS data are both sensitive to the outer bowl of the attractive well,[38] we may easily check whether any systematic errors in these data significantly bias the potentials extracted. Table 2-10 shows that the resulting potential differs only marginally from our preferred HFD potential, and that the error bounds of Table 2-8 accomodate these differences. It is interesting to note that the potential fit to the DCS, diffusion, and ICS data nicely reproduces the remaining viscosity and virial measurements. Alternatively, all these data may be fitted simultaneously, yielding a potential that can be distinguished only in the outer bowl region (Fig. 2.10). Other calculations demonstrate that fitting any two properties (e.g., DCS and virials as shown) yields potentials unable to reproduce at least two of the remaining three properties. Finally, trial fits to the DCS alone or including virials with enlarged low-temperature error bars illustrate the necessity of allowing the HFD C_8 parameter to be fit to the data: there is a strongly negative correlation between the α and C_8 HFD parameters when the data being fit are sensitive neither to the outer bowl nor to the repulsive wall. Table 2-10 shows that the potentials determined by fitting DCS and virial data alone can fail to reproduce several of the other properties.

Table 2-10. Effect of Data Sets used in Determining the HeXe Interatomic Potential[a]

	DCS,η,B[b]	DCS,D, ICS[c]	DCS,η,B, D,ICS[c]	DCS,B	DCS	DCS	DCS	DCS,B[d]
r_m(Å)	3.997	3.986	4.010	4.011	3.980	3.994	3.959	3.956
σ(Å)	3.565	3.555	3.573	3.563	3.564	3.564	3.562	3.552
ϵ(meV)	2.635	2.702	2.677	2.502	2.465	2.458	2.465	2.433
r(V=100 meV;Å)	2.778	2.774	2.766	2.717	2.812	2.774	2.858	2.830
α($Å^{-1}$)	3.422	3.432	3.379	3.306	3.644	3.464	3.994	3.881
A(keV)	2.953	3.079	2.957	2.022	4.289	2.668	1.123	7.340
C_6(eV-$Å^6$)	11.68	11.68	11.68	11.68	11.68	11.68	11.68	11.68
C_8(eV-$Å^8$)	93.6	94.4	101.8	96.0	68.6	79.2[f]	56.4[g]	56.4[g]
δ_{DCS}	0.970	1.107	1.050	0.845	0.805	0.810	0.822	0.852
δ_η	0.470	0.497	0.541	1.621	0.405	0.604	1.193	0.561
δ_B	1.135	1.024	1.023	1.195	2.282	1.748	3.044	2.659
δ_D	0.340	0.217	0.305	10.021	3.684	2.034	10.296	5.128
δ_{ICS}	1.741	1.086	0.785	2.930	5.728	4.883	6.978	7.303
$\delta_{overall}$[e]	1.095	0.951	0.869	3.992	3.057	2.457	5.051	3.932

[a] HFD potential of Eqn. (2-3) in all cases with D=1.28 and C_n determined by recursion[48] for $n \geq 10$. Fitted parameters r_m, α, and C_8 unless noted otherwise. C_6 is held fixed at the value given in Ref. 10. The ϵ and A parameters are not fitted independently. Diffusion data set uses data of Ref. 51(e) only, with error bars of ±0.3%.

[b] Best-fit potential of Table 2-5.

[c] Alternative potentials (see also Figs. 2.9 and 2.10).

[d] Error bars for fitting the virial data of Ref. 42(f) arbitarily increased to ±5 cm^3/mole to accommodate possible uncertainties in the vapour pressure of solid Xe[44]; other virial data with error bars as in Table 2-4.

[e] Eqn. (2-1) with $w_{DCS}=1.00$; $w_\eta=w_B=w_D=0.33$; $w_{ICS}=0.50$.

[f] Held fixed at the mean of Standard and Certain's bounds.[47a]

[g] Held fixed at the mean of Tang, Norbeck and Certain's bounds;[47b] $C_{10}=332$ eV-$Å^{10}$; $C_{12}=C_{14}=0$.

References

1. R.A. Aziz, in *Inert Gases: Springer Series in Chemical Physics*, edited by M. Klein (Springer, Berlin, 1984); Vol. **34**.
2. G.C. Maitland, M. Rigby, E.B. Smith, and W.A. Wakeham, *Intermolecular Forces: Their Origin and Determination* (Clarendon, Oxford, 1981).
3. G. Scoles, Annu. Rev. Phys. Chem. **31**, 81 (1980).
4. J.A. Barker, in *Rare Gas Solids*, edited by M. Klein and J.A. Venables (Academic, New York, 1976); Vol. **1**.
5. R.A. Aziz, P.W. Riley, U. Buck, G. Maneke, J. Schleusener, G. Scoles, and U. Valbusa, J. Chem. Phys. **71**, 2637 (1979).
6. (a) K.M. Smith, A.M. Rulis, G. Scoles, R.A. Aziz, and G. Duquette, J. Chem. Phys. **63**, 2250 (1975); (b) R. Ahlrichs, R. Penco, and G. Scoles, Chem. Phys. **19**, 119 (1977).
7. K.M. Smith, A.M. Rulis, G. Scoles, R.A. Aziz, and V. Nain, J. Chem. Phys. **67**, 152 (1977).
8. R.T Pack, J.J. Valentini, C.H. Becker, R.J. Buss, and Y.T. Lee, J. Chem. Phys. **77**, 5475 (1982).
9. L. Beneventi, P. Casavecchia, and G.G. Volpi, J. Chem. Phys. **84**, 4828 (1986).
10. L.J. Danielson, K.M. McLeod, and M. Keil, J. Chem. Phys. **87**, 239 (1987).
11. (a) R.T Pack, E. Piper, G.A. Pfeffer, and J.P. Toennies, J. Chem. Phys. **80**, 4940 (1984); (b) R.T Pack, J.J. Valentini, and J.B. Cross, J. Chem. Phys. **77**, 5486 (1982).
12. M. Faubel, K.H. Kohl, J.P. Toennies, and F.A. Gianturco, J. Chem. Phys. **78**, 5629 (1983).

13. (a) U. Buck, H. Meyer, M. Tolle, and R. Schinke, Chem. Phys. **104**, 345 (1986); (b) H. Meyer, U. Buck, R. Schinke, and G.H.F. Diercksen, J. Chem. Phys. **84**, 4976 (1986); (c) U. Buck, D. Otten, R. Schinke, and D. Poppe, J. Chem. Phys. **82**, 202 (1985).

14. L. Beneventi, P. Casavecchia, and G.G. Volpi, J. Chem. Phys. **85**, 7011 (1986).

15. (a) T.H. Ellis, S. Iannota, G. Scoles, and U. Valbusa, Phys. Rev. **B 24**, 2307 (1981); (b) T.H. Ellis, G. Scoles, and U. Valbusa, Chem. Phys. Lett. **94**, 247 (1983); (c) T.H. Ellis, G. Scoles, and U. Valbusa, Surf. Sci. **118**, L251 (1982); (d) G. Bracco, P. Cantini, A. Glachant, and R. Tatarek, Surf. Sci. **125**, L81 (1983); (e) G. Bracco, P. Cantini, E. Cavanna, R. Tatarek, and A. Glachant, Surf. Sci. **136**, 169 (1984); (f) J.Z. Larese, W.Y. Leung, D.R. Frankl, N. Holter, S. Chung, and M.W. Cole, Phys. Rev. Lett. **54**, 2533 (1985); (g) J.C. Ruiz, Ph.D. Thesis, University of Waterloo (1987); (h) S.J. Sibener, private communication.

16. (a) J.M. Hutson and C. Schwartz, J. Chem. Phys. **79**, 5179 (1983); (b) H. Jónsson, J.H. Weare, T.H. Ellis, G. Scoles, and U. Valbusa, Phys. Rev. **B 30**, 4203 (1984); (c) T.H. Ellis, G. Scoles, U. Valbusa, H. Jónsson, and Weare, Surf. Sci. **155**, 499 (1985); (d) H. Jónsson and J.H. Weare, Farad. Disc. Chem. Soc. **80**, 29 (1985); (e) S. Chung, N. Holter, and M.W. Cole, Phys. Rev. **B 31**, 6660 (1985).

17. D.R. Worsnop, S.J. Buelow, and D.R. Herschbach, J. Phys. Chem. **90**, 5121 (1986).

18. C.V. Boughton, R.E. Miller, P.F. Vohralik, and R.O. Watts, Mol. Phys. **58**, 827 (1986).

19. N.C. Blais, J.B. Cross, and G.H. Kwei, J. Chem. Phys. **66**, 2488 (1977).

20. J.P. Toennies and K. Winkelmann, J. Chem. Phys. **66**, 3965 (1977).

21. R.T Pack, J. Chem. Phys. **81**, 1841 (1984).

22. M. Keil and G.A. Parker, J. Chem. Phys. **82**, 1947 (1985).

23. R.T Pack, J. Chem. Phys. **60**, 633 (1974).

24. (a) H. Abe, Chem. Phys. **68**, 89 (1982); (b) E.F. Ezell, F. Pollock, and J.G. Daunt, J. Low Temp. Phys. **42**, 47 (1981); (c) T.J. Lee, Surf. Sci. **44**, 389 (1974); (d) J.G. Daunt and E. Lerner, J. Low. Temp. Phys. **8**, 79 (1972).

25. (a) J.M. Keller and W.L. Taylor, J. Chem. Phys. **51**, 4829 (1969); (b) R.J. Munn, F.J. Smith, and E.A. Mason, J. Chem. Phys. **42**, 537 (1965). Note the omission of a factor $(\ell+1)/(2\ell+5)$ for $Q^{(3)}$ and a typographical error for $Q^{(4)}$ in Ref. 21.

26. See, for example D. Beck, in *Proceedings of the International School of Physics*, edited by Ch. Schlier (Academic, New York, 1968) Course 44.

27. J.O. Hirschfelder, G.F. Curtiss, and R.B. Bird, *Molecular Theory of Gases and Liquids* (Wiley, New York, 1954).

28. R.A. Aziz, V.P.S. Nain, J.S. Carley, W.L. Taylor, and G.T. McConville, J. Chem. Phys. **70**, 4330 (1979).

29. (a) E.A. Mason, J. Chem. Phys. **27**, 75 (1957); (b) E.A. Mason, J. Chem. Phys. **22**, 169 (1954).

30. R.D. Trengove, K.R. Harris, H.L. Robjohns, and P.J. Dunlop, Physica **131A**, 506 (1985); *ibid.* **144A**, 254 (1987).

31. R.D. Trengove and P.J. Dunlop, Ber. Bunsenges. Phys. Chem. **87**, 874 (1983).

32. (a) M.E. Boyd, S.Y. Larsen, and J.E. Kilpatrick, J. Chem. Phys. **50**, 4034 (1969); (b) T. Kihara, Y. Midzuno, and T. Schizume, J. Phys. Soc. Japan **10**, 249 (1955).

33. F. Pirani and F. Vecchiocattivi, J. Chem. Phys. **66**, 372 (1977).
34. F. Vecchiocattivi, private communication. Two revisions to the published data of Ref. 33 were suggested by the authors: firstly, the calculated ICS's are compared to the data in the laboratory frame of reference, rather than to deconvoluted data in the centre-of-mass frame; secondly, a systematic error of 3% has been removed from the HeXe data, which was formerly too high.
35. G.A. Parker and R.T Pack, J. Chem. Phys. **68**, 1585 (1978).
36. J.P. Toennies, W. Welz, and G. Wolf, J. Chem. Phys **71**, 614 (1979).
37. Documented copies of this program are available on request to M.K.
38. M. Keil and L. Danielson, Can. J. Phys. **66**, 159 (1988).
39. Mixture Viscosities: (a) D.W. Gough, G.P. Matthews, and E.B. Smith, J. Chem. Soc. Farad. Trans. **I 72**, 645 (1976); (b) G.C. Maitland and E.B. Smith, J. Chem. Soc. Farad. Trans. **I 70**, 1191 (1974); (c) A.S. Kalelkar and J. Kestin, J. Chem. Phys. **52**, 4248 (1970); (d) J. Kestin, H.E. Khalifa, and W.A. Wakeham, Physica **90A**, 215 (1978).
40. B. Najafi, E.A. Mason, and J. Kestin, Physica **119A**, 387 (1983).
41. J.M.H. Levelt Sengers, M. Klein, and J.S. Gallagher in, *AIP Handbook*, edited by M. W. Zemansky and D. E. Gray (McGraw-Hill, New York, 1972).
42. Interaction Second Virials: (a) C.M. Knobler, J.J.M. Beenakker, and H.F.P. Knapp, Physica **25**, 909 (1959); (b) J. Brewer and G.W. Vaughn, J. Chem. Phys. **50**, 2960 (1969); (c) J. Brewer, Air Force Office of Scientific Res. Rept. No. 67-2795 (1967); (d) A.L. Blancett, K.R. Hall, and F.B. Canfield, Physica **47**, 75 (1970) and private communication with K.R. Hall; (e) N.K. Kalfoglou and J.G. Miller, J. Phys. Chem. **71**, 1256 (1967); (f) F.H. Kate, Jr. and R.L. Robinson, Jr., J. Chem. Thermodynamics **5**, 259 and 273 (1973); (g) D.D. Dillard, M. Waxman, and R.L. Robinson, Jr., J. Chem. Eng. Data **23**, 269 (1978).

43. J.H. Dymond and E.B. Smith, *The Virial Coefficients of Pure Gases and Mixtures* (Clarendon, Oxford, 1980).

44. F.H. Kate, Jr., Doctoral Thesis, Oklahoma State University (1972).

45. J.M. Parson and Y.T. Lee, Entropie **42**, 146 (1971).

46. A. Kumar and W.J. Meath, Mol. Phys. **54**, 823 (1985).

47. (a) J.M. Standard and P.R. Certain, J. Chem. Phys. **83**, 3002 (1985); (b) K .T. Tang, J.M. Norbeck, and P.R. Certain, J. Chem. Phys. **64**, 3063 (1976).

48. C. Douketis, G. Scoles, S. Marchetti, M. Zen, and A.J. Thakkar, J. Chem. Phys. **76**, 3057 (1982).

49. W.J. Meath, D.J. Margoliash, B.L. Jhanwar, A. Koide, and G.D. Weiss, in *Intermolecular Forces*, edited by B. Pullman (Reidel, Dordrecht, 1981).

50. K. Watanabe, A.R. Allnatt, and W.J. Meath, Chem. Phys. **68**, 432 (1982).

51. Mixture diffusions: (a) R.J.J. van Heijningen, J.P. Harpe, and J.J. Beenakker, Physica **38**, 1 (1968); (b) G.A. Dubro and S. Weissman, Phys. Fluids **13**, 2682 (1970); (c) W. Hogervorst, Physica **51**, 59 (1971); (d) M.A. Yabsley and P.J. Dunlop, Physica **85A**, 160 (1976); (e) P.S. Arora, H.L. Robjohns, and P.J. Dunlop, Physica **95A**, 561 (1979); (f) P.S. Arora and P.J. Dunlop, J. Chem. Phys. **71**, 2430 (1979); (g) C.J. Zwakhals and K.W. Reus, Physica **100C**, 231 (1980); (h) K.W. Reus, C.J. Zwakhals, and J.A. Smit, Physica **100C**, 221 (1980); (i) A.S.M. Wahby, M. Abdel-Rahman, and J. Los, Physica **112A**, 214, 225 (1982); (j) W.L. Taylor and D. Cain, J. Chem. Phys. **78**, 6220 (1983); (k) W.L. Taylor and D. Cain, High Temp. High Press. **15**, 433 (1983); (l) D. Cain and W.L. Taylor, J. Chem. Phys. **71**, 3601 (1979). The following data was not considered on the advice of P.J. Dunlop (private communication): P.J. Carson, M.A. Yabsley, and P.J. Dunlop, Chem. Phys. Lett. **15**, 436 (1972); P.J. Carson and P.J. Dunlop, Chem. Phys. Lett. **14**,

377 (1972); G.R. Staker, M.A. Yabsley, J.M. Symons, and P.J. Dunlop, J. Chem. Soc. Farad. Trans. I **70**, 825 (1974).

52. Mixture thermal diffusions: (a) J.M. Savirón, C.M. Santamaría, J.A. Carrión, and J.C. Yarza, J. Chem. Phys. **63**, 5318 (1975); (b) C.M. Santamaría, J.M. Savirón, and J.C. Yarza, Physica **84A**, 212 (1976); (c) C.M. Santamaría, J.M. Savirón, and J.C. Yarza, J. Chem. Phys. **64**, 1095 (1976); (d) G.P. Timov and P.E. Suetin, Sov. Phys. Tech. Phys. **21**, 336 (1976); (e) W.L. Taylor, J. Chem. Phys. **72**, 4973 (1980); (f) R.D. Trengove, H.L. Robjohns, T.N. Bell, M.L. Martin, and P.J. Dunlop, Physica **108A**, 488 (1981); (g) R.D. Trengove, H.L. Robjohns, M.L. Martin, and P.J. Dunlop, Physica **108A**, 502 (1981). The following data was not considered on the advice of P.J. Dunlop (private communication): J.M. Symons, M.L. Martin, and P.J. Dunlop, J. Chem. Soc. Farad. Trans. I **75**, 621 (1979).
53. A.A. Clifford, R. Fleeter, J. Kestin, and W.A. Wakeham, Physica **98A**, 467 (1979).
54. Integral Cross Sections: H.J. Beier, Zeitschrift für Physik **196**, 185 6); R. Düren, R. Feltgen, W. Gaide, R. Helbing, and H. Pauly, Phys. Lett. **18**, 282 (1965); H.J. Beier, Phys. Lett. **18**, 285 (1965); R. Düren, R. Helbing, and H. Pauly, Zeitschrift für Physik **188**, 468 (1965).
55. R. Candori, F. Pirani, and F. Vecchiocattivi, J. Chem. Phys. **84**, 4833 (1986).
56. G.C. Maitland and W.A. Wakeham, Mol. Phys. **35**, 1429; 1443 (1978).
57. R.B. Gerber, M. Shapiro, U. Buck, and J. Schleusener, Phys. Rev. Lett. **41**, 236 (1978).
58. U. Buck and H. Meyer, J. Chem. Phys. **84**, 4854 (1986).

CHAPTER 3

The HeNe Interatomic Potential From Multiproperty Fits and Hartree-Fock Calculations†

3.1. INTRODUCTION

Recent progress in determining interatomic potentials for weak interactions has been made largely in two parallel directions.[1,2] Firstly, there has been the systematic and increasingly extensive fitting of properties that are sensitive to the interatomic potential.[3–6] This approach has also met with considerable success in determining non-spherical atom+molecule potential energy surfaces.[7–11] However, the fitting approach requires assumption of a mathematical form for the interatomic potential, which if incomplete or incorrect could, and certainly has, biased the extraction of physically meaningful potential parameters.[1,12,13] More recent fitting procedures have avoided this shortcoming by increasing either the mathematical flexibility of the assumed parameterization,[4] or its physical reasonableness and thereby its mathematical correctness.[5,13] The latter endeavour has been especially fruitful with the advent of more accurate theoretical values of the dispersion coefficients and more reliable calculations for the repulsive potential wall.[1,2]

The parallel approach of directly inverting experimental data to the interatomic potential has been applied both to scattering[14,15] and dilute-gas data.[16] This approach avoids the question of mathematical flexibility or physical reliability of potential parameterizations and ultimately must be the preferred choice. It also lends itself, via applications of sensitivity analysis, to optimum extraction of the interatomic potential from the observable properties at hand.[17] However, the approach also has its limitations. Besides the practical difficulty in generating experimental data of sufficient range and accuracy is the more fundamental consideration of using such inverted interatomic potentials to predict other observable properties. Another practical consideration is joining two or more numerical potentials that may have been obtained from different properties and therefore are available for different interatomic separation ranges. Of related interest is the use of such numerical potentials in calculating observable properties, usually requiring interpolation and even more problematic, extrapolation beyond the range of interatomic separations probed.

---

† A version of this chapter has been accepted for publication.
M. Keil, L.J. Danielson, U. Buck, J. Schleusener, F. Huisken, and T.W. Dingle, J. Chem. Phys. (1988).

These considerations are best balanced for systems to which both approaches can be applied most favourably. Such an opportunity is provided by the HeNe interaction, for which two numerical direct-inversion potentials are available,[15,16] one of which was obtained from very high-resolution differential cross section (DCS) measurements.[15] From the fitting point of view, there are a wide variety of experimental measurements available over a broad range of conditions for the HeNe system: high-resolution DCS's at two collision energies newly presented in this paper; integral cross sections (ICS) for collision energies ranging down to the oscillatory region;[18] accurate diffusion coefficients near room temperature[19,20] and viscosities to elevated temperatures;[21] and virial coefficients to very low temperatures[22] where quantum effects become paramount. In addition to these experimental data, the HeNe system involves only 12 electrons, and *ab-initio* calculations, at least for highly repulsive interactions, should attain a reasonable level of accuracy. Such theoretical results, as calculated in the present work, can then be combined with available semi-empirical potential models[23,24] to increase the physical reliability of fitted mathematical parameterizations while reducing the number of fitted parameters.

This paper presents two-parameter fits, within the semi-empirical Hartree-Fock plus damped Dispersion (HFD) potential model,[23] to a wide variety of scattering and dilute-gas properties for the HeNe system. The results are used to compare to direct-inversion potentials in the manner indicated above. Section 3.2 of this paper outlines the experimental apparatus and procedures used to obtain DCS measurements at Alberta and Göttingen, both of which are considered in the fitting analysis. Section 3.3 describes the *ab-initio* Hartree-Fock calculations and their incorporation into the HFD semi-empirical potential model subsequently used in extracting the HeNe interatomic potential. Use of that potential form is discussed in Sec. 3.4, where we also present our calculational methods for the properties being fit, and our multi-property fitting procedure. This procedure is applied to data sensitive to the HeNe interaction, selected as described in Sec. 3.5. In Sec. 3.6 we present two independent interatomic potentials obtained from the data, and discuss their ability to reproduce the input data and to predict data excluded from the respective fitting calculations. We also compare the present potentials to the best currently available in the literature.[23,25(a)–26] Finally, we summarize our conclusions in Sec. 3.7.

3.2. EXPERIMENTAL

3.2.A. Alberta Scattering Apparatus

The scattering apparatus has been described previously,[5,28] so only a brief outline is given here. The main features of the apparatus are two supersonic beam sources intersecting at 90.3° and an in-plane rotatable liquid helium-cooled bolometer detector. The Ne beam is chopped and flagged for lock-in amplification and background suppression, respectively. The beams are characterized using a calibrated time-of-flight chopper in conjunction with a quadrupole mass spectrometer. Beam operating conditions are summarized in Table 3-1.

The computer-controlled data acquisition system and data collection scheme have also been described previously.[28] Periodic reference normalization is used to compensate for slow variations in detector sensitivity. The bolometer detects only He since the Ne collision partner is kinematically restricted to scattering angles $\Theta \gtrsim 35°$. Interfering Ne scattering appears rather sharply as a featureless quadrupling of the signal, first becoming noticeable at $\Theta \approx 35°$. Therefore, scattering data beyond 33° are not considered in the present analysis. Similarly, data are reported no closer than 4° to the primary beam, since its intense wings degrade the bolometer response below $\sim 3.5°$. The Ne beam attenuates the He beam by only 0.6%, ensuring single-collision conditions to a high degree of accuracy. Our experimental measurements are presented in Table 3-2 and are plotted in Fig. 3.1.

The very deep diffraction oscillations observed for HeNe necessitate careful attention to beam impurities and averaging effects. In particular, it can be important to recognize that He+^{20}Ne and He+^{22}Ne scattering may differ both kinematically and energetically. In our experiment, the two Ne isotopes have the same velocity, with the ^{22}Ne effectively "seeded" in the ^{20}Ne. The collision energies are different by 1.5% for the two isotopes, and the measured DCS signals are

Table 3-1. Beam Operating Conditions

	Alberta, ambient[a]			Göttingen, ambient		Göttingen, liq. N_2	
Gas	He	^{20}Ne	^{22}Ne	He	Ne	He	Ne
Temperature (K)	302.	302.	302.	298.5	303.	101.8	303.
Nozzle diameter (mm)	0.050	0.10	0.10	0.040	0.040	0.010	0.10
Nozzle pressure (atm)	14.9	6.2	6.2	3.0	2.6	93.	4.0
Most probable velocity (km/sec)	1.771	0.794	0.793	1.761	0.792	1.028	0.792
Velocity FWHM ($\Delta v/v_{mp}$)	0.04	0.087	0.081	0.111	0.079	0.010	0.054
Collision energy (E_{mp},meV)	—	64.8	65.8	—	65.0	—	29.2
Nozzle-scattering centre (mm)	58	54	54	120	44	120	44
Angular divergence (deg)	1.0	1.4	1.4	1.7	6.0	1.7	6.0
Overall angular resolution (deg)	—	1.65	1.65	—	1.26[b]	—	2.12[b]

[a] Ne isotopes characterized independently, and included in the analysis (Sec. 3.4.B), with measured abundances of 87% ^{20}Ne and 13% ^{22}Ne.

[b] Values are given in the CM system for $\Theta = 30°$ [Eqn. 2].

Table 3-2. Experimental Differential Cross Section Measurements[a]

Alberta, ambient			Göttingen, ambient[b]			Göttingen, liq. N_2[b]		
θ(°)	I(θ)	ΔI(θ)%	θ(°)	I(θ)	ΔI(θ)%	θ(°)	I(θ)	ΔI(θ)%
−11.32	62.82	4.3	5.66	264.45	1.8	6.97	925.27	2.0
−11.07	70.13	3.9	5.86	208.21	1.8	7.47	734.56	2.0
−10.82	77.72	3.7	6.06	156.74	1.7	7.97	548.04	2.0
−10.57	82.73	4.2	6.26	113.92	1.8	8.47	381.55	2.0
−10.32	87.89	4.9	6.46	81.35	1.6	8.97	236.23	2.0
−10.07	87.66	4.6	6.66	54.22	1.9	9.47	122.35	2.0
−9.82	83.85	3.4	6.86	34.68	2.1	9.97	51.37	2.0
−9.57	86.13	3.0	7.06	24.41	2.6	10.22	32.92	2.0
−9.32	77.56	3.8	7.26	19.81	3.2	10.47	24.24	2.0
−9.07	70.85	4.7	7.46	20.85	2.5	10.59	23.01	2.0
−8.82	59.26	5.2	7.66	24.45	2.2	10.72	24.59	1.9
−8.57	45.94	6.4	7.96	39.30	2.1	10.97	31.49	2.2
−8.32	36.94	8.1	8.26	55.41	1.5	11.47	66.78	2.0
−8.07	27.35	8.9	8.56	68.74	1.3	11.97	109.70	2.0
−7.82	25.10	8.5	8.86	83.87	1.0	12.47	153.88	2.0
−7.57	26.73	8.2	9.06	90.57	1.0	12.97	187.44	2.0
−7.32	33.43	8.6	9.26	95.10	1.0	13.47	202.82	2.0
−7.07	51.24	8.5	9.56	97.40	1.0	13.97	199.77	2.0
−6.82	77.82	7.8	9.86	94.10	1.0	14.47	178.20	2.0
−6.57	119.50	6.8	10.06	88.03	1.0	14.97	147.86	2.0
−6.32	170.34	5.4	10.31	77.07	1.2	15.47	109.28	2.0
−6.07	233.64	3.9	10.66	65.14	1.1	15.97	75.07	2.0
−5.82	311.73	3.1	10.96	51.76	1.4	16.47	47.81	2.0
−5.57	406.17	3.0	11.26	40.54	1.3	16.72	39.44	2.0
−5.32	510.62	3.0	11.56	31.11	1.4	16.97	32.73	2.0
−5.07	625.20	3.0	11.86	23.95	2.0	17.22	28.30	1.8
−4.82	758.89	3.0	12.16	19.51	2.1	17.47	28.02	1.8
−4.57	907.05	3.0	12.46	18.05	1.9	17.72	31.17	2.0
−4.32	1047.82	3.0	12.76	19.22	1.5	17.97	35.24	2.1
−4.07	1207.20	3.0	12.96	20.94	1.9	18.47	45.77	1.7
4.43	1061.98	3.0	13.26	24.55	1.8	18.97	61.35	1.2
4.68	917.09	3.0	13.76	30.26	1.5	19.47	75.54	1.0
4.93	759.98	3.0	14.26	35.45	1.1	19.97	84.46	0.9
5.18	629.00	3.0	14.76	37.25	1.0	20.47	87.83	0.7
5.43[c]	500.00	3.1	15.26	34.86	1.0	20.97	84.30	0.9
5.68	382.93	3.6	15.76	31.29	1.2	21.47	77.78	1.0
5.93	290.65	3.6	16.26	26.12	1.3	21.97	68.03	1.1
6.18	203.83	3.7	16.76	21.34	1.3	22.47	55.88	1.4
6.43	140.05	4.2	17.26	18.37	1.5	22.97	45.74	1.7
6.68	84.84	4.7	17.76	17.82	1.5	23.47	40.65	1.2
6.93	61.79	4.7	18.26	18.26	1.5	23.72	38.13	1.4

··· continued on the next page ···

Table 3-2 continued ···

Alberta, ambient			Göttingen, ambient[b]			Göttingen, liq. N_2[b]		
θ(°)	I(θ)	ΔI(θ)%	θ(°)	I(θ)	ΔI(θ)%	θ(°)	I(θ)	ΔI(θ)%
7.18	43.87	4.7	18.76	19.91	1.4	23.97	37.79	1.3
7.43	47.93	4.6	19.26	21.40	1.3	24.22	38.78	1.4
7.68	57.74	3.8	19.76	21.38	1.6	24.47	38.76	1.2
7.93	70.57	3.5	20.26	21.05	1.3	24.97	41.70	1.9
8.18	87.45	3.7	20.76	20.53	1.3	25.47	46.59	1.7
8.43	110.87	3.4	21.26	18.71	1.5	25.97	51.32	1.6
8.68	129.42	3.0	21.76	17.40	2.1	26.47	55.22	1.5
8.93	146.02	3.0	22.26	16.12	1.7	26.97	56.56	1.4
9.18	154.15	3.0	22.76	15.45	2.4	27.47	55.79	1.5
9.43	160.14	3.0	23.26	15.58	1.8	27.97	54.70	1.5
9.68	164.05	3.0	23.76	15.10	3.1	28.47	49.94	1.7
9.93	148.60	3.0	24.26	15.74	1.9	28.97	47.05	1.8
10.18	140.46	3.0	24.76	15.98	2.9	29.47	41.60	2.0
10.43	120.22	3.0	25.26	15.53	2.0	29.97	38.84	1.9
10.68	104.77	4.0	25.76	15.29	3.1	30.47	37.32	2.3
10.93	87.64	4.6	26.26	14.37	2.5	30.97	37.09	2.0
11.18	70.46	4.4	26.76	14.22	3.3	31.47	39.33	2.2
11.43	57.79	4.2	27.26	13.82	2.2	31.97	40.45	1.9
11.68	46.64	4.5	27.76	13.10	2.8	32.47	40.92	2.2
11.93	37.14	5.5	28.26	13.01	2.8	32.97	43.13	2.0
12.18	36.32	7.6	29.26	12.98	2.5	33.47	42.44	2.3
12.43	32.13	9.3	30.26	12.35	3.0	33.97	42.77	2.1
12.93	37.43	9.5	31.26	12.02	2.7	34.47	41.07	2.4
13.43	49.01	8.4	33.26	11.12	2.8	34.97	41.47	1.5
13.93	59.30	6.2	36.26	10.63	2.8	35.47	38.48	2.8
14.43	66.87	4.3	41.26	9.54	2.7	35.97	38.05	1.7
14.93	65.41	3.8	46.26	8.43	3.2	36.97	35.44	1.9
15.43	60.27	4.8	51.26	7.62	3.6	37.97	36.97	1.9
15.93	54.53	6.9	56.26	7.14	3.9	38.97	36.65	1.9
16.43	41.53	8.6	61.26	6.93	4.1	39.97	38.10	1.9
16.93	34.96	8.2	66.26	6.40	4.4	40.97	37.50	1.9
17.43	31.74	7.0	71.26	5.71	6.3	41.97	35.92	2.1
17.93	34.05	6.9	76.26	5.67	5.8	42.97	35.01	2.1
18.43	37.32	7.0	81.26	5.40	7.0	43.97	33.50	2.3
18.93	42.53	6.7				44.97	33.81	2.1
19.43	43.64	6.3				45.97	34.50	2.4
19.93	41.34	6.7				46.97	34.14	2.5
20.43	38.56	8.3				47.97	33.91	2.7
20.93	40.51	10.0				48.97	33.46	3.4
21.43	32.95	9.5				49.97	32.87	2.5
21.93	33.33	7.0				52.47	30.68	3.7
22.43	33.83	4.7				54.97	30.97	3.1

··· continued on the next page ···

Table 3-2 continued · · ·

Alberta, ambient			Göttingen, ambient[b]			Göttingen, liq. N_2[b]		
$\theta(°)$	$I(\theta)$	$\Delta I(\theta)\%$	$\theta(°)$	$I(\theta)$	$\Delta I(\theta)\%$	$\theta(°)$	$I(\theta)$	$\Delta I(\theta)\%$
23.43	33.52	3.9				59.97	29.79	3.4
24.43	31.99	5.0				64.97	28.49	3.9
25.43	31.16	8.0				69.97	27.54	4.2
26.43	27.64	10.4				74.97	25.90	5.1
27.43	27.28	9.2				79.97	24.50	7.8
28.43	28.88	5.9						
29.43	29.56	4.7						
30.43	27.69	7.2						
32.93	24.51	11.4						

[a] Experimental DCS measurements are in arbitrary units; percentage error bars represent one standard deviation.

[b] Corrected for the velocity dependence of the detection efficiency and for the angular dependence of the scattering volume and detector acceptance.

[c] Reference angle used for periodic normalization.

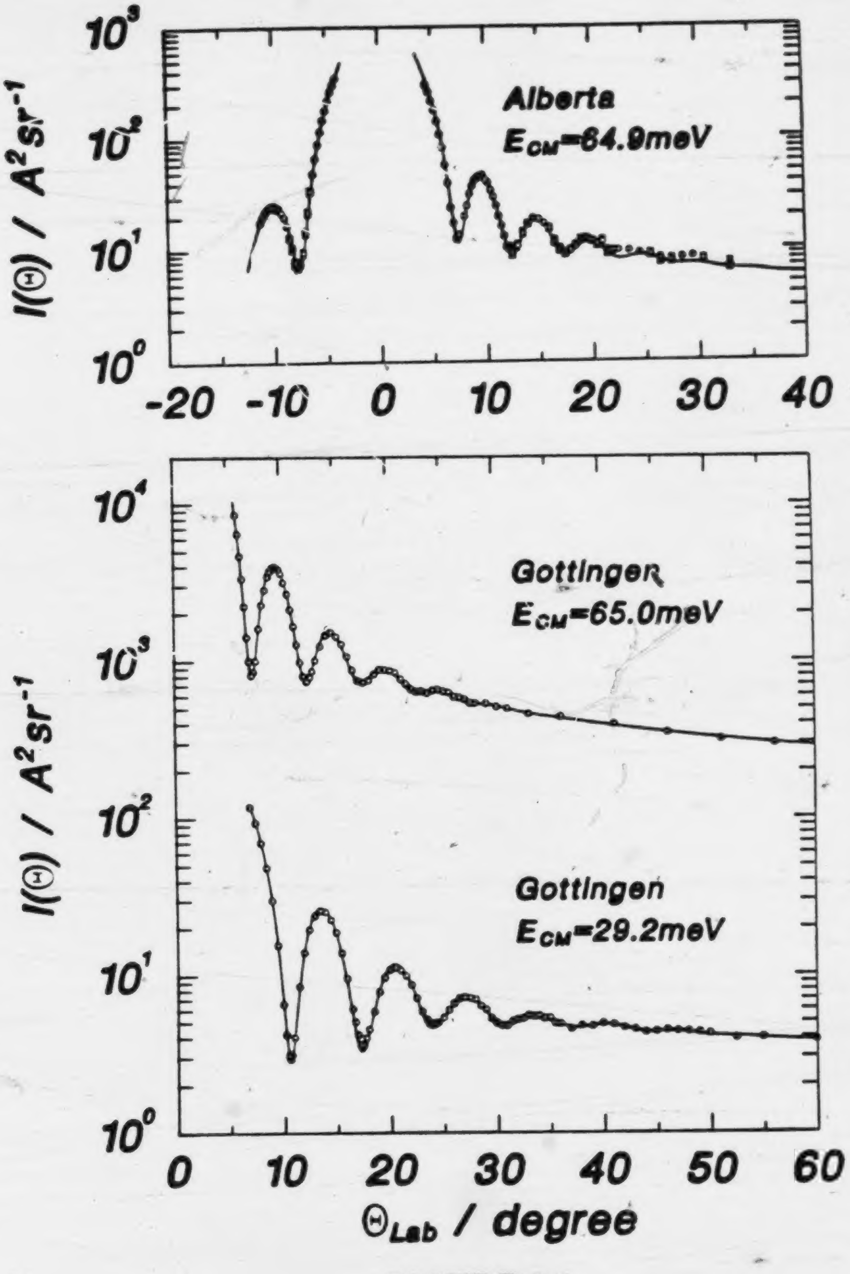

FIGURE 3.1

Differential cross sections for HeNe measured as functions of laboratory scattering angle for the Alberta room-temperature experiments, and for the Göttingen experiments at two different collision energies. The latter data are corrected for the velocity dependence of the detection efficiency and the angle dependence of the scattering volume and detector acceptance. Data points are given with error bars of one standard deviation. The smooth curves correspond to the best-fit HFD1 interatomic potential obtained as discussed in Sec. 3.6.A., which also provides the absolute scales. Data are shifted vertically for clarity of display. The HFD2 calculations cannot be distinguished on this scale (see Table 3-5).

weighted averages of the individual isotopic scattering patterns. The ^{22}Ne isotope has a slightly enhanced 13% abundance in the supersonic beam due to scattering of the lighter isotope out of the beam.

3.2.B. Göttingen Scattering Apparatus

The details of the molecular beam machine are discussed elsewhere.[10,29] Briefly, the two beams are produced as supersonic beams in two differentially pumped source chambers. They are introduced into the scattering chamber through skimmers which provide small angular divergences. At the scattering center the two beams cross at an angle of 90°. The angular dependence of the cross section is measured by rotating the source assembly about the scattering center. Scattered particles are detected in the plane of the two beams by a universal detector containing an electron bombardment ionizing source, a quadrupole mass filter and a particle multiplier. The detector unit is operated in a doubly differentially pumped chamber with background pressures of less than 10^{-10} mbar. The amplified multiplier pulses are fed to a dual channel scaler working as a digital lock-in system.

For varying the collision energy the primary beam source can be heated or cooled down to liquid nitrogen temperature. Most probable beam velocities and velocity distributions are measured by time-of-flight analysis using the pseudorandom chopping technique with a flight path of 449 mm. The absolute calibration of the angle is carried out by measurement of the scattering signals at positive and negative laboratory scattering angles to an accuracy of ±0.05°. The optimized operating conditions for the beams are listed in Table 3-1. The room-temperature measurements were carried out on an earlier version of the apparatus with smaller pump capacities. The low stagnation pressure for the secondary beam is chosen to avoid condensation effects. The laboratory results for room temperature and liquid nitrogen temperature He sources are presented in Fig. 3.1 and Table 3-2. The large angle part between 60° and 80° is not shown in Fig. 3.1 in order to emphasize the more important diffraction oscillations. The data have been corrected for the v'^{-1} dependence of the number density detector and the angular dependent product of scattering volume and detector acceptance angle. The error bars indicate one standard deviation and take into account both statistical fluctuations and systematic errors at small angles due to the influence of the primary beam.

To relate the measured lab angular intensity $\frac{dN}{dt}(\Theta_0)$ to the DCS $\frac{d\sigma}{d\omega}$ in the center of mass (CM) system, which is a function of the relative velocity g and the CM angle θ, a complicated averaging procedure has to be carried out[30,31]

$$\frac{dN}{dt}(\Theta_0) = n_1 n_2 < \Delta V \Delta \Omega > \int\int dg d\theta \frac{d\sigma}{d\omega} F(\Theta_0, \theta) \qquad (3-1)$$

where n_i are the densities, $< \Delta V \Delta \Omega >$ is the effective product of scattering volume and detector acceptance angle, and $F(\Theta_0, \theta)$ is a distribution function which contains the integration over both lab velocity distributions in magnitude and direction and all other velocity dependent variables including the Jacobian for the CM → lab transformation. In the present case F is calculated by Monte-Carlo techniques. The result can be described by a product of a gaussian distribution of the relative velocity and a rectangular function for the angular resolution. The actual parameters for the two beam conditions of Table 3-1 are $\frac{\Delta g}{g} = 0.060$ (low temperature) and 0.095 (ambient). The angular resolution depends slightly on the deflection angle and can be approximated by

$$\delta = \delta_0(1 + \delta_1 \theta_0) \qquad (3-2)$$

with $\delta_0 = 1.015°$ and $\delta_1 = 0.008$ deg^{-1} for the low temperature and $\delta_0 = 0.800°$ and $\delta_1 = 0.044$ deg^{-1} for the ambient temperature experiments.

3.3. HARTREE-FOCK SCF POTENTIAL CALCULATIONS

The *ab-initio* Hartree-Fock SCF calculations on the HeNe potential were carried out at six distances over the range 2.0-6.0 bohr using high quality gaussian basis sets. The basis set for the helium atom was an (11s) basis of Van Duijneveldt[32] contracted to (7s) and supplemented with four p functions to give the basis set (5111111/1111). The energy obtained for the isolated He atom using this basis was −2.8616730 Hartree compared to −2.861680 Hartree from numerical Hartree-Fock calculations.[33] The basis set for the neon atom was a (14s 10p) well-tempered basis of Huzinaga and Klobukowski[34] contracted to (7s 5p) and supplemented with three d functions to give a (7s 5p 3d) basis of the form (5671111/71111/111).[35] In both the He and Ne basis sets the exponents of the p and d functions were the same as some of the exponents of the s set for faster calculation of the two-electron integrals. The energy obtained for the isolated Ne atom was −128.54690 Hartree compared to −128.54710 Hartree from numerical Hartree-Fock calculations.[33]

The basis set superimposition errors (BSSE) were calculated using the counterpoise method of Boys and Bernardi[36] where the energy of the isolated atom is calculated with the basis set of the other atom located at the appropriate distance. Both basis sets appeared to be close to saturation since the BSSE was found to be small.

The SCF results are fitted to a repulsive potential of the form $V(r) = A\exp(-\alpha r - \beta r^2)$ for use in the HFD potential model (Sec. 3.4.A). Over the whole range of distances the relative error between the SCF results and those calculated using the fitted curve are $< 0.5\%$ indicating that this form is flexible enough to cover the whole range. The above results are all summarized in Table 3-3.

It has been suggested by Varandas and Brandao[37] that some of the corrections that should be included in the repulsive part of the potential (i.e., intra-atomic correlation and intra-inter coupling) have the same basic form as the SCF part; therefore, they can be incorporated into the potential by multiplying the pre-exponential factor A by some correction factor. Calculations carried out[38] on the interaction of H atoms with He, Ne and Ar atoms give correction factors of 3%, 28% and 12% respectively. We have treated this correction factor by calculating A from the HFD potential form and the r_m parameter fitted to the experimental data, as discussed below (Sec. 3.4.A and 3.6.B).

Table 3-3. Summary of Hartree-Fock SCF Calculations on the HeNe Potential[a]

r	V_{SCF}	$V_{BSSE}(He)$	$V_{BSSE}(Ne)$	$\left[\frac{V_{SCF}-A\exp(-\alpha r-\beta r^2)}{V_{SCF}}\right]^{b}$
2.200	0.2014433	0.00000008	0.0000063	−0.0032
2.600	0.0818723	0.00000012	0.0000061	0.0027
3.600	0.0081821	0.00000011	0.0000051	0.0039
4.800	0.0004747	0.00000006	0.0000034	−0.0049
5.688	0.0000554	0.00000011	0.0000022	−0.0015
6.000	0.0000259	0.00000004	0.0000019	0.0045

[a] Distances and energies in atomic units.

[b] Fitted parameters are $\alpha = 2.133$ a.u.; $\beta = 0.02764$ a.u.; $A = 25.211$ a.u.

3.4. ANALYSIS

3.4.A. Interatomic Potential Parameterizations

The HeNe interaction was analyzed using the Hartree-Fock plus damped Dispersion (HFD) potential form.[23] The HFD prescription provides a dependable parameterization of interatomic potentials, even when being fit without reliable Hartree-Fock data.[5,25(a)] Furthermore, it exhibits sufficient flexibility with only three adjustable parameters, reducing parameter correlation difficulties encountered when fitting large numbers of parameters. For one of the HFD potentials obtained in this work, Hartree-Fock results are used explicitly, necessitating a slight variation to the usual HFD formulation.[39]

For isotropic interactions, this slightly generalized HFD potential has the following formulation[5]:

$$\begin{aligned}
V_{HFD}(r) &= V_{HF}(r) + F(r)V_D(r) \ , \\
V_{HF}(r) &= A \exp(-\alpha r - \beta r^2) \ , \\
V_D(r) &= -\sum_{n=0}^{4} C_{2n+6} r^{-(2n+6)} \ , \\
F(r) &= \exp\left[-\left(Dr_m r^{-1} - 1\right)^2\right] \ , \quad r \leq Dr_m \ , \\
F(r) &= 1 \ , \quad r \geq Dr_m .
\end{aligned} \qquad (3-3)$$

Two HFD potentials are obtained from the present analysis, both of which are essentially two-parameter fits. The first, designated HFD1, utilizes the calculated Hartree-Fock α and β repulsion parameters (Sec. 3.3), and only r_m and C_8 are fit to the data. The C_6 dispersion coefficient is fixed at the value calculated by Kumar and Meath,[40] estimated by them to be accurate to 1%, while the $C_{10} - C_{14}$ coefficients are obtained using the recursion equations of Douketis et al.[41] The damping parameter is held fixed at $D = 1.28$.[23] For HFD1, the requirement that the potential minimum position occur at the r_m parameter value then fixes A in terms of α, β and r_m, whereupon the well depth ϵ is also fixed.[5]

The second potential, designated HFD2, utilizes the C_6, C_8, and C_{10} dispersion coefficients of Tang, Norbeck, and Certain[42] as a starting point, while fitting only A and α to the data (β is set to zero). In this case, all dispersion coefficients higher than C_{10} are ignored, and the damping parameter is held fixed at D = 1.32. The HFD2 potential is then refined by allowing the dispersion coefficients C_i to vary within their theoretical error bounds,$\Delta C_i^{\mathrm{theory}}$. In practice an additional parameter γ is fitted according to

$$C_i = C_i^{\mathrm{theory}} \left(1 + \gamma\, \Delta C_i^{\mathrm{theory}}\right). \qquad (3-4)$$

In this way the positions of the diffraction oscillations determine the point where the potential is zero and thus fixes A, while the amplitudes of the diffraction oscillations and the second virial coefficients are mainly sensitive to α in the inner attractive well and to a lesser extent, to γ. Then also the minimum parameters r_m and ϵ are fixed.

The HFD1 potential is fit to data including low-energy integral cross sections and low-temperature virial coefficients, both of which are quite sensitive to the outer bowl region of the attractive potential well.[5,43] Accurate values for the dispersion coefficients are therefore required for the HFD1 fits; they are however, difficult to obtain beyond C_6 because of uncertainties in the data used to estimate them semi-empirically.[44] Our experience with the heavier He+rare gas potentials suggests that fitting C_8 to the data compensates for possible errors in its semi-empirical estimation, especially since the somewhat correlated α parameter[5] is fixed by the Hartree-Fock calculations. Conversely, since the HFD2 potential is not fit to data of similar sensitivity to the outer bowl of the attractive well, the C_8 coefficient could be fixed within its semi-empirical bounds, while the α parameter is fit to the data.

3.4.B. Calculations of the Fitted Properties

Scattering calculations for the DCS, ICS, and transport properties, and semi-classical calculations of the virial coefficients, have been presented previously for spherical potentials.[5] Some modifications to these procedures were required, as described below.

The DCS calculations included all instrumental velocity- and angular-averaging effects. The Alberta apparatus was simulated by Gaussian numerical integration over beam velocity and angular distributions, combined with an effective overall apparatus angular resolution obtained from analysis of HeAr scattering results.[5] Laboratory-frame DCS's were calculated independently for He+^{20}Ne and He+^{22}Ne scattering, and were averaged using the measured isotopic abundances in the supersonic beam. The increased collision energy of the He+^{22}Ne scattering compensated almost exactly for the different kinematic transformations to the laboratory frame.

The Göttingen data were analyzed by calculating a CM DCS using exact quantum phase shifts and the partial wave summation, which was truncated for phase shifts less than 0.001 rad. The cross sections are then converted to averaged lab distributions according to the procedure described in detail in Sec. 3.2.B. For saving computational time the DCS at different velocities are calculated using the scaling relation

$$\sigma(g,\theta) = \left(\frac{g}{g_0}\right)^{\beta} \sigma\left[g_0, \theta\left(\frac{g}{g_0}\right)^{\alpha}\right] \qquad (3-5)$$

with $\alpha = 1.00$ and $\beta = 1.25$ for the low energy data, and $\alpha = 0.95$ and $\beta = 1.42$ for the room-temperature data.

The ICS calculations also included instrumental averaging effects. The low-energy experiments of Grace et al.[18] were simulated by averaging over the collision velocity. We did not however, average over beam angular spreads, nor did we apply angular resolution corrections for the primary beam geometry[45,46] (Sec. 3.6.B). More properly, the absolute ICS measurements of Pirani and Vecchiocattivi[47] could be reproduced by averaging over the primary beam velocity distribution including Boltzmann integration over the target gas distribution.[48] As in earlier work,[5] the absolute calibration error of ±3%[48] was accomodated by allowing the data as a whole to be adjusted by no more than this amount.

In obtaining the transport properties, collision integrals were calculated quantum mechanically from 10-1600 K. Calculational parameters were identical to those detailed earlier,[5] including Chapman-Cowling calculations up to high orders. Where required, like-atom collision integrals for HeHe and NeNe were also calculated quantum mechanically from the HFDHe$_2$[49] and HFD-C2[50] potentials respectively, and include symmetry considerations. A more recent HeHe potential[51] would not have affected these calculations significantly.[5]

Interaction second virial coefficients can be calculated using a semi-classical expansion up to third order[52] for low temperatures. However, these calculations became too inaccurate below ~ 30 K. Comparisons to experimental data at temperatures as low as 15 K[22] therefore required fully quantum calculations.[52(a),53] Since numerically propagated wavefunctions yield phase shifts modulo 2π, their absolute values were obtained at low energies by node counting relative to phase shifts for the corresponding centrifugal potentials. For collision energies well above the three classical turning point regime, absolute quantum phase shifts were obtained using WKB phases for guidance. These absolute phase shift calculations were found to be more efficient and numerically reliable than using the phase shift derivatives alternatively required for the quantum virial calculations.[54]

Phase shifts required for the quantum virials were calculated at the same energies used for the transport properties. Similarly, the continuum contribution[52] was obtained by 16-point Gauss-Laguerre quadrature over the energy.[5] This procedure appeared to be more efficient than Simpson's rule integration,[51,52(a)] without loss of accuracy.

Bound states, including rotational levels, were located quantum mechanically to within 10^{-4} meV of dissociation. We began the outward numerical propagation at a distance corresponding to a potential energy of 1000 meV; the inward propagation began 50 Å beyond the outer classical turning point. Propagation stepsizes were 0.005 Å and 0.05 Å up to, and beyond, the outer classical turning point respectively. The bound state contribution to the virial coefficient amounted to $\sim$ 11% at 10 K, declining to $\tilde{<}$ 5% at 30 K, by which temperature the third-order semiclassical approximation was accurate to 0.3 cm^3/mole. Trial calculations compared favourably with the tabulated Boyd et al. results.[52(a)] For HeNe, the present calculations are precise to $\sim$ 0.1% for temperatures down to at least 10 K. For temperatures above 90 K, the quantum virials agreed with the third-order semiclassical virials to better than 0.1 cm^3/mole; for convenience, we continued to use the quantum virials for comparison to the Knobler et al.[55] and Brewer et al. virials.[56]

3.4.C. Multiproperty Fitting

As in previous work, parameters of the assumed intermolecular potential form are fit to the experimental data by an automated non-linear least-squares fitting program.[57] The least-squares functional to be minimized is given by the dimensionless quantity

$$\delta = \left[\sum_{j=1}^{N} w_j \delta_j^2 \Big/ \sum_{j=1}^{N} w_j \right]^{1/2} , \qquad (3-6)$$

where the δ_j are the corresponding quantities for each of N properties being fit,

$$\delta_j = \left[\frac{1}{n_j}\sum_{i=1}^{n_j}\left(\frac{S_{ij}^{calc} - S_{ij}^{exp}}{\Delta S_{ij}^{exp}}\right)^2\right]^{1/2} . \qquad (3-7)$$

Here, S_{ij}^{exp} and S_{ij}^{calc} is the measured datum and the corresponding calculated quantity, and ΔS_{ij}^{exp} is the absolute experimental error. Error bars correspond to one standard deviation in all cases. Overall weights w_j for each class of data reflect the sensitivity with which each property probes the interatomic potential.[43] The angular or velocity range of the scattering data, and the temperature range of the dilute-gas properties, is also considered.

As discussed in Sec. 3.5 below, the HFD1 interatomic potential obtained in this work was simultaneously fit to the Alberta DCS data, all the ICS results,[18,47] the mixture diffusion data of Arora et al.[19] and limiting diffusion measurements near room temperature of Dunlop,[20(a)] the mixture viscosity data of Kestin et al.,[21] and all the interaction virial coefficients.[22,55,56] The DCS, ICS, and dilute-gas data were assigned equal weights, with each of the dilute-gas properties having equal individual weights.

The HFD2 interatomic potential was obtained by simultaneously fitting only the Göttingen DCS data at both collision energies and the interaction virial coefficients, but excluding the low-temperature data of Iomtev et al.[22] Weights assigned were equal for the three properties.

3.5. DATA SELECTION

3.5.A. Differential Cross Sections

The two HFD potentials presented in this work were obtained using almost completely independent data sets. This independence was obviated by the different methods used to simulate the averaging effects of both scattering machines. Nevertheless, simultaneously fitting all the results, though unwieldy, was certainly possible. This possibility was not pursued however, since the two potentials obtained independently serve as a check on their accuracy, and the consistency of other available experimental data with the interatomic potentials derived.

3.5.B. Integral Cross Sections

ICS measurements at sufficiently low collision energy show pronounced oscillatory structure reflecting the existence of meta-stable bound states in the centrifugal potential. In principle, such measurements should then be highly sensitive to the detailed shape of the attractive well.[43,46] Since the HeNe attractive well is so shallow, oscillatory structure can be observed only for collision energies below ~ 0.5 meV. The recent ICS measurements of Grace et al.[18] clearly resolve one such oscillation, making these data useful despite the arbitrary scale of the measured cross sections.

Conversely, absolute ICS measurements, even for collision energies above the oscillatory regime, can provide useful constraints on measures of the attractive well "size" (such as $\epsilon . r_{\rm m}^6$). When the attractive well depth is determined by fits to other properties, absolute ICS data can provide useful constraints on the outer bowl of the attractive well.[5,43] For this purpose, we consider the absolute ICS data measured by Pirani and Vecchiocattivi.[47]

Error bars for the Grace et al. data[18] are assigned according to the authors' claim as independent of the collision energy. They suggested ±6% for data using Ne as their primary beam, and ±10% for their He primary beam. These two sets of data are normalized independently to the calculated ICS's since they were not accurately calibrated to one another. The absolute ICS data have velocity-dependent error bars as given by the authors[47]; the absolute scaling error of the data as a whole is also accomodated in the analysis (Sec. 3.4.B).

3.5.C. Dilute-Gas Properties

While the scattering properties discussed above posess a great deal more direct sensitivity to the interatomic potential, dilute-gas properties usually have the virtue of being absolute quantities. In addition, recent measurements, particularly of diffusion coefficients near room temperature,[19,20] have become both precise and reliable.[4,5,13] Such data, though not necessarily well suited to determining interatomic potentials by themselves,[51] nicely complement the scattering properties in severely restricting the range of interatomic potentials describing both types of data.

For the level of accuracy attained by Dunlop and co-workers,[19,20] room-temperature diffusion measurements place significant constraints on both the weakly repulsive wall and on the attractive well.[5,13,43] We consider their published data in the range 273-325 K,[19] as well as more recent results from 280-320 K.[20(a)] Newer measurements in the latter range[20(b)] became available to us only after our fitting calculations had been completed, and are therefore used only for comparison to the best-fit predictions. These data near room temperature are considered to be accurate to ±0.3%.[5,19,20] Unfortunately, it has proven difficult to extend these measurements to temperatures below 273 K and above 325 K,[5,20(b)] and the unpublished data for these temperatures are not used for fitting purposes.

Other published diffusion data[58] are significantly less accurate than the room-temperature measurements of Dunlop and co-workers. In addition, our experience with the heavier He+rare gas pairs has shown that many of these data sets exhibit large inconsistencies, both internally and with other authors.[5] Consequently, only the Dunlop data near room temperature[19,20(a)] are considered in fitting the potential (Sec. 3.6.C.1).

Viscosity measurements for gas mixtures are sensitive to a different collision integral than the diffusion coefficients, in principle providing complementary information on the interatomic potential. In practice, mixture viscosity measurements are strongly dependent on the like-pair interactions (from which diffusions are independent in the first-order Chapman-Cowling approximation), and their accuracy ultimately is not as high as that achieved for diffusions. Nevertheless, viscosities measured by Kestin et al.[21] are available up to higher temperatures, and therefore serve to probe the interatomic potential higher up the repulsive wall. Of the two reported sets of mixture viscosity measurements at 298 K, the earlier Kestin et al. data[21(a)] appear to be considerably less accurate, based on our attempts to extract an interaction viscosity coefficient at that temperature. None of the other mixture viscosities present any similar difficulty. We therefore consider only their later measurements at 298 K,[21(b)] along with their earlier data from 373-973 K. These authors' pure-gas viscosities, measured concurrently with their mixture properties,[21] are used as outlined in earlier work.[5] The error bars reflect deviation plots reported in a recent paper.[59]

Three sets of second virial coefficients have been reported for the HeNe interaction. The lowest-temperature measurements (15-20 K) are subject to the largest errors, 2-3 cm^3/mole,[22] but are highly sensitive to the attractive well region. These measurements thus complement the low-energy Grace et al. ICS data.[18] Measurements at higher temperatures[55,56] complement the diffusion and viscosity measurements. These data, and their error bars, are re-calculated from the original mixture virial measurements using the accurate and consistent National Bureau of Standards compilation[60] of pure-gas virials, as in earlier work.[5]

Thermal diffusion measurements are complicated functions of high-order collision integrals and mixture composition.[61] In principle, they may be somewhat more sensitive to the attractive well of the interatomic potential, but in practice their usefulness is limited by the relatively large errors that must be assigned to the measurements for them to be reasonably consistent with one another.[5,43] They are therefore excluded from the data sets used to fit the interatomic potential, as in earlier work.[5]

Thermal conductivity measurements, sensitive in the first-order Chapman-Cowling approximation to the same collision integral as viscosity measurements, are available only at 308 K.[62] Thus, to the best of our knowledge, the available mixture thermal conductivities provide no new information, and are not included in the fitting calculations (Sec. 3.6.C.3).

3.6. RESULTS AND DISCUSSION

3.6.A. Fitted Properties

The best-fit HFD1 and HFD2 potential parameters for the HeNe interaction are collected in Table 3-4. The corresponding fitting qualities δ, for those properties considered as discussed in Sec. 3.5, appear in Table 3-5. Our best-fit interatomic potentials are plotted in Fig. 3.2. For comparison, Fig. 3.2 also shows the HFD potential of Aziz,[25(a)] and the numerical potentials obtained by direct inversion of DCS data,[15] and of transport properties.[16] Likewise, fitting qualities for other published HeNe interatomic potentials appear in Table 3-5. These published potentials will be discussed below (Sec. 3.6.D).

It is immediately apparent from Fig. 3.2 that the various HeNe potentials illustrated are quite similar, with only slight differences in their attractive well depths and the positions of their weakly repulsive walls. The properties most sensitive to these slight differences[43] are the low-energy ICS[18] and (Göttingen) DCS measurements, the low-temperature virials,[22] and the room-temperature diffusion coefficients.[19,20(a)] The experimental and best-fit calculated DCS's are compared in Fig. 3.1. The experimental ICS, diffusion, viscosity, and virial data are shown in Figs. 3.3-3.6 respectively, along with the corresponding properties calculated from the best-fit HFD1 and HFD2 potentials obtained in this work.

Both HFD1 and HFD2 reproduce the mixture viscosity data to 973 K [Fig. 3.5], lending confidence to their repulsive walls and in particular, to our treatment of the Hartree-Fock calculations for the HFD1 potential. The HFD2 predictions are slightly too large at high temperatures. The good fits obtained for all three DCS's [Fig. 3.1 and Table 3-5], in two different laboratories using different detectors and simulation procedures, demonstrates that the low-energy repulsive region and attractive well of these potentials are well characterized. This

Table 3-4. Best-Fit Interatomic Potential Parameters

	HFD1[a,b]	HFD2[a,c]
r_m(Å)	3.029[d]	3.023[e]
σ(Å)	2.699[e]	2.686[d]
ϵ(meV)[e]	1.827	1.823
α(Å^{-1})	4.031[f]	4.426[d]
β(Å^{-2})	0.0987[f]	0.0
A(keV)[e]	0.797	0.955
D	1.28	1.32
C_6(eV-Å^6)	1.810[g]	1.895[h]
C_8(eV-Å^8)	5.503[d]	5.768[h]
C_{10}(eV-Å^{10})	20.5[i]	22.24[h]
C_{12}(eV-Å^{12})	96.[i]	0.00
C_{14}(eV-Å^{14})	554.[i]	0.00

[a] Eqn. 3-3.

[b] Fitted to the Alberta DCS; and the ICS's [Refs. 18,47], Dunlop diffusions near room temperature [Refs. 19,20(a)], mixture viscosities [Ref. 21], and all the virials [Refs. 22,55,56]. The HFD repulsive parameters, calculated as described in Sec. 3.3, are held constant as described in Sec. 3.4.A.

[c] Fitted to the Göttingen DCS's, and the virials above 80 K [Refs. 55,56]. The HFD2 γ parameter was adjusted to 0.5 [Eqn. 3-4]. HFD repulsive parameters also fitted. This is the "HFD3" potential reported in Ref. 25(a).

[d] Fitted to the data.

[e] Derived from the fitted parameters.

[f] Calculated and held fixed; see Sec. 3.3.

[g] Ref. 40.

[h] Fitted to the data of Ref. 42 within the error bounds given there.

[i] Calculated from recursion relations of Ref. 41.

Table 3-5. Interatomic Potentials and Fitting Qualities for HeNe

	HFD1[a]	HFD2[a]	HFD[b]	XC[c]	inv.[d]	TT[e]	HFD[f]
r_m(Å)	3.029	3.023	3.016	2.998	2.97	3.004	3.017
σ(Å)	2.699	2.686	2.684	2.675	2.67	2.680	2.690
ϵ(meV)	1.827	1.825	1.893	1.996	1.97	1.932	1.866
r(V=100meV;Å)	2.029	2.018	2.031	2.046	2.00[g]	2.053	2.046
δ_{DCS}(Alberta)	1.33	1.50	1.56	1.80	2.16	1.65	1.46
δ_{DCS}(Göttingen, ambient)	1.04	0.67	0.73	1.05	1.29	0.85	0.84
δ_{DCS}(Göttingen, liq. N_2)	1.22	1.07	1.51	2.43	2.51	1.86	1.35
δ_{ICS}[h]	1.29	1.31	1.43	1.82	1.58	1.38	1.31
δ_{ICS}[i]	0.92	1.06	1.19	1.31	1.30	1.10	0.99
δ_{DFN}[j]	0.35	3.84	0.32	3.57	5.43	4.56	3.23
δ_{VIS}[k]	0.27	0.65	0.19	0.60	0.87	0.72	0.58
δ_{VIR}[l]	0.53	1.34	2.44	3.27	2.79	1.95	1.04
δ_{VIR}[m]	0.81	0.39	0.36	0.37	0.39	0.56	0.70
$\delta_{overall}$[n]	1.07	1.56	1.25	1.94	2.35	1.88	1.46

[a] Present work; potential parameters in Table 3-4.

[b] Ref. 25, potential "HFD2j". The r_m and ϵ values entered in the table correspond to the actual minimum position and depth respectively, as obtained from Aziz' HFD reduced potential form; his r_m and ϵ parameters are slightly different since the reduced HFD form does not necessarily have its minimum at the r_m scaling parameter value [Ref. 25(b)].

[c] Ref. 26, potential "U_b".

[d] Ref. 15, used as discussed in Sec. 3.6.D.1. The fitting qualities are almost identical using third-order interpolation for the tabulated numerical potential instead of linear interpolation.

[e] Ref. 27.

[f] Ref. 23.

[g] Extrapolated

[h] Ref. 18, 47 measured cross sections in arbitrary units.

[i] Ref. 47, 23 measured absolute cross sections; calibration accurate to ±3%.

[j] Refs. 19 and 20(a).

[k] Ref. 21.

[l] Ref. 22, 6 measurements from 15-20 K.

[m] Ref. 55 at 90 K; Ref. 56, 9 measurements from 123-323 K.

[n] Eqn. 3-6 with w_{DCS}(Alberta) = w_{DCS}(Göttingen) = w_{ICS} = 1.00; w_{DFN} = w_{VIS} = w_{VIR} = 0.33.

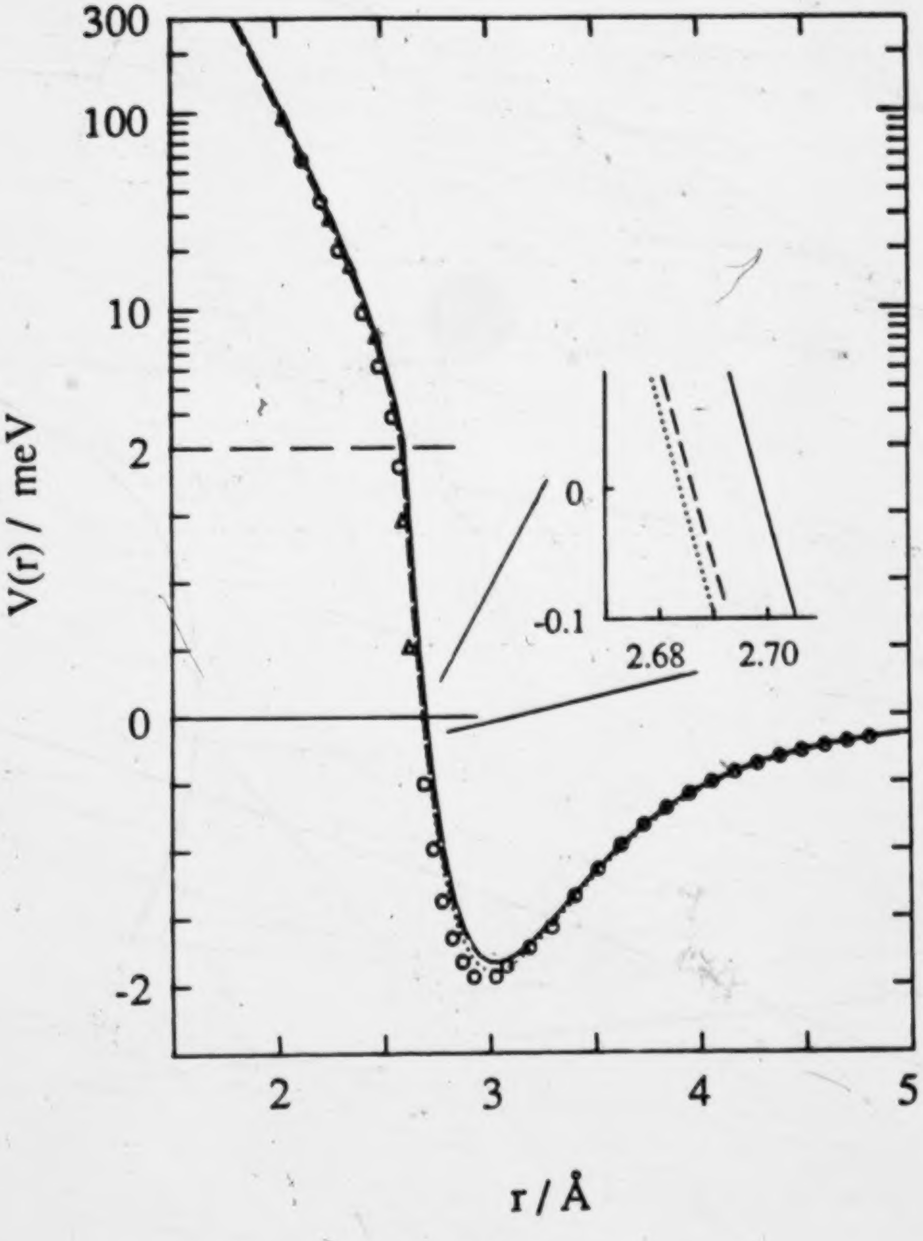

FIGURE 3.2

HeNe interatomic potentials. The solid and (barely distinguishable) dashed lines are the best-fit HFD1 and HFD2 potentials obtained as described in the text. The dotted line is the HFD potential of Aziz,[24(a)] obtained by minor adjustment of an earlier best-fit potential also based on DCS data. The symbols correspond to numerical potentials obtained by direct inversion of DCS data[14] (○), and of transport property data[15] (△). The inset enlarges the region near the potential zero crossing.

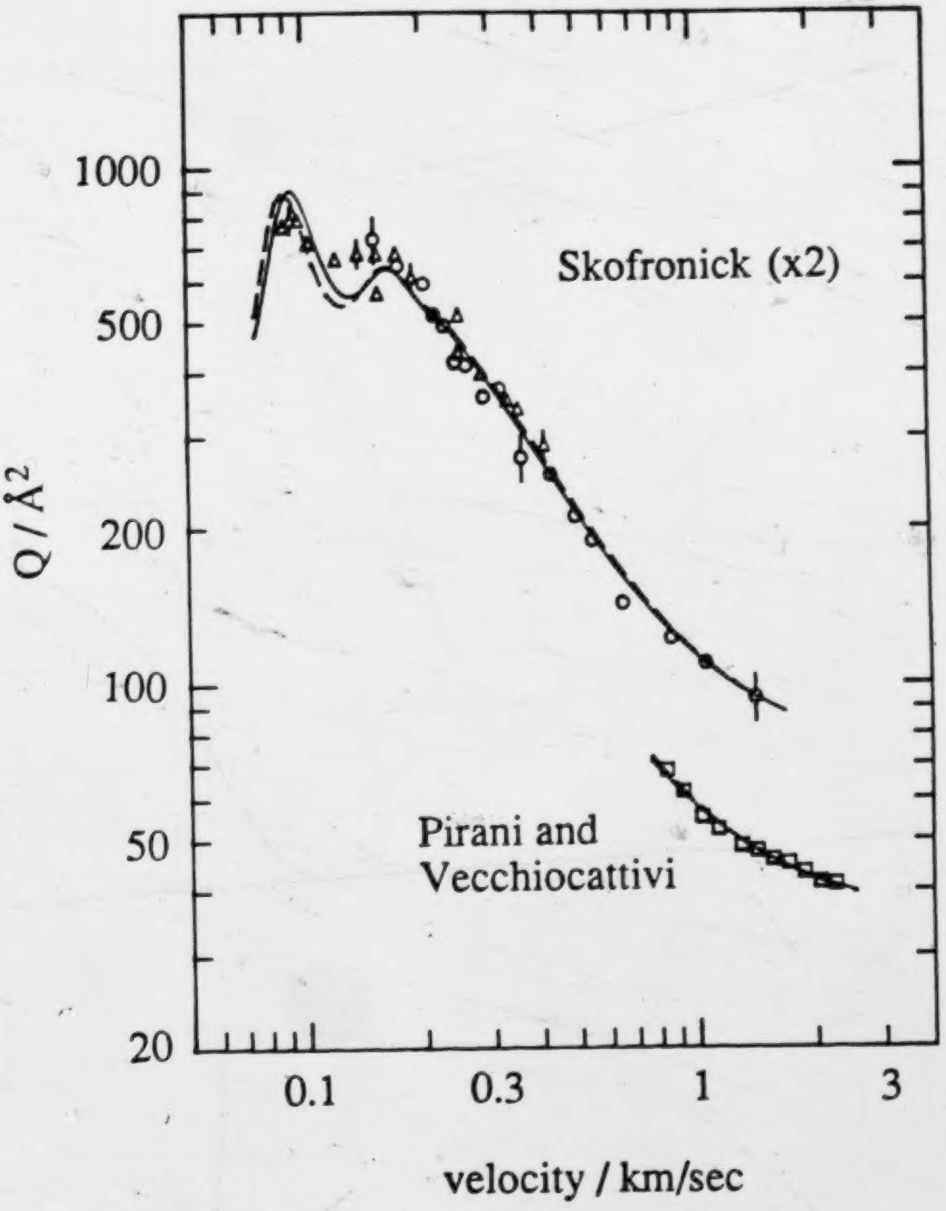

FIGURE 3.3

Integral cross sections for HeNe obtained from experiment (symbols) and from the HFD1 and HFD2 potentials (line types as in Fig. 3.2). Some of the experimental data have been deleted for clarity, and only representative error bars are shown. Symbols used are: △ and ○, Grace et al.[17] arbitrary cross sections as functions of collision velocity; and □, Pirani and Vecchiocattivi[46] absolute (±3%) cross sections as functions of the He beam velocity. The actual adjustment of the "absolute" experimental cross sections is 1.5%. The data depicted as triangles and circles were obtained with Ne or He primary beams, respectively.[17]

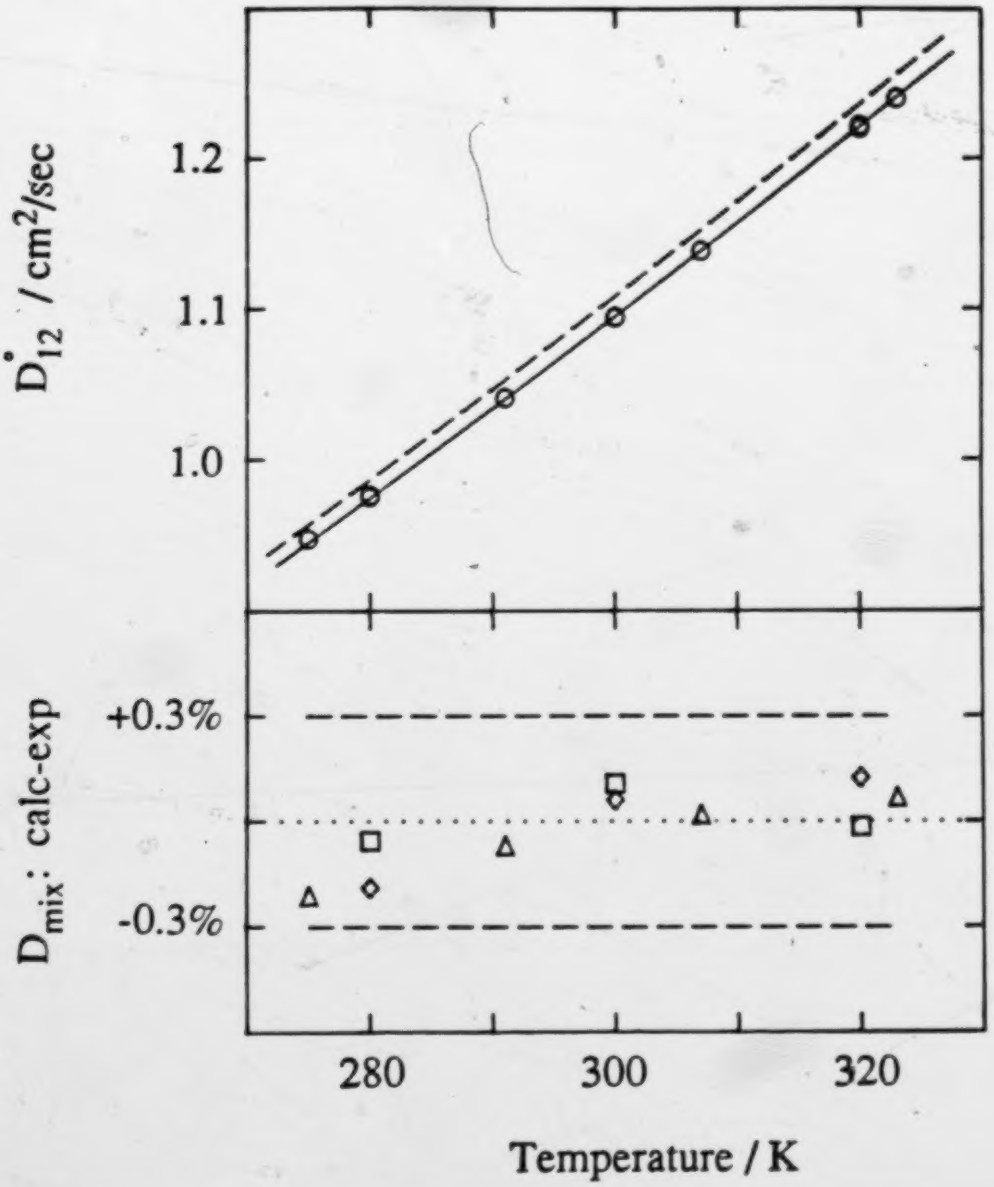

FIGURE 3.4

Limiting diffusion coefficients (upper frame) and deviations of the best-fit HFD1 calculated diffusions from experimental measurements (lower frame; HFD2 deviations are not shown). Upper-frame line types as in Fig. 3.2. Symbols used are: △, Arora et al.[18]; ◇, Dunlop[19(a)]; and □, Dunlop.[19(b)] Dashed lines in the lower frame depict the authors' error bounds. Only the mixture diffusions of Ref. 18 and the limiting diffusions of Ref. 19(a) were used in the fitting procedure. Some of the experimental data of Ref. 18 have been deleted for clarity.

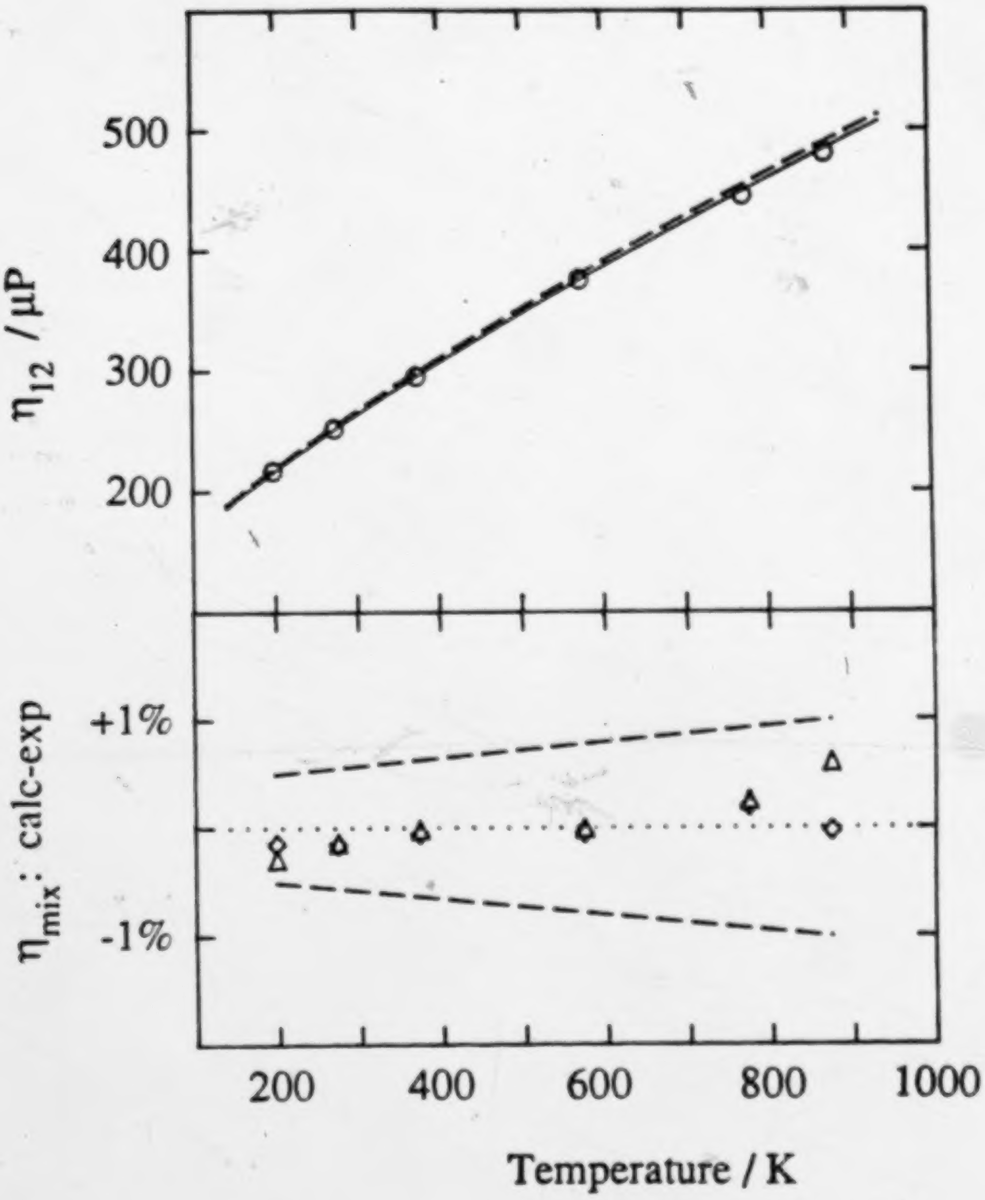

FIGURE 3.5

Interaction viscosity coefficients (upper frame) and deviations of the best-fit HFD1 calculated viscosities from experimental measurements for two near-equimolar mixtures (lower frame; HFD2 deviations are not shown). Upper-frame line types as in Fig. 3.2. Symbols used are: △, Kestin et al., 40% He[20]; ◇, Kestin et al., 63% or 78% He.[20] Dashed lines in the lower frame depict the error bounds discussed in Sec. 3.5.C. Only the mixture viscosities were used in the fitting procedure. The experimental data of Ref. 20(a) at 298 K have been deleted as discussed in Sec. 3.5.C.

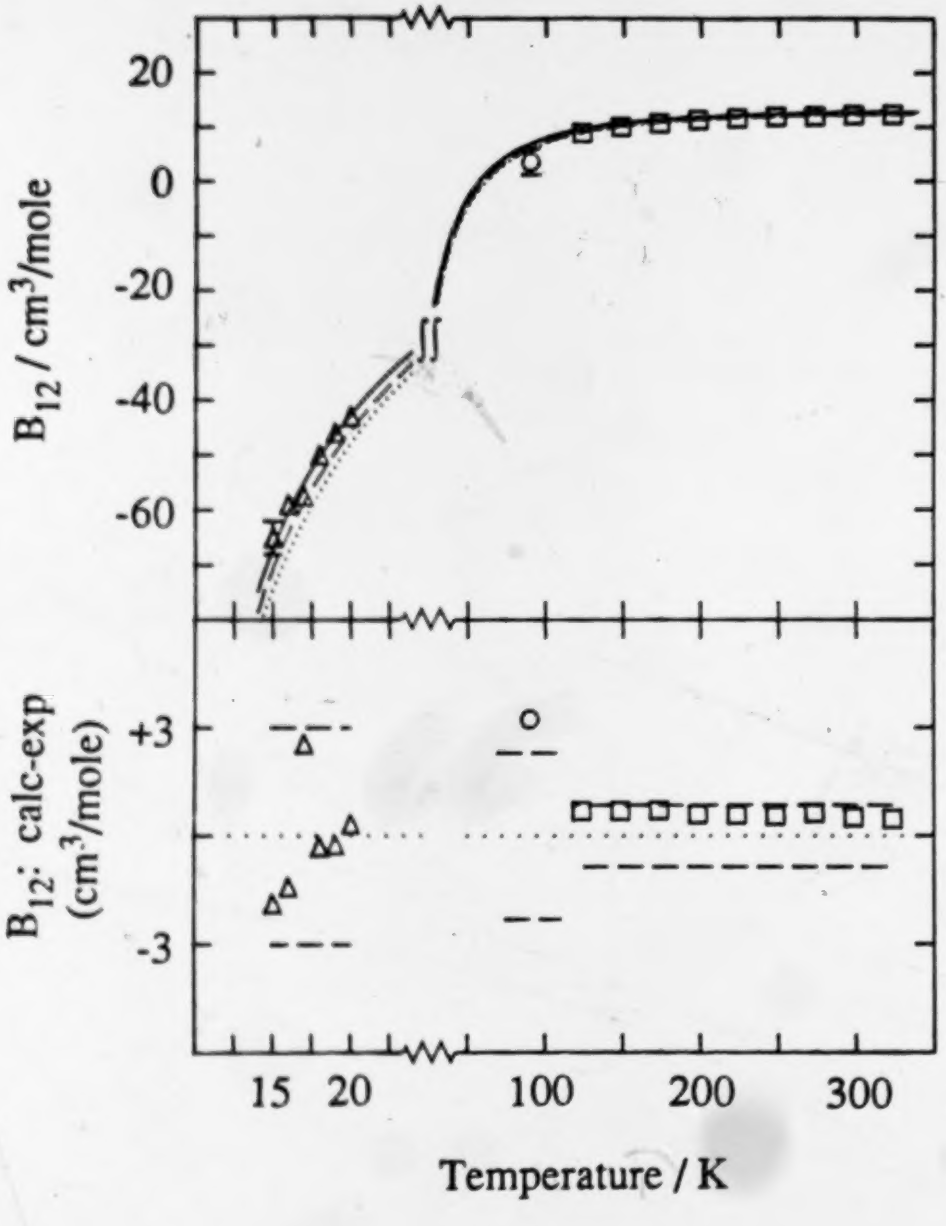

FIGURE 3.6

The upper frame shows interaction second virial coefficients obtained from experiment (symbols) and from the best-fit HFD1 and HFD2 potentials (line types as in Fig. 3.2). The dotted curve is obtained from the Aziz potential.[24(a)] The lower frame details deviations of the best-fit HFD1 calculations from the measured interaction virial coefficients; HFD2 deviations are not shown. Note the temperature scale break at 25 K. Dashed lines depict the error bounds discussed in Sec. 3.5.C. Symbols used are: △, Iomtev et al.[21]; □, Knobler et al.[54]; and ○, Brewer et al.,[55] for which only representative error bars are shown.

is substantiated by good reproduction of the virials above 80 K[55,56] [Fig. 3.6]. Reproduction of the ICS data[18,47] [Fig. 3.3] then ensures a reliable shape for the outer bowl of the attractive well.[5,43] The only noticeable difference between HFD1 and HFD2 is the latter potential's failure to predict the precise diffusion measurements near room temperature[19,20(a)] [Fig. 3.4]. These have been accurately reproduced almost 10 years after the original measurements,[19] ensuring at least their precision. Based on previous experience with similar data for the heavier He+rare gas pairs,[5] we believe these data to be accurate as well.

The overall fitting qualities provided by both the HFD1 and the HFD2 potentials are quite satisfying. The somewhat poorer HFD2 result is due almost solely to the Dunlop diffusions.[19,20(a)] Thus, we prefer the HFD1 potential as the best available in fitting all the properties presently considered, provided of course that the diffusion measurements really are accurate to 0.3% near room temperature. Nevertheless, we remark that the differences between HFD1 and HFD2 are so slight that they can be distinguished in Fig. 3.2 only by repulsive walls displaced by about 0.01 Å. In addition, we consider the overall performance of HFD2, as fitted to such a restricted data set, to illustrate the usefulness of highly precise and accurate DCS data at different scattering energies. Finally, we remark that the fitting quality for the Alberta DCS data could not be brought below $\delta \approx 1.2$ even when fit without any other properties, due primarily to some unevenness in the measured DCS at ~ 23° [Fig. 3.1] for which we currently have no explanation. Similarly, the lowest fitting quality obtained for any potential fit to the Grace et al. ICS data[18] is $\delta \approx 1.3$, due to our somewhat inadequate [Fig. 3.3] simulation of the experimental averaging (Sec. 3.4.B). Neither of these deficiencies have any significant effect on the best-fit HFD1 potential.

3.6.B. Fitted Interatomic Potentials

In obtaining the best-fit HFD1 potential, several further trial calculations were performed. As in earlier work,[5] three adjustable parameters of the Morse-spline-van der Waals (MSV) potential form were fit to the complete data set. The resulting potential is virtually indistinguishable from HFD1, in terms of the potential, its parameters, and the fitting qualities. Only a slight deterioration for the low-temperature virials mitigates against the MSV potential. The observed similarities, despite mathematical forms that are quite different, strongly suggests that the potentials obtained are largely independent of the parameterizations chosen to represent them.

A possible drawback in using the HFD parameterization is due to its discontinuous second derivative at $r = Dr_m$ [Eqn. 3-3]. This might be troublesome in evaluating low-temperature virial coefficients semi-classically, which require the third derivative of the potential.[52] Another possible problem lies with the HFD parameterization's use of a single damping function for all the dispersion terms.[41,63] Both these possible difficulties can be avoided by fitting the (revised) Tang-Toennies potential model,[24] with its appealing characteristics of being analytic everywhere and using a multi-damping function. As with the MSV form, a two-parameter Tang-Toennies fit yields potentials and calculated properties indistinguishable from the HFD1 best-fit potential. We conclude that the HFD parameterization is acceptable, and we prefer it for computational efficiency.

Comparing the dispersion coefficients for the HFD1 and HFD2 potentials (Table 3-4) suggests that HFD1 might be obtained even without fitting the higher-order dispersion terms at all. This entails adjusting r_m in one-parameter fits to a large body of independent data. The HeNe interaction probably provides the best such test, because of the expected greater accuracy for both the HF calculations (Sec. 3.3) and the semi-empirical dispersion estimates.[40,44] Indeed, fixing C_8 at 5.462 eV-Å^8, the mean of Standard and Certain's bounds[44] while fitting only r_m, yields results that again are indistinguishable from the HFD1 best-fit potential. This illustrates the importance of accurate dispersion coefficients within semi-empirical potential forms[63] such as the HFD model; it is especially dramatic because the present data set includes properties that are highly sensitive to the outer bowl of the attractive well[43] whose shape is largely controlled by the dispersion coefficients. If this experience with HeNe is a general one, it is unfortunate that the higher-order dispersion coefficients do not yet seem to be as reliable for the heavier rare-gas interactions.[4,5]

In distilling the HFD fits to one-parameter models wherein only r_m is adjusted, even this last parameter could be eliminated if the HF value for the pre-exponential A parameter in Eqn. 3-3 were accurate enough. This is a very severe test indeed, because most of the properties being considered are highly sensitive to the distance scale of the potential, especially for a system as diffractive as HeNe. For this fixed-parameter calculation, the HF value obtained in Sec. 3.3 of A = 686 eV is used, and predicts r_m and σ values of 2.945 Å and 2.616 Å, respectively. These values are too small by only 0.08 Å relative to the HFD1 fitted values (ϵ is too deep by 0.3 meV), but produce disastrous results for all the properties being considered (fitting qualities of 3.8 for the Alberta DCS, and errors of 5% for the Dunlop diffusions,[19,20(a)] for example!). It is clear that the distance scale provided by HF calculations of the present quality, even for a light and non-relativistic interaction like HeNe, is inadequate. Nevertheless, our excellent reproduction of the mixture viscosities up to 973 K, especially for HFD1, and the similarity between the HFD1, HFD2, and MSV potentials, show that the HF calculations apparently do give reliable results for the slope of the HeNe exponentially repulsive wall. At least one adjustable parameter must be retained for the fitting calculations, until more accurate HF calculations become available.

3.6.C. Properties Excluded From the Fits

3.6.C.1. Diffusion

As mentioned in Sec. 3.5.C above, the diffusion coefficients reported in Ref. 58 were not used in the fitting calculations. Our best-fit calculated diffusions are compared to these measurements in Table 3-6, but achieve only limited success. This is identical to our experience for the heavier He+rare gas systems.[5] The Zwakhals and Reus[58(d)] and Taylor and Cain[58(f)] data are not internally consistent enough, within the error bars claimed, to be reproduced by any potential. The most recent Dunlop diffusions[20(b)] are well reproduced in the 280-320 K range [see also Fig. 3.4], but are somewhat poorer for the remaining data from 220-400 K. As for the HeAr case,[5] we believe these discrepancies are caused by temperature calibration difficulties,[20(b)] which again would not affect the measurements near room temperature that have been included in the fits.[19,20(a)]

Systematic deviations from the HFD1 predictions are shown by the Hogervorst diffusion data[58(c)] and by the Wahby et al. diffusion ratios.[58(e)] The latter ratios lie 1.1% higher than the predicted ones at 419 K, and 0.2% lower at 238 K. The HFD2 predictions are almost identical at 419 K but are 0.7% lower at 238 K. The Hogervorst data[58(c)] clearly lie below the calculated diffusions reaching discrepancies of 6.5% at 1400 K. It is unlikely that these discrepancies can be attributed to the fitted HFD1 potential, since with it we obtain excellent fits to the mixture viscosities, even up to 973 K [Fig. 3.5]. The Hogervorst data also lie systematically below predictions for the heavier He+rare gas diffusions,[5,25(a)] though the Wahby et al. ratios are predicted somewhat more faithfully for those systems.[5]

Table 3-6. Fitting Qualities for Properties Excluded from the HFD1 Fits[a]

Property	Reference	Temperature (K)	Error(%)[b]	δ[c]
Diffusion	57(a)	65-295	1.5	0.53
	57(b)	77-365	3.8	0.93
	57(c)	300-1400	0.75	5.77
	57(d)	297-1268	1.35	2.76
	57(e)	238-419	0.3[d]	1.98[d]
	57(f)	388-1199	2.0	1.40
	19(b)	220-400	0.3	1.02
	all[e]	—	—	1.84
Thermal Diffusion	63(a)	295	3.5	0.73
	63(b)	67-300	6-3	1.21
	63(c)	300	2.0	1.09
	63(d)	251-750	2.1-5.5	1.95
	63(e)	31-203	1.3-4.5	2.40
	all	—	—	1.67
Thermal Conductivity	61	308.15	0.2	5.71

[a] HFD1 potential of Table 3-4 and Fig. 3.2.

[b] Precision claimed by the authors, adjusted for Refs. 58(b) and 58(e) as discussed in Ref. 5.

[c] Eqn. 3-7.

[d] Diffusion ratios.

[e] Excluding the data of Ref. 58(c), which is sytematically too low (Sec. 3.6.C.1).

The most reliable of the diffusion data[58(a),58(b)] range in temperature from 65-419 K, and therefore provide little new information. Diffusions below 200 K[58(a),58(b)] are well reproduced, providing some corroboration for the low-temperature virial data.

3.6.C.2. Thermal Diffusion

Thermal diffusion measurements for the heavier He+rare gas pairs appear to suffer from the same lack of consistency as many of the diffusion measurements.[5] Based on this experience, we again avoided including thermal diffusion measurements[64,65] in the fitting calculations. Nevertheless, we compare experimental thermal diffusions with the corresponding predictions from HFD1 and HFD2 in Table 3-6 and Fig. 3.7. The best-fit potentials nicely reproduce the overall shape of the measurements throughout the temperature range of 31-750 K, and generally yield fitting qualities near unity. For the Taylor et al. data near 100 K,[64(e)] the data clearly exhibit consistency problems (Fig. 3.7). None of the data appears to deviate systematically from the best-fit predictions.

3.6.C.3. Thermal Conductivity

To the best of our knowledge, the only HeNe thermal conductivity data available are mixture measurements at 308 K.[62] These data are predicted very poorly by the HFD1 potential (Table 3-6). There are at least three reasons to believe that this is caused by the very restrictive 0.2% error bars claimed for this data: firstly, second-order Chapman-Cowling inversion of the mixture data results in deviations exceeding the claimed error bars; and secondly, thermal conductivity data are (to first-order) directly related to viscosity, which are fit very well by the HFD1 potential. Moreover, it is difficult to see how the HFD1 potential could be adjusted to fit the thermal conductivity data within its claimed error, without

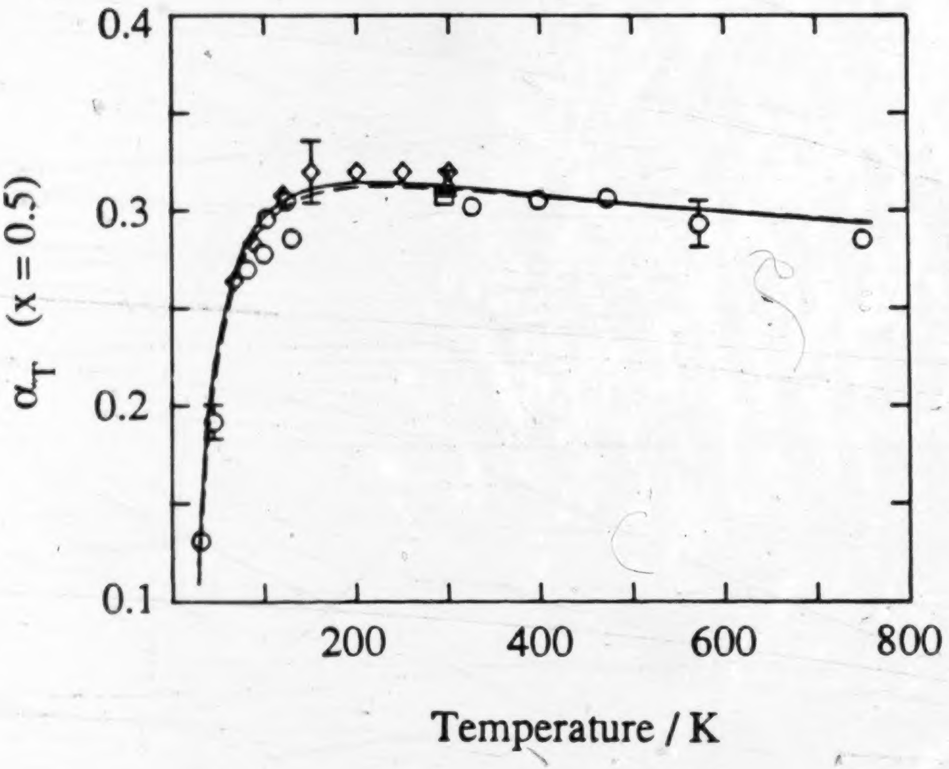

FIGURE 3.7

Equimolar thermal diffusion data from experiment (symbols) and from the best-fit HFD1 and HFD2 potentials (line types as in Fig. 3.2). Symbols used are: ○, Taylor [Ref. 63(d) for temperatures above 250 K and Ref. 63(e) below 250 K]; ◇, Grew et al.[63(b)]; □, Timov et al.[63(a)]; and △, Trengove et al.[63(c)] Some of the experimental data of Refs. 63(b), 63(d), and 63(e) have been deleted for clarity, and only representative error bars claimed by the authors are shown. The thermal diffusion data were not included in the fits.

sacrificing the excellent reproduction attained for many of the other properties. Finally, HeAr mixture thermal conductivity measurements from the same type of apparatus,[66] even more difficult to invert to interaction thermal conductivities than for HeNe, could not be accomodated using any of three independently determined HFD potentials for that system.[5]

3.6.D. Comparison to Literature Potentials

The most reliable of recently proposed HeNe potentials, and their fitting qualities for the various properties being analyzed, are summarized in Table 3-5. A few other potentials have been discussed in the recent review by Aziz,[25(a)] and will not be further considered here. Our treatment goes considerably beyond that carried out in the Aziz review, adding our two new independent DCS's, the ICS's,[18,47] and the low-temperature virial[22] measurements to the data set.

All the potentials summarized in Table 3-5 have attractive well depths of 1.8-2.0 meV, and minimum positions and zero crossings within 0.03 Å of 3.00 Å and 2.68 Å, respectively. At this point, it becomes clear that the HeNe interaction is very well characterized, especially considering the dearth of bound-state spectroscopic data for this system.[67] We are therefore looking for rather small refinements, which can only be made using data that are most sensitive to the interatomic potential. We note also that none of the potentials listed in Table 3-5 is any more successful than HFD1 in predicting properties excluded from the fits (Table 3-6 and Sec. 3.6.C).

3.6.D.1. Numerical Potentials

The numerical potentials obtained from DCS and dilute-gas data cannot be used to calculate the observed properties directly, since they are available only at the tabulated distances. Although it would be most convenient to fit them to analytical forms, this would defeat the original purpose of inverting the data directly to the interatomic potential.

For the Gerber et al. potential,[15] we used linear interpolation between their tabulated points. For extrapolating below their lowest value of $r = 2.128$ Å, we used $V(r) = A \exp(-\alpha r - \beta r^2)$, with $\alpha = 4.031$ Å^{-1} and $\beta = 0.0987$ Å^{-2} being obtained from the Hartree-Fock calculations of Sec. 3.3, and $A = 0.4796$ keV being obtained by averaging their five highest-energy numerical points. For extrapolating beyond their highest value of $r = 5.286$ Å, we used $V(r) = -C_6 r^{-6} - C_8 r^{-8}$, with dispersion parameters obtained from Refs. 40 and 42, respectively.

The data of Table 3-5 show that the Gerber et al. numerical potential,[15] while having the advantage of not requiring assumption of any particular parameterization, fails to reproduce the diffusion and low-temperature virial measurements. The two data sets probe very fine details of the potential in the weakly repulsive wall and the outer attractive well, respectively, to which the room temperature differential cross section are not extremely sensitive. Also the DCS data which have not been used for the inversion procedure are not reproduced accurately enough. This result reflects the high accuracy which is achieved in both the data and the potential determination for this system. The agreement obtained between the best fit potential of this work and the potential obtained by inversion is best documented in Fig. 2. A better accuracy cannot be expected for such a method.

The Maitland and Wakeham numerical potential was obtained by direct inversion of dilute-gas data.[16] It seems to be in good accord with the Gerber et al.[15] numerical potential for the repulsive wall between 1-50 meV [Fig. 3.2], but is insensitive to the attractive well region.[16] Their numerical potential is also in reasonable accord with HFD1 and HFD2, though it deteriorates for more weakly repulsive interactions as its sensitivity decreases. We did not use their fitted potential to compare its predictions to the observed properties, because many of these properties are very sensitive to the attractive well region and could be obtained from the Maitland and Wakeham results only by extrapolation.[16] In addition, we note their fitted potential yielded average deviations of 0.025 Å even on the repulsive wall.[16]

3.6.D.2. Model Potentials

The Tang-Toennies HeNe potential[27] also predicts most properties rather well, except for the diffusions and the low-temperature virials. These deficiencies are caused by an attractive well that is slightly too deep, and a weakly repulsive wall occuring at distances that are slightly too small. Also rather successful is the Ahlrichs et al. HFD potential,[23] proposed with justifications similar to the Tang-Toennies potential. This HFD potential fails only in predicting the room-temperature diffusions with the necessary high accuracy, due to a repulsive wall which climbs slightly too steeply,[43] and is reflected also by somewhat poorer predictions for the viscosity measurements. Nevertheless, the Ahlrichs et al. potential reproduces the low-temperature virials reasonably well, with the slightly smaller well position compensating for a slightly deeper attractive well. Considering that these potentials were obtained without any adjustable parameters, the Tang-Toennies[27] and Ahlrichs et al.[23] potentials are surprisingly accurate. In view of our experience with HFD potentials having no adjustable parameters (Sec. 3.6.B), this circumstance can be attributed to using a surprisingly accurate repulsive A parameter.

3.6.D.3. Fitted Potentials

The room-temperature diffusion measurements of Dunlop and co-workers[19,20(a)] provide an especially fine filter for the various interatomic potentials.[13] For potentials with the same attractive well depths, the 0.3% measurement error corresponds to a weakly repulsive wall position error of ~ 0.005 Å.[5,13,43] The HFD1 and HFD2 potentials, with nearly identical well depths, have repulsive walls shifted sufficiently to render the HFD2 prediction inaccurate [Fig. 3.4]. The low-temperature virials are also somewhat too negative [Fig. 3.6], due to the slightly wider attractive well of HFD2.

The Watanabe et al. XC potential[26] fails to reproduce the diffusion and low-temperature virial measurements, as well as the low-energy Göttingen DCS. This is probably caused by an attractive well that is too deep, but might be rectified by including the low-temperature virials originally excluded in the XC single-parameter fits.

In considering the Aziz potential,[25] it is apparent that its diffusion predictions are almost identical to HFD1, which is achieved by a repulsive wall occuring at slightly shorter distances offset by an attractive well that is slightly deeper. This deeper well then produces low-temperature virials that are too negative by ~ 6 cm^3/mole, over twice the error bars claimed. Unfortunately, the low-energy ICS data[18] are too poorly resolved to provide better discrimination, or to corroborate the low-temperature virial measurements. Likewise, the low-temperature thermal diffusion data of Taylor et al.[64(e)] are too inaccurate [Sec. 3.6.C.2], a common problem for measurements of this difficult property. Although the low-energy DCS data are reproduced better by HFD1 than by the Aziz potential, the room-temperature DCS's favour the latter. Thus, the only property considered that really discriminates against the Aziz HFD potential[25(a)] is the low-temperature virials. Without sufficient corroboration of these data therefore, the Aziz potential must be regarded as quite reliable.

We continue to prefer the HFD1 potential however, because of its effective use of only a single adjustable parameter [Sec. 3.6.B] and its theoretically calculated hard wall. In addition, the Aziz HFD potential was obtained by adjustments made after fitting to DCS measurements, a difficult procedure to systematize for systems not quite so well characterized as HeNe.

It is apparent that discrepancies between HFD1 and the Aziz potential can be taken as indicating the reliability of the present determination of the HeNe potential. In particular, the error bars proposed for the heavier He+rare gas interaction potentials[5] accomodate twice the present discrepancy between HFD1 (or HFD2) and the Aziz HFD potential. Nevertheless, we also note that the r_m potential parameter cannot be changed by 0.01 Å without seriously affecting the HFD1 predictions (Table 3-5, HFD1 vs HFD2 for example), unless there is a correlated change in the well depth. Consequently, the potential minimum parameter values are even more restricted than the above error bars suggest: the potential parameters should not be used independently of the HFD1 potential that they characterize. A worst-case estimate based on the analysis of Ref. 5 would likely demonstrate uncertainties of ±0.01 Å for the position of the attractive minimum and repulsive wall, and ±2% for the attractive well depth.

3.7. SUMMARY

In this paper we present new high-resolution DCS measurements for room-temperature (Alberta) and liquid N_2-cooled (Göttingen) beams for the highly diffractive HeNe system. These experiments are supported by Hartree-Fock calculations that are incorporated into HFD model potentials. Two HFD potentials are obtained independently: HFD1 uses the Hartree-Fock calculations explicitly in multiproperty fits to the Alberta DCS data as well as all other reliable ICS and dilute-gas properties; HFD2 is obtained by simultaneously fitting the Göttingen DCS's at two collision energies and virial measurements at moderate temperatures.[55,56]

The HFD1 and HFD2 potentials obtained are almost indistinguishable. It is shown that the HFD1 potential provides a good description of all reliable HeNe measurements, including predictions of the Göttingen DCS's which were not fit. The HFD2 potential adequately predicts almost all the data, except for very precise diffusion measurements near room temperature.[19,20(a)] We believe the HFD1 potential presents the best systematic representation for the HeNe interaction, with error bars of ±0.01 Å in the position of the attractive minimum and repulsive wall, and ±2% in the attractive well depth. These error bars must be regarded as highly correlated.

Of several literature potentials compared to the present HFD1 and HFD2 fits, the Aziz HFD potential[25(a)] can be regarded as quite reliable, with only three minor drawbacks: it was obtained in a manner difficult to systematize; it includes neither HF calculations (such as the present ones) nor the accurate C_6 dispersion results of Kumar and Meath[40]; it does not quite fit the low-temperature virial measurements of Iomtev et al.[22] The numerical potential obtained by direct inversion of high-quality DCS data[15] is not as accurate as the potentials presently obtained by multiproperty fits in the reproduction or prediction of several of the various properties available.

It is shown that the HFD1 potential can equivalently be obtained by fitting a single parameter controlling the potential's range. The present Hartree-Fock calculations are not quite sufficiently accurate to eliminate this last adjustable parameter within the HFD model.

Acknowledgements

We wish to thank M. Klobukowski (Alberta) for assistance with the HF calculations; P. J. Dunlop (Adelaide) for sharing his diffusion data prior to publication and for extensive discussions regarding temperature calibrations; and J. G. Skofronick (Florida State) and F. Vecchiocattivi (Perugia) for assistance in interpretting their experimental ICS results; and R. A. Aziz (Waterloo) for assistance with his HFD2j potential. We also thank Deb Danielson, Gary Samek, and Karen McLeod for their assistance in obtaining the Alberta DCS data and Burkhard Schmidt for carrying out several calculations concerning the Göttingen data. This research was supported by grants from the Natural Sciences and Engineering Research Council (Canada), and from the Research Corporation. Acknowledgement is also made to the donors of the Petroleum Research Fund, administered by the American Chemical Society, for partial support of this research.

References

1. G.C. Maitland, M. Rigby, E.B. Smith, and W.A. Wakeham, *Intermolecular Forces: Their Origin and Determination*, (Clarendon, Oxford, 1981). See especially Chapter 9.
2. G. Scoles, Ann. Rev. Phys. Chem. **31**, 81 (1980).
3. C.H. Chen, P.E. Siska, and Y.T. Lee, J. Chem. Phys. **59**, 601 (1973).
4. R.T Pack, J.J. Valentini, C.H. Becker, R.J. Buss, and Y.T. Lee, J. Chem. Phys. **77**, 5475 (1982).
5. L.J. Danielson and M. Keil, J. Chem. Phys. **88**, 851 (1988).
6. L. Beneventi, P. Casavecchia, and G.G. Volpi, J. Chem. Phys. **84**, 4828 (1986).
7. R.T Pack, J.J. Valentini, and J.B. Cross, J.Chem. Phys. **77**, 5486 (1982); R.T Pack, E. Piper, G.A. Pfeffer, and J.P. Toennies, J. Chem. Phys. **80**, 4940 (1984).
8. J.M. Hutson and B.J. Howard, Mol. Phys. **45**, 769 (1982).
9. M. Keil and G.A. Parker, J. Chem. Phys. **82**, 1947 (1985); L.J. Danielson, M. Keil, and P.J. Dunlop, J. Chem. Phys. **88**, 4218 (1988).
10. J. Andres, U. Buck, F. Huisken, J. Schleusener, and F. Torello, J. Chem. Phys. **73**, 5620 (1980).
11. H. Meyer, U. Buck, R. Schinke, and G.H.F. Diercksen, J. Chem. Phys. **84**, 4976 (1986).
12. J.O. Hirschfelder, G.F. Curtiss, and R.B. Bird, *Molecular Theory of Gases and Liquids*, (Wiley, New York, 1954).
13. R.A. Aziz, P.W. Riley, U. Buck, G. Maneke, J. Schleusener, G. Scoles, and U. Valbusa, J. Chem. Phys. **71**, 2637 (1979).
14. U. Buck, Rev. Mod. Phys. **46**, 369 (1974); Comp. Phys. Rep. **5**, 1 (1986).

15. R.B. Gerber, M. Shapiro, U. Buck, and J. Schleusener, Phys. Rev. Lett. **41**, 236 (1978).
16. G.C. Maitland and W.A. Wakeham, Mol. Phys. **35**, 1429; 1443 (1978).
17. R. Guzman and H. Rabitz, J. Chem. Phys. **86**, 1395 (1987).
18. R.S. Grace, D.L. Johnson, and J.G. Skofronick, J. Chem. Phys. **67**, 2443 (1977).
19. P.S. Arora, H.L. Robjohns, and P.J. Dunlop, Physica **95A**, 561 (1979). The data of G.R. Staker, M.A. Yabsley, J.M. Symons, and P.J. Dunlop, J. Chem. Soc. Farad. Trans. **I70**, 825 (1974) was not considered on the advice of P.J. Dunlop (private communication to L.J.D.).
20. (a) P.J. Dunlop, private communication to M.K. (October, 1987); (b) P.J. Dunlop, private communication to M.K. (January, 1988).
21. (a) J. Kestin, S.T. Ro, and M.A. Wakeham, J. Chem. Phys. **56**, 5837 (1972); (b) J. Kestin, O. Korfali, J.V. Sengers, and B. Kamgar-Parsi, Physica, **106A**, 415 (1981).
22. M.B. Iomtev, A.I. Doroshenko, L.S. Kushner, Kh.M.A. Sarov, and L.T. Kalinichenko, Russ. J. Phys. Chem. **51**, 808 (1977).
23. R. Ahlrichs, R. Penco, and G. Scoles, Chem. Phys. **19**, 119 (1977).
24. K.T. Tang and J.P. Toennies, J. Chem. Phys. **80**, 3726 (1984).
25. (a) R.A. Aziz, in *Inert Gases: Springer Series in Chemical Physics* **34**, M.L. Klein, ed. (Springer-Verlag, Berlin, 1984); (b) R.A. Aziz, private communication to M.K.
26. K. Watanabe, A.R. Allnatt, and W.J. Meath, Chem. Phys. **68**, 432 (1982).
27. K.T. Tang and J.P. Toennies, J. Chem. Phys. **66**, 1496 (1977).
28. L.J. Danielson, K.M. McLeod, and M. Keil, J. Chem. Phys. **87**, 239 (1987).
29. U. Buck, F. Huisken, J. Schleusener, and J. Schaefer, J. Chem. Phys. **72**, 1512 (1980).

30. U. Buck, in *Atomic and Molecular Beam Methods*, G.Scoles, ed. (Oxford, New York, 1988) Chapter 20.

31. M. Shapiro, R.B. Gerber, U. Buck, and J. Schleusener, J. Chem. Phys. **67**, 3570 (1977).

32. F.B. Van Duijneveldt, IBM Report RJ 945 (1971), IBM, San Jose.

33. C. Froese-Fischer, *The Hartree-Fock Method for Atoms*, (Wiley, New York, 1977).

34. S. Huzinaga and M. Klobukowski, J. Mol. Struct. (THEOCHEM) **167**, 1 (1988).

35. T.W. Dingle, S. Huzinage, and M. Klobukowski, to be published.

36. S.F. Boys and F. Bernardi, Mol. Phys. **19**, 553 (1970).

37. A.J.C. Varandas and J. Brandao, Mol. Phys. **45**, 857 (1982).

38. G. Das, A.F. Wagner, and A.C. Wahl, J. Chem. Phys. **68**, 4917 (1978).

39. R.A. Aziz and H.H. Chen, J. Chem. Phys. **67**, 5719 (1977).

40. A. Kumar and W.J. Meath, Mol. Phys. **54**, 823 (1985).

41. C. Douketis, G. Scoles, S. Marchetti, M. Zen and A.J. Thakkar, J. Chem. Phys. **76**, 3057 (1982).

42. K.T. Tang, J.M. Norbeck, and P.R. Certain, J. Chem. Phys. **64**, 3063 (1976).

43. M. Keil and L.J. Danielson, Can. J. Phys. **66**, 159 (1988).

44. J.M. Standard and P.R. Certain, J. Chem. Phys. **83**, 3002 (1985).

45. These refinements were applied by the authors of Ref. 18. Nevertheless, our HFD1 calculated ICS's in the oscillatory regime are very similar to those we obtain from the HFD potential of Ref. 23, which reproduce the experimental measurements very well according to Fig. 3.1 of Ref. 18.

46. J.P. Toennies, W. Welz, and W. Wolf, J. Chem. Phys. **64**, 5305 (1976).

47. F. Pirani and F. Vecchiocattivi, J. Chem. Phys. **66**, 372 (1977).

48. F. Vecchiocattivi (private communication to M.K.) suggested that the calculated ICS's should be compared to the data of Ref. 47 in the laboratory frame of reference, rather than to deconvoluted data in the CM frame.

49. R.A. Aziz, V.P.S. Nain, J.S. Carley, W.L. Taylor, and G.T. McConville, J. Chem. Phys. **70**, 4330 (1979).

50. R.A. Aziz, W.J. Meath, and A.R. Allnatt, Chem. Phys. **78**, 295 (1983).

51. R.A. Aziz, F.R.W. McCourt, and C.C.K. Wong, Mol. Phys. **61**, 1487 (1987).

52. (a) M.E. Boyd, S.Y. Larsen, and J.E. Kilpatrick, J. Chem. Phys. **50**, 4034 (1969); (b) T. Kihara, Y. Midzuno, and T. Schizume, J. Phys. Soc. Japan **10**, 249 (1955).

53. The virial measurements of Ref. 22 achieve temperatures down to 15 K, and therefore appear to be too low for even the improved semiclassical technique of A.J. Thakkar, Mol. Phys. **36**, 887 (1978).

54. M.E. Boyd, S.Y. Larsen, and J.E. Kilpatrick, J. Chem. Phys. **45**, 499 (1966).

55. C.M. Knobler, J.J.M. Beenakker, and H.F.P. Knapp, Physica **25**, 909 (1959).

56. J. Brewer and G.W. Vaughn, J. Chem. Phys. **50**, 2960 (1969); J. Brewer, Air Force Office of Scientific Res. Rept. No. 67-2795, 1967 (unpublished).

57. Documented copies of this program are available on request to M.K.

58. (a) R.J.J. van Heijningen, J.P. Harpe, and J.J.M. Beenakker, Physica **38**, 1 (1968); (b) G.A. Dubro and S. Weissman, Phys. Fluids **13**, 2682 (1970); (c) W. Hogervorst, Physica **51**, 59 (1971); (d) C.J. Zwakhals and K.W. Reus, Physica **100C**, 231 (1980); (e) A.S.M. Wahby, M. Abdel-Rahman, and J. Los, Physica **112A**, 214; 225 (1982); (f) W.L. Taylor and D. Cain, High Temp. High Press. **15**, 433 (1983).

59. B. Najafi, E.A. Mason, and J. Kestin, Physica **119A**, 387 (1983).

60. J.M.H. Levelt Sengers, M. Klein, and J.S. Gallagher, in *AIP Handbook*, M.W. Zemansky and D.E. Gray, eds. (McGraw-Hill, New York, 1972).

61. E.A. Mason, J. Chem. Phys. **27**, 75 (1957); E.A. Mason, J. Chem. Phys. **22**, 169 (1954).

62. M.J. Assael, M. Dix, A. Lucas, and M.A. Wakeham, J. Chem. Soc. Farad. Trans. **I77**, 439 (1981).

63. W.J. Meath, D.J. Margoliash, B.L. Jhanwar, A. Koide, and G.D. Weiss, in *Intermolecular Forces*, B. Pullman, ed. (Reidel, Dordrecht, 1981).

64. (a) G.P. Timov and P.E. Suetin, Sov. Phys. Tech. Phys. **21**, 336 (1976); (b) K.E. Grew and W.A. Wakeham, J. Phys. **B11**, 2045 (1978); (c) R.D. Trengove, H.L. Robjohns, T.N. Bell, M.L. Martin, and P.J. Dunlop, Physica, **108A**, 488 (1981); (d) W.L. Taylor, J. Chem. Phys. **72**, 4973 (1980); (e) W.L. Taylor, D. Cain, F.R. Meeks, and P.T. Pickett, J. Chem. Phys. **82**, 2745 (1985).

65. The data of J.M. Symons, M.L. Martin, and P.J. Dunlop, J. Chem. Soc. Farad. Trans. **I75**, 621 (1979) was not considered on the advice of P.J. Dunlop (private communication to L.J.D.).

66. A.A. Clifford, R. Fleeter, J. Kestin and W.A. Wakeham, Physica **98A**, 467 (1979).

67. Y. Tanaka and K. Yoshino, J. Chem. Phys. **57**, 2964 (1972).

CHAPTER 4

Sensitivity of Experimental Measurements in Fitting Interatomic Potential Energy Curves†

4.1. INTRODUCTION

Much of the recent progress in determining interatomic potential energy curves has been accomplished by fitting parameters of suitable potential functions to many properties simultaneously.[1-4] To ensure that such multiproperty fits are not merely curve-fitting to enlarged data sets, it is essential to know how sensitive the various data are to specific regions or features of the interatomic potential.

Recent measurements of high-resolution differential cross sections (DCS),[2,5-7] and the possible manifestation of quantum effects for low-temperature transport and virial measurements for light systems, make it worthwhile to determine directly the sensitivity of these properties to interatomic potentials. Earlier investigations of this sort focussed exclusively on dilute gas properties for heavy systems[8] or low-resolution DCS measurements.[9-10] Properties best suited for multiproperty fits can then be selected commensurate with their sensitivity, relative to the accuracy with which they are measured. It is also desirable for these properties to be somewhat redundant in their sensitivity to the potential, to ensure that the properties selected are consistent with each other.

In this paper, we investigate the usefulness of each particular property by varying given regions or features of the interatomic potential while leaving the remainder of the potential unaltered. In Sec. 4.2 we describe the types of modifications applied to a "standard" potential energy curve chosen for convenience to be the HeKr interaction obtained by Smith et al.[11] The effect of these modifications on DCS, integral cross section (ICS), transport, and virial properties are presented in Sec. 4.3. These results are discussed in Sec. 4.4 and suggest the most fruitful multiproperty fitting procedure.

---

† A version of this chapter has been published. M. Keil and L.J. Danielson, Can. J. Phys. 66, 159 (1988).

In a previous paper,[7] the multiproperty fitting procedure was applied to determine interatomic potentials for HeAr, HeKr, and HeXe. Their accuracy, independent of mathematical parameterization, and their range of validity, were determined using the sensitivity studies presented in this paper. The present approach will later be generalized to non-spherical systems (in preparation), for which very detailed data are currently obtainable.[12]

We choose the present finite-variation approach rather than one based on sensitivity analysis.[13] Though formally more elegant and powerful, the latter approach has not yet explicitly included the substantial[13] effects of instrumental averaging of scattering cross sections or Boltzmann averaging of transport cross sections. More fundamentally, the formal sensitivity approach may provide a basis for the direct inversion of experimental data to the interatomic potential.[13,14] However, our present approach is directed to the more generally applicable procedure of fitting parameterized potential energy functions simultaneously to a wide variety of properties.

4.2. CALCULATIONS

Each type of modification to the HeKr standard potential[11] allows the selected region to be strengthened in potential energy or displaced in distance arbitrarily. In each case, the modified potential is calculated analytically, with continuous function and first derivative, using cosine-squared functions to switch between modified and unmodified regions of the potential. For example, the potential modified for the attractive well depth is given by;

$$\begin{aligned} U(r) &= V(r)\,, \quad r \le r_1 \\ &= V(r)\left\{1 + (f-1)\cos^2\left[\frac{\pi}{2}\left(\frac{r-r_1}{r_m - r_1}\right)\right]\right\}\,, \quad r_1 \le r \le r_m \qquad (4-1) \\ &= V(r)\left\{1 + (f-1)\cos^2\left[\frac{\pi}{2}\left(\frac{r-r_2}{r_2 - r_m}\right)\right]\right\}\,, \quad r_m \le r \le r_2 \\ &= V(r)\,, \quad r \ge r_2, \end{aligned}$$

where $V(r)$ is the standard potential energy function, and f is the factor by which the well depth is increased, and r_m is the position of the attractive minimum.

Five types of modified potentials are displayed in Fig. 4.1, with characteristics summarized in Table 4-1. Each observable property is calculated to a high degree of accuracy utilizing the calculational parameters of Ref. 7. The DCS's are calculated for room-temperature molecular beams. For differential and integral cross sections, instrumental averaging effects[7,15] are included to simulate experiments reported in the recent literature. Transport properties are calculated to high orders in the Chapman-Cowling approximation: second order for viscosity,[16] third order for thermal conductivity and thermal diffusion, and fourth order for diffusion.[17] All cross sections (DCS, ICS, transport) are calculated quantum mechanically; quantum corrections to third order are applied for the virial calculations.[18]

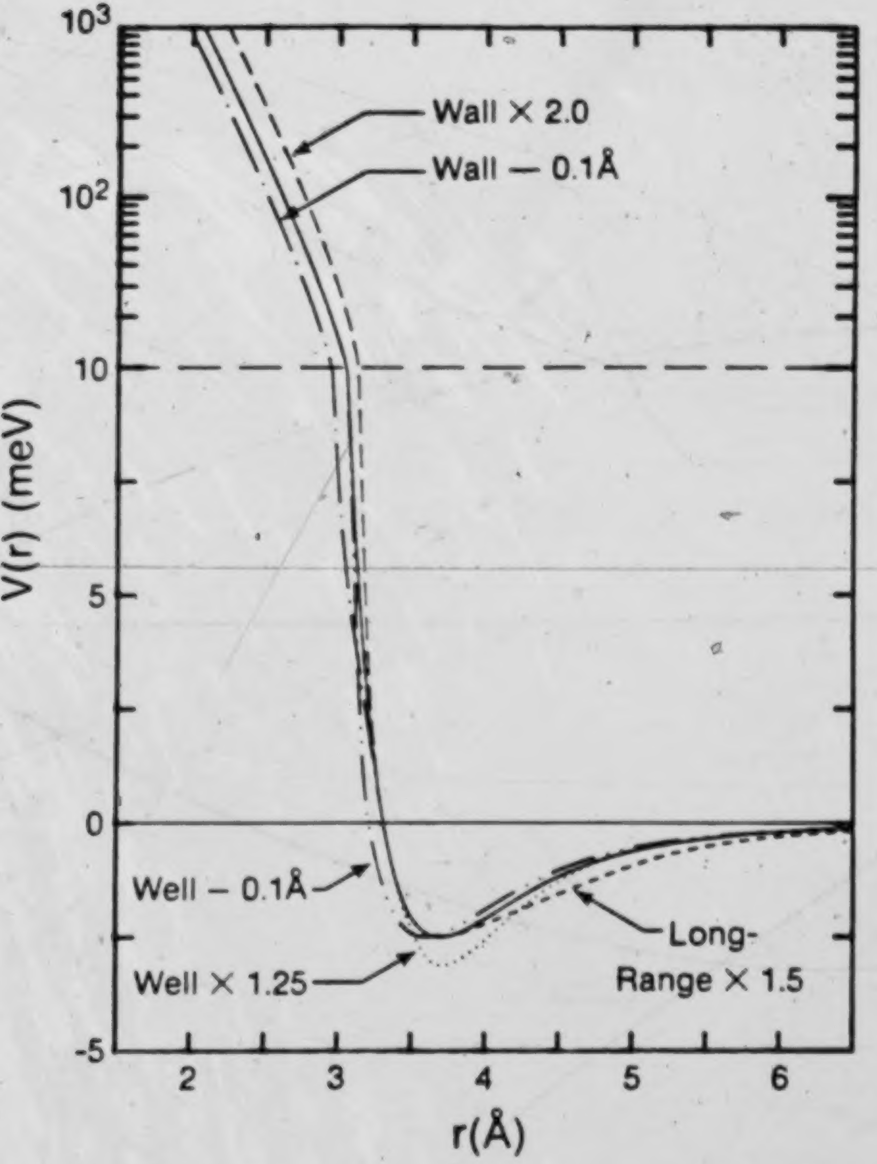

Figure 4.1

The standard model potential (solid line) and modifications to it (broken lines). The HeKr interaction shown is due to Smith et al.,[11] with modifications applied smoothly and detailed in Table 4-1.

Table 4-1. Modification Types Characterized[a]

Type	Modification
wall × 2.0	Repulsive slope doubled for $V(r) \geq 10$ meV; potential unchanged for $V(r) \leq 0$ meV.
wall − 0.1Å	Repulsive wall displaced by 0.1Å for $V(r) \geq 10$ meV; potential unchanged for $V(r) \leq 0$ meV.
well − 0.1Å	Attractive well displaced by 0.1Å; potential unchanged for $V(r) \geq 10$ meV.
well × 1.25	Well depth increased by 25% at minimum; potential unchanged for $V(r) \geq -0.6$ meV.
long-range × 1.5	Attraction increased by 50% for $V(r) \geq -0.6$ meV; potential unchanged for $r \leq r_m$.

[a] Standard potential taken from Ref. 11 with attractive well parameters r_m = 3.70Å; ϵ = 2.51 meV; σ = 3.31Å. The conclusions reached are independent of this particular potential's accuracy.

For estimating error bounds on the potential energy curves determined in a previous paper,[7] the potential energy strengthening factor or displacement distance was varied simultaneously with the other potential parameters in fitting the data.

4.3. RESULTS

Figures 4.2-4.5 display the effects on various properties used to determine interatomic potentials due to each of the modifications outlined above. The DCS and ICS appear directly as calculated from the modified and standard potentials. For clarity of display, the mixture transport properties and interaction virial coefficients are shown as deviations from the standard potential for each modification type. Error bars shown in each plot roughly denote the accuracy currently attained for the He-containing mixtures, as discussed in Ref. 7.

4.3.A. Differential Cross Sections

For DCS measurements, Fig. 4.2 shows that scattering beyond ~ 35° is wholly insensitive to the attractive well region. Sensitivity to the repulsive wall is limited to scattering angles beyond ~ 30°, as the two kinds of repulsive modifications produce nearly parallel DCS curves elsewhere and only relative DCS measurements are usually made. This sensitivity often is limited even further by experimental errors for large-angle scattering. Calculations with repulsive wall modifications moved to higher energies show that the DCS measurements lose all sensitivity for $V(r) \gtrsim 20$ meV. We remark that this is considerably below the collision energy used for the calculations (67 meV).

Modifying the long-range attraction significantly affects the first diffraction oscillation and is the only modification to affect the classical rainbow region (~ 4°). The latter changes are small ($\lesssim 0.2°$ shift in scattering angle), and the former can largely be duplicated with changes in the attractive well region. Thus, the DCS sensitivity is restricted almost entirely to the attractive well and weakly repulsive wall regions of the interatomic potential.

Changes in the depth and position of the attractive well independently affect the amplitude and frequency of the diffraction oscillations, respectively. The

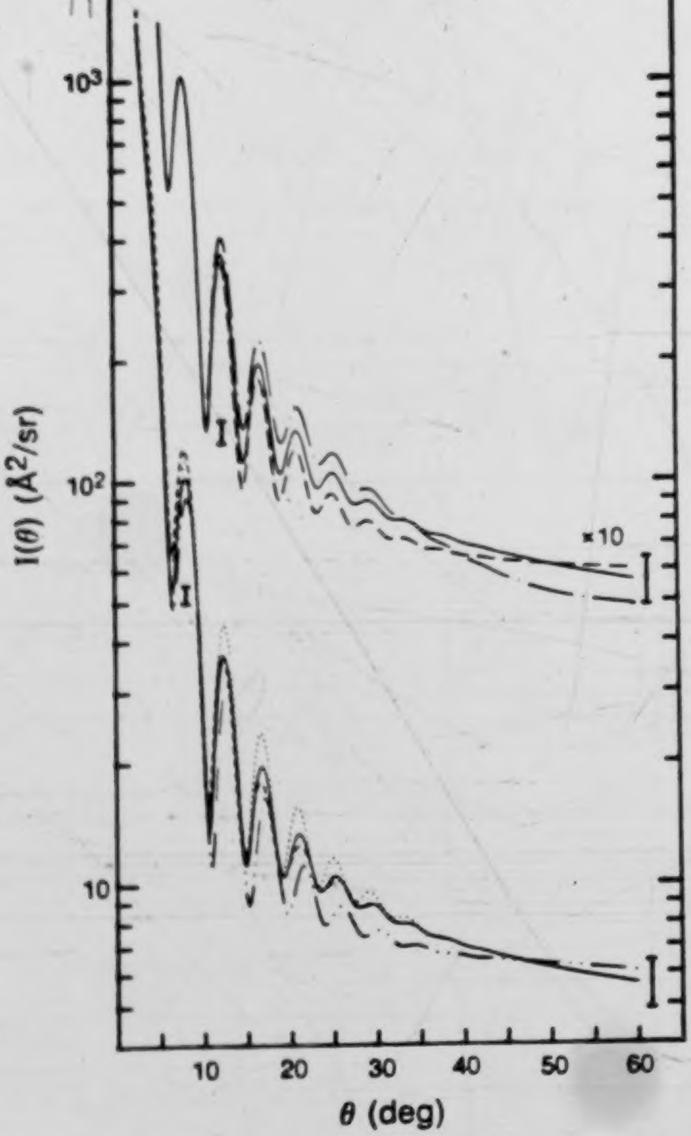

Figure 4.2

Differential cross sections as functions of laboratory scattering angle I(θ) calculated from the standard HeKr potential (solid line) and modifications to it (broken lines). Line types correspond to the modified potentials shown in Fig. 4.1. Typical instrumental averaging has been included.[7] The DCS's calculated using repulsive wall modifications are displaced by one decade for clarity of display. Error bars denote typical uncertainties for relative measurements.[7]

latter effect is usually attributed to the position of the repulsive wall, but is more clearly related to the inner portion of the attractive well. It is also seen that a stronger attractive well causes DCS oscillations to persist to higher scattering angles, with these wide-angle oscillations being affected proportionately more than narrow-angle ones. It is apparent that DCS measurements provide sensitivity to the position and depth of the attractive well, largely independently of each other, even though the collision energy is ~ 25 times the attractive well depth. However, earlier calculations have shown that a shallower well can be offset by a displaced weakly repulsive wall.[9] Hence, DCS measurements alone may not be sufficient to characterize the attractive well region accurately.

4.3.B. Integral Cross Sections

The most direct characterization for the attractive well would be provided by low-energy ICS measurements, which show pronounced structure for collision velocities below ~ 0.3 km/sec in Fig. 4.3. These oscillations appear at collision velocities depending sensitively on all features of the attractive well, even if the ICS calibration is not absolute. Clearly resolved metastable bound-state resonances have been observed for a variety of interactions involving H and H_2[19] and for HeNe.[15]

Modifications to the repulsive wall affect ICS measurements only for collision velocities above ~ 2 km/sec. This is usually beyond the range measured, except for very high energy beams. Attractive well modifications produce ICS curves that are parallel for collision velocities above the oscillatory region. Hence, only absolute ICS measurements are useful for such velocities, and even they are sensitive only to a "well capacity" parameter like $\epsilon.r_m^6$. Moreover, many possible combinations of well depths, and inner and outer attractive bowl shapes, would yield indistinguishable absolute ICS curves for collision velocities above ~ 0.7 km/

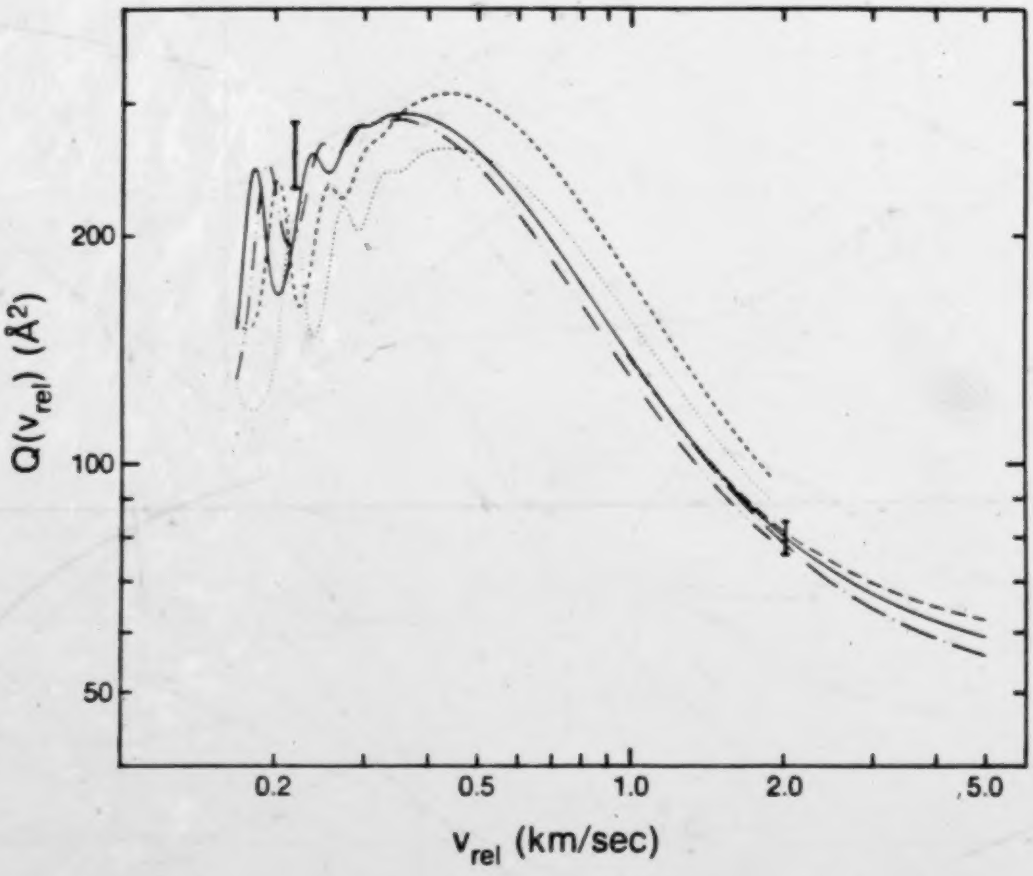

Figure 4.3

Integral cross sections as functions of relative collision velocities, $Q(v_{rel})$. Line types correspond to the potentials shown in Fig. 4.1. Instrumental averaging due to typical beam velocity dispersion has been included.[13] The low- and high-velocity error bars denote typical uncertainties for relative[13] and absolute[18] ICS measurements respectively.

sec. It is worth noting that typical absolute calibration errors of 3%[20] correlate with changes roughly double that proportion in C_6 or $\epsilon.r_m^6$. For ICS measurements to be more useful, they must be available in the oscillatory region, a difficult task experimentally but rewarding for their detailed sensitivity to the attractive well.[19]

4.3.C. Transport Properties

The collision integrals required for the evaluation of transport properties are heavily weighted by large-angle scattering cross sections, due to high angular moments in the generalized integral cross sections used to calculate them. In addition, Boltzmann averaging drastically reduces the effect of metastable bound-state resonances. Nevertheless, transport properties are measured as absolute quantities, unlike most microscopic scattering experiments, and can often be measured with considerably greater accuracy.

Changes in the attractive well region have little perceptible influence on the mixture viscosities and thermal conductivities shown in Fig. 4.4, even for the lowest temperatures attainable (~ 100 K, except for HeNe). The influence on thermal diffusions might be perceptible, but only at the lowest temperatures, and only if experimental errors can be reduced somewhat.[7,16] On the other hand, diffusions are significantly reduced by a stronger attractive well, at least for T $\lesssim$ 300 K. Even for this property however, correlated changes of the attractive well depth, and its shape, can produce invariant low-temperature diffusions. Not surprisingly, this is characteristic of the ICS for velocities exceeding 0.7 km/sec from which the transport properties are calculated.

The usefulness of the transport properties for the light systems being considered rely instead on their sensitivity to the repulsive wall of the interatomic potential. This is in contrast to the sensitivity of low-temperature transports for interactions between heavy atoms.[2,16] It is well known, and clearly reproduced in

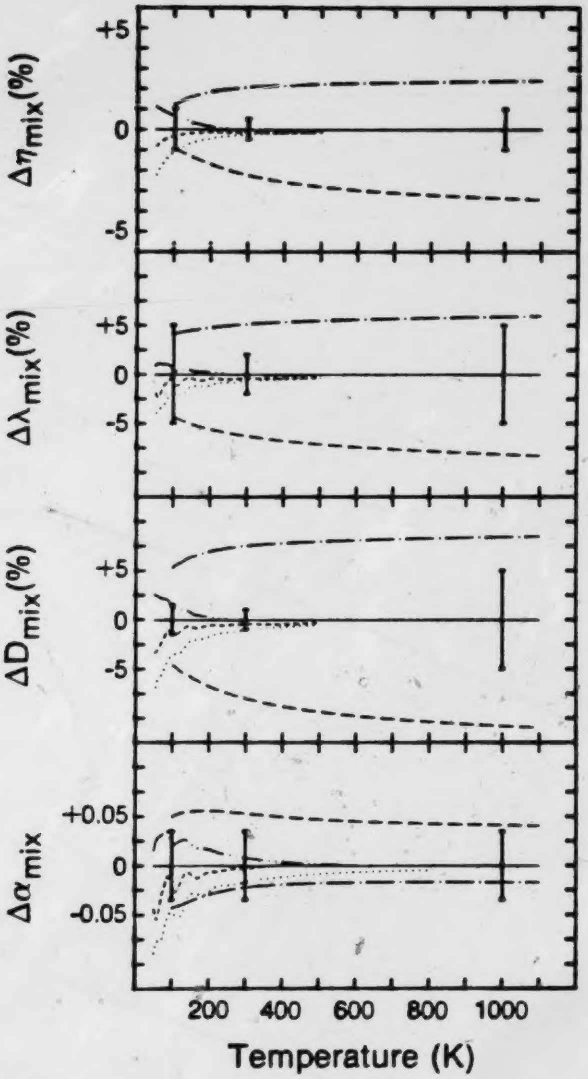

Figure 4.4

Mixture transport properties, plotted as deviations from the HeKr model potential[11], as functions of the temperature (viscosity, η; thermal conductivity, λ; diffusion, D; thermal diffusion, α; $\Delta \equiv$ modified − standard). Line types correspond to the potentials shown in Fig. 4.1. Thermal diffusion deviations are plotted directly; other transport properties are plotted as percentage deviations. Equimolar mixture properties are calculated in all cases. Error bars denote accuracies obtained for these measurements.[7]

Fig. 4.4, that a "harder" repulsive wall decreases the viscosity, thermal conductivity and diffusion of a gas mixture. This sensitivity appears to be greatest for diffusion, but unfortunately measurements of this property often have not been reproducible, especially at high temperatures.[7] Despite much reduced sensitivity, mixture viscosity measurements appear most useful because of the high precision and reproducibility with which they have been measured, even at high temperatures.[21] Calculations with repulsive wall modifications moved to higher energies show that the mixture viscosity for temperature T is sensitive to the potential energy for $V(r) \overset{\sim}{<} kT$, as found by Dymond and Alder[8] for heavier systems. It is interesting to note that the temperature dependence of thermal conductivity and viscosity differ slightly for $T \overset{\sim}{<} 500$ K, owing to higher-order Chapman-Cowling terms included in the calculation.

The sensitivity of thermal diffusion data to the interatomic potential has often been highly acclaimed.[16,22] This is not reflected by the plots in Fig. 4.4 however; the more modest sensitivity demonstrated is only partially due to the large errors that must be assigned for thermal diffusion measurements to be reasonably consistent with one another.[7]

4.3.D. Interaction Virial Coefficients

Figure 4.5 shows the very direct relation between atomic size and the virial coefficient. It is also clear that any change to the repulsive wall cannot be compensated for, except by very large changes in the attractive region of the potential, especially for high temperature virials. The virial coefficients therefore supplement the transport-property sensitivity to the repulsive wall. For a temperature T, the virial coefficient is sensitive to the potential energy for $V(r) \overset{\sim}{<} kT$, as for the viscosity.

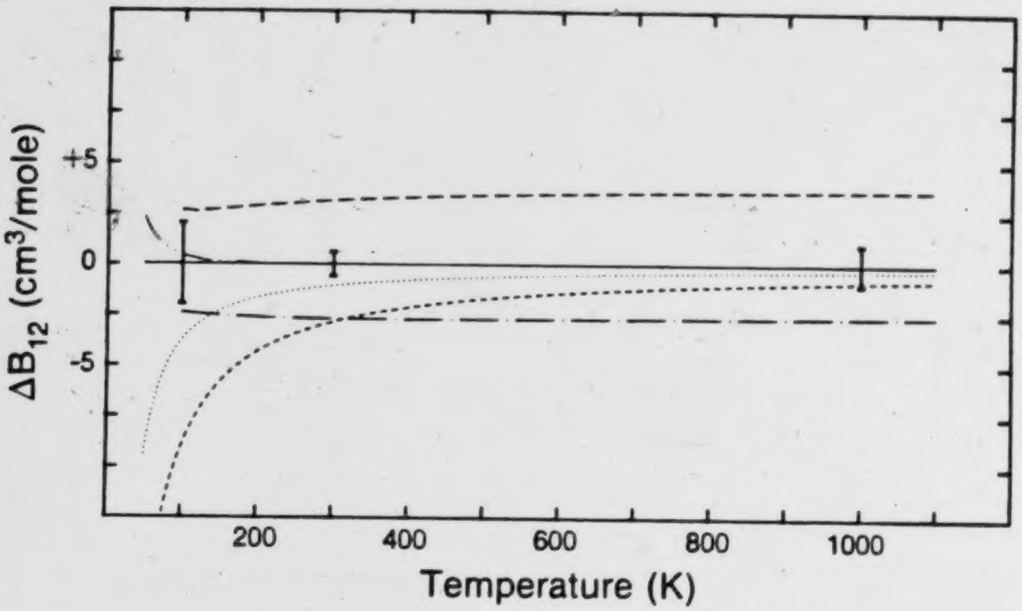

Figure 4.5

Interaction second virial coefficients B_{12}, plotted directly as deviations from the HeKr model potential. Other characteristics are as in Fig. 4.4.

Sensitivity of the virial coefficient to changes in the attractive well region can also be quite marked. The two types of strengthening modifications produce rather parallel curves however, so modifications that increase the well depth can be offset by weakening the long-range attraction. Also, the virial coefficient is totally insensitive to the position of the attractive well for accessible temperatures (T $\gtrsim$ 100 K except for HeNe), if the modified inner wall is extended to slightly repulsive interactions (Fig. 4.1). Thus, the virial coefficient is sensitive to the repulsive wall, and the attractive well, but not to their shape or their positions relative to one another.

4.4. MULTIPROPERTY FITTING PROCEDURE

By analytically modifying a model interatomic potential energy function for the HeKr interaction, we have determined the sensitivity of various properties to the interaction potential quantitatively. A fruitful procedure for determining interatomic potentials for low reduced mass van der Waals interactions by fitting measurements of properties sensitive to them can now be developed easily. The ICS data should be used whenever available for velocities low enough to exhibit resolved metastable bound-state resonances. Such data helped to determine the attractive well in detail for a variety of interactions involving H and H_2[19] but, unfortunately, are available only for the HeNe interaction[15] amongst He-containing systems. The DCS also provides great sensitivity to the attractive well depth and position, even for relatively large collision energies, and to the weakly repulsive wall. Instrumental averaging must be included carefully, because the oscillation amplitudes help determine the attractive well depth. The DCS is available for many interactions, and should be used whenever possible. Nevertheless, it is insensitive to the outer bowl of the attractive well and, furthermore, cannot distinguish between potentials with shallower attractive wells offset by steeper repulsive walls.[9] The former sensitivity is provided only by low-temperature virial measurements, which however, are useful only if there is an independent measure of the attractive well depth. High-temperature virial measurements further complement the DCS in fixing the repulsive wall position, especially if independently supplemented by measurements of any one transport property.

Once the repulsive wall is fixed by a transport property and high- temperature interaction virial measurements, the DCS sensitively determines the weakly repulsive wall and the attractive well around its minimum. The DCS is necessary, because interatomic potentials obtained by fitting transport and virial measurements alone could have incorrect attractive well shapes or depths. This would arise even using a variety of transport properties, as their sensitivities to the interatomic potential are quite similar. The only exception is thermal diffusion, which however, has been difficult to measure to the requisite accuracy.[7,16] Viscosity will be the most useful of the three remaining transport properties until diffusions can be measured consistently and accurately over a wide range of temperatures.[7] Low temperature virials then determine the outer bowl of the attractive well.

As all of the foregoing influences are correlated, the DCS (and ICS, if available), mixture viscosity, and interaction second virial coefficient should be fit simultaneously. The multiproperty fits should be performed with realistic potential energy parameterizations (ref. 16 and see, for example, ref. 23) so that only a few of their parameters need to be adjusted to the data. Otherwise, the correlations just referred to may render best-fit procedures difficult to converge. This procedure should yield reliable interatomic potential energy curves, especially since these data also provide significant redundancy.[2,7]

Acknowledgements

We wish to thank Margaret Yu for assistance with some of the potential modifications. This research was supported by grants from the Natural Sciences and Engineering Research Council of Canada. Acknowledgement is also made to the donors of The Petroleum Research Fund, administered by the American Chemical Society, for partial support of this research.

References

1. C.H. Chen, P.E. Siska, and Y.T. Lee, J. Chem. Phys. **59**, 601 (1973).
2. R.T Pack, J.J. Valentini, C.H. Becker, R.J. Buss, and Y.T. Lee, J. Chem. Phys. **77**, 5475 (1982).
3. J.M. Hutson and B.J. Howard, Mol. Phys. **43**, 493 (1981).
4. M. Keil and G.A. Parker, J. Chem. Phys. **82**, 1947 (1985).
5. R.A. Aziz, P.W. Riley, U. Buck, G. Maneke, J. Schleusener, G. Scoles, and U. Valbusa, J. Chem. Phys. **71**, 2637 (1979).
6. L. Beneventi, P. Casavecchia, and G.G. Volpi, J. Chem. Phys. **84**, 4828 (1986).
7. L.J. Danielson and M. Keil, J. Chem. Phys. **88**, 851 (1988).
8. J.H. Dymond and B.J. Alder, J. Chem. Phys. **51**, 309 (1969).
9. D. Bassi, M.G. Dondi, F. Tommasini, F. Torello, and U. Valbusa, Phys. Rev. A **13**, 583 (1976).
10. M. Keil and A. Kuppermann, J. Chem. Phys. **69**, 3917 (1978).
11. K.M. Smith, A.M. Rulis, G. Scoles, R.A. Aziz, and V. Nain, J. Chem. Phys. **67**, 152 (1977).
12. M. Faubel, Adv. At. Mol. Phys. **19**, 345 (1983).
13. R. Guzman and H. Rabitz, J. Chem. Phys. **86**, 1395 (1987).
14. R.B. Gerber, M. Shapiro, U. Buck, and J. Schleusener, Phys. Rev. Lett. **41**, 236 (1978).
15. R.S. Grace, D.L. Johnson, and J.G. Skofronick, J. Chem. Phys. **67**, 2443 (1977).
16. G.C. Maitland, M. Rigby, E.B. Smith, and W.A. Wakeham (Editors). *Intermolecular Forces: Their Origin and Determination*. Clarendon, Oxford. 1981.

17. (a) E.A. Mason, J. Chem. Phys. **27**, 75 (1957); (b) E.A. Mason, J. Chem. Phys. **22**, 169 (1954).

18. (a) M.E. Boyd, S.Y. Larsen, and J.E. Kilpatrick, J. Chem. Phys. **50**, 4034 (1969); (b) T. Kihara, Y. Midzuno, and T. Schizume, J. Phys. Soc. Japan **11**, 249 (1955).

19. J.P. Toennies, W. Welz, and G. Wolf, J. Chem. Phys. **71**, 614, (1979).

20. F. Pirani and F. Vecchiocattivi, J. Chem. Phys. **66**, 372 (1977).

21. (a) D.W. Gough, G.P. Matthews, and E.B. Smith, J. Chem. Soc. Farad. Trans. **I 72**, 645 (1976); (b) G.C. Maitland and E.B. Smith, J. Chem. Soc. Farad. Trans. **I 70**, 1191 (1974); (c) A.S. Kalelkar and J. Kestin, J. Chem. Phys. **52**, 4248 (1970); (d) J. Kestin, H.E. Khalifa, and W.A. Wakeham, Physica **90A**, 215 (1978).

22. G.C. Maitland and W.A. Wakeham, Molec. Phys. **35**, 1443 (1978).

23. See for example, R.A. Aziz, in M. Klein (Editor). *Inert Gases: Springer Series in Chemical Physics*, Vol. **34**. Springer, Berlin. 1984.

CHAPTER 5

Damping of Total Differential Cross Sections: Observations and Empirical Anisotropic Potentials for HeC_2H_2 and HeOCS†

5.1. INTRODUCTION

Molecular beam experiments currently provide the most direct and detailed information for studying atom-molecule van der Waals interactions.[1-6] Molecular beam electric resonance techniques are used to characterize van der Waals complexes whose molecular partners possess permanent dipole[7,8] or quadrupole[9,10] moments. These experiments yield spectroscopic precision for bound states of van der Waals molecules in the region of their equilibrium configurations. Beam scattering techniques yield information for broad ranges of potential energy surfaces beyond their absolute minima. The most detailed beam scattering data are provided by rotationally inelastic state-to-state measurements,[11-13] or by DCS measurements of incompletely resolved rotational inelasticities.[14] Total DCS measurements, which do not resolve rotationally inelastic scattering from elastic scattering, can also be used to extract qualitatively correct potential energy surfaces.[15-17] All of these studies have been complemented by less detailed data for dilute gas properties which have proven useful for multiproperty empirical fits.[15-18]

For systems with small reduced masses, molecular anisotropy appears as damping of the quantum mechanical diffractive oscillations. This has been attributed primarily to anisotropy in the position of the potential minimum and the repulsive wall1.[9] For diatomic molecules interacting with H or He atoms, damping of the diffractive oscillations is barely noticeable.[13,20,21] For polyatomic molecules, experimentally observed damping has either been rather small,[15,21–23] or it has been severe for all scattering angles.[14,16,21] Moderate damping, and any angular dependence of that damping, has not been commonly observed or extensively studied.

---

† A version of this chapter has been published. L.J. Danielson, K.M. McLeod and M. Keil, J. Chem. Phys. 87, 239 (1987).

This work presents total DCS measurements for the $HeOCS$ and HeC_2H_2 systems, which have not been measured before, and which exhibit severe and moderate damping of the diffractive oscillations, respectively. We also measured the $HeCO_2$ DCS, which shows severe damping much like $HeOCS$. All of these systems involve interactions between closed-shell atoms and linear molecules, rendering the theoretical interpretation relatively straightforward within the infinite-order-sudden approximation (IOSA).[16(b),24]

The $HeOCS$ interaction is of astrophysical interest[25] and, judging from the $HeCO_2$ interaction,[14(a),16] is expected to be highly anisotropic. In addition, comparisons of experiment to theory have often been frustrated by the inadequacy of available $HeOCS$ interaction potentials.[25(a),25(b),25(e)] The extent to which total DCS data can be used in extracting intermolecular potentials asymmetric about the molecular centre-of-mass can also be tested with the $HeOCS$ system.

The HeC_2H_2 interaction was also expected to be highly anisotropic, based on the C_2H_2 molecular length. Although damping of the large-angle oscillations is observed to be severe, the low-angle scattering data retains pronounced oscillatory structure. This manner of intermediate damping could be predicted qualitatively using classical mechanics arguments, despite the highly quantum mechanical nature of the DCS oscillatory structure.[26] The damping observed for HeC_2H_2 presents a particular challenge for extracting potential energy surfaces that can reproduce the data, and might show very interesting behaviour for rotationally inelastic DCS measurements. The HeC_2H_2 potential energy surface may also have application to the production and structure of $(C_2H_2)_2$ molecules important in studies of intramolecular vibrational energy relaxation.[27]

In Sec. 5.2 of this paper, we briefly describe the experimental apparatus newly constructed at Alberta, and used to measure the HeC_2H_2 and HeOCS scattering data. Also in Sec. 5.2, we discuss utilization of a HeAr DCS measured exclusively for apparatus calibration.[28] The scattering calculations used to reproduce DCS data from assumed intermolecular potentials are discussed in Sec. 5.3. In Sec. 5.4, we present the scattering results and the HeC_2H_2 and HeOCS intermolecular potential energy surfaces extracted from them. We also demonstrate that the present $HeCO_2$ total DCS complements partially resolved inelastic DCS measurements reported recently.[14(a)] Finally, we summarize our results in Sec. 5.5.

5.2. EXPERIMENTAL

5.2.A. Apparatus

The experiments were performed using a crossed molecular beam apparatus newly constructed at the University of Alberta and shown schematically in Figure 5.1. The principal features are two supersonic beam sources, a rotatable liquid helium-cooled bolometer detector, and a non-rotatable quadrupole mass spectrometer. Each beam source consists of a nozzle-skimmer (Nz-Sk) arrangement in separately pumped chambers. Further collimation of each beam occurs in the scattering chamber at C_1 and C_2 respectively, with no intervening stage of pumping. The secondary (molecular) beam nozzle may be heated to inhibit dimerization in the molecular beam. Helium atoms scattered out of the primary beam by the modulated secondary beam are detected by the bolometer (Bolo). This detector is rotated in the plane of the molecular beams about the beam intersection region to measure the DCS.

The beams were optimized using a quadrupole mass spectrometer (EAI 200) in conjunction with a time-of-flight slotted-disc chopper. Beam operating conditions are summarized in Table 5-1. For each of the molecular beams, we maximized the intensity and simultaneously minimized the velocity spread, while maintaining a very low dimer/monomer signal ratio on the mass spectrometer ($\lesssim 10^{-4}$).[29] For the Ar secondary beam, inlet pressures above 0.6 atm or nozzle diameters smaller than 0.25 mm promoted dimer and trimer formation, observed directly on the mass spectrum and indirectly as broadening of the monomer velocity distribution.[14(b)] For this beam, the dimer/monomer signal ratio was $\sim 10^{-3}$. For the CO_2 and OCS beams, dimer/monomer ratios of $\lesssim 10^{-4}$ could be attained only by heating the nozzle to 290 and 150°C respectively. Typical pressures in the source chambers were 1×10^{-3} torr for the He primary beam and $\sim 3 \times 10^{-4}$ torr

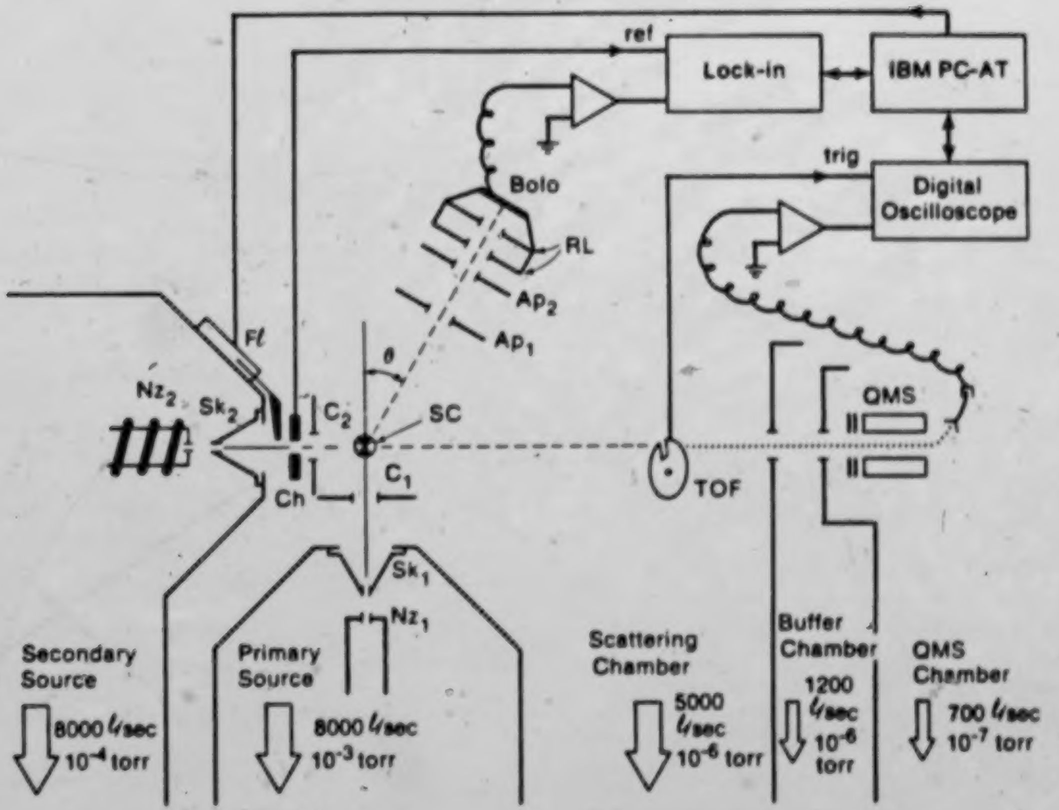
ref
Lock-in
IBM PC-AT
trig
Bolo
Digital Oscilloscope
RL
Ap2
Ap1
Fℓ
θ
Nz2
Sk2
C2
SC
QMS
C1
Ch
TOF
Sk1
Nz1
Secondary Source
8000 ℓ/sec
10-4 torr
Primary Source
8000 ℓ/sec
10-3 torr
Scattering Chamber
5000 ℓ/sec
10-6 torr
Buffer Chamber
1200 ℓ/sec
10-6 torr
QMS Chamber
700 ℓ/sec
10-7 torr

Figure 5.1

Schematic diagram of the Alberta crossed beam scattering apparatus (not to scale). The beams originate from nozzles Nz, are skimmed at Sk, collimated at C, and intersect at the scattering center SC. The rotatable bolometer detector Bolo views SC through beam apertures Ap and radiation-limiting apertures RL for laboratory scattering angle θ. The secondary beam is chopped at Ch for synchronous lock-in detection and flagged at Fℓ for background correction. A time-of-flight chopper TOF, in conjunction with the mass spectrometer QMS, is used for beam characterizations only.

Table 5-1. Beam Operating Conditions

	Primary Beam	Secondary Beams			
Gas	He	Ar	C_2H_2	CO_2	OCS
Temperature (K)	303	303	303	562	418
Nozzle diameter (mm)[a]	0.050	0.30	0.30	0.30	0.30
Flow (atm.cm^3/sec)[a]	13.0	8.3	4.1	5.8	2.5
Nozzle-skimmer distance (mm)[a]	9.5	15	11	13	13
Skimmer diameter (mm)	0.53	0.50	0.50	0.50	0.50
Nozzle pressure (atm)[b]	14.9	0.57	0.28	0.62	0.30
Most probable velocity (m/sec)[b,c]	1775	562	915	890	682
Velocity FWHM ($\Delta v/v_{mp}$)	0.04	0.072	0.217	0.180	0.177
Collimator diameter (mm)	0.79	0.97	0.97	0.97	0.97
Nozzle-to-scattering center (mm)	57.7	63.2	59.2	61.2	61.2
Angular divergence (deg)[d]	1.0	1.2	1.3	1.2	1.2
Attenuation of He beam (%)[b]	—	0.25	0.03	0.05	0.05

[a] Optimized.

[b] Measured.

[c] Corrected for ion flight times (Ref. 30) and for an instrumental response time of about 10 μs. For the He beam, this instrumental response artifically broadened the measured velocity FWHM, which was obtained instead from Ref. 55 using our nozzle conditions. Substitution of the experimentally measured FWHM of 0.062 or the value of 0.04 (actually used) did not affect the scattering calculations significantly (see Sec. 5.3.B).

[d] Calculated.

for the secondary beams. With both beams on, the scattering chamber pressure was $\sim 2 \times 10^{-6}$ torr.

The mass spectrometer detector is not rotatable, but may be positioned directly opposite either beam source. The beam enters the electron-impact ionizer (Extrel 041-1) after interruption by a 4-blade chopper, two blades of which have narrow slots. This chopper may be used simultaneously for modulation and velocity distribution measurements. The time-of-flight data is corrected for ion flight times,[30] chopper errors and detector response. The resulting velocities have a measured accuracy of $\sim 0.5\%$.

Scattered He atoms were detected with a commercial (Infrared Laboratories) composite Ge bolometer operated at 1.5 K by pumping on a liquid helium dewar. The detector is a 3 mm wide × 9 mm high sapphire heat absorber, to which the Ge bolometer is attached. The specified noise-equivalent power is $\sim 10^{-14}$ W$/\sqrt{Hz}$. The bolometer detector's view of the scattering chamber is restricted by two scattered-beam apertures (Ap_1 and Ap_2 in Fig. 5.1). These apertures are attached to a liquid nitrogen-cooled radiation shield surrounding the pumped liquid helium dewar. They are located 33.4 mm and 66.7 mm from the beam intersection region and have diameters of 0.64 mm and 0.67 mm respectively.

The bolometer aperture diameters are chosen so that the detector may view the entire beam intersection region. The size of the scattering volume is dictated by the beam collimators (C_1 and C_2 in Fig. 5.1) and by the nozzle-skimmer distances (Table 5-1). It ranges from $\sim 1.04 \times 1.04 \times 1.28$ mm for the HeAr experiment, to $\sim 1.04 \times 1.04 \times 1.32$ mm for the HeC_2H_2 experiment, with the longer dimension along the direction of the primary beam. The detector viewing cone is calculated to have a diameter of 1.95 mm at the scattering center, ensuring that the bolometer detector views the entire scattering volume regardless of the scattering angle. The bolometer detector has two additional apertures (RL in Fig. 5.1) that are maintained at the 1.5 K operating temperature to reduce the thermal radiation load. They are large enough that all He atoms passing through apertures Ap_1 and Ap_2 impinge on the sapphire heat absorber.

The overall angular resolution of the apparatus may be estimated by considering the maximum possible deflection angle that a He atom may suffer and still be detected when the bolometer is positioned directly opposite the He beam. Taking the He nozzle as a point source, this angle is calculated to be 1.25°, serving as a useful starting point for obtaining the overall effective apparatus angular resolution (see Sec. 5.3.A).

A more complete description of the apparatus will be presented in a forthcoming publication.[31]

5.2.B. Data Acquisition

DCS scattering data were obtained by measuring the bolometer signal synchronous with a tuning fork chopper (Ch in Fig. 5.1) used to modulate the secondary beam at 25.9 Hz. The bolometer signal was dc amplified (Infrared Laboratories LN-6) and then detected by a lock-in amplifier (Stanford Research SR 510) controlled by a microcomputer (IBM PC-AT). The computer integrated the signal for 10 to 100 seconds and then closed the secondary beam flag ($F\ell$ in Fig. 5.1), repeating the measurement for the background signal. The "flag:off" signal subtracted from the "flag:on" signal was taken to be proportional to the intensity[32] of He atoms scattered by the crossed beam. This difference signal was measured four times, and then averaged, for each laboratory scattering angle. The averaged data were time-normalized to the scattered signal at a periodically measured reference angle of 5°, to account for long-term drifts (primarily in detector sensitivity). The entire DCS was measured three or four times to improve the signal-to-noise ratio and to establish the statistical uncertainty of the measurements. Total integration times ranged from 5 minutes for measurements at the lowest scattering angles to ~ 1 hour for the highest angles.

Spurious signals generated by the bolometer's sensitivity to thermal infrared radiation were suppressed by carefully masking the tuning fork chopper from the scattering center. No modulated signal could be detected with either of the beam gas flows turned off. During a scattering experiment, typical "flag:off" (background) signals were $\tilde{<}$ 10% of the corresponding "flag:on" signal at all scattering angles. This low background signal could be attained only by modulating the secondary beam. The 5° reference signal seldom varied by more than 5% within a given day's experimentation, or by more than 10% between days.

Scattered He beam signals were measured for angles between $-14°$ and $+20°$ using a computer-controlled stepping motor with a precision of 0.010°. Data for $\theta_{lab} < 0°$ was used to establish the zero position of the angular scattering scale, after accounting for the appropriate angle and intensity transformations. The true scattering zeroline correction, determined to within ±0.02°, was then used to shift the angular scale of the measured data. The error in the zeroline was convoluted with the statistical measurement uncertainty at each angle to give the appropriate overall error bars for each data point. Our experimental DCS measurements are presented in Figure 5.2 for HeAr, HeC_2H_2, $HeCO_2$ and HeOCS.

For laboratory scattering angles below about 3.5°, the bolometer began to be heated by the wing of the intense He primary beam. This degraded the bolometer response and resulted in non-linear behaviour below this angle on either side of the He beam. Consequently, we have reported scattering data no closer than 4° to the scattering zeroline.

Using a bolometer detector, one must be careful to avoid detection of particles other than the ones of interest (He in the present case). This arises

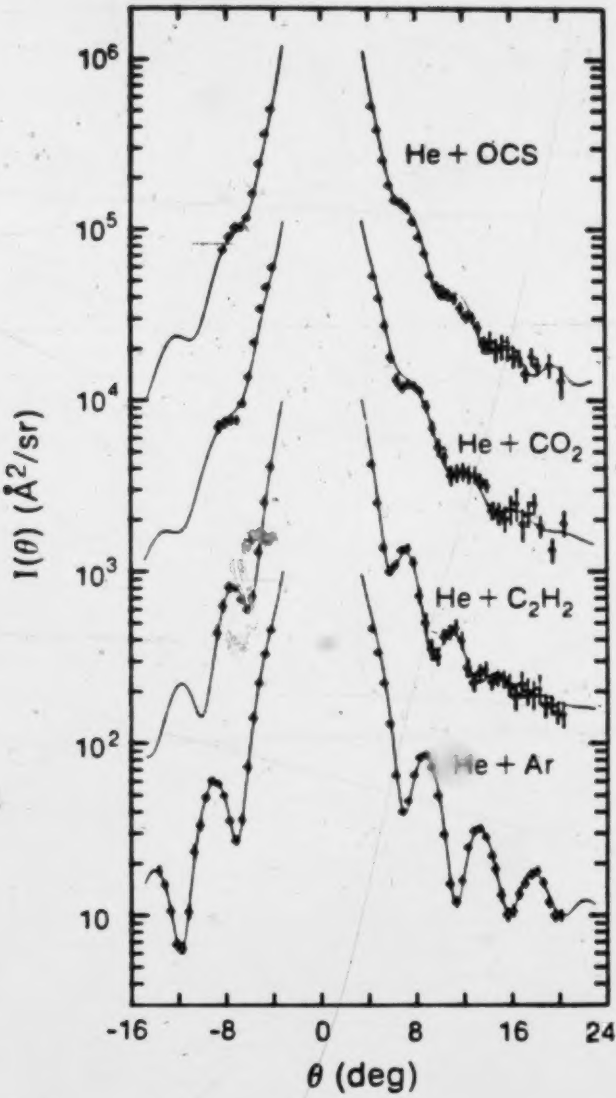

Figure 5.2

Measured total differential cross section scattering data for HeAr, HeC_2H_2, $HeCO_2$ and HeOCS. The ordinate scale in Å^2/sr is generated in calculating the DCS, and should be multiplied by 1 for HeAr, 0.1 for HeC_2H_2, 0.01 for $HeCO_2$ and 0.001 for HeOCS. The vertical height of the error bars portray the signal measurement error convoluted with the angular scale uncertainty of ±0.02° (the horizontal ticks exaggerate this error by a factor of 25). The solid curves are calculated from best-fit HFD anisotropic potentials for HeC_2H_2 and HeOCS, from the Aziz et al. potential for HeAr (Ref.28), and from a modified ESMMSV potential for $HeCO_2$ [14(a) and 16(b)]. The HeAr DCS was used for instrument calibration only, not for adjusting its interatomic potential.

from the bolometer functioning as an energy flux detector, with no direct ability to distinguish the source of that energy flux. Therefore, the range of scattering angles accessible in these experiments are restricted kinematically to $\theta_{lab} \leq +50°$ for all systems studied here. Beyond that angle, the secondary beam could be scattered into the detector, systematically raising the measured signal. This error would appear independently of which beam had been modulated.

5.3. ANALYSIS

5.3.A. Scattering Calculations

For a given intermolecular potential, the DCS is calculated directly in the center-of-mass reference frame using the partial wave expansion[33] and the infinite-order sudden approximation[24] (IOSA). It is then transformed to the laboratory reference frame using a number of Newton diagrams, chosen to reflect the beam velocity and angular spreads. This transformation also accounts for the bolometer detector's enhanced sensitivity to scattered He atoms whose laboratory-frame velocity has increased for $\theta > 0°$, and its correspondingly decreased sensitivity for $\theta < 0°$.[32] The laboratory-frame DCS's are then averaged over the Newton diagrams, and further averaged over the overall apparatus angular resolution. The latter quantity is determined by comparing our measured HeAr data to that calculated from a reliable HeAr interatomic potential.[28] This calibration results in an overall effective apparatus angular resolution of 1.66°, including the detector resolution convoluted with the primary beam angular spread (see Sec. 5.2.A).

The highly oscillatory structure of the HeAr DCS, and the high precision with which it is measured,[28(a)] necessitate an exact solution of the Schrödinger equation for the small angular momentum partial wave phase shifts. A Numerov propagator step size of ~ 0.01 Å gives the requisite accuracy with $\ell \lesssim 45$. The WKB approximation gives sufficiently accurate phase shifts with $\ell \gtrsim 45$ for HeAr, and for all of the HeC_2H_2, $HeCO_2$ and HeOCS phase shifts.

The transformation and averaging procedure for HeAr requires explicit DCS calculations for six collision energies and uses 16 Newton diagrams. For HeC_2H_2, $HeCO_2$ and HeOCS, 144 Newton diagrams are required to accommodate the broader velocity spreads of the molecular scattering partners (Table 5-1). For these molecular systems, four collision energies were sufficient for explicitly calculating the DCS in the center-of-mass frame.

The infinite-order sudden approximation (IOSA) allows straightforward calculation of DCS's that do not resolve elastic from rotationally inelastic scattering. This procedure has proven to be valid for He + molecule systems using room temperature beams.[15(b)–17,34] Furthermore our supersonic molecular beams are likely to be quite cold internally (see Table 5-1), so that adjacent molecular rotational levels will be nearly degenerate as required for IOSA validity. The anisotropic IOSA integration was converged using six potential angles for HeC_2H_2 and eight for $HeCO_2$ and HeOCS, of which half are obtained by symmetry in each case (see Sec. 5.4.B).

Potential parameters are fitted by an automated non-linear least-squares fitting algorithm.[35] It is convenient to define a dimensionless fitting quality parameter δ as[36]

$$\delta = \frac{1}{n}\left[\sum_{i=1}^{n}\left(\frac{I_i^{calc} - I_i^{exp}}{\Delta I_i^{exp}}\right)^2\right]^{1/2}, \qquad (5-1)$$

where I_i^{calc} is the calculated DCS at angle i, I_i^{exp} is the corresponding measured DCS and ΔI_i^{exp} is its error (one standard deviation). This fitting quality parameter is independent of any arbitrary DCS normalization, and properly weights each data point according to its error bar. Resulting values for δ lower than unity correspond, on average, to fitting all the data within their respective error bars.

5.3.B. Intermolecular Potentials

The HeAr results were analyzed using the HFD potential of Aziz et al.[28] without modification. For the $HeCO_2$ results, we wanted our analysis to be consistent with that of Buck et al.[14(a)] in modifying the ESMMSV potential of Keil and Parker.[16(b)] All their ESMMSV parameters were retained except for the radial anisotropy parameters, $r_{m,2}$, which was fitted to the data in the above least-squares sense.

The HeC_2H_2 and HeOCS results were analyzed using an anisotropic modification to the Hartree-Fock plus damped dispersion (HFD) potential form.[21,28] For isotropic interactions, the HFD potential has the following formulation[21]:

$$\begin{aligned} V_{HFD}(r) &= V_{HF}(r) + F(r)V_D(r) , \\ V_{HF}(r) &= A\exp(-\alpha r) , \\ F(r) &= \exp\left[-\left(Dr_m r^{-1} - 1\right)^2\right] , \quad r \leq Dr_m , \\ F(r) &= 1 , \quad r \geq Dr_m , \\ V_D(r) &= -C_6 r^{-6} - C_8 r^{-8} - C_{10} r^{-10} , \end{aligned} \qquad (5-2)$$

For fitting this potential form to our measured total DCS's, we regarded only r_m and α as adjustable parameters. The damping parameter D was held fixed at 1.28.[21,28] Requiring the potential minimum position to occur at r_m then sets A in terms of α and r_m:

$$A = \alpha^{-1}\exp(\alpha r_m)\left[F'(r_m)V_D(r_m) + F(r_m)V'_D(r_m)\right] , \qquad (5-3)$$

and then the well depth ϵ may be calculated also:

$$\epsilon = -\left[V_{HF}(r_m) + F(r_m)V_D(r_m)\right] . \qquad (5-4)$$

Molecular anisotropy is introduced into the potential by expanding some of the potential parameters in Legendre series[15–17,19,21]:

$$r_m = r_m(\gamma) = r_{m,0} + r_{m,2}P_2(\cos\gamma) , \qquad (5-5)$$

$$C_6 = C_6(\gamma) = C_{6,0} + C_{6,2}P_2(\cos\gamma) , \qquad (5-6)$$

$$C_8 = C_8(\gamma) = C_{8,0} + C_{8,2}P_2(\cos\gamma) + C_{8,4}P_4(\cos\gamma) , \qquad (5-7)$$

$$C_{10} = C_{10}(\gamma) = C_{10,0} + C_{10,2}P_2(\cos\gamma) + C_{10,4}P_4(\cos\gamma) , \qquad (5-8)$$

For the r_m parameter expansion [Eq.(5-5)], we found it more convenient to least-squares optimize the r_m values parallel and perpendicular to the molecular axis (i.e., $r_m^{\parallel}$ and $r_m^{\perp}$), along with the α parameter. The Legendre expansion coefficients $r_{m,0}$ and $r_{m,2}$ are easily calculated from the $r_m^{\parallel}$ and $r_m^{\perp}$ fitted parameters. Replacement of r_m in Eq.(5-2) by $r_{m,0}$ yields the spherical limit (as distinct from the spherical average) of the HFD potential, which can be useful in reproducing gas transport and virial data.[15–17,24] Note that the A and ϵ values are anisotropic only because of the r_m and C_n anisotropies in Eqns.(5-3)–(5-8).

The HFD potential form requires evaluation of van der Waals coefficients at least to C_8.[37] Fortunately however, the accuracy of these coefficients is not crucial when using the HFD potential form for fitting to measured cross sections.[21] Therefore, we have calculated or estimated the long range coefficients rather than fitting them to the scattering data. For HeC_2H_2, we calculated the $C_{6,0}$ coefficient by applying the geometric combination rule[38] to literature values for C_2H_2-C_2H_2[39] and He-He.[28(b)] For HeOCS, we calculated $C_{6,0}$ by summing the semiempirical oscillator strengths given by Meath and coworkers for OCS[40] and He.[41] The $C_{6,2}$ coefficient for HeOCS was then estimated from the $C_{6,2}/C_{6,0}$ ratio appropriate for this system,[3,42] including the induction terms. The $C_{6,2}$ coefficient for HeC_2H_2 and all of the C_8 coefficients were estimated from the relations given by Pack.[43] The C_{10} coefficients were estimated by applying the recursion rule given by Scoles et al.[38] for three atom-molecule orientation angles and then fitting the results to a Legendre polynomial [Eqn (5-8)]. Data for the van der Waals calculations were taken from several sources.[25(c),25(e),39–42,44–46]

5.4. RESULTS AND DISCUSSION

5.4.A. Data Reliability and Sensitivity

The DCS for HeAr scattering was measured to establish the apparatus' capability of producing accurate scattering data, and is shown in Fig. 5.2. We used the HFD potential of Aziz et al.,[28] without modification, to compare the calculated DCS to the experimental one. This comparison also served to check our true scattering zeroline correction (consistent with the value found in Sec. 5.2.B. to within ±0.005°), and to determine the *effective* overall apparatus angular resolution as outlined in Sec. 5.3.A. Finally, the HeAr DCS provides a completely spherical system to which the He + molecule results may be compared, for approximately the same reduced mass and collision energy. Those DCS measurements are also presented in Fig. 5.2.

Both Fig. 5.2 and Table 5-2 show that our measured HeAr results correspond excellently with those calculated from the Aziz et al.[28] potential. This establishes the reliability of the apparatus and the accuracy of the results obtained.

The DCS for $HeCO_2$ scattering was measured to establish the sensitivity of the present damped total DCS data to the intermolecular anisotropy, and also to demonstrate the compatibility of these data with the more detailed results published recently for this system.[14(a)] By measuring incompletely resolved rotationally inelastic DCS's for $HeCO_2$, Buck et al. showed that the empirical anisotropic potential of Keil and Parker[16(b)] provided an inadequate description of their data. Nevertheless, Buck et al. were able to obtain satisfactory agreement with their data by manually adjusting the $r_{m,2}$ radial anisotropy parameter of the semi-empirical ESMMSV potential, while keeping all of the other parameters fixed. When we perform the same procedure with the present $HeCO_2$ total DCS, we obtain the same $r_{m,2}$ parameter (1.09 Å) as did Buck et al. (1.13 Å) to

Table 5-2. Intermolecular Potential Parameters

	Fitted parameters	Derived values for the potential minimum[a]	van der Waals coefficients[b]	Fitting quality δ^c
HeAr HFD[d]	none	none	—	0.97
$HeCO_2$ ESMMSV[e]	$r_{m,2} = 1.089$ Å	—	—	1.45
$He+C_2H_2$ HFD				
Anisotropic[f]	$r_m^{\parallel} = 4.352$ Å	$\epsilon^{\parallel} = 1.99$ meV	$C_{6,0} = 10.99$ eV Å^6	0.82
	$r_m^{\perp} = 3.708$ Å	$\epsilon^{\perp} = 2.69$ meV	$C_{6,2} = 2.46$ eV Å^6	
	$\alpha = 3.98$ Å^{-1}	$r_{m,0} = 3.923$ Å	$C_{8,0} = 54.2$ eV Å^8	
		$r_{m,2} = 0.430$ Å	$C_{8,2} = 56.0$ eV Å^8	
		$\epsilon_0 = 2.46$ meV	$C_{8,4} = 9.1$ eV Å^8	
		$\epsilon_2 = -0.47$ meV	$C_{10,0} = 423$ eV Å^{10}	
			$C_{10,2} = 732$ eV Å^{10}	
			$C_{10,4} = 142$ eV Å^{10}	
$He+C_2H_2$ HFD				
Spherical Limit[g]	$r_{m,0} = 3.916$ Å	$\epsilon = 2.60$ meV	$C_{6,0} = 10.99$ eV Å^6	1.20
	$\alpha = 4.16$ Å^{-1}		$C_{8,0} = 54.2$ eV Å^8	
			$C_{10,0} = 423$ eV Å^{10}	
He+OCS HFD				
Anisotropic[f]	$r_m^{\parallel} = 4.784$ Å	$\epsilon = 1.67$ meV	$C_{6,0} = 13.71$ eV Å^6	1.16
	$r_m^{\perp} = 3.606$ Å	$\epsilon^{\perp} = 4.77$ meV	$C_{6,2} = 4.29$ eV Å^6	
	$\alpha = 6.55$ Å^{-1}	$r_{m,0} = 3.998$ Å	$C_{8,0} = 63.7$ eV Å^8	
		$r_{m,2} = 0.786$ Å	$C_{8,2} = 66.4$ eV Å^8	
		$\epsilon_0 = 3.74$ meV	$C_{8,4} = 13.1$ eV Å^8	
		$\epsilon_2 = -2.07$ meV	$C_{10,0} = 467$ eV Å^{10}	
			$C_{10,2} = 780$ eV Å^{10}	
			$C_{10,4} = 150$ eV Å^{10}	

[a] Calculated from the fitted $r_m^{\parallel}$, $r_m^{\perp}$ and α [Eqns. (5-3)-(5-5)] parameters: not fitted independently.

[b] Calculated and held fixed, as discussed in Sec. 5.3.B.

[c] See Eqn. (5-1).

[d] See Ref. 28 for potential parameters (not fitted to the present data).

[e] Using potential parameters from Ref. 16(b) without modification, except for $r_{m,2}$ which is modified using a procedure similar to that of Ref. 14(a).

[f] The ϵ anisotropy is determined poorly in fits to total DCS data (Refs. 16 and 18-21).

[g] Obtained by replacing $r_m(\gamma)$ by $r_{m,0}$ in Eqns. (5-2) and (5-5).

within the respective precision of the experiments. Consequently, it is clear that the present total DCS is sufficiently precise and highly resolved to be compatible with – and complementary to – the rotationally inelastic DCS data.[14(a)]

A more detailed analysis of the scattering data will be required to further improve the intermolecular potential [e.g., the residue of the first diffractive oscillation in Fig. 5.2, and the intensities of the rotational rainbow maxima in Figs. 7-8 of Ref. 14(a)]. Such an analysis should use the present $HeCO_2$ results, which supersede the total DCS data reported by one of us on an earlier apparatus.[16(a),47]

5.4.B. Diffraction Oscillations

The most striking feature of Fig. 5.2 is the clear progression of oscillatory structure damping from the Ar scattering partner through C_2H_2 (moderate) to CO_2 and OCS (strong). This trend is exhibited directly by the DCS data, without referring to the intermolecular potentials extracted from them. Also striking is the difference between the first two HeC_2H_2 oscillations (below $\sim 12°$) which are clearly resolved, and wider-angle oscillations which are completely damped. We emphasize that the instrumental resolution was identical for all four of the DCS measurements presented, and was independent of scattering angle (Sec. 5.2.A.).

Damping of diffraction oscillations is primarily caused by the molecular radial anisotropy, which is better determined than the well depth anisotropy for these low reduced mass systems.[15(b)–17,21] Such damping was predicted by Cross semiclassically,[26] and more recently, by Pack using IOSA quantum mechanical calculations.[19] Both of those studies showed roughly uniform damping for all the diffractive oscillations, independent of the scattering angle.

The observed angular dependence in the damping of our measured HeC_2H_2 oscillations suggests that different regions of the potential are responsible for damping different angular ranges of the DCS. From a classical mechanics point of view, wide-angle scattering is dominated by strong repulsion, while small-angle scattering samples weak repulsions and is more influenced by the attractive well. Since highly repulsive interactions are much more anisotropic than long-range interactions, the classical DCS would be influenced by anisotropy more for large scattering angles than for small, matching the HeC_2H_2 results qualitatively. Obviously however, this interpretation of anisotropy damping is useful only heuristically for a system as quantal as thermal-energy He atom scattering.

The $HeCO_2$ and HeOCS results are severely damped for all scattering angles, though even these systems show clear shoulders near 7 and 11°. We have yet to discover any diffractive system damped severely enough that even such vestiges of the low-angle oscillations are washed out.

5.4.C. Potential Energy Surfaces

Parameters of the anisotropic HFD potential form [Eqn. (5-2)] were fit to the HeC_2H_2 and HeOCS total DCS experimental data. Three adjustable parameters – $r_m^{\parallel}$, $r_m^{\perp}$, and α in Eqns. (5-2) and (5-5) – were optimized as outlined in Sec. 5.3.A. The experimental DCS's and the corresponding best-fit calculated results are shown in Fig. 5.2. The potential parameter values are collected in Table 5-2, along with the van der Waals coefficients (not varied), and the fitting quality parameter δ [Eqn. (5-1)]. Radial potential cuts along $\gamma = 0°$, $30°$, $60°$, and $90°$ atom-molecule orientation angles for the best-fit potentials are shown in Figs. 5.3 and 5.4. We also present contour plots of the HeC_2H_2 and HeOCS potential energy surfaces in Figs. 5.5 and 5.6, as calculated from the respective anisotropic HFD potentials. We emphasize that the well depth anisotropy portrayed does not result from a direct fit to the scattering data. Rather, it is a consequence of the physically reasonable HFD potential form and of the much greater sensitivity of

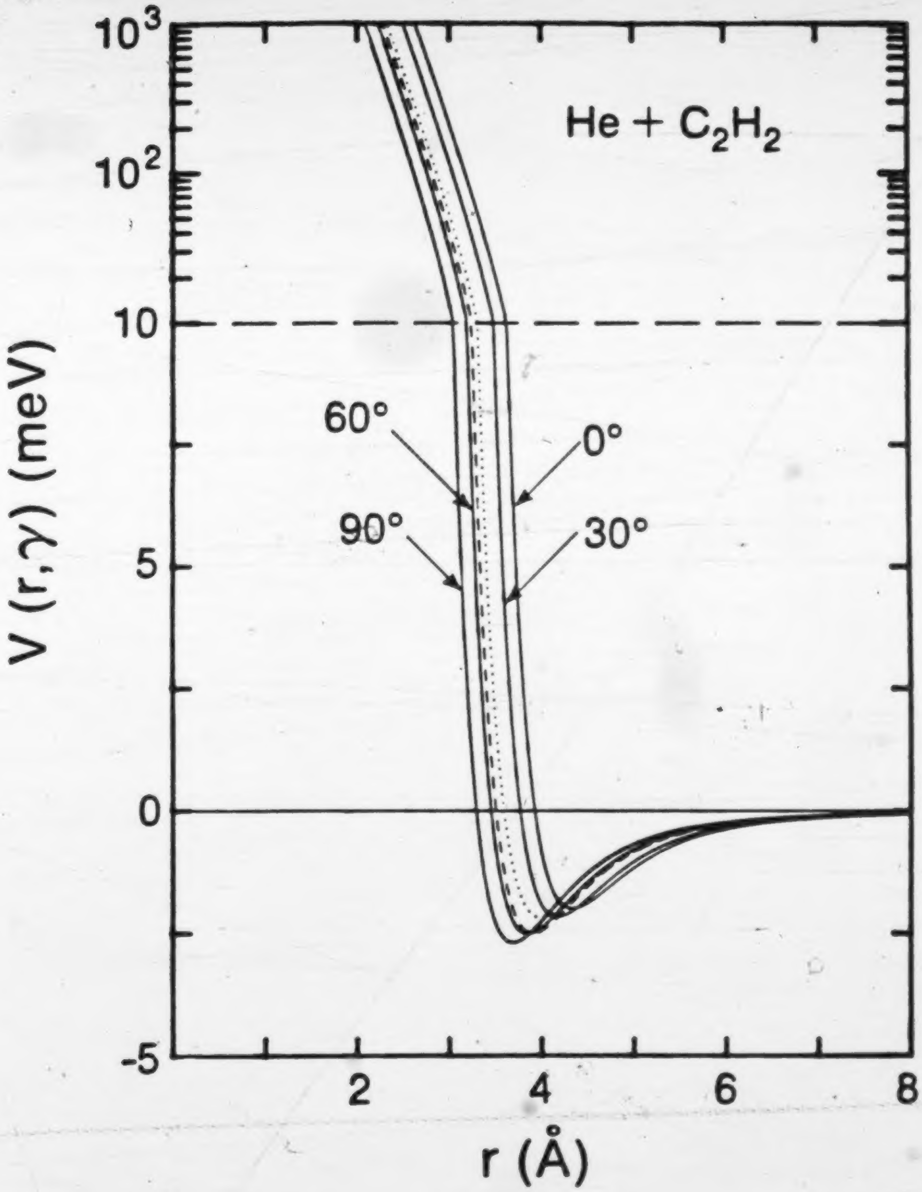

Figure 5.3

Radial cuts across the anisotropic HFD potential for HeC_2H_2, plotted parametrically as a function of the orientation angle γ (solid lines). The dashed line represents the spherical limit of the potential and the dotted line is the spherical average of the anisotropic potential. A plot of the best-fit HeC_2H_2 spherical limit potential (Table 5-2) would be indistinguishable from the dashed line.

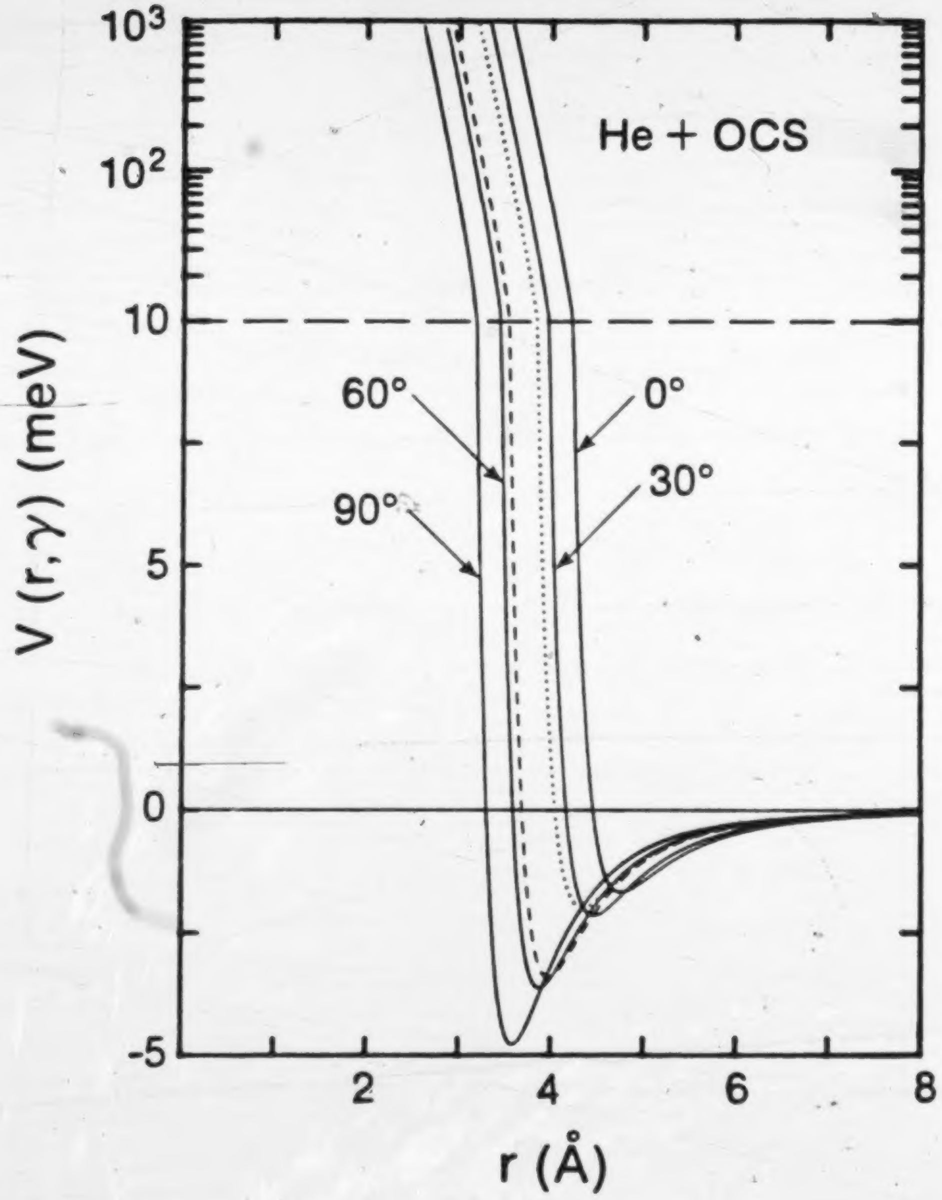

Figure 5.4

Radial cuts across the anisotropic HFD potential for HeOCS, plotted parametrically as a function of the orientation angle γ. Line types as in Figure 5.3.

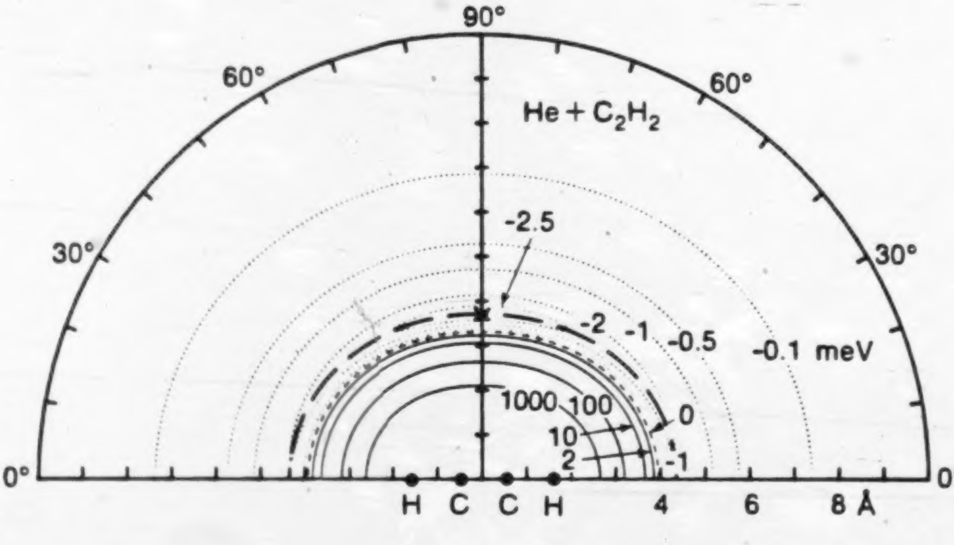

Figure 5.5

Potential energy contour plot of the HeC_2H_2 HFD intermolecular potential. Contours are given in units of meV up to $V(r,\gamma) = 1000$ meV. The polar coordinates are r in Å and γ in deg. Solid contours: $V(r,\gamma) > 0$; dashed contour: $V(r,\gamma) = 0$; dotted contours: $V(r,\gamma) < 0$. The long dashed line traces the angular dependence of the minimum position $r_m(\gamma)$. The absolute minimum on the surface is denoted by the heavy cross at $r = 3.708$ Å; $\gamma = 90°$, where $V(r,\gamma) = -2.69$ meV. The positions of the C and H atoms are also shown for reference.

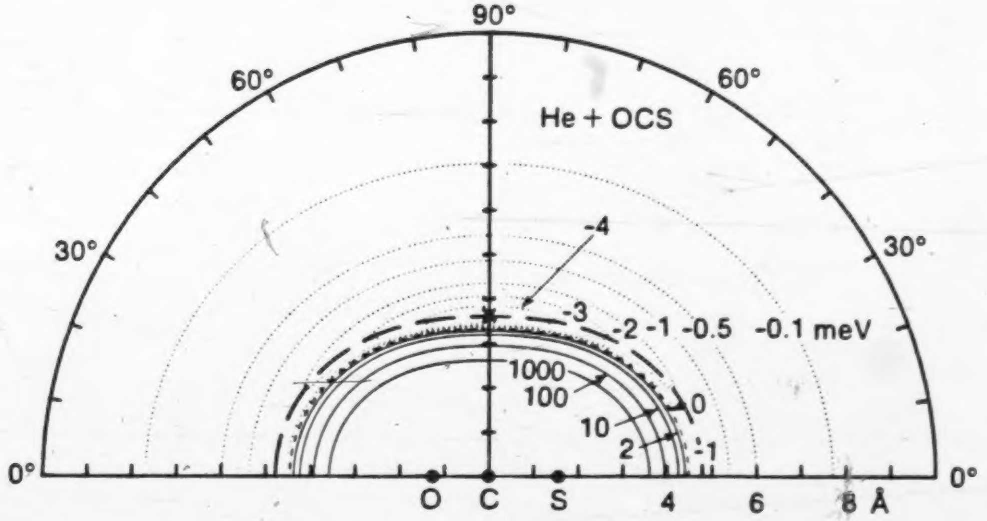

Figure 5.6

Potential energy contour plot of the HeOCS HFD intermolecular potential. Symbols as in Figure 5.5. The absolute minimum on the surface occurs for $r = 3.606$ Å; $\gamma = 90°$, where $V(r,\gamma) = -4.77$ meV. The positions of the O, C and S atoms are also shown for reference.

the total DCS data to the repulsive wall anisotropy,[16,17,19] and thereby to the $r_m^{\parallel}$ and $r_m^{\perp}$ fitted parameters.

For the HeC_2H_2 results, the pronounced oscillatory structure for the lower scattering angles induced us to try fitting the results using a "spherical limit" HFD potential form. In this case, only two potential parameters – $r_{m,0}$ and α of Eqns. (5-2) and (5-5) – were fit to the data. The resulting parameter values appear in Table 5-2 along with the fitting quality parameter δ. The anisotropic HFD potential gives a better fit to the DCS data than does the spherical limit potential, while the $r_{m,0}$ fitted parameter, and the well depths, are quite similar for these two potentials (Table 5-2). This point will be discussed further.

The intermolecular potentials displayed in Figs. 5.3-5.6 have an associated range of validity. The present total DCS data by themselves are known not to be sensitive to strongly repulsive interactions (above roughly 20 meV) nor to long-range interactions (beyond roughly 7 Å).[6(a),48] Nevertheless, the physically reasonable nature of the HFD potential form (for example only 3 parameters are required for good fits to the data) suggests that the potentials displayed in Figs. 5.3-5.6 ought to provide reasonable descriptions of the molecular anisotropies for modest extrapolations beyond this validity range. The potential energy surfaces for both the HeC_2H_2 and HeOCS systems would be improved by multi-property fits, especially if supplemented by high- quality SCF calculations and by accurate van der Waals coefficients.[15(b),16,49,50] Such an undertaking awaits the availability of such calculations and/or additional experimental results.

The present data are most sensitive to the potential minimum position and the weakly repulsive wall, and their anisotropies, having much less sensitivity to the well depth and its anisotropy.[16,17,19] As Figs. 5.3-5.6 show, the HeOCS interaction has a much larger radial anisotropy than does the HeC_2H_2 interaction.

In terms of minimum positions, the HeOCS parallel interaction is 33% longer than the perpendicular one, while it is only 17% longer for HeC_2H_2. At 20 meV on the repulsive wall, corresponding elongations are 33% for HeOCS and only 19% for HeC_2H_2. These observations make it clear that models based on van der Waals radii[51] must be regarded cautiously,[52] since the van der Waals outline of C_2H_2 is longer and narrower than either CO_2 or OCS.

Two qualitative possibilities for the relatively weak anisotropy of the HeC_2H_2 interaction can be proposed. Firstly, the C≡C triple bond concentrates the electron density about the C atoms, perhaps increasing the overall effective molecular sphericity as probed by a He atom. Secondly, the terminal H atoms of the C_2H_2 molecule may not extend the molecular length as much as heavier atoms, nor as much as their van der Waals radii would suggest. It is interesting to note that the radial anisotropy for HeC_2H_2 appears to be significantly less than that obtained for an empirical $H + C_2H_2$ intermolecular potential.[21] This may be due to greater interaction of the single H-atom electron with the C_2H_2 π electrons in the perpendicular approach to the molecule. These points will be investigated in future work.

The contour plots (Figs. 5.5 and 5.6) and the results of Table 5-2 show pronounced well depth anisotropy for both systems. Despite the fact that this type of anisotropy is not determined very well,[16] it is clear that both systems exhibit T-shaped equilibrium configurations.[53] The HeC_2H_2 and the HeOCS interactions are similar in this respect to ArC_2H_2 and ArOCS, both of which have T-shaped equilibrium geometries as determined from molecular beam electric resonance experiments.[7,10]

For the HeOCS results, the intermolecular potential's angular dependence was approximated by a potential symmetric about $\gamma = \pi/2$, and the molecular center-of-mass was taken as the C atom. This approximation eliminated the need to fit parameters like $r_{m,1}$ [see Eqn. (5-5)], and was therefore convenient. It also appeared to be necessary since there is very little information on the angular asymmetry of the HeOCS potential.[25a] Nevertheless, the approximation could not be made if the potential with even angular symmetry were unable to fit the DCS data. Judging from Fig. 5.2 and Table 5-2, the fitting quality, even with this approximation, is good. We can conclude from this that the present total DCS data are relatively insensitive to the OCS molecular asymmetry despite the non-negligible dipole moment of 0.7124 D.[45] Determining the angular asymetry of the HeOCS potential therefore requires supplementary theoretical calculations and experimental results such as line-broadening,[25(a)] molecular beam electric resonance, and rotationally inelastic scattering. It may also be possible to simulate one hemisphere of the HeOCS potential by the known $HeCO_2$ potential,[14(a),16(b)] with adjustments being made principally to the C=S hemisphere. These possibilities will also be explored in future work.

Using the observed moderate damping of the HeC_2H_2 results, we can discuss the physical significance of effective spherical potentials. For weakly or moderately anisotropic systems such as HeN_2,[17,54] $HeSF_6$,[15(b)] or HeC_2H_2 (Table 5-2), approximate "spherical limit" potentials may be extracted from the scattering data. This is no longer true for severely damped systems such as $HeCO_2$[16(b)] or HeOCS, despite the continuing usefulness of spherical limit potentials in calculating dilute gas properties for all these systems.[15,16] The major proportion of the total integral scattering cross section arises from highly probable low-angle scattering. Since these data are the last to suffer the effects of molecular anisotropy, properties depending on total integral and generalized collision cross sections do not probe the potential anisotropy until it becomes very strong. Furthermore, since scattering at low angles can be well represented by a spherical limit potential for such moderately anisotropic interactions as HeC_2H_2, it is this effective spherical potential that is extracted from properties depending on integral and generalized cross section data. This suggests that the spherical limit potential can be relied upon to provide good descriptions of gas transport properties, provided the potential is reliable for the energy range probed by these properties (see above).

5.5. SUMMARY

Measurements of the differential cross sections for scattering of a room-temperature He beam by crossed beams of C_2H_2 and OCS are used to determine anisotropic intermolecular potentials for these interactions. The scattering data, which do not resolve elastic from rotationally inelastic contributions, show directly that the $HeCO_2$ and HeOCS potentials are much more anisotropic than the HeC_2H_2 one. This illustrates that estimates of anisotropy based on bond distances and van der Waals radii, which predict that the C_2H_2 molecule is both longer and narrower than the CO_2 or OCS molecules, can be qualitatively and quantitatively incorrect.[52(b)] Damping of diffractive oscillatory structure for the HeC_2H_2 data show a pronounced angular dependence, suggesting that different regions of the potential exhibit varying degrees of anisotropy.

The HeOCS scattering data are reproduced quite well with an angularly symmetric anisotropic potential. Therefore, these total DCS measurements are not, by themselves, sufficiently sensitive to allow extraction of an asymmetric potential which would reflect correctly the $C_{\infty v}$ symmetry of OCS. Both the HeC_2H_2 and HeOCS potentials are found to have T-shaped equilibrium geometries, as do their Ar analogues.[7,10]

Acknowledgements

It is a pleasure to acknowledge the expert technical support provided by the Chemistry Department Machine Shop in constructing the apparatus. We wish especially to thank Messrs. Ernie Young and Hubert Hofmann. The Technical Services, Physics, and Electronics Shops provided further valuable assistance. We also thank Mr. Gary Samek for assistance in obtaining the scattering data, and in calibrating the time-of-flight measurements. We are grateful to J. C. Polanyi, University of Toronto, for donation of the bolometer detector and dewar system, and to G. Scoles, Princeton University, for helpful discussions. This research was supported by grants from the Natural Sciences and Engineering Research Council (Canada) and from the Research Corporation. Acknowledgement is also made to the donors of The Petroleum Research Fund, administered by the American Chemical Society, for partial support of this research.

References

1. M. Faubel, Adv. Atomic Mol. Phys. **19**, 345 (1983).
2. Faraday Disc. Chem. Soc. **73** (1982).
3. G.C. Maitland, M. Rigby, E.B. Smith, and W.A. Wakeham, *Intermolecular Forces: Their Origin and Determination*, (Clarendon, Oxford, 1981).
4. *Atomic-Molecule Collision Theory: A Guide for the Experimentalist*, R.B. Bernstein, ed. (Plenum, New York, 1979).
5. L. Eno and H. Rabitz, J. Chem. Phys. **74**, 3859 (1981).
6. (a) R.B. Gerber, M. Shapiro, U. Buck, and J. Schleusener, Phys. Rev. Lett. **41**, 236 (1978); (b) R.B. Gerber, V. Buch, and U. Buck, J. Chem. Phys. **72**, 3596 (1980).
7. S.J. Harris, K.C. Janda, S.E. Novick, and W. Klemperer, J. Chem. Phys. **63**, 881 (1975).
8. E.J. Campbell, A.C. Legon, and W.H. Flygare, J. Chem. Phys. **78**, 3494 (1983).
9. J.M. Steed, T.A. Dixon, and W. Klemperer, J. Chem. Phys. **70**, 4095 (1979).
10. R.L. DeLeon and J.S. Muenter, J. Chem. Phys. **72**, 6020 (1980).
11. U. Buck, H. Meyer, and R.J. LeRoy, J. Chem. Phys. **80**, 5589 (1984).
12. U. Hefter, G. Ziegler, A. Mattheus, A. Fischer, and K. Bergmann, J. Chem. Phys. **85**, 286 (1986); A. Mattheus, A. Fischer, G. Zeigler, E. Gottwald, and K. Bergmann, Phys. Rev. Lett. **56**, 712 (1986).
13. M. Faubel, K.H. Kohl, J.P. Toennies, and F.A. Gianturco, J. Chem. Phys. **78**, 5629 (1983).
14. (a) U. Buck, H. Meyer, M. Tolle, and R. Schinke, Chem. Phys. **104**, 345 (1986); (b) U. Buck, D. Otten, R. Schinke, and D. Poppe, J. Chem. Phys. **82**, 202 (1985).

15. (a) R.T Pack, J.J. Valentini, and J.B. Cross, J. Chem. Phys. **77**, 5486 (1982); (b) R.T Pack, E. Piper, G.A. Pfeffer, and J.P. Toennies, J. Chem. Phys. **80**, 4940 (1984).
16. (a) G.A. Parker, M. Keil, and A. Kuppermann, J. Chem. Phys. **78**, 1145 (1983); (b) M. Keil and G.A. Parker, J. Chem. Phys. **82**, 1947 (1985).
17. L. Beneventi, P. Casavecchia, and G.G. Volpi, J. Chem. Phys. **85**, 7011 (1986).
18. F. Pirani and F. Vecchiocattivi, Chem. Phys. **59**, 387 (1981).
19. R.T Pack, Chem. Phys. Lett. **55**, 197 (1978).
20. M. Keil, J.T. Slankas, and A. Kuppermann, J. Chem. Phys. **70**, 541 (1979).
21. G.O. Este, D.G. Knight, G. Scoles, U. Valbusa, and F. Grein, J. Phys. Chem. **87**, 2772 (1983).
22. R.T Pack, J. Chem. Phys. **81**, 1841 (1984).
23. U. Buck, K.H. Kohl, A. Kohlhase, M. Faubel, and V. Staemmler, Mol. Phys. **55**, 1255 (1985).
24. G.A. Parker and R.T Pack, J. Chem. Phys. **68**, 1585 (1978).
25. (a) M. Broquier, A. Picard-Bersellini, B.J. Whitaker, and S. Green, J. Chem. Phys. **84**, 2104 (1986) and references therein; (b) A. Picard-Bersellini, and B.J. Whitaker, J. Mol. Struc. **115**, 47 (1984); (c) K. Tanaka, H. Ito, K. Harada, and T. Tanaka, J. Chem. Phys. **80**, 5893 (1984); (d) M.L. Mandich and G.W. Flynn, J. Chem. Phys. **73**, 3679 (1980); (e) G.K. Johri, R.P. Rishishwar, and S.C. Mehrotra, Ind. J. Pure Appl. Phys. **20**, 510 (1982); (f) S.C. Mehrotra, G.K. Johri, and S.L. Srivastava, Ind. J. Pure Appl. Phys. **16**, 747 (1978) and references therein.
26. R.J. Cross, J. Chem. Phys. **52**, 5703 (1970).
27. G. Fischer, R.E. Miller, P.F. Vohralik, and R.O. Watts, J. Chem. Phys. **83**, 1471 (1985).

28. (a) R.A. Aziz, P.W. Riley, U. Buck, G. Maneke, J. Schleusener, G. Scoles, and U. Valbusa, J. Chem. Phys. **71**, 2637 (1979); (b) R.A. Aziz in *Inert Gases: Springer Series in Chemical Physics* edited by M.K. Klein (Springer-Verlag, Berlin, 1984); Vol. 34.
29. U. Buck and H. Meyer, J. Chem. Phys. **84**, 4854 (1986).
30. N.C. Blais, J.B. Cross, and G.H. Kwei, J. Chem. Phys. **66**, 2488 (1977).
31. L.J. Danielson and M. Keil, J. Chem. Phys. **88**, 851 (1988).
32. More precisely, the bolometer signal is proportional, for a ground-state He beam, to the kinetic energy flux rather than to the particle flux. This neglects the lack of accommodation of the kinetic energy and adsorption effects on the bolometer surface. For an estimate of the adsorption energy of 4He on cold surfaces, see E.F. Ezell, F. Pollock, and J.G. Daunt, J. Low Temp. Phys. **32**, 47 (1981) and H. Abe, Chem. Phys. **68**, 89 (1982)]. For the present measurements where $|\theta_{\mathrm{lab}}| \tilde{<} 20^\circ$, these effects were found to be negligible.
33. H.M. Seip, in *Selected Topics in Structure Chemistry*, edited by P. Andresen, O. Bastarsen and S. Furberg, (Scandinavian University, Oslo, 1967), p. 25.
34. G. Rotzoll and A. Lubbert, J. Chem. Phys. **71**, 2275 (1979).
35. D.W. Marquardt, J. Soc. Indust. Appl. Math. **11**, 431 (1963).
36. R.T Pack, J.J. Valentini, C.H. Becker, R.J. Buss, and Y.T. Lee, J. Chem. Phys. **77**, 5475 (1982).
37. G. Scoles, Ann. Rev. Phys. Chem. **31**, 81 (1980).
38. C. Douketis, G. Scoles, S. Marchetti, M. Zen, and A.J. Thakkar, J. Chem. Phys. **76**, 3057 (1982).
39. A.T. Amos and J.A. Yoffe, Chem. Phys. Lett. **39**, 53 (1976).
40. A. Kumar and W.J. Meath, Chem. Phys. **91**, 411 (1984).
41. R.E. Johnson, S.T. Epstein, and W.J. Meath, J. Chem. Phys. **47**, 1271 (1967).

42. J.O. Hirschfelder, G.F. Curtiss, and R.B. Bird, *Molecular Theory of Gases and Liquids*, (Wiley, New York, 1954).

43. R.T Pack, J. Chem. Phys. **64**, 1659 (1976).

44. Polarizeabilities: N.J. Bridge and A.D. Buckingham, Proc. Roy. Soc. London, **A295**, 334 (1966); L.H. Sharpen, J.S. Muenter, and V.W. Laurie, J. Chem. Phys. **53**, 2513 (1970); S. Green and S. Chapman, Astrophys. J. Supp. Ser. **37**, 169 (1978).

45. J.S. Muenter, J. Chem. Phys. **48**, 4544 (1968).

46. D.E. Stogryn and A.P. Stogryn, Mol. Phys. **11**, 371 (1966).

47. The present apparatus uses a rotationally cold CO_2 molecular beam, whereas the CalTech data were taken with a room temperature rotational distribution. This affects the validity of the IOSA, and may contribute to the discrepancies between the more recent data and those first published in Ref. 53.

48. M. Keil and A. Kuppermann, J. Chem. Phys. **69**, 3917 (1978).

49. Calculations in progress by S. Huzinaga and coworkers, University of Alberta and by W.J. Meath and coworkers, University of Western Ontario.

50. C. Douketis, J.M. Hutson, B.J. Orr, and G. Scoles, Mol. Phys. **52**, 763 (1984).

51. G.J.B. Hurst, P.W. Fowler, A.J. Stone, and A.D. Buckingham, Int. J. Quantum Chem. **29**, 1223 (1986).

52. (a) A.D. Buckingham and P.W. Fowler, J. Chem. Phys. **79**, 6426 (1983); (b) F.A. Baiocchi, W. Reiher and W. Klemperer, J. Chem. Phys. **79**, 6428 (1983).

53. M. Keil, A. Kuppermann, and G.A. Parker, Chem. Phys. Lett. **59**, 443 (1978).

54. M. Faubel, K.H. Kohl, J.P. Toennies, K.T. Tang, and Y.Y. Yung, Faraday Discuss. Chem. Soc. **73**, 205 (1982).

55. J.P. Toennies and K. Winkelmann, J. Chem. Phys. **66**, 3965 (1977).

CHAPTER 6

Anisotropic Intermolecular Potentials for HeC_2H_2, HeC_2H_4, and HeC_2H_6, and an Effective Spherical Potential for $HeCHF_3$ from Multiproperty Fits†

6.1. INTRODUCTION

Over the past several years, there has been considerable interest in van der Waals complexes containing hydrocarbon molecules.[1-7] This interest has focussed on the photodissociation of van der Waals complexes containing ethylene,[1-3,6,7] with additional interest in acetylene-containing complexes.[4,5] The structure of these van der Waals complexes, which is important in understanding photodissociation processes,[2(a)] can often be probed directly by molecular beam electric resonance (MBER) spectroscopy.[5,8,9] However, for molecules which do not possess permanent dipole moments, MBER structural determinations are very difficult, and only ArC_2H_2 has been studied amongst hydrocarbon-containing systems.[5] The potential energy (PE) surfaces for these systems are more amenable to study by crossed-beam scattering techniques, even though such determinations are likely to be less accurate than MBER ones.[10] The inaccuracy of the scattering potentials can be ameliorated by fitting scattering and dilute-gas properties simultaneously.[11-13] This is underscored by observing that there have been, to our knowledge, no literature potentials determined for any of these systems, excepting combination rule estimates for HeC_2H_4 based on Lennard-Jones potential parameters.[7]

In this work we report differential cross section (DCS) measurements for HeC_2H_2, HeC_2H_4, HeC_2H_6 and $HeCHF_3$ scattering. The HeC_2H_2 results have appeared in a previous paper.[10] The present measurements do not resolve elastic from rotationally (or vibrationally) inelastic scattering collisions. To supplement the scattering measurements, we also report accurate diffusion measurements for all of these interactions, and second virial coefficients for HeC_2H_4 and HeC_2H_6. These data are fit simultaneously, using the infinite-order sudden approximation (IOSA) to account for the collision dynamics,[14] resulting in anisotropic PE surfaces for the He-hydrocarbon interactions. Only an "effective" spherical potential can reliably be extracted for the $HeCHF_3$ interaction.

---

† A version of this chapter has been published. L.J. Danielson, M. Keil, and P.J. Dunlop, J. Chem. Phys. 88, 4218 (1988).

Literature results for scattering of light atoms by hydrocarbons include DCS measurements for HeC_2H_6, including inelastic effects,[15] unresolved $H+C_2H_2$ and $H+C_2H_6$ DCS's,[16] and integral cross sections for $H+C_2H_2$,[17] and for LiC_2H_4 and LiC_2H_6.[18] Integral cross sections have also been measured for a series of Li+fluorocarbon interactions, including $LiCHF_3$.[18] Vibrationally inelastic collisions have also been studied.[19]

In Sec. 6.2 of this paper, we provide a brief description of the scattering apparatus used to measure the DCS's. We also describe briefly the experimental apparatus for the dilute-gas measurements. The calculations used to reproduce DCS, diffusion and virial data from assumed PE surfaces are discussed in Sec. 6.3. In Sec. 6.4, we present the experimental results and the PE surfaces extracted from them. Finally, we summarize our results in Sec. 6.5.

6.2. EXPERIMENTAL

6.2.A. Crossed Molecular Beams Apparatus

The scattering apparatus has been described previously,[10,11(a)] so only a brief outline is given here. The main features of the apparatus are two supersonic beam sources intersecting at 90° and an in-plane rotatable liquid helium-cooled bolometer detector. The beams are optimized using a quadrupole mass spectrometer, which also indicates an insignificant fraction of dimers. Time-of-flight measurements show considerable relaxation of molecular internal degrees of freedom. Beam operating conditions, where different from our previous publications,[10,11(a)] are summarized in Table 6-1.

The computer-controlled data acquisition system and data collection scheme have also been described previously.[10] Phase-sensitive lock-in and background subtraction techniques with periodic reference normalization are used to extract signals proportional to the intensity of the scattered He atoms. The bolometer detects only He since the heavy molecular partner is kinematically restricted to scattering angles $\theta \gtrsim 50°$. Our experimental DCS measurements are presented in Table 6-2 for HeC_2H_2, HeC_2H_4, HeC_2H_6, and $HeCHF_3$.

6.2.B. Dilute-Gas Measurements

6.2.B.1. Diffusion

Diffusion coeficients, D_{12}, were measured in a stainless steel two-bulb cell[20] suspended in a bath containing distilled water thermostatted to ±1 mK by means of a thermistor bridge containing an operational amplifier (Type 725) adjusted for a gain of 3×10^5. A second water bath, with a refrigeration unit containing a by-pass valve in conjunction with a heat exchanger, was used to obtain temperatures below ambient. The diffusion coefficients were calculated from the relation;

$$d\,[\ln \Delta x_2]\,/dt = KD_{12}\ , \qquad (6-1)$$

Table 6-1. Beam Operating Conditions for DCS Measurements

	Primary Beam[a]	Secondary Beams[b]			
Gas	He	C_2H_2	C_2H_4	C_2H_6	CHF_3
Flow ($atm.cm^3/sec$)	13.0	4.1	4.2	4.2	3.3
Nozzle pressure (atm)	14.9	0.28	0.28	0.29	0.36
Nozzle-skimmer distance (mm)	9.5	11	11	11	13
Most probable velocity (km/sec)	1.771	0.915	0.890	0.875	0.552
Velocity FWHM ($\Delta v/v_{mp}$)	0.04	0.22	0.23	0.24	0.18
Collision Energy (E_{mp},meV)	—	70.6	70.2	71.6	66.5
Angular divergence (deg)[c]	1.0	1.3	1.3	1.3	1.2
Beam gas purity (%)[d]	99.995	99.6	99.5	99.0	98.0

[a] Nozzle temperature = 302 K; nozzle diameter = 0.050 mm.
[b] Nozzle temperature = 302 K; nozzle diameter = 0.300 mm.
[c] Calculated.
[d] Stated by the supplier.

Table 6-2. Experimental Total Differential Cross Section Measurements [a]

HeC_2H_2			HeC_2H_4			HeC_2H_6			$HeCHF_3$		
θ(°)	I(θ)	ΔI(θ)%	θ(°)	I(θ)	ΔI(θ)%	θ(°)	I(θ)	ΔI(θ)%	θ(°)	I(θ)	ΔI(θ)%
						-9.05	104.46	19.6			
-8.70	159.35	7.3	-8.56	207.99	17.0	-8.55	147.33	14.7			
-8.20	228.86	6.5	-8.06	290.64	12.5	-8.05	241.84	10.3			
-7.70	294.65	4.8	-7.56	368.73	9.5	-7.55	288.56	7.8			
-7.20	290.24	3.0	-7.06	374.76	8.7	-7.05	295.21	7.5			
-6.70	249.24	3.0	-6.56	305.05	8.5	-6.55	295.86	8.1			
-6.20	218.45	4.0	-6.06	307.08	8.4	-6.05	300.81	7.6			
-5.70	262.17	5.6	-5.56	396.44	8.3	-5.55	383.62	6.5			
-5.20	472.88	6.2	-5.06	641.33	6.9	-5.05	619.32	6.2			
-4.70	922.65	5.6	-4.56	1254.36	4.9	-4.55	1015.15	6.2			
-4.20	1487.51	4.3	-4.06	2015.20	3.5	-4.05	1546.55	6.0			
4.30	1543.95	3.4	4.44	1401.44	6.2	4.45	1095.87	5.2	4.43	1002.43	3.3
4.80	914.66	4.1	4.94	766.29	8.1	4.95	686.72	5.9	4.93	739.65	5.1
5.30[b]	500.00	4.5	5.44[b]	500.00	8.4	5.45[b]	500.00	6.6	5.43[b]	500.00	6.4
5.80	362.04	4.2	5.94	499.80	6.5	5.95	474.45	5.4	5.93	311.89	7.1
6.30	396.50	3.7	6.44	548.80	4.5	6.45	471.66	3.9	6.43	249.12	8.3
6.80	481.64	3.5	6.94	625.12	4.3	6.95	450.90	4.0	6.93	229.55	8.5
7.30	497.21	4.1	7.44	518.95	6.2	7.45	402.36	5.6	7.43	281.89	7.3
7.80	408.85	6.0	7.94	385.53	8.9	7.95	300.67	7.3	7.93	253.27	7.7
8.30	262.25	8.8	8.44	247.67	11.4	8.45	216.21	8.9	8.43	224.85	10.6
8.80	182.05	11.5	8.94	174.77	12.3	8.95	162.78	11.6	8.93	146.88	14.4
9.30	127.91	12.4	9.44	139.77	10.5	9.45	134.12	13.9	9.43	91.43	19.0
9.80	116.26	10.5	9.94	186.14	8.3	9.95	165.47	13.6	9.93	66.51	23.3
10.30	150.80	8.6	10.44	195.48	9.0	10.45	169.72	13.7	10.43	67.93	23.8
10.80	159.44	8.6	10.94	188.37	11.7	10.95	163.60	17.1	10.93	84.14	20.5
11.30	170.45	9.7	11.44	131.40	13.5	11.45	121.53	20.7	11.43	84.14	16.6
11.80	144.17	10.6	11.94	114.34	14.9	11.95	97.33	20.7	11.93	94.30	16.1
12.30	100.24	10.6	12.44	115.23	17.4	12.45	81.14	19.6	12.43	69.54	19.2
12.80	81.66	9.8	12.94	97.47	19.6	12.95	79.49	19.1	12.93	45.84	23.1
13.30	93.40	9.2	13.44	91.09	18.6	13.45	90.37	16.7	13.43	34.26	25.8
13.80	97.24	9.3	13.94	78.74	15.5	13.95	81.32	14.0	13.93	33.03	24.5
14.30	82.72	9.6	14.44	103.77	14.5	14.45	72.63	13.0	14.43	37.81	18.1
14.80	86.69	9.6	14.94	88.13	17.7	14.95	94.23	12.1	14.93	44.39	12.1
15.30	86.05	10.7	15.44	85.26	23.0	15.45	70.59	11.6	15.43	46.09	10.1
15.90	80.01	13.6	15.94	77.39	23.2	15.95	87.00	14.5			
16.30	67.87	16.0	16.44	77.10	18.6	16.45	82.70	21.6	16.43	34.68	12.9
16.80	79.96	16.2	16.94	55.20	20.2	16.95	88.31	30.9			
17.30	73.14	16.4	17.44	79.03	28.8	17.45	54.17	37.9	17.43	24.56	22.6
17.80	69.85	18.0									
18.30	75.35	18.1	18.44	94.41	33.1	18.45	68.87	36.4	18.43	26.45	33.3
18.80	60.45	14.7									
19.30	60.93	11.3	19.44	59.53	30.2	19.45	42.90	30.4	19.43	31.05	34.9
19.80	54.44	12.2									
20.30	53.59	16.0	20.44	79.77	25.8	20.45	67.30	28.7	20.43	30.71	29.9

[a] Experimental DCS measurements are in arbitrary units; percentage error bars represent one standard deviation.

[b] Reference angle used for periodic normalization.

where Δx_2 is the difference in mole fraction of the heavy component between the upper and lower bulbs of the cell, and K is the cell constant, which is a function of these volumes and the dimensions of the tubes connecting them. An accurate thermistor bridge, a digital voltmeter and a data-logger were used[21] to measure the variation with time of Δx_2. The cell constant was determined[22] from accurate diffusion coefficients for He-Ar measured at 300 K in this laboratory with a cell[23] which yielded absolute values.

Diffusion coefficients were measured for each system at 300 K as a function of concentration and the results least-squares fitted to the expression;

$$D_{12} = D_{12}^{\circ}\left[1 + a_1x_2/(1 + a_2x_2)\right] \ , \qquad (6-2)$$

where D_{12}° is the limiting diffusion value at $x_2 = 0$ and a_1 and a_2 are constants; values for D_{12}°, a_1 and a_2 are listed in Table 6-3. Values of D_{12} were also measured at 280 and 320 K and, using Eqn.(6-2), were extrapolated to $x_2 = 0$ to yield the limiting values given in Table 6-4. It is estimated that these values are accurate to ±0.3% or better.

6.2.B.2. Second Virial Coefficients

In order to obtain interaction second virial coefficients B_{12} for use in the multiproperty fits, excess virial coefficients B^E were obtained in an apparatus which has been described in detail previously.[24] The values of B^E were obtained[24,25] by accurately measuring the pressure change when equal volumes of two gases, initially at the same temperature and pressure, were mixed. Since B^E is defined by

$$B^E = B_{12} - \tfrac{1}{2}(B_{11} + B_{22}) \ , \qquad (6-3)$$

where B_{11} and B_{22} are second virial coefficients for the like-pair interactions, B_{12} may be calculated directly. Unfortunately, accurate B_{22} values are availble only

Table 6-3. Least-Squares Coefficients for Eqn. (6-2)[a]

System	D°_{12}	a_1	a_2	$\Delta D_{12}(\%)$[b]
He-C_2H_2	0.5936	0.05880	2.0201	0.04
He-C_2H_4	0.5417	0.06502	1.7888	0.03
He-C_2H_6	0.4998	0.08827	2.6496	0.01
He-CHF_3	0.5103	0.08972	1.5130	0.05

[a] Approximately 15 experiments were performed for each system.

[b] Average deviations between the experimental points and the smooth curves.

Table 6-4. **Limiting Diffusion Coefficients, D°_{12}, at one Atmosphere Pressure**[a]

T(K)	HeC_2H_2	HeC_2H_4	HeC_2H_6	$HeCHF_3$
280.0	0.5304	0.4838	0.4464	0.4556
300.0	0.5936	0.5417	0.4998	0.5103
320.0	0.6614	0.6034	0.5566	0.5691

[a] Units: cm^2/sec.

for C_2H_4 and C_2H_6,[26] so that B_{12} values could be obtained only for the interaction of He with these two gases. The results for B^E and the corresponding values of B_{12} are listed in Table 6-5. The B^E and B_{12} values are estimated to be accurate to ±0.5 and ±1.5 cm^3/mole, respectively, with the latter accuracy being estimated by propagating the B_{11} and B_{22} errors of the Dymond and Smith compilation.[26]

All gases used in the diffusion and second virial coefficient measurements had stated purities of 99.99% except for CHF_3 (98.0%) and C_2H_2 which was stated to be better than 99.6%. Unfortunately, acetylene is supplied dissolved in acetone, so that this impurity had to be removed by slowly bubbling the cylinder gas through three vessels in series each containing a litre of the best available concentrated sulphuric acid. When the diffusion coefficients measured with this on-line purified acetylene increased by approximately 0.2%, the acid was discarded and the vessels filled with fresh material. No such problems were encountered with the DCS measurements however, since the most significant damping of the HeC_2H_2 DCS was caused by the molecular anisotropy.

Table 6-5. Experimental Excess and Cross-Term Virial Coefficients[a,b]

	HeC_2H_4		HeC_2H_6	
T(K)	B^E	B_{12}	B^E	B_{12}
290.0	101.7	33.5	127.0	34.8
300.0	97.6	34.4	121.1	35.9
320.0	88.7	34.5	109.9	35.7

[a] Units: cm^3/mole.

[b] The B_{11} and B_{22} values were taken from Ref. 26.

6.3. ANALYSIS

6.3.A. Intermolecular Potential Parameterizations

The He+hydrocarbon interactions are analyzed using an anisotropic modification to the Hartree-Fock plus damped Dispersion (HFD) potential form.[10,16,27] Such an anisotropic analysis is mandated by the damping of diffractive oscillatory structure observed in the total DCS scattering measurements, especially beyond the second oscillation.[10] The HFD parameterization provides a reasonable description of atom+molecule interactions, even when being fit without reliable Hartree-Fock data.[16] Furthermore, it exhibits sufficient flexibility with only three adjustable parameters, reducing parameter correlation difficulties encountered when fitting large numbers of parameters. Nevertheless, care is required in constructing the dispersion coefficients (see below).

For isotropic interactions, the HFD potential has the following formulation[10,16]:

$$\begin{aligned} V_{HFD}(r) &= V_{HF}(r) + F(r)V_D(r)\ , \\ V_{HF}(r) &= A\ \exp(-\alpha r)\ , \\ V_D(r) &= -\sum_{n=0}^{4} C_{2n+6}r^{-(2n+6)}\ , \\ F(r) &= \exp\left[-\left(Dr_m r^{-1} - 1\right)^2\right]\ , \quad r \le Dr_m\ , \\ F(r) &= 1\ , \quad r \ge Dr_m. \end{aligned} \qquad (6-4)$$

For fitting this potential form to our experimental data, we regard only r_m and α as adjustable parameters. The damping parameter was held fixed at 1.28.[16,27] Requiring the potential minimum position to occur at the r_m parameter value then fixes A in terms of α and r_m, wherupon the well depth ϵ is also fixed.[10,16]

Molecular anisotropy is introduced into this potential by expanding r_m and the dispersion coefficients in Legendre polynomials[10,16]:

$$r_m = r_m(\gamma) = r_{m,0} + r_{m,2}P_2(\cos\gamma) \ , \qquad (6-5)$$

$$C_6 = C_6(\gamma) = C_{6,0} + C_{6,2}P_2(\cos\gamma) \ , \qquad (6-6)$$

$$C_8 = C_8(\gamma) = C_{8,0} + C_{8,2}P_2(\cos\gamma) + C_{8,4}P_4(\cos\gamma) \ . \qquad (6-7)$$

This form for the molecular anisotropy is strictly correct only for rigid rotator molecules possessing $D_{\infty h}$ symmetry. It is therefore only approximately correct for the systems being discussed, particularly for the HeC_2H_4 and HeC_2H_6 interactions. However, PE surfaces with the correct symmetry would require so many unknown parameters that fitting data of the present information content would be inappropriate. Accounting for vibrational degrees of freedom would only render the present problem more intractable. Nevertheless, previous experience[10,16] has shown that even the crude PE parameterizations above can provide good fits to the data, while adequately describing the PE surface anisotropy (see Sec. 6.4).

For fitting purposes, we found it more convenient to optimize the r_m values parallel and perpendicular to the principal molecular axis (i.e., $r_m^{\parallel}$ and $r_m^{\perp}$, respectively). Note that the A and ϵ values of the fitted HFD potential are anisotropic only because of the r_m and C_n anisotropies in Eqs. (6-5)-(6-7). We note that the "spherical limit"[10,13] for anisotropic HFD potentials may be defined by using the spherically-averaged r_m and C_n parameter values in Eqn. (6-4).

The HFD parameterization requires evaluation of van der Waals coefficients at least to C_8.[16] Fortunately however, the accuracy of these coefficients is not crucial when fitting the HFD potential form,[16] unless the data being fit (or predicted) are sensitive to the outer bowl region of the attractive potential well.[11]

Therefore, we have calculated or estimated the C_6 and C_8 coefficients, and their anisotropies, rather than fitting them to the data.

For HeC_2H_2 and HeC_2H_4, we estimated the $C_{6,0}$ coefficients by applying the geometric combination rule[29] to literature values for C_2H_2-C_2H_2, C_2H_4-C_2H_4[30] and He-He.[31(a)] For HeC_2H_6, we calculated $C_{6,0}$ by summing the semiempirical oscillator strengths given by Meath and co-workers for C_2H_6[31(b)] and He.[31(c)] The $C_{6,2}$ coefficients and all of the C_8 coefficients were estimated from the relations given by Pack.[32] Data for the van der Waals calculations were taken from several sources.[33–36] Higher-order dispersion coefficients (up to C_{14}), useful in the HFD parameterization, were estimated using the recursion equations of Douketis et al.,[29] for each atom-molecule orientation angle γ as required.

For the $HeCHF_3$ interaction, the total DCS shows pronounced oscillatory structure. In such a case, a non-spherical analysis becomes practicable only with very good signal-to-noise.[12(b)] Nevertheless, the large molecular dipole moment suggests that $HeCHF_3$ C_7 dipersion coefficients would contribute significantly to the HFD potential. Explicit neglect of these contributions in the spherical potential analysis might distort the repulsive wall of a fitted HFD potential, and so we used the piecewise Morse-spline-van der Waals (MSV) parameterization[13,37] instead. For this analysis, r_m, ϵ, and the reduced Morse parameter β were fitted to the data. The $C_{6,0}$ term of the $HeCHF_3$ van der Waals potential, including the induction part, was estimated[38] using polarizabilities[39] the molecular dipole moment,[40] and ionization potentials.[41]

6.3.B. Calculations

Calculations for the total DCS, transport properties, and virial coefficients, have been described previously for spherical potentials.[11(a)] For performing scattering calculations (total DCS and transport properties) with the present anisotropic potentials, we used the IOSA.[13,14] For the DCS calculations, 10 orientation angles γ were used, whereas the Boltzmann-averaged collision integral calculations required only 4 such angles for convergence to within 0.1%.

The DCS calculations included instrumental velocity- and angular-averaging effects. In calculating the transport properties, collision integrals were generated only in the narrow temperature range from 200 to 400 K. For further computational economy, with no sacrifice in precision, the quantum phase shifts required for low collision energies were calculated with larger step sizes than previously.[10,11(a)] Assumed like-pair interaction parameters had negligible influence on the calculated limiting diffusion coefficients that were compared to the corresponding experimental data (Sec. 6.2.B), even though the diffusion coefficients were calculated using the fourth-order Chapman-Cowling approximation.[42]

Virial coefficients were calculated using the method of Pack,[43] with radial quantum corrections up to third order,[44] and angular corrections to first order. Only the first-order radial quantum corrections were significant for any of the He+hydrocarbon systems, even when using the smallest principal moment of inertia for the HeC_2H_4 and HeC_2H_6 angular quantum corrections.

6.3.C. Multiproperty Fitting

As in previous work, parameters of the assumed intermolecular potential form are fit to the experimental data by an automated non-linear least-squares fitting program.[45] The least-squares functional to be minimized is given by the dimensionless quantity

$$\delta = \left[\sum_{j=1}^{N} w_j \delta_j^2 \Big/ \sum_{j=1}^{N} w_j \right]^{1/2} , \qquad (6-8)$$

where the δ_j are the corresponding quantities for each of N properties being fit,

$$\delta_j = \left[\frac{1}{n_j} \sum_{i=1}^{n_j} \left(\frac{S_{ij}^{calc} - S_{ij}^{exp}}{\Delta S_{ij}^{exp}} \right)^2 \right]^{1/2} . \qquad (6-9)$$

Here, S_{ij}^{calc} is the calculated value of property j at point i, S_{ij}^{exp} is the experimental measurment, and ΔS_{ij}^{exp} is its absolute experimental error. Error bars correspond to one standard deviation in all cases, and assume that there are no dynamical errors in using rigid rotator mechanics or the IOSA. Overall weights w_j for each class of data reflect the narrow experimental temperature range of the dilute-gas properties and their sensitivities to the intermolecular potential.[11(b)]

The best-fit PE surfaces reported in this work are obtained by simultaneously fitting the DCS, limiting diffusion coefficients, and interaction second virial data where available. The DCS and accurate room-temperature diffusion measurements are particularly suited for these fits, since they depend on the weakly repulsive wall and attractive well regions of the PE surface.[11(b)] Furthermore, the use of limiting diffusions ensures virtually complete independence from hydrocarbon+hydrocarbon interactions, which are poorly known. Interaction second virial coefficients probe similar radial regions of the PE surface, but involve different averaging over atom-molecule orientation angles. Unfortunately, the mixed virials are useful only for HeC_2H_4 and HeC_2H_6, since the pure-gas virials for $C_2H_2+C_2H_2$ and CHF_3+CHF_3 are not reliably known.[26]

6.4. RESULTS AND DISCUSSION

6.4.A. Total Differential Cross Sections

The experimentally measured DCS's are presented in Table 6-2 and are plotted in Fig. 6.1. Also shown are the corresponding DCS's calculated using the best-fit potential parameters appearing in Tables 6-6 and 6-7. Comparison of these data with a completely spherical system, such as HeAr,[11(a),27(a)] leads to a number of qualitative observations regarding damping of the diffraction oscillations.

Firstly, the $HeCHF_3$ DCS exhibits only slight damping at all angles. Nevertheless, there does appear to be noticeably more damping than for the total DCS data of Frick for $HeCF_4$.[15] For the present total DCS data however, and in the absence of any explicitly inelastic scattering measurements, the weak damping and low signal-to-noise ratio precludes a reliable anisotropic analysis for the $HeCHF_3$ PE surface. Improved precision, even without inelastic measurements, would facilitate an anisotropic analysis, such as recently obtained for SF_6 interactions with rare gas atoms including He.[12]

Secondly, the HeC_2H_2 and HeC_2H_4 total DCS's are remarkably similar, showing only moderate damping until the second diffraction oscillation around 12°, and complete damping for larger scattering angles. In contrast, the HeC_2H_6 DCS exhibits strong damping even for the two lowest-angle oscillations (Fig. 6.1). For these low reduced mass systems, damping of diffraction oscillations is primarily caused by the molecular radial anisotropy, while well depth anisotropies are largely ineffective in washing out the diffractive structure.[12(b),28,46] Consequently, one would conclude, solely on the basis of the measured DCS data, that the molecular shape of C_2H_6 is more anisotropic than C_2H_2 and C_2H_4. The latter two molecules appear to have very similar anisotropies (as probed by a He atom).

These qualitative observations can be compared to the conclusions expressed by authors studying the scattering data of somewhat similar systems. The

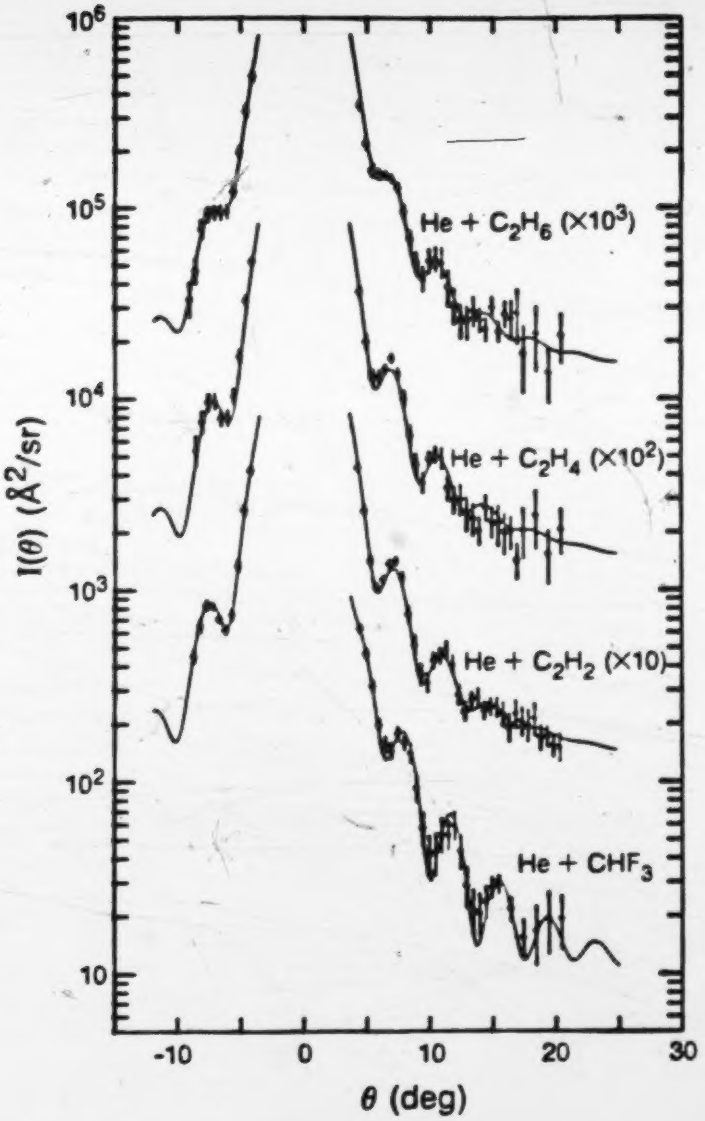

Figure 6.1

Total differential cross sections measured as functions of laboratory scattering angle. Data points are given with error bars of one standard deviation. Smooth curves correspond to the best-fit intermolecular potentials (Tables 6-6 and 6-7), which also provide the absolute scale. Successive curves are multiplied as shown for clarity of display.

Table 6-6. Best-Fit HFD Anistotropic Intermolecular Potential Parameters and Fitting Quality[a]

	HeC_2H_2	HeC_2H_4	HeC_2H_6
α(Å^{-1})[b]	3.439	3.437	3.748
$r_m^{\perp}$(Å)[b]	3.730	3.867	3.807
$r_m^{\parallel}$(Å)[b]	4.418	4.639	4.830
$\sigma^{\perp}$(Å)[c]	3.30	3.43	3.41
$\sigma^{\parallel}$(Å)[c]	3.99	4.19	4.39
$\sigma^{\parallel} - \sigma^{\perp}$(Å)	0.68	0.76	0.99
$\epsilon^{\perp}$(meV)[c]	2.70	2.68	3.74
$\epsilon^{\parallel}$(meV)[c]	1.88	1.45	1.05
$C_{6,0}$(eV-Å^6)[d]	11.00	12.90	13.60
$C_{6,2}$(eV-Å^6)[d]	1.70	1.60	0.70
$C_{8,0}$(eV-Å^8)[d]	72.0	83.0	87.3
$C_{8,2}$(eV-Å^8)[d]	55.4	50.7	21.3
$C_{8,4}$(eV-Å^8)[d]	6.9	4.5	0.8
δ_{DCS}	0.931	0.992	0.809
δ_D	0.692	0.514	0.294
δ_B	—	0.789	0.346
$\delta_{overall}$[e]	0.878	0.877	0.660

[a] Eqn. (6-4). Errors for the perpedicular and parallel configuration are likely to be similar to those suggested in Ref. 13.

[b] Fitted to the data.

[c] Derived from the fitted parameters.

[d] Calculated and held fixed; see Sec. 6.3.A.

[e] Eqn. (6-8) with $w_{DCS}=1.00$; $w_D=w_B=0.33$.

Table 6-7. Spherical Limit Potential Parameters and Fitting Quality

	HFD[a]			MSV[b]
	HeC_2H_2	HeC_2H_4	HeC_2H_6	$HeCHF_3$
α(Å^{-1})[c]	3.439	3.437	3.748	—
β	—	—	—	6.890[c]
$r_{m,0}$(Å)	3.96[d]	4.12[d]	4.15[d]	3.954[c]
$<\sigma>_\gamma$(Å)	3.53[d]	3.69[d]	3.74[d]	3.56[d]
$<\epsilon>_\gamma$(meV)	2.38[d]	2.17[d]	2.38[d]	3.600[c]
$C_{6,0}$(eV-Å^6)[e]	11.00	12.90	13.60	7.96
$C_{8,0}$(eV-Å^8)[e]	72.0	83.0	87.3	0.00
δ_{DCS}	1.458	1.415	1.836	0.844
δ_D	1.501	1.000	1.511	0.507
δ_B	—	1.092	0.269	—
$\delta_{overall}$[f]	1.469	1.282	1.581	0.775

[a] Spherical limit of the best-fit anisotropic HFD potentials, whose anisotropic parameters appear in Table 6-6.

[b] References 13,36; best-fit.

[c] Fitted to the data.

[d] Derived from the fitted parameters.

[e] Calculated and held fixed; see Sec. 6.3.A.

[f] Eqn. (6-8) with $w_{DCS}=1.00$; $w_D=w_B=0.33$.

velocity dependence of total integral cross sections for Li atoms interacting with a series of fluorocarbons show that CHF_3 is only slightly more damped than CH_4.[18] The largest damping observed for this series occurs for CH_2F_2, the least symmetric of the substituted fluorocarbons. Rothe and Helbing also studied the LiC_2H_4 and LiC_2H_6 interactions and found that the LiC_2H_6 total integral cross section was somewhat *less* damped than LiC_2H_4.[18] Similarly, the total DCS measurements of Este et al.[16] for $H+C_2H_2$ and $H+C_2H_6$ suggest, solely from the observed damping of their diffraction oscillations, that $H+C_2H_6$ is more isotropic than $H+C_2H_2$. Their HFD potential parameters support this suggestion. Unfortunately, error bars for their $H+C_2H_2$ total DCS are nearly twice as large as for their $H+C_2H_6$ measurements. Consequently, these DCS data are completely super-imposable, within the respective error bars, for all scattering angles. We note that both the H and Li atom experiments involve interactions between open-shell atoms and the hydrocarbon, unlike the present study.

Total DCS measurements for HeC_2H_6 scattering have also been obtained by Frick.[15] In his analysis, Frick used a hard ellipsoid model to determine $\sigma^{\|} = 4.2 \pm 0.2$ Å, and $\sigma^{\perp} = 3.4 \pm 0.1$ Å. These values agree well with the present results (Table 6-6).

6.4.B. Dilute-Gas Data

The experimental limiting diffusion and interaction second virial coefficients presented in Tables 6-4 and 6-5 are plotted in Figs. 6.2 and 6.3, respectively. Also shown are the corresponding properties calculated using the best-fit potential parameters (Tables 6-6 and 6-7).

To the best of our knowledge, the only other dilute-gas data available for these systems are interaction virials for HeC_2H_4 at temperatures of 323 and 373 K.[47] However, these data exhibit the wrong temperature dependence and fall

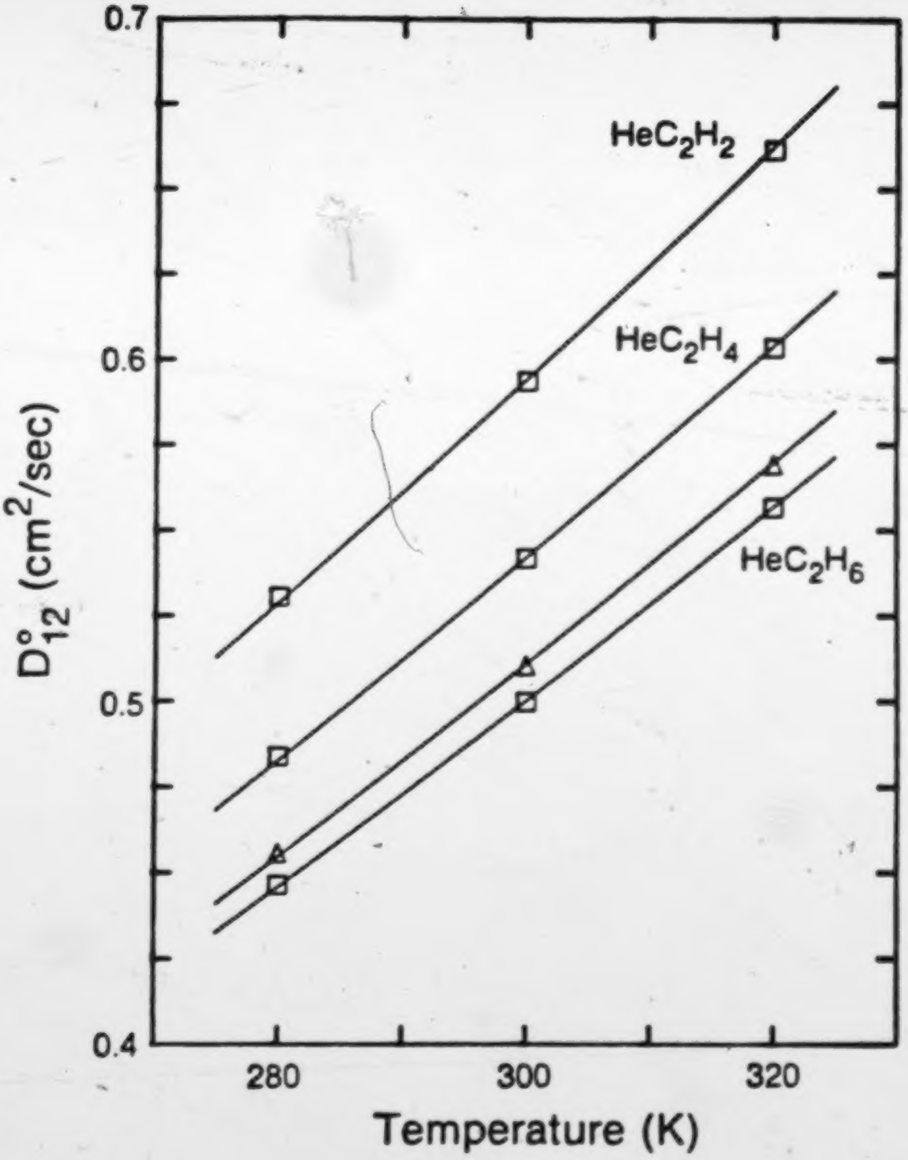

Figure 6.2

Limiting diffusion coeffcients D°_{12} (symbols) measured as a function of temperature, and the corresponding best-fit calculated results (solid curves). Diffusions are shown in the limit of zero mole fraction of the heavy component ($x_2 = 0$), and for one atmosphere pressure. Symbols used are: □, He+hydrocarbons; △, $HeCHF_3$.

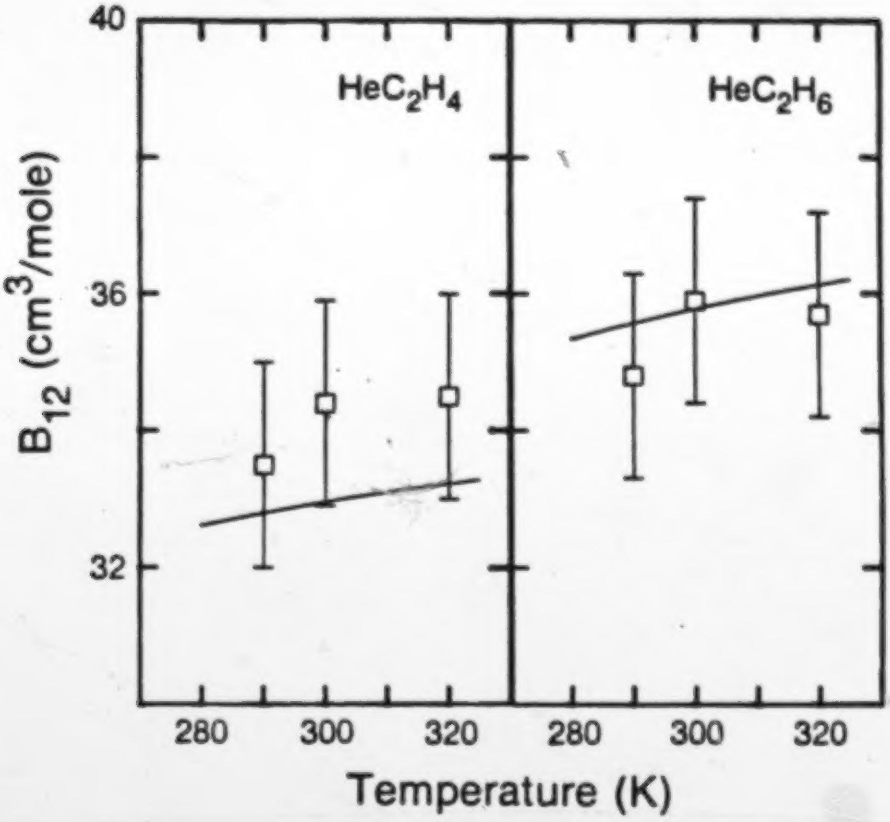

Figure 6.3

Interaction virial coefficients B_{12} (symbols) measured as a function of temperature. Symbols and solid curves as for Fig. 6.2.

well below the present measurements. Therefore, we did not include them in any of our fitting calculations.

It is important to note that, although the diffusion coefficients show no discernable influence on molecular anisotropy (see Sec. 6.4.D), they nevertheless constrain the spherical limit of the potential. This is especially noticeable for diffusions measured to the level of accuracy currently attainable near room temperature.[11] The interaction virials weight the angular averaging differently from the diffusions (and the DCS's), and provide additional potential information, even though they are measured less accurately. Unfortunately, the usefulness of the interaction virials for the present systems is hampered by unknown errors for the pure-gas virials.

6.4.C. Potential Energy Surfaces

Parameters of the anisotropic HFD potential form [Eqn. (6-4)-(6-7)] were fit to the HeC_2H_2, HeC_2H_4, and HeC_2H_6 total DCS, diffusion, and second virial data (except for HeC_2H_2). Three adjustable parameters – $r_m^{\parallel}$, $r_m^{\perp}$, and α – were optimized as outlined in Sec. 6.3. The best-fit He+hydrocarbon potential parameters are collected in Table 6-6, along with the dispersion coefficients (not varied), and the fitting quality δ [Eqn. (6-8)]. Radial potential cuts along $\gamma = 0°$, $45°$, and $90°$ atom-molecule orientation angles for the corresponding potentials are shown in Fig. 6.4.

For $HeCHF_3$, as discussed in Sec. 6.3.B, the r_m, ϵ, and β parameters of the isotropic MSV potential form were fit to the total DCS and diffusion data. The best-fit $He+CHF_3$ potential parameters are collected in Table 6-7, along with the fitting quality δ. That table also displays the spherical limits of the He+hydrocarbon PE surfaces (as defined in Sec. 6.3.B). All these spherical limit potentials are plotted in Fig. 6.5.

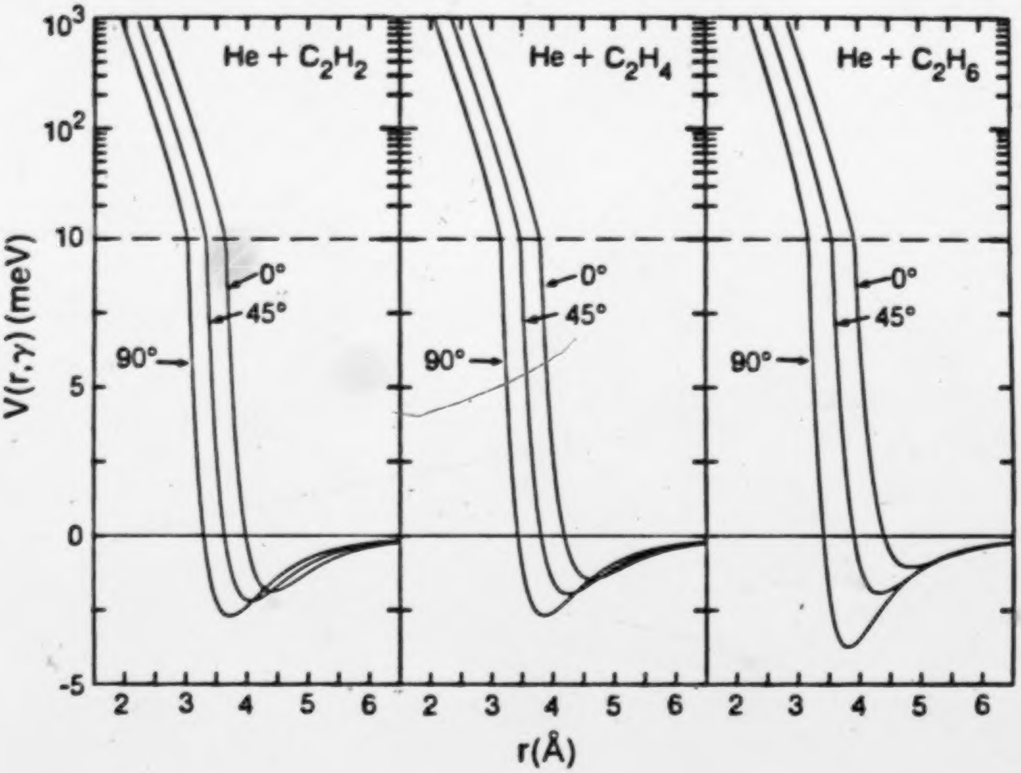

Figure 6.4

Radial cuts across the best-fit anisotropic HFD potentials for HeC_2H_2, HeC_2H_4, and HeC_2H_6. The potential energy is plotted parametrically as a function of the orientation angle γ. The corresponding potential parameters are collected in Table 6-6.

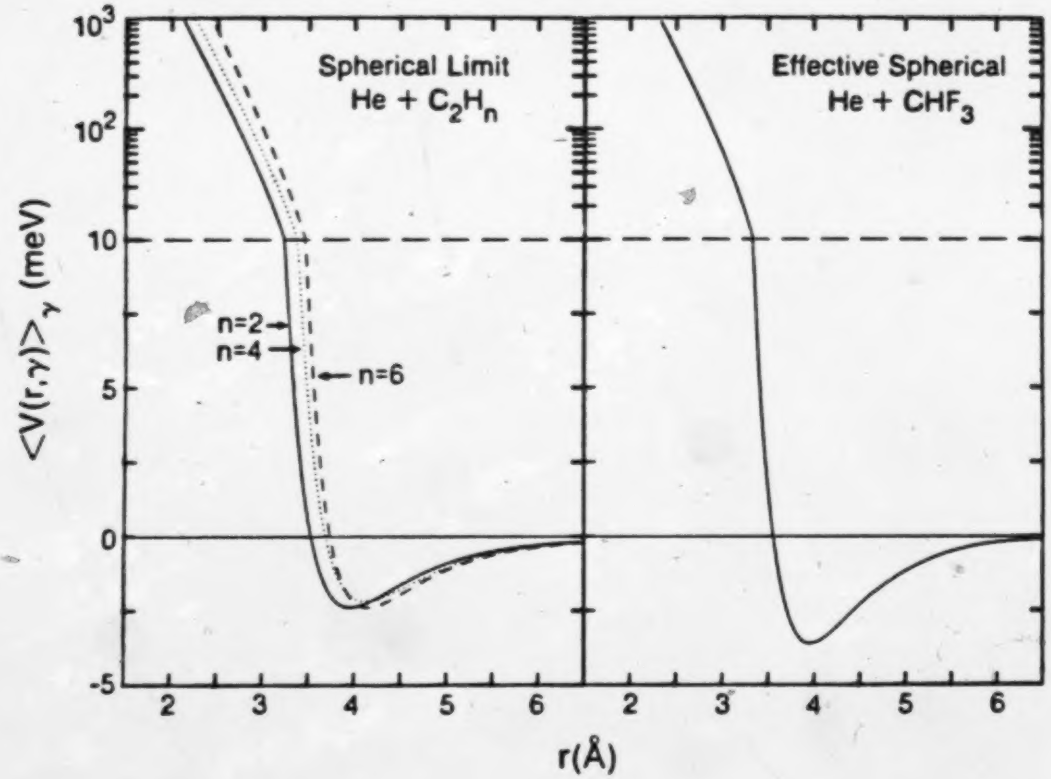

Figure 6.5

Spherical limits of the best-fit anisotropic potentials for HeC$_2$H$_2$ (solid curve in left frame), HeC$_2$H$_4$ (dotted curve), and HeC$_2$H$_6$ (dashed curve), and the best-fit effective spherical potential for HeCHF$_3$ (solid curve in right frame). Potential parameters as in Table 6-7.

For our initial fitting calculations, we determined the intermolecular potentials for these interactions based only on the DCS data. These PE surfaces were topographically correct in the gross sense that they had "T-shaped" equilibrium geometries and were longer along the principal axes than perpendicular to them, but they failed to reproduce the dilute-gas properties. This failure was particularly evident for the HeC_2H_4 diffusion measurements, for which the predictions were in error by up to 5%. Including the diffusions along with the DCS's in simultaneous fits improved the description of the dilute-gas properties markedly, without adversely affecting the DCS fits. Again however, the HeC_2H_4 interaction was the most troublesome case, and its interaction virials were still not predicted to within their error bars. Consequently, we included all three properties (DCS, diffusions, and virials) in the simultaneous multiproperty fits. Unfortunately, this was not possible for the HeC_2H_2 system, which, however, had the least inconsistency between the DCS-only potential of the present work and the measured diffusions. We note the rather large difference between the present determination of the HFD α value and that of our preliminary HeC_2H_2 potential,[10] which would have led to predicted diffusion coefficients in error by up to 5%.

The above experiences are similar to those encountered by Pack and coworkers[12] in determining potentials for the rare gases interacting with SF_6. Having to include all of the available data in the fitting procedure however, does not allow us to independently assess the accuracy of the intermolecular potentials extracted. Therefore, the ability of our potentials to predict new measurements not included in the fitting may be restricted to a limited temperature range. Conversely, any new data outside the temperature range presently considered could be used to improve the PE surfaces, and hence their predictive abilities.

From Fig. 6.1 and Tables 6-6 and 6-7, one can see that the best-fit intermolecular potentials provide good reproduction of the total DCS data. The limiting diffusion data are also well reproduced (Fig. 6.2), as are the HeC_2H_6 virial measurements (Fig. 6.3). However, reproduction of the HeC_2H_4 virials is less satisfactory. In fact, the HeC_2H_4 interaction consistently presented the greatest challenge in finding a suitable potential consistent with all the data. We note that it is for just this system that one might encounter dynamical inaccuracies in using the IOSA, due to the rather large rotational constant of C_2H_4 (4.828 cm^{-1} [48]). It should be noted however, that our molecular beam time-of-flight measurements (Table 6-1) indicate significant relaxation of the internal degrees of freedom, and we would expect much of the population to relax into low-lying rotational states.

The IOSA is not the only approximation used in our analysis that could affect the accuracy of the resulting potentials. Specifically, the rigid rotor and linear molecule approximations are particularly unrealistic for the HeC_2H_6 interaction. Nevertheless, the potentials obtained provide apparently acceptable phenomenological descriptions of the data analyzed. Furthermore, we note that the IOSA has been compared favourably with close coupling or coupled-states calculations for HeHF,[49] HeH_2,[50] HeCO,[51] $HeCO_2$,[14,52] and HeN_2.[53] Our assumption that the IOSA should provide an adequate description for the hydrocarbon interactions discussed here therefore appears reasonable. Molecular vibrational motions at thermal energies are unlikely to significantly perturb the angular dependence of the intermolecular potentials at the accuracy level of the present determinations. Finally, the internal rotational motion in C_2H_6 occurs on a time scale somewhat faster than the collision time at thermal energy, and should result in significantly smearing out the methyl groups.

6.4.D. Spherical Limit Potentials

The best-fit anisotropic HFD potentials can be used to generate effective spherical potentials by setting all the anisotropy parameters in Eqns. (6-5)-(6-7) to their spherical averages. That such an effective spherical potential is different from the spherical average of the anisotropic potential has already been discussed extensively in the literature.[12,13,16] Also previously noted was the apparently good predictive ability of spherical limit potentials in reproducing dilute-gas data.[13] In the present case however, diffusions calculated from the spherical limit potentials lie significantly above the curves shown in Fig. 6.2, but parallel to them. The differences are about 0.4%, 0.3%, and 0.5%, for HeC_2H_2, HeC_2H_4, and HeC_2H_6, respectively. Thus, the spherical limit potential does not provide a sufficiently reliable description for diffusion measurements as accurate as the ones obtained in this study, and the full anisotropic potential must be used instead. Similar statements pertain to the interaction virials, but here the differences are smaller than the error bars presently attained (the spherical limit potentials predict virials 0.2-0.5 cm^3/mole smaller than the corresponding anisotropic ones).

We note that the multiproperty fitting procedure used in this work yields anisotropic potentials only because the total DCS diffraction oscillations are damped, and not because of any feature of the dilute-gas measurements. Nevertheless, accurate diffusion measurements, such as the ones reported here, provide tight constraints for the PE surfaces extracted from the data. In particular, correlations between spherical limit parameters ($r_{m,0}$, α) and anisotropic parameters ($r_{m,2}$) are reduced signifcantly. Thus, although it is apparent that somewhat different PE surfaces can fit the DCS data alone, only a small subset of such surfaces can reliably reproduce the diffusion data as well. This improves our confidence in the PE surfaces obtained, particularly in their anisotropies.

6.5. SUMMARY

We have measured total (unresolved elastic + inelastic) DCS's, as well as diffusion and virial coefficients, for the interactions of He with C_2H_2, C_2H_4, C_2H_6, and CHF_3. These measurements are subjected to simultaneous fits to extract anisotropic PE surfaces capable of reproducing all of the fitted data.

For the hydrocarbon series, the observed anisotropy trend is clearly $HeC_2H_6 > HeC_2H_4 \sim HeC_2H_2$. This decreasing anisotropy, as measured by $r_m^{\parallel} - r_m^{\perp}$ (Table 6-6), closely parallels the decreasing carbon-carbon bond length in the same sequence. Thus, while $r_m^{\perp}$ is about the same for all three He+hydrocarbon sytems, we observe $r_m^{\parallel} \approx r_{C-C} + 3.3$ Å. The anisotropy trend is opposite to that observed both for H and Li atoms interacting with the same molecules. It is possible that the observed differences are due to the open shell atoms interacting more strongly with the molecular π-bonds, thus attaining shorter interaction distances for the perpendicular approach than for the corresponding closed-shell He atom interactions. The observed anisotropy trend is also opposite to the one expected on the basis of end-to-end hydrogen-hydrogen distances, illustrating the ineffectiveness of the terminal H atoms in extending the van der Waals molecular shape.[54]

For the $HeCHF_3$ interaction, only an effective spherical analysis could be performed. Anisotropic analysis of this system nevertheless remains an interesting problem, since it could address the role played by bonded H atoms in the overall molecular shape as probed by the He atom.

Acknowledgements

We wish to thank Karen McLeod and Deb Danielson (Alberta), and Caroline Bignell (Adelaide), for their assistance in obtaining the experimental DCS and dilute-gas data, respectively. This research was supported by grants from the Natural Sciences and Engineering Research Council (Canada), from the Research Corporation, and from the Australian Research Grants Scheme. Acknowledgement is also made to the donors of the Petroleum Research Fund, administered by the American Chemical Society, for partial support of this research.

References

1. F. Huisken and T. Pertsch, J. Chem. Phys. **86**, 106 (1987).
2. (a) M.P. Casassa, D.S. Bomse, and K.C. Janda, J. Chem. Phys. **74**, 5044 (1981); (b) C.M. Western, M.P. Casassa, and K.C. Janda, J. Chem. Phys. **80**, 4781 (1984); (c) M.P. Casassa, C.M. Western, and K.C. Janda, J. Chem. Phys. **81**, 4950 (1984).
3. M.A. Hoffbauer, K. Liu, C.F. Giese, and W.R. Gentry, J. Chem. Phys. **78**, 5567 (1983).
4. (a) G. Fischer, R.E. Miller, and R.O. Watts, Chem. Phys. **80**, 147 (1983); (b) G. Fischer, R.E. Miller, P.F. Vohralik, and R.O. Watts, J. Chem. Phys. **83**, 1471 (1985); (c) Z.S. Huang and R.E. Miller, J. Chem. Phys. **86**, 6059 (1987).
5. R.L. DeLeon and J.S. Muenter, J. Chem. Phys. **72**, 6020 (1980).
6. J. Hager, W. Krieger, T. Ruegg, and H. Walther, J. Chem. Phys. **70**, 2859 (1979).
7. I.R. Dagg, L.A.A. Read, and W. Smith, Can. J. Phys. **60**, 1431 (1982).
8. (a) S.J. Harris, K.C. Janda, S.E. Novick, and W. Klemperer, J. Chem. Phys. **63**, 881 (1975); (b) J.M. Steed, T.A. Dixon, and W. Klemperer, J. Chem. Phys. **70**, 4095 (1979).
9. E.J. Campbell, A.C. Legon, and W.H. Flygare, J. Chem. Phys. **78**, 3494 (1983).
10. L.J. Danielson, K.M. McLeod, and M. Keil, J. Chem. Phys. **87**, 239 (1987).
11. (a) L.J. Danielson and M. Keil, J. Chem. Phys. **88**, 851 (1988); (b) M. Keil and L.J. Danielson, Can. J. Phys. **66**, 159 (1988).
12. (a) R.T Pack, J.J. Valentini, and J.B. Cross, J. Chem. Phys. **77**, 5486 (1982); (b) R.T Pack, E. Piper, G.A. Pfeffer, and J.P. Toennies, J. Chem. Phys. **80**, 4940 (1984).

13. M. Keil and G.A. Parker, J. Chem. Phys. **82**, 1947 (1985).

14. G.A. Parker and R.T Pack, J. Chem. Phys. **68**, 1585 (1978).

15. J. Frick, Ph.D. Dissertation, Max-Planck-Institut Für Strömungsforschung, Göttingen, Germany (May, 1984).

16. G.O. Este, D.G. Knight, G. Scoles, U. Valbusa, and F. Grein, J. Phys. Chem. **87**, 2772 (1983).

17. W. Bauer, R.W. Bickes Jr., B. Lantzsch, J.P. Toennies, and K. Walaschewski, Chem. Phys. Lett. **31**, 12 (1976).

18. E.W. Rothe and R.K.B. Helbing, J. Chem. Phys. **50**, 3531 (1969).

19. U. Gierz, M. Noll, and J.P. Toennies, J. Chem. Phys. **82**, 217 (1985).

20. R.D. Trengove, K.R. Harris, H.L. Robjohns, and P.J. Dunlop, Physica **131A**, 506 (1985).

21. M.A. Yabsley and P.J. Dunlop, J. Phys. E **8**, 834 (1975).

22. P.S. Arora, I.R. Shankland, T.N. Bell, M.A. Yabsley, and P.J. Dunlop, Rev. Sci. Instrum. **48**, 673 (1977).

23. G.R. Staker and P.J. Dunlop, Chem. Phys. Letters **42**, 419 (1976).

24. T.N. Bell and P.J. Dunlop, Rev. Sci. Instrum. **53**, 83 (1982).

25. C.M. Knobler, Rev. Sci. Instrum. **38**, 184 (1967).

26. J.H. Dymond and E.B. Smith, *The Virial Coefficients of Pure Gases and Mixtures* (Claredon, Oxford, 1980).

27. (a) R.A. Aziz, P.W. Riley, U. Buck, and G. Maneke, J. Schleusener, G. Scoles, and U. Valbusa, J. Chem. Phys. **71**, 2637 (1979); (b) R.A. Aziz, in *Inert Gases: Springer Series in Chemical Physics*, edited by M. Klein (Springer, Berlin, 1984); Vol. **34**.

28. R.T Pack, Chem. Phys. Lett. **55**, 197 (1978).

29. C. Douketis, G. Scoles, S. Marchetti, M. Zen, and A.J. Thakkar, J. Chem. Phys. **76**, 3057 (1982).

30. A.T. Amos and J.A. Yoffe, Chem. Phys. Lett. **39**, 53 (1976).

31. (a) A. Kumar and W.J. Meath, Mol. Phys. **54**, 823 (1985); (b) B.L. Jhanwar and W.J. Meath, Mol. Phys. **41**, 1061 (1980); (c) R.E. Johnson, S.T. Epstein, and W.J. Meath, J. Chem. Phys. **47**, 1271 (1967).

32. R.T Pack, J. Chem. Phys. **64**, 1659 (1976).

33. M. Gupta and S. Bhattacharyya, J. Chem. Soc. Faraday Trans. 2, **80**, 1405 (1984).

34. N.J. Bridge and A.D. Buckingham, Proc. Roy. Soc. London Ser. **A 295**, 334 (1966).

35. D.E. Stogryn and A.P. Stogryn, Mol. Phys. **11**, 371 (1966).

36. J.M. Standard and P.R. Certain, J. Chem. Phys. **83**, 3002 (1985).

37. J.M. Parson and Y.T. Lee, Entropie **42**, 146 (1971).

38. (a) G.C. Maitland, M. Rigby, E.B. Smith, and W.A. Wakeham, *Intermolecular Forces: Their Origin and Determination* (Clarendon, Oxford, 1981); (b) J.O. Hirschfelder, G.F. Curtiss, and R.B. Bird, *Molecular Theory of Gases and Liquids* (Wiley, New York, 1954).

39. (a) M. Karplus and R.N. Porter, *Atoms and Molecules An Introduction for Students of Physical Chemistry* (W.A. Benjamin, Inc., New York, 1970); (b) F. Baas and K.D. van den Hout, Physica **A95**, 597 (1979).

40. R.D. Nelson Jr., D.R. Lide Jr., and A.A. Maryott, *Selected Values of Electric Dipole Moments for Molecules in the Gas Phase*, Natl. Stand. Ref. Data Ser. Natl. Bur. Stand. **10** (U.S. GPO, Washington, D.C., 1967).

41. (a) *Handbook of Chemistry and Physics* 56th Edition, edited by R.C. Weast (CRC Press, Cleveland, Ohio, 1975); (b) R.J. Blint, T.B. McMahon, and J.L. Beauchamp, J. Am. Chem. Soc. **96**, 1269 (1974).

42. E.A. Mason, J. Chem. Phys. **27**, 75 (1957).

43. R.T Pack, J. Chem. Phys. **78**, 7217 (1983).

44. M.E. Boyd, S.Y. Larsen, and J.E. Kilpatrick, J. Chem. Phys. **50**, 4034 (1969).

45. Available on request to M. Keil.

46. L. Beneventi, P. Casavecchia, and G.G. Volpi, J. Chem. Phys. **85**, 7011 (1986).

47. L.R. Linshits, I.B. Rodkina, and D.S. Tsiklis, Russ. J. Phys. Chem. **51**, 1381 (1977).

48. G. Herzberg, *Molecular Spectra and Molecular Structure III. Electronic Spectra and Electronic Structure of Polyatomic Molecules* (Van Nostrand Reinhold Co., New York, 1966).

49. (a) F. Battaglia, F.A. Gianturco, and A. Palma, J. Chem. Phys. **80**, 4997 (1984); (b) C.V. Boughton, R.E. Miller, P.F. Vohralik, and R.O. Watts, Mol. Phys. **58**, 827 (1986).

50. (a) J.M. Bowman and S.C. Leasure, J. Chem. Phys. **66**, 288 and 4724 (1977); (b) S.C. Leasure and J.M. Bowman, Chem. Phys. Lett. **48**, 179 (1977); (c) G. Pfeffer and D. Secrest, J. Chem. Phys. **67**, 1394 (1977).

51. (a) R. Goldflam, S. Green, and D.J. Kouri, J. Chem. Phys. **67**, 4149 (1977); (b) V. Khare, D.E. Fitz, and D.J. Kouri, J. Chem. Phys. **73**, 2802 (1980).

52. R.T Pack, J. Chem. Phys. **66**, 1557 (1977).

53. M. Faubel, K.H. Kohl, and J.P. Toennies, Faraday Discuss. Chem. Soc. **73**, 205 (1982).

54. A.D. Buckingham and P.W. Fowler, J. Chem. Phys. **79**, 6426 (1983).

CHAPTER 7

General Discussion

This thesis has reported DCS measurements for the elastic scattering of thermal energy He atoms by crossed beams of Ne, Ar, Kr, Xe, OCS, CO_2, C_2H_2, C_2H_4, C_2H_6, and CHF_3. For the most part, these results were used along with other published scattering data, when available, and dilute-gas data from the literature to determine interatomic and intermolecular potential energy surfaces from multiproperty fitting. The reported best-fit potentials were obtained by adjusting parameters of assumed analytical forms to minimize a dimensionless fitting quality parameter δ,[1,2] with an automated nonlinear least-squares fitting algorithm.[3] The sensitivity of scattering cross sections and dilute gas properties to the interatomic potential energy for thermal energy, low reduced-mass, atom + atom van der Waals interactions was also investigated.[4]

By analytically modifying a model interatomic potential energy function for the HeKr interaction, the sensitivity of various properties to the interaction potential was determined.[4] The ICS should be used whenever available for velocities low enough to exhibit resolved orbiting resonances. Such data help determine the attractive well. The DCS also provides great sensitivity to the attractive well depth and position, and to the weakly repulsive wall. It is nevertheless insensitive to the outer bowl of the attractive well. Low temperature virial measurements though, are sensitive to the outer bowl of the attractive well. The repulsive wall can be fixed by high temperature virials and a transport property measured accurately over a wide temperature range (usually only true for viscosity measurements). All of the foregoing influences are correlated and therfore, when available, the DCS, the ICS, mixture viscosity, and interaction second virial data should be fitted simultaneously. The He + heavier inert gas studies presented in this thesis utilized these results.

The highly oscillatory HeAr DCS results[1,2] established the capability of the newly-constructed apparatus to produce accurate, high-quality scattering data. We used the best available interatomic potential for this system, the HFD potential of Aziz et al.,[5] without modification, to compare the calculated DCS with our measured one.[1] The comparison was excellent at all scattering angles and, therefore, established the reliability of the apparatus and the accuracy of the measured DCS results. This comparison also served to determine our true scattering zeroline. Initial calculations for HeAr also allowed the *effective* overall apparatus angular resolution[1,2] to be fitted to the DCS data, simultaneously with the potential parameters. The optimized angular resolution parameter for the HFD and MSV parameterizations was 1.69° and 1.67°, respectively. This calibration is, therefore, independent of the assumed interatomic potential, and thus reliably estimates an apparatus characteristic that would otherwise be very difficult to determine for our apparatus.

The HFD potential of Aziz et al.[5] was used to calculate the DCS in the center-of-mass reference frame. Transforming the DCS to the laboratory frame, accounting for the kinematics, and averaging over the velocity distributions of the crossed beams and the angular resolution of the apparatus, allowed a direct comparison to our measured data. The true scattering zeroline was determined as the average of the angular shifts necessary to ensure scattering symmetry of the first and second oscillations, on either side of the He beam, including kinematic transformations for the angle and the intensity but without reference to the interatomic potential. The HeAr DCS therefore initially served as a calibration system for our apparatus.

More extensive DCS measurements conducted for HeAr as well as DCS's for HeKr, and HeXe fulfilled Aziz' call for high quality DCS measurements for these systems.[5(b)] Including these measurements in multiproperty fits with literature mixture viscosity and interaction second virial data lead to the determination of accurate interatomic potentials for these interactions.[2] The potentials reproduced the above properties faithfully and consistently, and predict diffusion and thermal diffusion more accurately than current measurements allow. Our best-fit HeAr HFD interatomic potential is essentially identical to the one reported by Aziz et al.[5(a)] One of the HeKr potentials reported by Watanabe et al.,[6] although they were unable to state a strong preference for any of their four proposed XC potentials, is indistinguishable from our best-fit HFD potential, which is slightly deeper than the Smith et al.[7] HFD potential. Our HeXe HFD interaction potential has a deeper and wider attractive well than the previously reported potential.[7]

When fitting parameters of assumed mathematical forms to experimental data, the interatomic potentials obtained accurately represent the true interatomic potential only to the extent that the mathematical form can reproduce the true potential. We checked the model dependence for the He + heavier inert gas interactions by using the HFD and MSV potential forms to fit the data. Both are physically reasonable, but parametrize the repulsive wall and attractive well regions differently. They will give similar potential energy curves only to the extent that they are constrained by the sensitivity, consitency, and accuracy of the properties to which they are fit. The best-fit HFD and MSV potentials are essentially indistinguishable for the HeAr, HeKr, and HeXe interactions.[2] Consequently, we have confidence that our best-fit potentials for these systems are the correct ones. We prefer the HFD potential however, because the MSV potential yields repulsive walls that become to soft at very high energies (though beyond the range sampled by the data considered).

Model bias was further investigated for the fitted potentials using the best-fit HFD and MSV results for HeAr, HeKr, and HeXe, along with some modification studies[2,4] for the HeKr and HeXe data, to estimate the accuracy with which various regions of the potential energy curves were known, independent from the paramters used to describe them. The attractive well depth was determined to ±3%, the attractive minimum position to ±0.03 Å, and the zero crossing of the potential to ±0.015 Å. We believe that these results represent the best determined interatomic potentials reported for the He + heavier inert gas interactions.[5(b),8,9]

The extensive studies performed for the heavier rare gases was extended, in collaboration with U. Buck et al. and T. W. Dingle, to include the HeNe interaction.[10] There are more scattering data (DCS's and ICS's) and dilute-gas data covering a wider temperature range for this system than for any of the other rare gas systems reported in this work. As well, SCF calculations have been performed for this system,[10] and there exist interatomic potentials obtained from the direct inversion of high-quality DCS results,[11] and from the direct inversion of transport data.[12] The best-fit HFD potential reported for HeNe in this thesis (our HFD1),[10] provided the best reproduction of all of these properties with only two adjustable parameters (r_m and C_8). Consequently, the direct inversion technique to determine interatomic potentials,[13] even from high-quality DCS measurements, is not as accurate as the potentials presently obtained by multiproperty fits in the reproduction or prediction of several of the various properties available.[10]

The HeNe interaction also demonstrated that more accurate SCF calculations are required to fix the repulsive wall and eliminate the need to adjust the parameter controlling the potentials range. Further, providing there exist accurate dispersion coefficients, and accurate SCF repulsive walls, the HFD interatomic potential could be entirely determined. For the HeNe interaction, the dispersion coefficients are accurately known,[14] therefore a single parameter (r_m) fit was possible. This fit yielded the same HFD potential as the previous two parameter fit.[10] The availability of accurate SCF and long range dispersion coefficients for the He + rare gas interactions will, therefore, allow an even better determination of the interatomic potentials, than those reported in this work.

When He atoms are scattered from crossed beams of polyatomic, Σ-state molecules, the intermolecular potential energy is not only a function of the separation, but also of the relative orientation and the internal coordinates of the molecules (i.e. is anisotropic). Further, inelastic processes can occur during the collisions at thermal energies due to the internal degrees of freedom of the molecular partner. Total DCS's, reported in this thesis, do not resolve elastic from inelastic contributions to the scattering. It is also important to note that the highly oscillatory behaviour observed for He + rare gas scattering[2,10] is not observed for our He + molecule systems due to damping by the molecular anisotropy.[1,15]

It was therefore not clear that total DCS results provided sufficient information to be used to extract correct anisotropic intermolecular potential energy surfaces. By measuring incompletely resolved rotationally inelastic DCS's for $HeCO_2$, Buck et al.[16] showed that the empirical anisotropic potential, from multiproperty fits, of Keil and Parker[17] provided an inadequate description of their data. We remeasured the total DCS for $HeCO_2$ and were able to demonstrate, following the same procedure as given by Buck et al.,[16] that we obtained the same radial anistotropy parameter as they did to within the respective precision of the experiments.[1] Consequently, total DCS results can be sufficiently precise and highly resolved, and used to extract "reasonable" anisotropic intermolecular potentials.

The HeC_2H_2 and HeOCS total DCS's were also measured.[1] These cross sections exhibit moderate and severe damping of the oscillatory structure, respectively. Damping of diffraction oscillations is primarily caused by the molecular radial anisotropy, which is better determined than the well depth anisotropy for these low reduced-masss systems.[17-21] Such damping was predicted by Cross semiclassically,[22] and by Pack using IOSA quantum mechanical calculations.[23] It was also clear, from these DCS's, that estimates of molecular anisotropy based on van der Waals radii,[24] which predicted that C_2H_2 was both longer and narrower than the CO_2 and OCS molecules, could be qualitatively and quantitatively incorrect.[25] Damping of diffractive oscillatory structure for the HeC_2H_2 interaction also showed a pronounced angular dependence, suggesting that different regions of the potential exhibit varying degrees of anisotropy. The HeOCS data were reproduced quite well with an angularly symmetric anisotropic potential. This suggests that, for these low reduced-mass systems, the total DCS is not sensitive enough by itself, to allow extraction of an asymmetric potential correctly reflecting the $C_{\infty v}$ symmetry of OCS.

The moderate damping observed for the HeC_2H_2 interaction led us to investigate the HeC_2H_4, and HeC_2H_6 interactions as well.[15] These interactions allow one to investigate the effect of the π electrons on the scattering, compared to open shell atom + hydrocarbon interactions,[21,26] and the effectiveness of the terminal hydrogens in extending the overall molecular length. In collaboration with P. J. Dunlop, who measured limiting diffusion coefficients and interaction second virial data for these systems, we determined anisotropic intermolecular potentials for these interactions from multiproperty fits. We also determined an effective spherical potential for $HeCHF_3$.[15]

The observed anisotropy trend was $HeC_2H_6 > HeC_2H_4 \sim HeC_2H_2$. This decreasing anisotropy trend, as measured by $r_m^{\parallel} - r_m^{\perp}$, closely parallels the decreasing carbon-carbon bond length in the same sequence. The anisotropy trend is opposite to that observed for both H and Li atoms interacting with the same molecules. It is possible that the open shell atoms interact more strongly with the molecular π bonds, attaining shorter interaction distances for the perpendicular approach than for the corresponding closed-shell He atom interactions. The observed anisotropy trend is also opposite to the one expected on the basis of end-to-end hydrogen-hydrogen distances, illustrating the ineffectiveness of the terminal H atoms in extending the van der Waals molecular shape.

In summary, this thesis has reported accurate interatomic potentials for HeNe, HeAr, HeKr, and HeXe. The number of parameters necessary to determine these potentials (presently 2 or 3) could be reduced if accurate short range SCF, and long range dispersion calculations were available. Nevertheless, the interatomic potentials reported for these interactions are among the most accurately known. Total DCS measurements can provide correct determinations of anisotropic intermolecular potential energy surfaces. Although not determined as accurately as the He + rare gas potentials, He + molecule potentials, particularly when dilute-gas data is available to constrain parts of the potential, can be determined very well from multiproperty fits. We have reported anisotropic intermolecular potentials for HeOCS, HeC_2H_2, HeC_2H_4, HeC_2H_6, and an effective spherical potential for $HeCHF_3$. Until such time as accurate *ab initio* calculations can be performed for the entire potential energy surface, the DCS, along with other scattering data (ICS), and the dilute-gas data will remain essential properties for determining accurate potential energy surfaces.

References

1. L.J. Danielson, K.M. McLeod, and M. Keil, J. Chem. Phys. **87**, 239 (1987).
2. L.J. Danielson and M. Keil, J. Chem. Phys. **88**, 851 (1988).
3. D.W. Marquardt, J. Soc. Indust. Appl. Math. **11**, 431 (1963).
4. M. Keil and L.J. Danielson, Can. J. Phys. **66**, 159 (1988).
5. (a) R.A. Aziz, P.W. Riley, U. Buck, G. Maneke, J. Schleusener, G. Scoles, and U. Valbusa, J. Chem. Phys. **71**, 2637 (1979); (b) R.A. Aziz in *Inert Gases: Springer Series in Chemical Physics* edited by M.K. Klein (Springer-Verlag, Berlin, 1984); Vol. 34.
6. K. Watanabe, A.R. Allnat, and W.J. Meath, Chem. Phys. **68**, 432 (1982).
7. K.M. Smith, A.M. Rulis, G. Scoles, R.A. Aziz, and V. Nain, J. Chem. Phys. **67**, 152 (1977).
8. G.C. Maitland, M. Rigby, E.B. Smith, and W.A. Wakeham, *Intermolecular Forces: Their Origin and Determination* (Clarendon, Oxford, 1981).
9. G. Scoles, Ann. Rev. Phys. Chem. **31**, 81 (1980).
10. M. Keil, L.J. Danielson, U. Buck, J. Schleusener, F. Huisken, and T.W. Dingle, J. Chem. Phys. (in preparation).
11. R.B. Gerber, M. Shapiro, U. Buck, and J. Schleusener, Phys. Rev. Lett. **41**, 236 (1978).
12. G.C. Maitland and W.A. Wakeham, Mol. Phys. **35**, 1429 and 1443 (1978).
13. U. Buck, Rev. Mod. Phys. **46**, 369 (1974).
14. (a) A. Kumar and W. J. Meath, Mol. Phys. **54**, 823 (1985); (b) K.T. Tang, J.M. Norbeck, and P.R. Certain, J. Chem. Phys. **64**, 3063 (1976).
15. L.J. Danielson, M. Keil, and P.J. Dunlop, J. Chem. Phys. **88**, 4218 (1988).
16. U. Buck, H. Meyer, M. Tolle, and R. Schinke, Chem. Phys. **104**, 345 (1986).
17. M. Keil and G.A. Parker, J. Chem. Phys. **82**, 1947 (1985).

18. R.T Pack, E. Piper, G.A. Pfeffer, and J.P. Toennies, J. Chem. Phys. **80**, 4940 (1984).

19. G.A. Parker, M. Keil, and A. Kuppermann, J. Chem. Phys. **78**, 1145 (1983).

20. L. Beneventi, P. Casavecchia, and G.G. Volpi, J. Chem. Phys. **85**, 7011 (1986).

21. G.O. Este, D.G. Knight, G. Scoles, U. Valbusa, and F. Grein, J. Phys. Chem. **87**, 2772 (1983).

22. R.J. Cross, J. Chem. Phys. **52**, 5703 (1970).

23. R.T Pack, Chem. Phys. Lett. **55**, 197 (1978).

24. G.J.B. Hurst, P.W. Fowler, A.J. Stone, and A.D. Buckingham, Int. J. Quantum Chem. **29**, 1223 (1986).

25. (a) A.D. Buckingham and P.W. Fowler, J. Chem. Phys. **79**, 6426 (1983); (b) F.A. Baiocchi, W. Reiher and W. Klemperer, J. Chem. Phys. **79**, 6428 (1983).

26. E.W. Rothe and R.K.B. Helbing, J. Chem. Phys. **50**, 3531 (1969).

APPENDIX A

Experimental Details

A.1. GENERAL

A.1.A. Design Considerations

Before proceeding to discuss each of the experimental components in detail, we shall consider the necessary design criteria for a high-resolution crossed beam apparatus.[1] There are several important considerations in this regard. First, and most important, is the vacuum in which the beams are formed and their interactions studied. It must be able to allow the generation of high intensity beams and provide pressures low enough, in the chamber where the collisions will be studied, to ensure that only single collisions are significant. Second, the signal-to-noise ratio must be good enough to allow statistically meaningful measurements to be made. This criterion is coupled with the vacuum considerations (necessary to ensure low background gas levels), with the generation of high-intensity beams, with the sensitivity of available detectors, and with the desired apparatus angular resolution. Third, the overall apparatus angular resolution must be sufficient to resolve the expected structure in the measured data. Finally, the alignment of the crossed beams into a well defined zone, and the rotation of the detector (or sources) about that zone, is crucial in order to determine accurate results. Each of these criteria will be discussed in more detail in this section.

The vacuum in which the beams are formed (the source chambers) must be able to handle the gas load from the beam sources and maintain low enough pressures to prevent significant attenuation of the beams on their way into the scattering chamber (where the collisions are studied). To ensure that the beam intensities are large, to overcome some of the signal-to-noise limitations (discussed later in this section), one can use supersonic expansions to form the beams.[2] Such beams are produced by expanding a gas in a region of high pressure, through a small hole into a region of low pressure. The amount of gas exiting the source, entering the source chamber, can be as high as $\sim$ 10 torr-ℓ sec^{-1} for a good He beam.[3] Typical nozzle-skimmer distances are $\sim$ 10 mm. The vacuum requirements for the source chambers can therefore be determined by the pressure required to ensure that the mean free path, λ, of the expanded gas is at least on the order of 10 mm. For He, the product of the mean free path with the pressure, for hard sphere interactions, is given by $\lambda P = 18.0 \times 10^{-3}$ cm-torr (near room temperature).[4] However, for the beams considered here, soft collisions will lead to scattering out of the beam. The λP for such collisions is $\sim 1.5 \times 10^{-3}$ cm-torr. To obtain a λ of 15 mm therefore, requires a pressure of 1.0×10^{-3} torr. Given the throughput of 10 torr-ℓ sec^{-1}, and the required pressure, leads to a minimum required pumping speed of $\sim$ 6000 ℓ sec^{-1} for the source chambers. These speeds are easily attained with commercially available diffusion pumps.

The amount of gas entering the scattering chamber depends on the angular divergence of the beams. For typical conditions,[3] with a nozzle-skimmer distance of 10 mm and a skimmer diameter of 0.5 mm, the angular divergence is $\sim 3^\circ$ (assuming the nozzle is a point source). The angular distribution from a supersonic source is represented by a $\cos^2\theta$ function.[1,2] Therfore, the proportion of all molecules with forward intensity is given by

$$\int_0^{\frac{\pi}{2}} \sin\theta\cos^2\theta d\theta = -\frac{1}{3}\cos^3\theta\Big|_0^{\frac{\pi}{2}} = \frac{1}{3} \ . \qquad (A-1)$$

Considering the angular divergence of $\sim 3^\circ$ (0.053 radians) we integrate from 0 to 0.026 to get

$$\int_0^{0.026} \sin\theta\cos^2\theta d\theta = -\frac{1}{3}\cos^3\theta\Big|_0^{0.026} = 3.5 \times 10^{-4} \ . \qquad (A-2)$$

Thus, of the total flux in the forward direction, the proportion 1.0 x 10^{-3} emerges from the source chamber into the scattering chamber.

Recalling that we had 10 torr-ℓ sec^{-1} into the source chambers, results in a beam gas load of ~ 0.01 torr-ℓ sec^{-1} into the scattering chamber for each beam. Now, considering the source chamber as an effusive source, we can determine the effusive gas load into the scattering chamber. The number of molecules leaving the effusive source (i.e. passing through the skimmer) can be determined from[1]

$$N = \frac{1}{4} n \bar{v} A_s \qquad (A-3)$$

where A_s is the area of the skimmer orifice, n the number density, and $\bar{v}$ the mean velocity of the molecules in the source chamber. Assuming a pressure of ~ 1 x 10^{-3} torr and a temperature of ~ 300 K, gives $n = 3.2 \times 10^{13}$ molecules cm^{-3}. Taking $\bar{v}$ as ~ 1100 m/sec and $A_s \sim 2 \times 10^{-3}$ cm^2 leads to $N \approx 2 \times 10^{15}$ molecules sec^{-1}. Recall that 1 torr-ℓ corresponds to ~ 3.5 x 10^{19} molecules. Therefore the effusive gas load from the source chamber into the scattering chamber is ~ 5 x 10^{-5} torr-ℓ sec^{-1}. This load is much smaller than the beam gas load and need not be considered in the pumping speed requirements for the scattering chamber.

Assuming that the background gas, in the scattering chamber, is a mixture of beam gases, and that the detector is located ~ 50 mm from the intersection zone of the beams, we want to ensure that there are no secondary collisions during this 50 mm path length. In other words, we want the mean free path, λ, to be much larger than 50 mm. Assuming an average λP of 1.2 x 10^{-3} cm-torr for soft (or low-angle) collisions, and a λ of at least 100 cm, leads to a minimum required pressure of ~ 1 x 10^{-5} torr. For the 0.02 torr-ℓ sec^{-1} throughput, this pressure requires a minimum pumping speed of ~ 2000 ℓ sec^{-1} for the scattering chamber.

Before discussing signal-to-noise considerations, the requirements for the angular resolution of the apparatus will be presented. In order to measure highly resolved He + rare gas DCS's (as we have in this thesis), the required apparatus angular resolution can be estimated from the spacing of the diffraction oscillations. This spacing can, in turn, be estimated from Fraunhoffer diffraction theory[5] where

$$\sin\theta = \frac{\lambda \#_i}{\pi d} , \qquad (A-4)$$

with λ the de Broglie wavelength (~ 0.56 Å for He atoms with a velocity of 1775 m/sec), $\#_i$ are the ith zeroes of the first (for minima) and second (for maxima) order Bessel functions, and d is the target diameter (2σ, with σ the target cross section). For He atoms scattered by Ne atoms (σ_{Ne} = 2.69 Å), one would predict minima at 7.3°, 13°, 20° etc., and maxima at 9.8°, 16°, 23° etc. using this simple theory. Thus, the spacing between the first minimum and the first maximum is ~ 2.5°. If the target atom were Xe (σ_{Xe} = 3.6 Å), one would predict minima at 5.4°, 10°, 15° etc., and maxima at 7.3°, 12°, 17° etc. The spacing from the first minimum to the first maximum for HeXe is only ~ 1.9°. Therefore, resolving the oscillations for the HeXe interaction would require an apparatus angular resolution of less than 1.9°. This is a rather restrictive angular resolution, putting very high demands on the sensitivity of the detector. Such an angular resolution is usually accomplished with careful selection of beam and detector collimators.[3]

With the desired angular resolution in mind, the next consideration is one of signal-to-noise. The scattered signal obtained will depend on the intensities of the beams, the angular resolution, the vacuum conditions, and the sensitivity of the detector. The noise will arise from the usual sources of electrical interferences,[6] and from the background gas detected by the detector. In order to estimate the signal-to-noise ratio, one must estimate the expected scattered signal intensity. To achieve the desired angular resolution, let us assume that we collimate the molecular beams down to an angular divergence of ~ 1° inside the scattering chamber. From Eqns. (A-1) and (A-2), we would therefore expect the proportion 1.2×10^{-4} (or 1.2×10^{-3} torr-ℓ $\sec^{-1}$) to reach the interaction zone (or scattering center). Estimating that the nozzle is ~ 60 mm from the scattering center, for an angular divergence of 1°, the beam cross sectional area is ~ 0.009 cm^2. The number of collisions, leading to scattering out of the collision zone, can be given by

$$N_c = j_1 j_2 \sigma V \frac{1}{v_{rel}} , \qquad (A-5)$$

where j_1, j_2 are the beam fluxes (# cm^{-2} $\sec^{-1}$), σ the collision cross section (cm^2), V the collision volume (cm^3), and v_{rel} the relative velocity of the crossed beams.

The volume of the collision zone is ~ 0.003 cm^3, and for He + Ar, the collision cross section is ~ 6 $Å^2$ sr^{-1} (6×10^{-16} cm^2 sr^{-1}) for wide-angle scattering, and the relative velocity is ~ 1860 m/sec. Recall that for He we estimated a flux of 1.2×10^{-3} torr-ℓ $\sec^{-1}$ which is equivalent to ~ 4.7×10^{18} molecules cm^{-2} $\sec^{-1}$. Further, recall that the mean free path for this beam, in the source chamber, is on the order of the nozzle-skimmer distance. Therefore, we would expect to lose a factor of ~ 3 (e^1; Beer's law) in the beam intensity, giving 1.6×10^{18} molecules cm^{-2} $\sec^{-1}$ for this beam. For Ar, we would expect the flux to be about one-half of this[3] giving ~ 7.8×10^{17} molecules cm^{-2} $\sec^{-1}$. Substituting into Eqn. (A-5) we find that the number of collisions is, $N_c \approx 1.0 \times 10^{13}$ $\sec^{-1}$. That is, ~ 1.0×10^{13} molecules $\sec^{-1}$ are scattered out of the collision zone. Now, assuming the detector is collimated to view only the collision zone ($\theta_{det} \sim 1.29°$), it will see ~ 5×10^{-5} steradians. Therefore, the detector will receive ~ 5×10^{8} molecules $\sec^{-1}$.

If we detect the scattered He atoms, with a velocity of ~ 1775 m/sec, then each He atom contains ~ 1×10^{-20} Joules of kinetic energy. Consequently, the detector will receive ~ 5×10^{-12} J $\sec^{-1}$ or ~ 5×10^{-12} Watts of power.

The detector must, therefore, be very sensitive in order to get a good signal-to-noise ratio. A good infrared detector will have a noise equivalent power (NEP) of $\sim 10^{-14}$ W/$\sqrt{\mathrm{Hz}}$ giving a signal-to-noise ratio of $\sim$ 100 or better for these signal levels, assuming a noise level on the order of $\sim 1 \times 10^{-8}$ Volts and a chopping frequency of $\sim$ 26 Hz. This is, in fact, $\sim$ 10 times better signal-to-noise than we observe (Sec. A.4.A) due to the poor assumption that the source chamber pressure, in the region of the nozzle and the skimmer, is the same as it is everywhere else in the chamber. To give the correct signal-to-noise ratio (about 10), the pressure in this region would have to be about 3 times greater than what we have calculated. Also, the noise level at the chopping frequency is usually somewhat higher than $\sim 1 \times 10^{-8}$ Volts.

Finally, the alignment of the two beams into a well defined collision zone is very important. The detector must also rotate about this collision zone to avoid introducing systematic errors into the measured DCS's. Proper alignment can be ensured by defining the scattering center with an alignment pin and the beam path with the skimmer and the alignment pin. The nozzle and collimators can be positioned onto the beam path using an optical telescope. Alternatively, one can machine alignment edges and steps into the various components to ensure their proper alignment once assembled. The alignment edges can be properly positioned using either an optical telescope or a HeNe laser to define the beam path through the scattering chamber. The second approach, although more time consuming and costly at the construction stage, is far more versatile and time saving in the operation of the apparatus, and is the alignment method used by us. That is, once the alignment edges and steps are properly positioned, the various components (nozzle, skimmer, source chambers, etc.) can be removed and replaced without any need for realignment. The repositioning accuracy can be as good as $\pm 25\ \mu$m - $\pm 40\ \mu$m depending on the machined tolerances.

A.1.B. Apparatus Description

Our experimental apparatus has, for the most part, been described in Secs. 2.2 and 5.2. With reference to Fig. 2.1, the apparatus consists of two supersonic beam sources (S_1 and S_2) intersecting at 90°, and an in-plane rotatable liquid helium cooled bolometer detector (B). Also shown is a non-rotatable mass spectrometer used for beam optimization and monitoring. These components are bolted to the central scattering chamber in prealigned locations, and their characterization and optimization will be discussed in this appendix.

The source chambers are "tee" shaped with a vertical height of ~ 53 cm, and a horizontal length of ~ 54 cm. The vertical diameter is ~ 40 cm, to be consistent with the inner diameter of the Varian VHS-400 diffusion pumps (8000 ℓ sec^{-1} for air) used for these chambers. The front end of the "tee", which mates to the scattering chamber, has an inner diameter of ~ 25 cm. The other end of the "tee" has an inner diameter of ~ 40 cm (see Fig. 2.1). The VHS-400 diffusion pumps are backed independently by Leybold-Heraeus S160C mechanical pumps (40 ℓ sec^{-1}), through ~ 4-5 m of ~ 18 cm diameter PVC tubing. With no gas flowing into these chambers, their pressures are ~ 1 x 10^{-7} torr, with backing pressures of ~ 35 mtorr. With a fully optimized He beam on, the primary source chamber pressure, corrected for He,[4] is ~ 3 x 10^{-3} torr with a backing pressure of ~ 250 mtorr. For an Ar beam in the secondary source chamber, the pressure is ~ 1 x 10^{-3} torr with a backing pressure of ~ 300 mtorr.

The scattering chamber is essentially a box with dimensions of ~ 60 cm long x ~ 60 cm wide x ~ 41 cm high. It contains four "ports" (two sets directly opposite one another; see Fig. 2.1) which have been precision machined with an inner diamter of 24.133 ±0.003 cm; their centers all being at the same vertical height. The source chambers couple to the scattering chamber using precision alignment steps with an outer diamter of 24.125 ±0.003 cm. The positioning of the ports on the scattering chamber walls can be seen from Fig. 2.1. This chamber is pumped by a Varian VHS-10 diffusion pump (5000 ℓ sec^{-1}) which is backed by a Leybold-Heraeus D8A mechanical pump (~ 3 ℓ sec^{-1}). There is a gate-valve between the VHS-10 and the scattering chamber, allowing the VHS-10 to be valved off, and remain pumping, while the apparatus is open to the atmosphere for servicing. With no beams coming into the scattering chamber, its pressure is $\sim 1 \times 10^{-7}$ torr with a backing pressure of ~ 30 mtorr. With both beams on, the scattering chamber pressure goes up to $\sim 5 \times 10^{-6}$ torr (corrected for He) with a backing pressure of $\sim$ 50-70 mtorr.

The scattering chamber also houses the rotating bolometer detector. One can design an apparatus with either rotating sources or a rotating detector. Rotating sources are difficult to construct due to their large mass and bulk. Similarly, a rotating mass-spectrometer detector is both very difficult to construct and very expensive. Use of a rotating bolometer detector, which is small and light, alleviates both the design and cost problems of the alternative methods of obtaining DCS's. Our detector, donated by Prof. J. C. Polanyi (University of Toronto), is an excellent detector for the elastic DCS measurements reported in this work due to its sensitivity (it has a stated NEP of 10^{-14} W/$\sqrt{\mathrm{Hz}}$).

It will also be very useful in the inelastic HF + Rare gas experiments which are currently in progress. In these experiments, a beam of HF molecules will be formed in the ground vibrational and rotational state. A crossed atomic beam will cause translation-to-rotation energy transfer, producing HF in an excited rotational state. A line-tunable HF chemical laser then probes the HF + Rg scattering volume, exciting only those HF molecules in the specific state to which the laser is tuned. The increased vibrational energy in the scattered HF can then be detected by the bolometer detector (a thermal flux detector), which rotates about the scattering volume. Thus, the laser + bolometer experiments provide the capablility of measuring the scattered angular distributions for HF in any specific rotational state. Consequently, the rotating bolometer detector will prove to be very useful in future experiments conducted on this apparatus.

The non-rotatable mass spectrometer is used, in this work, to characterize the various atomic and molecular beams used in this thesis. It is differentially pumped; the outer chamber is identical to the source chambers described earlier. This chamber is pumped by an NRC-6 diffusion pump ($\sim$ 1500 ℓ sec^{-1}) which is backed by the same Leybold-Heraeus D8A mechanical pump ($\sim$ 3 ℓ sec^{-1}) used for the scattering chamber VHS-10 diffusion pump. The inner mass spectrometer chamber, which houses the mass spectrometer, is separated from the outer chamber by isolation valves and is pumped by an Edwards 6" water-cooled baffled Diffstak (700 ℓ sec^{-1}) backed by its own D8A mechanical pump. When not used for beam characterizations, the Diffstak is closed off with a butterfly valve, and a Varion I-3 Triode Vacion pump (20 ℓ sec^{-1}) is used to maintain the vacuum ($\sim$ 1 x 10^{-6} torr) in the inner chamber. As shown in Fig. 2.1, the mass spectrometer is separated from the scattering chamber by a gate-valve. This allows it to be repositioned, if desired, without interrupting the vacuum of the inner chamber. It also permits opening the scattering chamber to atmosperic pressure without shutting off the mass spectrometer diffusion pumps. With no beam entering the mass spectrometer, the outer chamber vacuum is $\sim$ 1 x 10^{-6} torr and the inner chamber vacuum, pumped by the Edwards Diffstak, is $\sim$ 1 x 10^{-7} torr with a backing pressure of $\sim$ 25 mtorr. These pressures do not change significantly when a beam enters the mass spectrometer due to its differential pumping.

All of these pumps are controlled individually by a central panel. This panel allows each pump to be switched on or off and also serves as a safety interlock system for the apparatus. The interlock system ensures that the apparatus will shut down (terminates all power to the diffusion and mechanical pumps) if the diffusion pumps are not receiving adequate cooling water; if the diffusion pumps get too hot; if a mechanical pump fails; if the pressure in the scattering chamber exceeds some adjustable preset limit; or if the backing pressures of the source chamber diffusion pumps, or the scattering chamber diffusion pump, or the inner mass spectrometer diffusion pump exceeds some preset limit. It will also send a signal to the University Control room indicating a failure, and someone there will notify one of the people from the laboratory of that failure.

A.2. BEAM NOZZLE AND SKIMMER ASSEMBLIES

A.2.A. Nozzle Assembly

Both the primary (always He in these experiments) and the secondary beams are generated using essentially identical nozzle assemblies. The beam gas passes through a mass flow controller (Tylan FC260) before it enters the source chamber. The gas then travels through an Inconel 600 nozzle tube (Fig. A.1) which has a machined step to hold a Pelco platinum aperture disk. These disks are 3 mm in diameter by 0.240 mm thick, and can be chosen to give nozzle diameters between 20 μm and 400 μm. The disk is sealed (metal to metal seal) into the machined step with a retaining nozzle cap (Fig. A.1) which has a 30° cone near its front end to facilitate nozzle alignment. The platinum nozzle disks seal very reliably, even after several uses at high temperature and pressure.

The nozzle tube fits into a stainless steel nozzle alignment tube (Fig. A.1) with a front end inner cone. The essential difference between the primary and secondary nozzle assemblies is the ability to heat the secondary nozzle to a maximum temperature of ~ 500 °C. A length of nichrome wire has been wrapped around the secondary nozzle tube and nozzle alignment tube to provide the heating element. The heater is controlled with a Love Model 49-886 temperature controller using a K-type thermocouple. The nozzle alignment tube is mounted, with water cooled brass mounts, to an aluminum channel. This channel is mounted, using alignment pins and bolts, to a Deltron Model S3-12 bearing plate allowing the nozzle assembly to be moved along the beam axis with an external beam pusher. The bearing assembly is in turn bolted to an inverted NRC Model 39 tilt platform which is itself separated from, and bolted to a second NRC Model 39 tilt platform to give the entire nozzle assembly three degrees of freedom. These degrees of freedom, which to a certain extent, can be affected by external controls

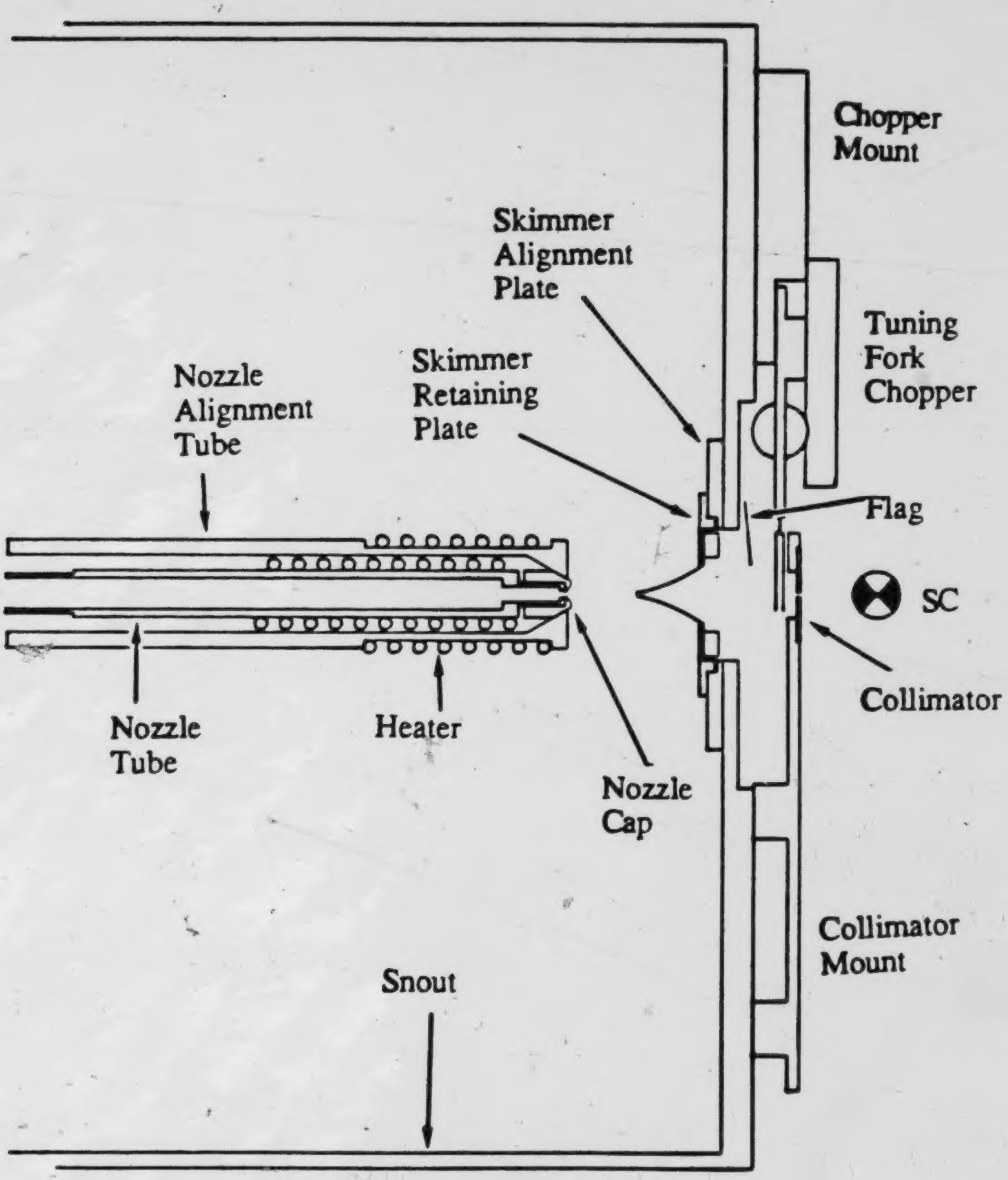
Chopper Mount
Skimmer Alignment Plate
Tuning Fork Chopper
Nozzle Alignment Tube
Skimmer Retaining Plate
Flag
SC
Collimator
Nozzle Tube
Heater
Nozzle Cap
Collimator Mount
Snout

Figure A.1

Side view of the nozzle skimmer assembly, showing the alignment stages used for these components. The scale is 0.75 inches = 1 inch.

(through mechanical feedthroughs into the source chambers), allow optimization of the nozzle alignments through the skimmers and collimators, onto the detector, not just alignment for the nozzle-skimmer separation.

A HeNe laser beam, was set up to pass through the center of two opposite ports on the scattering chamber, with the nozzle assembly removed from the the source chamber, defining the beam path. The machined alignment cone of the nozzle tube was properly positioned by adjusting the two tilt platforms to obtain a good HeNe laser diffraction pattern, opposite the nozzle, with the laser beam passing through the nozzle tube (the Pelco aperture disk was removed). This alignment was optimized to allow the nozzle-skimmer distance to be varied from ~ 5 mm up to ~ 40 mm retaining its alignment integrity. Final nozzle alignment was ensured using either the mass spectrometer or bolometer detector (at 4 K) to optimize the beam signal, by adjusting the external tilt platform controls. Once properly aligned, the nozzle tube could be removed, the Pelco aperture disk changed, and replaced without being realigned. This alignment philosophy, used throughout the apparatus, greatly facilitated the many beam characterizations conducted in this work (Sec. A.3).

A.2.B. Skimmer Manufacture and Mounting

The skimmers used in the work reported in this thesis were manufactured in our laboratory (by two summer students; Donald Stanley and Gary Samek) by electroplating nickel onto a machined mandril.[7] The mandril, made out of stainless steel, has a 1.9 cm base diameter and is 1.3 cm long, from the base to the apex of the cone. The 1.9 cm stainless steel rod is machined to a point on a 3.6 cm radius originating 3.51 x 2.04 cm (X,Y) from the center of the rod. This results in the apex of the mandril being ~ 50 μm in diameter and the larger end of the cone being 1.19 cm in diameter.

The electroplating solution, donated by Harshaw Chemical of Canada Ltd., contains 280 g/ℓ nickel sulphamate, 12.5 g/ℓ nickel chloride, and 31.2 g/ℓ of boric acid. The nickel metal used, in the form of crucibles ~ 8 cm in diameter and ~ 8 cm high, is from Sargent-Welch. Prior to use, the electroplating solution is pH buffered to a pH of ~ 4.0 by adding nickel carbonate. Further, 16 mls of a wetting agent (NPA) are added to 950 mls of the electroplating solution to prevent pitting. A nickel crucible, connected to the positive terminal of a Lambda Model LL-903 power supply, is submerged in approximately 700 mls of the electroplating solution in a 1000 ml beaker. The mandril, connected to the negative terminal, is immersed up to the 1.9 cm base into the solution inside the nickel crucible.

The mandril was rotated slowly and the electroplating solution heated to 55 ±2 °C. Good plating results were then obtained by passing 0.25 amperes of current through the solution for ~ 43 minutes. The cones thus obtained were ~ 50-100 μm thick. Removal of the nickel cones from the mandril proved to be the most difficult part of the skimmer manufacturing process. This problem was surmounted by placing the plated mandril in liquid nitrogen for ~ 5 minutes and then immediately into boiling water (repeating if necessary) until the nickel cone fell off.

These cones were then drilled out to a slightly smaller hole size than was required. The desired hole size was then obtained by dipping the drilled tips of the cones into concentrated nitric acid for up to 9 minutes. The resulting holes were very sharp (nearly knife edge), and circular. If left in the acid too long, the holes became less circular and eventually too thin and jagged at the tip. In this way, we prepared skimmers ranging is size from ~ 125 μm to ~ 1000 μm in diameter. Obtaining a specific skimmer size (to within a few microns) generally required a trial and error method using several nickel cones.

Following the same alignment philosophy as for the nozzle assembly described earlier, the skimmers were mounted in self aligning retainer plates (Fig. A.1). The base size of the skimmers, at their largest ends, was very reproducible and provided a suitable alignment edge for the retaining plates. These plates were then mounted in prealigned (using a HeNe laser as above) alignment plates (Fig. A.1). In this way, just as for the nozzles, the skimmers could be changed without requiring any realignment.

A.3 BEAM CHARACTERIZATIONS

As discussed in Sec. 2.2.A, the atomic and molecular beams used in this work were characterized using the mass spectrometer detector (Extrel 041-1 ionizer, EAI 200 quadrupole mass filter, and Gallileo 4770 Channeltron). Beam intensities and velocity distributions were measured as functions of nozzle size, mass flow through the nozzle, nozzle-skimmer distance, nozzle temperature, and dimer-to-monomer ratio in the beam. The optimized beam conditions for these characterizations are collected in Table A-1.

The results presented in Table A-1 were obtained by determining the optimum mass flow, at a fixed nozzle-skimmer distance (usually 10 mm), for a given nozzle size at room temperature, by monitoring the beam intensity. Subsequently, the best nozzle-skimmer distance was determined at the optimum mass flow. Once these two parameters were fixed at their optimum values, the velocity distribution and dimer-to-monomer ratio were measured. The mass flow used was often lower than the optimum value to ensure lower dimer concentrations in the beams, and to conserve gas (particularly for the costly Xe and Kr beams). At this point, the nozzle temperature was increased, if necessary, to suppress dimer formation. The optimum mass flow and nozzle-skimmer distance are unaffected by increases in the nozzle temperature (when using mass flow controllers to control the gas throughput of the nozzle). This entire procedure was then repeated for a different nozzle size. For most of the beams generated in this work, the formation of dimers in the beams limits the intensities that can be obtained. For the He and Ne beams this is not the case. The intensity of these beams can be increased only by higher pumping speeds in the source chambers and higher nozzle pressures.

In an effort to achieve a more intense He beam, we investigated reducing the backing pressure to the VHS-400 diffusion pump for this beam. That is, if the

Table A-1. Optimized Beam Conditions

Gas	Nozzle (μm)	Flow (sccm)	NSD (mm)	$\Delta v/v$ (%)	Temp. (K)	Press. (atm)	D/M[a]
He	50	800	9.5	$\sim 4^b$	302	14.9	—
	100	700	10.0	$\sim 5^b$	302	4.5	—
	150	1100	8.0	$\sim 5^b$	302	4.4	—
Ne	70	500	11.0	5.4	302	10.2	—
	100	700	12.0	5.4	302	5.1	—
Ne^c	100	426	6.0	8.4	302	6.4	—
Ar	150	150	10.5	6.7	302	1.6	—
	200	350	13.0	6.6	302	1.0	0.006
	250	350	15.0	6.9	302	0.97	0.004
	300	500	15.0	7.2	302	0.57	0.004
	400	500	15.0	7.8	302	240	—
Kr	300	150	13.0	7.6	513	0.35	0.004
Xe	300	100	12.0	9.5	734	0.35	0.0003
CO_2	300	350	13.0	18.0	562	0.62	0.0002
OCS	300	150	11.0	17.7	418	0.30	0.00004
C_2H_2	300	250	11.0	21.7	303	0.28	0.0004
C_2H_4	300	250	11.0	23.0	303	0.28	—
C_2H_6	300	250	11.0	24.0	303	0.29	—
CHF_3	300	200	13.0	18.0	303	0.36	—

[a] Measured dimer-to-monomer ratio.
[b] Estimated from Reference 6.
[c] After some nozzle problems with the Ne beam (see text Sec. A.3).

backing pressure is too high, then the diffusion pump's effective pumping speed will be reduced. With the Leybold-Heraeus S160C mechanical pump (40 ℓ sec^{-1}) backing this diffusion pump, we inlet ~ 10 torr-ℓ sec^{-1} of He gas (through a 50 μm nozzle with a driving pressure of 14.9 atmospheres). The source chamber pressure was ~ 3.6 x 10^{-3} torr, the backing pressure 250 mtorr, and the scattering chamber pressure ~ 4 x 10^{-6} torr (all corrected for He). Backing the VHS-400 with a Leybold-Heraeus WAU-500 Roots Blower (~ 150 ℓ sec^{-1}) lead to a source chamber pressure of ~ 2.4 x 10^{-3} torr, a backing pressure of 160 mtorr, and a scattering chamber pressure of ~ 4 x 10^{-6} torr. Since the pressure in the source chamber decreased by roughly the same proportion as the backing pressure, one could conclude that the S160C backing pump may be limiting the beam intensity. This is not certain however, since the beam intensity was not directly determined.

For the more condensable gases, CO_2, OCS, and to some extent the hydrocarbons, the S160C backing pump gave us some trouble. For the worst case, OCS, the backing pressure would slowly rise from ~ 250 mtorr to > 500 mtorr in a few hours (with an optimized OCS beam inlet into the secondary chamber), attenuating the beam in the source chamber. It would appear that these gases dissolve slightly in the backing pump oil, building up pressure over time, until at backing pressures > 500 mtorr the diffusion pump's pumping speed is reduced substantially. For these gases, we found it necessary to "purge" the S160C with dry nitrogen gas, inlet directly into the gas ballast valve on the S160C, continuosly during an experiment. The combined backing pressure due to OCS and the nitrogen "purge" was maintained between 300 mtorr and 400 mtorr. It was also necessary to "purge" the S160C for up to 15 minutes, once the OCS beam was turned off, in order to reach a backing pressure of less than 100 mtorr with no gas flowing and the "purge" turned off.

One can see two entries in Table A-1 for the Ne beam with a 100 μm nozzle diameter. On the first day of experimentation for the HeNe DCS, the Ne beam optimized at the first entry in Table A-1 for this nozzle size. On the second day however, a large sudden increase in the nozzle pressure was observed for the Ne flow rate of 700 sccm. The nozzle pressure in the secondary chamber cannot exceed $\sim$ 7 atmospheres since, unlike the primary nozzle assembly, the gas feed line into the secondary chamber is teflon. At pressures greater than $\sim$ 7 atmospheres in this teflon line, we noticed that there were leaks at several of the teflon connectors inside the source chamber (checked previously). Therefore, the flow rate had to be reduced to provide an acceptable nozzle pressure for this beam. Reoptimizing the nozzle-skimmer distance at this lower flow, we found it to be 6 mm rather than 12 mm. The crucial issue was whether or not the measured DCS data for these two beam conditions would be the same. We found that the two DCS's were completely superimposable at all angles, and proceeded to complete the HeNe work with the "new" beam conditions without further investigation of this problem.

Typical mass flow scans for He and Ar are shown in Fig. A.2 for several nozzle sizes at fixed nozzle-skimmer distances. The beam intensity is not measured on an absolute scale with the mass spectrometer detector, and consequently the observed relationships (along the vertical scale) between the plotted curves in Fig. A.2 do not contain any information. The shape of the curves however, contain the information sought in beam characterizations. At low mass flows, as the flow through the nozzle is increased, the beam intensity increases reflecting the larger number of gas molecules exiting the nozzle and reaching the detector. Continued increases in the mass flow eventually lead to a decrease in the measured beam intensity. For the He primary beam, this effect is due to "choking" of the diffusion

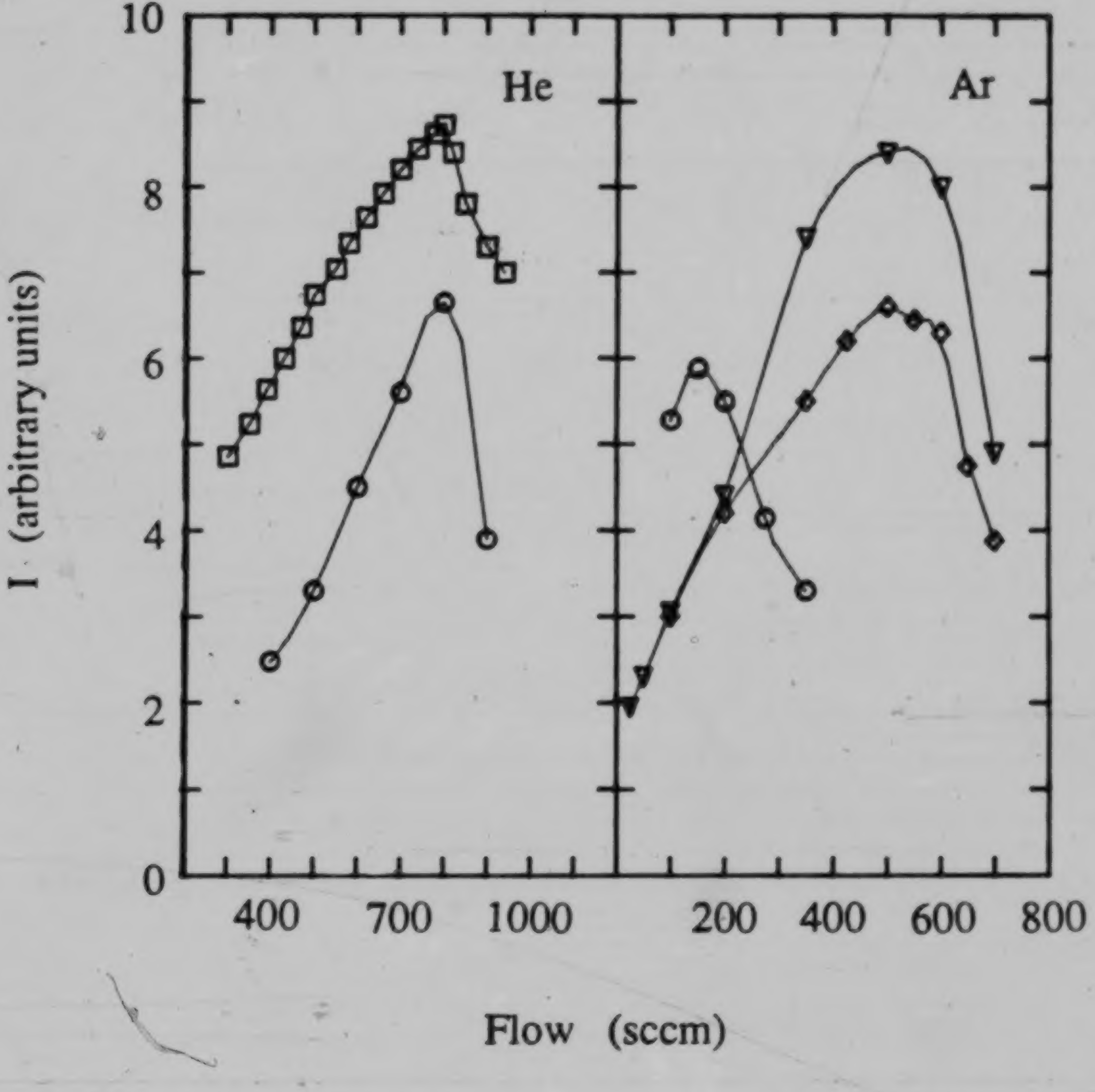

Figure A.2

Flow scans for He and Ar. Symbols correspond to different nozzle sizes and are: (i) He, □; 50 μm, ○; 100 μm, (ii) Ar, ○; 150 μm, ◇; 300 μm, ▽; 400 μm. The relationships between the curves, along the vertical axis, are not meaningful.

pump which pumps the source chamber. From Fig. A.2, the He beam intensity begins to fall sharply for flows $\gtrsim$ 800 sccm, or equivalently, for throughputs $\gtrsim$ 10.5 torr-ℓ sec^{-1}. This is very close to the maximum throughput of the VHS-400 for He gas. Further, from our earlier Roots Blower experiment, the S160C mechanical pump may be limiting the beam intensity. For this throughput, one would estimate a mean free path of $\lesssim$ 1 cm based on a He-He λP of $\sim 1.5 \times 10^{-3}$ cm-torr for soft (low-angle) collisions. This λ may not be correct, since we do not really know what the pressure in the nozzle-skimmer region of the source chamber is. Therefore from our earlier discussion (Sec. A.1.A), the correct λ may be a short as $\sim$ 0.5 cm. The He beam intensity may be falling off due to limitations of both the mechanical pump and the diffusion pump. The background pressure in the nozzle-skimmer region is too high, causing a significant number of collisions between the beam gas atoms and the background gas atoms, scattering beam gas atoms out of the beam.

For the secondary beams, there are two effects which may lead to a decrease in the measured beam intensity. First, as discussed above, the diffusion pump may be "choking". Second, dimer formation in the beam may lead to scattering of beam gas molecules out of the beam. Considering the Ar secondary beam, one can see from Fig. A.2 that for a small nozzle diameter (150 μm) the beam intensity decreases for flows > 150 sccm. For the larger nozzle diameter ($\gtrsim$ 300 μm), the drop in beam intensity occurs at much larger flows (> 500 sccm). It would seem therefore, that there are different, or at least additional, effects leading to decreased beam intensities for smaller nozzle sizes.

Consider the Ar beam generated from the 300 μm nozzle. For this case (see Fig. A.2) the beam intensity begins to drop for a flow of $\sim$ 600 sccm, which corresponds to a throughput of $\sim$ 7.6 torr-ℓ sec^{-1}. As in the He case discussed earlier, this is approximately the maximum throughput (8 torr-ℓ sec^{-1} for air) for the VHS-400 diffusion pump. Assuming the VHS-400 is still pumping 8000 ℓ sec^{-1} gives a source chamber pressure of $\sim 1 \times 10^{-3}$ torr. This pressure corresponds to a mean free path of $\sim$ 1 cm (for low-angle scattering) which is less than the nozzle-skimmer distance of 15 mm for this beam. Consequently, for the larger nozzles with large flows, the diffusion pump cannot maintain a low enough background pressure to prevent a significant number of collisions between the beam gas and the background gas, in the nozzle-skimmer region, and the beam is attenuated.

For the smaller nozzles, the maximum intensity occurs at lower mass flows and therfore attenuation of the beam intensity cannot be explained with the background gas argument employed above. For the 150 μm nozzle used to generate an Ar beam, the maximum flow occurs at $\sim$ 150 sccm. This corresponds to a throughput of only $\sim$ 2 torr-ℓ sec^{-1}, which should give a source chamber pressure of $\sim 2 \times 10^{-4}$ torr and a λ of $\sim$ 4.5 cm. The nozzle-skimmer distance for this beam is $\sim$ 10 mm. Therefore, this λ is $\sim$ 4.5 times longer than the nozzle-skimmer distance. It is unlikely that this will lead to significant attenuation of the beam intensity. For the smaller nozzles, the drop in beam intensity is probably due to the onset of dimers in the beam. Formation of dimers in a molecular beam requires the collision of three molecules. The third molecule removes some of the kinetic energy from the dimer-forming pair allowing a dimer to be formed. These three body collisions may lead to beam molecules being scattered off of the beam axis, reducing the measured intensity. This conclusion is corroborated by the measured velocity distributions presented later in this section.

Nozzle-skimmer scans for He and Ar are shown in Fig. A.3 for several nozzle sizes at their optimum flows. At nozzle-skimmer distances of 1-2 mm, not shown here, the skimmer allows all of the incomming beam to pass into the scattering chamber and consequently one observes a very large beam intensity.[1,2,8] It

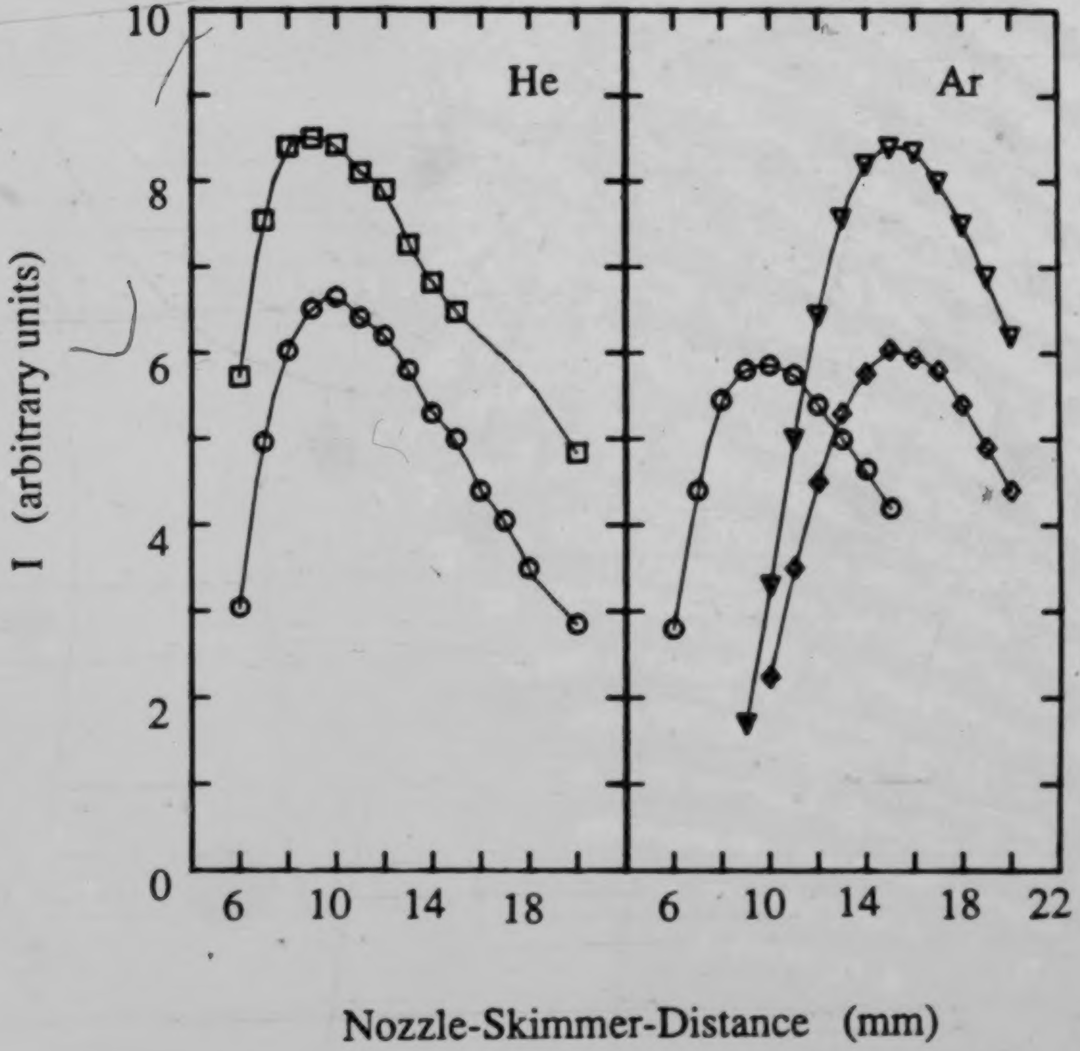

Figure A.3

Nozzle-skimmer scans for He and Ar. Symbols as for Fig. A.2 at the maximum flow for each nozzle size. That is: (i) He, □; 800 sccm, ○; 800 sccm, (ii) Ar, ○; 150 sccm, ◇; 500 sccm, ▽; 500 sccm. The vertical scale is arbitrary as in Fig. A.2.

is well known however, that under these conditions the velocity distribution of the beam is very broad.[5] As the nozzle is moved away from the skimmer, the intensity drops off sharply due to the beam gas interacting with the skimmer (called nozzle-skimmer interference) causing backscattering (attenuation) of the beam. At greater nozzle-skimmer distances, this interference is reduced and the intensity of the beam passes through a maximum. At larger nozzle-skimmer distances, the beam intensity falls off slowly due to attenuation of the beam by the background gas.[2]

Velocity distributions as a function of mass flow are shown in Fig. A.4 for Ar at the optimized beam parameters (Table A-1) for each nozzle size (solid curves). The minima of these curves occur at nearly the same flow as do the maxima for the flow scans (dotted curves) of Fig. A.2. This means that for the smaller nozzle sizes the increase in the velocity distribution, at flows beyond the minima, is due to dimer formation in the beam. For the larger nozzles, the increase in the velocity distribution at large flows is also due to the onset of dimers, rather than to "choking" of the diffusion pump as was the case in the beam intensity plots of Fig. A.2. That is, velocity distributions are unlikely to be affected by attenuation of the beam in the source chamber which should only reduce the number of molecules entering the scattering chamber. The large velocity distributions observed for low flows is due to incomplete relaxation of the beam gas velocities travelling perpendicular to the beam axis upon expansion through the nozzle. These curves generally have very broad minima where the relaxation of the beam due to the expansion is complete and dimer formation is minimal. This allows one to select a flow which will best suit the experiment conducted.

The optimum conditions collected in Table A-1 minimize the velocity distribution and dimer formation in the beam, while optimizing the mass flow and

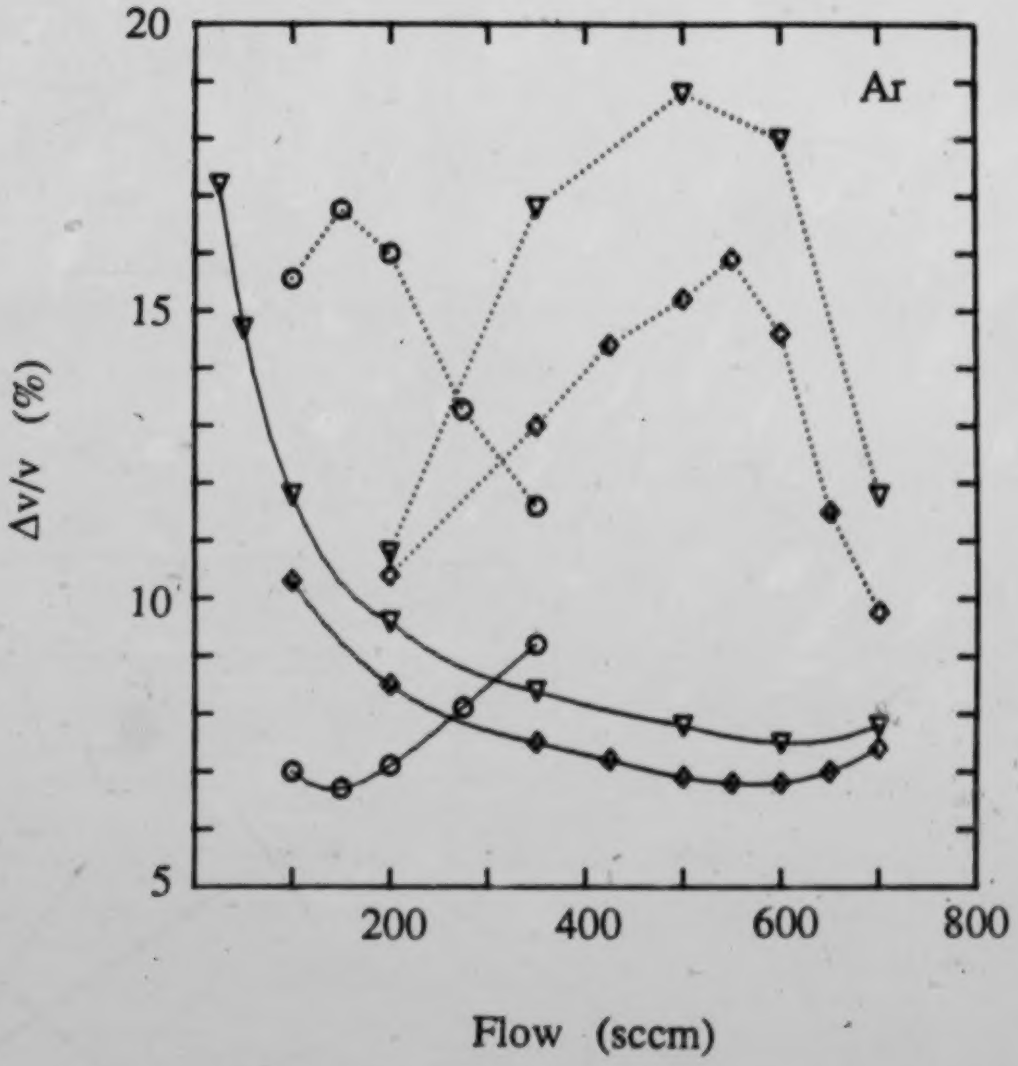

Figure A.4

Measured velocity distributions for Ar (solid curves). The intensity scans from Fig. A.2 are included in this figure (dotted curves) only to aid the discussion (Sec. A.3) Symbols as for Fig. A.2.

nozzle-skimmer distance. In this way, we have selected our best beam conditions for the experiments reported in this work.

The angular profiles of the He and Ar beams are shown in Fig. A.5 as measured by the bolometer detector. For these measurements the bolometer detector was operated at 4 K since the on beam signal generated by the detector at 1.5 K was > 500 mV, the maximum possible signal that can be input to the lockin amplifier. At 4 K however, the detector is not nearly as sensitive as it is at 1.5 K and the output signal is much smaller. For the beam profiles shown in Fig. A.5, the maxima correspond to a measured output signal (from the lockin amplifier) of ~ 100 mV which includes a gain of x200 from the LN-6C bolometer amplifier. The He beam is "flat" on top since at the detector it is only 1.90 mm in diameter, whereas the detector is 2.34 mm wide (see Sec. A.4.B). The Ar beam profile is characteristic of all of the secondary beams used in this work. One can also see that the beam centerlines are at an angle of 90.3° from one another. This is the intersection angle of the two beams. It is important to recognize here that the detector does not rotate about the origin of the molecular beams, but rather about the scattering center. If the beams do not pass through the scattering center, the observed angular profiles would be very different since the detector may not "see" all of the beams. Recall that the nozzle position can be changed with external controls (Sec. A.2.A). Positioning the bolometer detector on the He beam centerline (~ 0°) and adjusting the external controls to move the nozzle off axis by $\lesssim$ 0.5 mm causes the beam signal to drop sharply (intensity decreases by a factor of 2 or 3). The beam signal is therefore very sensitive to the alignment of the beams through the scattering center.

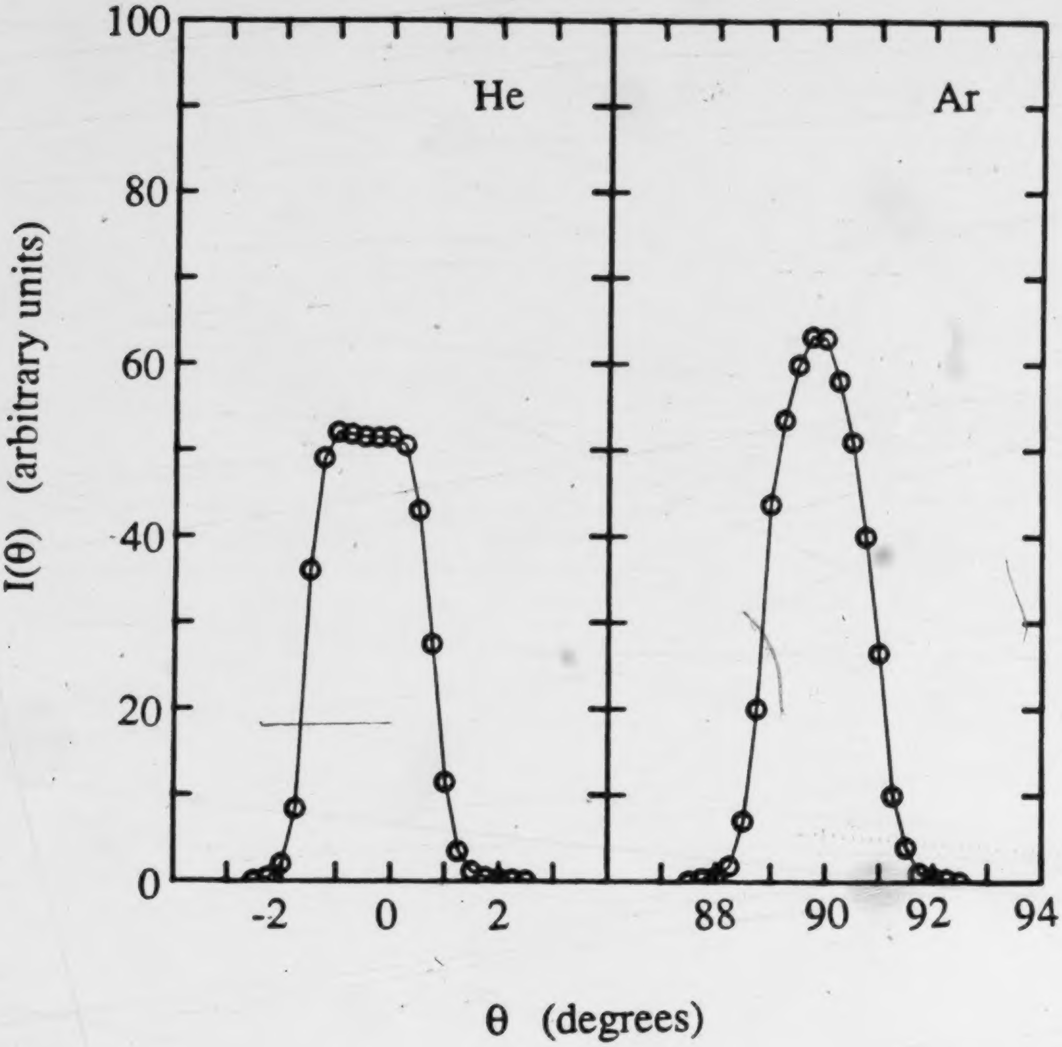

Figure A.5

Angular profiles for the He and Ar beams. Symbols represent measured points. The solid curve is generated from a polynomial fit the the measured data.

A.3.A. Mass Spectrometer Calibration

As discussed in Secs. 2.2.A and A.1.B, the mass spectrometer consists of an Extrel 041-1 ionizer, an EAI 200 quadrupole mass filter, and a Gallileo 4770 channeltron. It has a mass range of 1-500 amu available in three steps: the low mass range, 1-50 amu; the medium mass range, 10-150 amu; and the high mass range 50-500 amu. As indicated in Fig. 2.1, the mass spectrometer is aligned (using a HeNe laser beam as before) to allow an unobstructed flight path of the incoming beam. When not in use, it is maintained in a "standby" status. The gate-valve separating the mass spectrometer from the scattering chamber is closed (Fig. 2.1), the outer chamber vacuum is $\sim 1 \times 10^{-6}$ torr, and the innner chamber vacuum is maintained at 1×10^{-6} torr by an ion pump (Sec. A.1.B). The oil diffusion pump for the inner chamber is valved off with an electro-pneumatic butterfly valve, and is allowed to pump on itself. The ionizer filament is kept warm by applying ~ 1 Watt of power (1 ampere at 1 volt) to it, to keep it clean.

To use the mass spectrometer for beam characterizations, the ion pump is valved off and the butterfly valve on the oil diffusion pump is opened. The isolation valves, located on the beam path at the front and back of the inner chamber (Fig. 2.1) are opened via mechanical feedthroughs into the outer mass spectrometer chamber. The mass spectrometer is then set for an emission current of 8.3 mA and an electron energy of 74 V. The remaining settings are unchanged: ion energy, 25 V; extractor, 15 V; lens 1, 132 V; lens 2, 1.5 V; lens 3, 132 V. The ionizer filament under these conditions heats up to ~ 48 Watts (6 amperes and 8 volts). The channeltron voltage is usually set at ~ 1000 V and a 10^7 Ω input resistance is used. The gate-valve separating the scattering chamber and mass spectrometer outer chamber can then be opened and a beam allowed to enter the mass spectrometer.

The time-of-flight (TOF) chopper used with the mass spectrometer is a four blade chopper 11.5 cm in diameter with slots in two blades and holes in the other two. The slots are 0.391 mm wide located 180° apart on the TOF chopper. The holes are 0.142 mm in diameter located 180° apart on the TOF chopper, and 3.98 cm from its center. This chopper is mounted on a Rofin-Sinar Model 7511 light chopper and operated at 280 Hz (corresponding to a physical frequency of 70 Hz). The circumference of the blade at the center of the holes is 25.00 cm giving a radial velocity of 1750 cm/sec at 70 Hz. A slot is therefore "open" for 22.3 μsec and a hole for 8.1 μsec.

Recall that the beam divergence is $\sim 1.2°$ resulting in a beam spot size of ~ 0.6 mm at the TOF chopper. Therefore, since the slot moves across the beam, the pulse of gas emanating from the TOF chopper will be longer than it would be if the beam was the same width as the slot at the TOF chopper. Further, the beam will continue to diverge on its way to the mass spectrometer. It is necessary, therefore, to aperture down the entrance to the mass spectrometer to provide correct determinations of the beam characteristics. That is, the effective "open" time of the chopper function is a convolution of the chopper slit width with the size of the mass spectrometer entrance aperture and the radial velocity of the chopper. This aperture is located directly in front of the front isolation valve on the inner chamber of the mass spectrometer. A 1.0 mm diameter aperture will result in an effective "open" time of 58.1 μsec (at 70 Hz) while a 0.25 mm diameter aperture will have an "open" time of 14.5 μsec. Therefore, for beams with narrow velocity distributions ($\tilde{<}$ 60 μsec in time) the small collimator was used to prevent mechanical broadening of the measured velocity distributions. For the remaining beams the velocity distributions were larger than 60 μsec in time and the larger collimator was used.

For our He beam, the measured velocity distribution was broadened even though we used a shutter width of 4 μsec (TOF chopper rotated at 150 Hz physical frequency, using the 0.142 mm diameter holes, with a front end mass spectrometer collimator of 0.137 mm in diameter). These conditions should not have caused mechanical broadening of the velocity distribution. The channeltron electronics however have a rise time of ≈ 8.5 μsec and a fall time of ≈ 13 μsec. This corresponds to a minimum measurable velocity distribution of ~ 22 μsec, which for our He beam gives a $\frac{\Delta v}{v} \approx 6\%$ which is what we observe (the He flight time is ~ 370 μsec). Using our He beam conditions to calculate the velocity distribution[10] we find a $\frac{\Delta v}{v} \approx 4\%$.

Beam velocities and their distributions were measured with the TOF chopper (and the mass spectrometer) calibrated using the method of Cross et al.[11] Signals were accumulated by a Lecroy 9400 digital averaging oscilloscope functioning as a multi-channel analyzer. Ion flight times were determined using SF_n^+ fragments from an SF_6 beam, while the flight distance and trigger error were determined by using highly expanded He and Ar beams. This calibration procedure was carried out by an undergraduate student: Gary Samek.

Since the distance from the TOF chopper to the mass spectrometer ionizer is a constant, the flight time of the neutral SF_6 (t_n) will also be a constant, independent of the mass spectrometer electronics and trigger delay. The flight times of the ions SF_5^+, SF_4^+, SF_3^+, SF_2^+, SF^+, F^+, and S^+ (t_i) will all be different depending on their velocities and the distance to the detector. The ion velocity depends on the square root of its mass and energy. The trigger delay (t_{del}) and the electronics delay (t_{el}) will also be constants if the frequency of the TOF chopper and the mass spectrometer settings (ion energy, emission current, preamplifier resistor, and chaneltron voltage) remain constant respectively. The observed flight time (t_{obs}) is then,

$$t_{obs} = (t_{del} + t_{el}) + t_n + t_i \; . \qquad (A-6)$$

Plotting t_{obs} versus $(m/e)^{1/2}$ for the SF_6 fragments, Fig. A.6, should yield a straight line with slope t_i and intercept $(t_{del} + t_{el}) + t_n$. One can see from Fig. A.6 that the SF_6 fragments do fall on a straight line. Therefore, from this plot, we can determine t_i for any m/e value.

The distance from the TOF chopper to the ionizer cannot be determined accurately with a tape measure, since we do not really know where ionization actually occurs in the ionization region. To accurately determine this distance, and also the constant $(t_{del} + t_{el})$, we must measure t_{obs} for some gases whose velocities we know. The obvious choices are members of the rare gas family. We can measure the temperature of our nozzle very accurately (±1 K) and consequently the velocity of the rare gas expansion. We want to find t_n where,

$$t_n = \frac{d_n}{v_n} \qquad (A-7)$$

with d_n the distance from the TOF chopper to the ionizer and v_n the velocity of the gas. Plotting

$$t'_{obs} = t_{obs} - t_i \; , \qquad (A-8)$$

where t_i is determined from Fig. A.6, versus v^{-1} should yield a straight line with slope d_n and intercept $(t_{del} + t_{el})$. This plot is given in Fig. A.7 for He through Kr. From these two plots, we can then determine the true flight time for any m/e as follows,

$$t_{true} = t_{obs} - t_i - (t_{del} + t_{el}) \; . \qquad (A-9)$$

Using the appropriate numbers, determined from the plots (A.6 and A.7) , we have,

$$t_{true} = t_{obs} - 3.9016(m/e)^{1/2} - 13.031 \;\; (\mu sec) \; . \qquad (A-10)$$

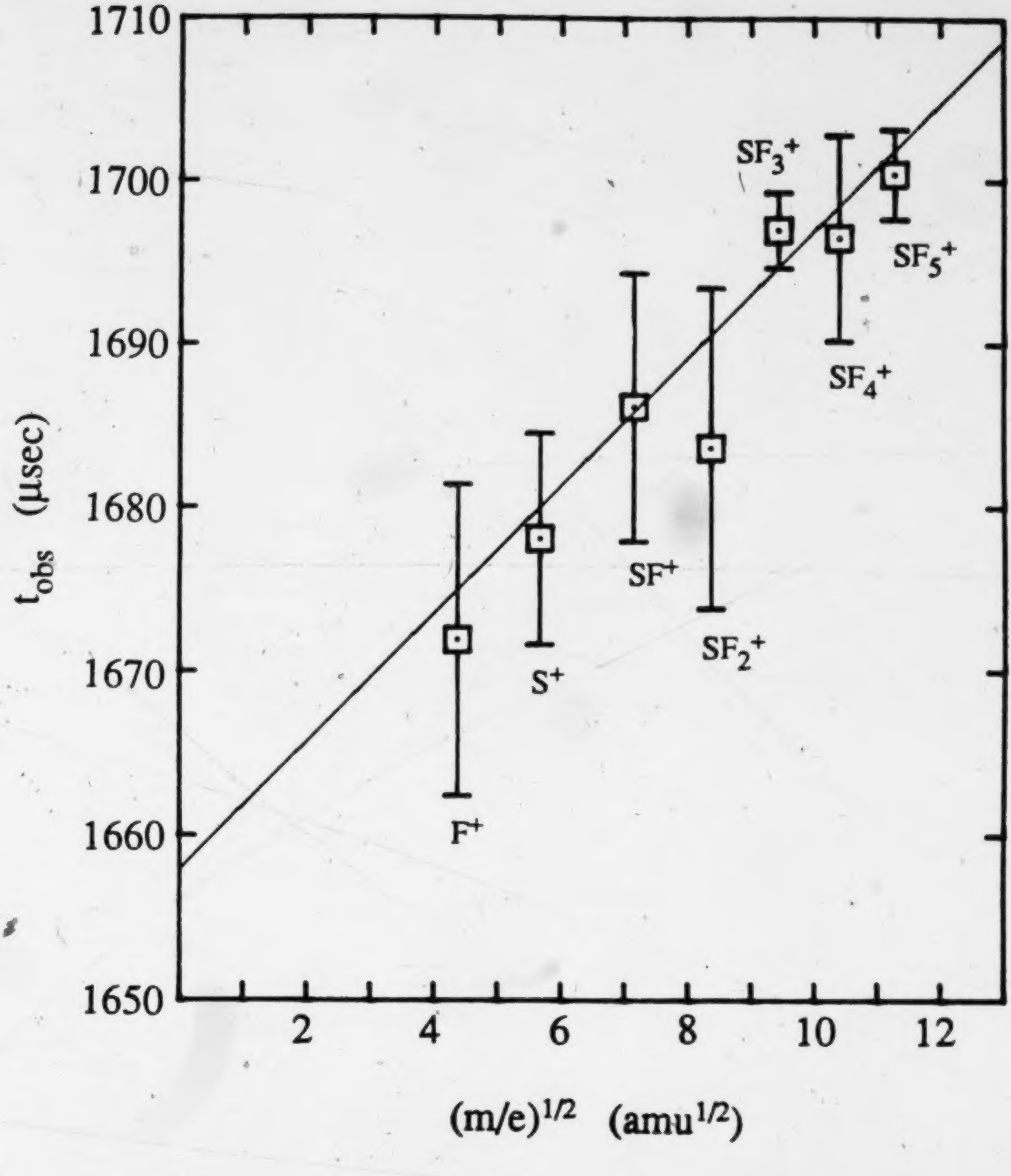

Figure A.6

Mass spectrometer calibration with SF_6. The error bars represent the deviation from several flight time measurements for the indicated fragments. The solid line is generated from a linear regression fit to the data. The slope gives the ion flight time for any m/e value.

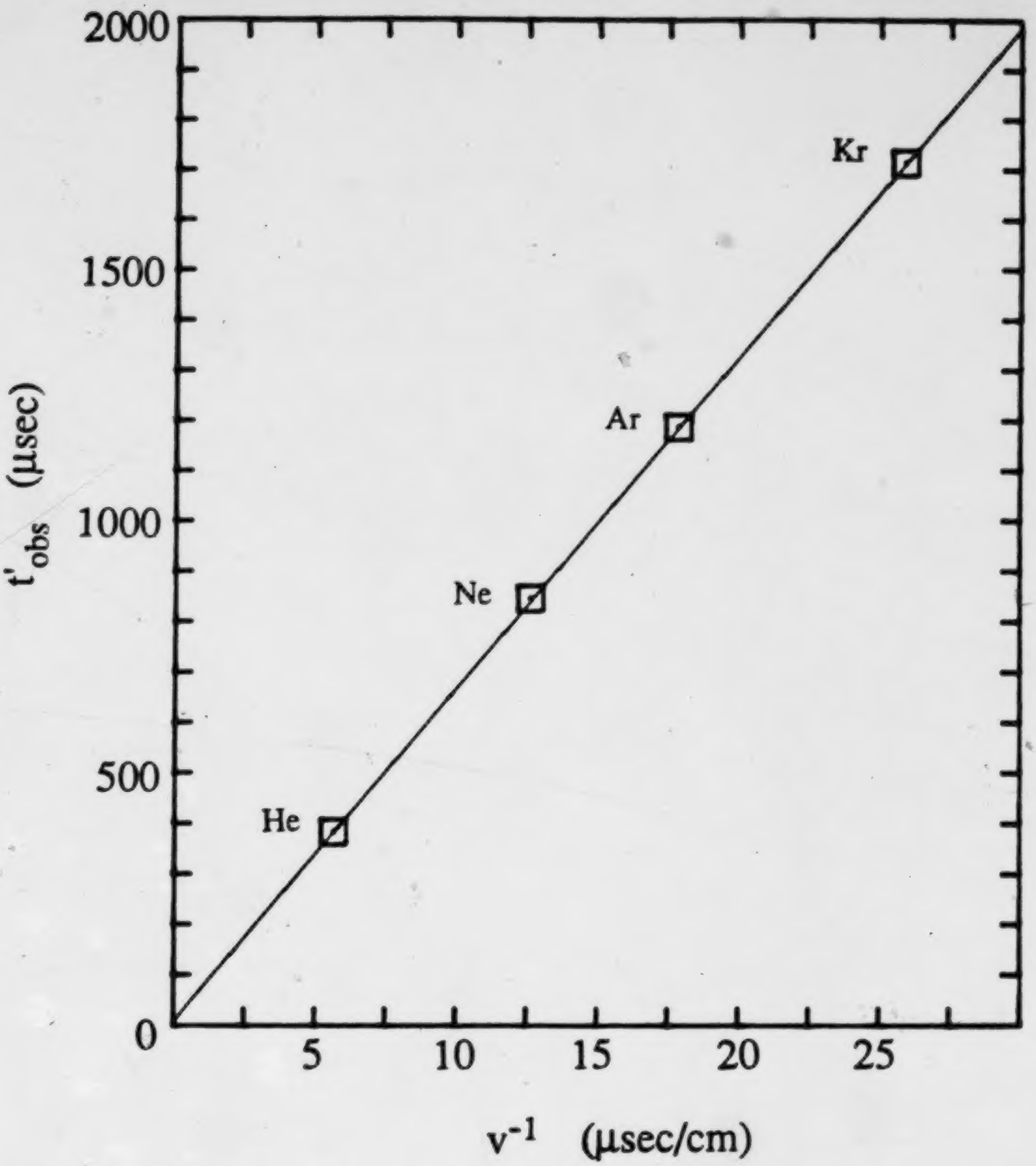

Figure A.7

Mass spectrometer calibration with rare gases. The errors in determining the flight time of these species are smaller than the symbol size used. The solid line, generated from linear regression as in Fig. A.6, gives the trigger delay plus electronics delay (intercept) of the mass spectrometer. The slope gives the distance from the TOF chopper to the ionizer.

The distance from the TOF chopper to the ionizer as determined from Fig. A.7 is 65.674 cm. This agrees well with our crude tape measure measurement of 66 cm.

Using the OCS molecular beam characterizations to demonstrate the application of this procedure, we will step through the entire time-of-flight determination for this molecule. First, the mass spectrometer is used to determine where the OCS beam fragments occur. Figures. A.8 and A.9 show the mass spectrometer background (solid lines) with the OCS beam off and also the background + OCS beam on signals (dotted curves). From Fig. A.8 one can see that at masses below m/e = 29 amu, we do not see any OCS fragments. The large background peaks labelled m/e = 18 and m/e = 28 amu are due to water and nitrogen in the mass spectrometer respectively, which is not a baked system. We would expect to see peaks due to OCS in this mass range; m/e = 28 amu for CO^+, which has a relative abundance (R.A.) of ~ 7%,[12] and m/e = 12 amu for C^+ with an R.A. of ~ 3%.[12] The reason that we do not see these peaks is due to our rather "dirty" mass spectrometer and the low R.A.'s for these peaks (they would be ~ 7-10 times smaller than the OCS parent peak). In the mass range from around m/e = 28 to m/e = 62 amu (Fig. A.9) we can see two peaks due to the OCS beam resulting from S^+, m/e = 32 amu, and OCS^+, m/e = 60 amu. These peaks have R.A.'s of 30% and 52% respectively.[12] The cluster of peaks around m/e = 41 amu are due to hydrocarbon fragments originating from the diffusion pump oil used in the mass spectrometer diffusion pumps. The remaining time-of-flight information was obtained from the OCS parent peak at m/e = 60 amu.

To calculate the velocity distribution of the beam, we must know two things; the flight time of OCS from the chopper to the ionizer, and the width of the OCS beam in terms of time. Using a Lecroy 9400 digital oscilloscope to average the mass spectrometer signals, we determined the flight time of the OCS by

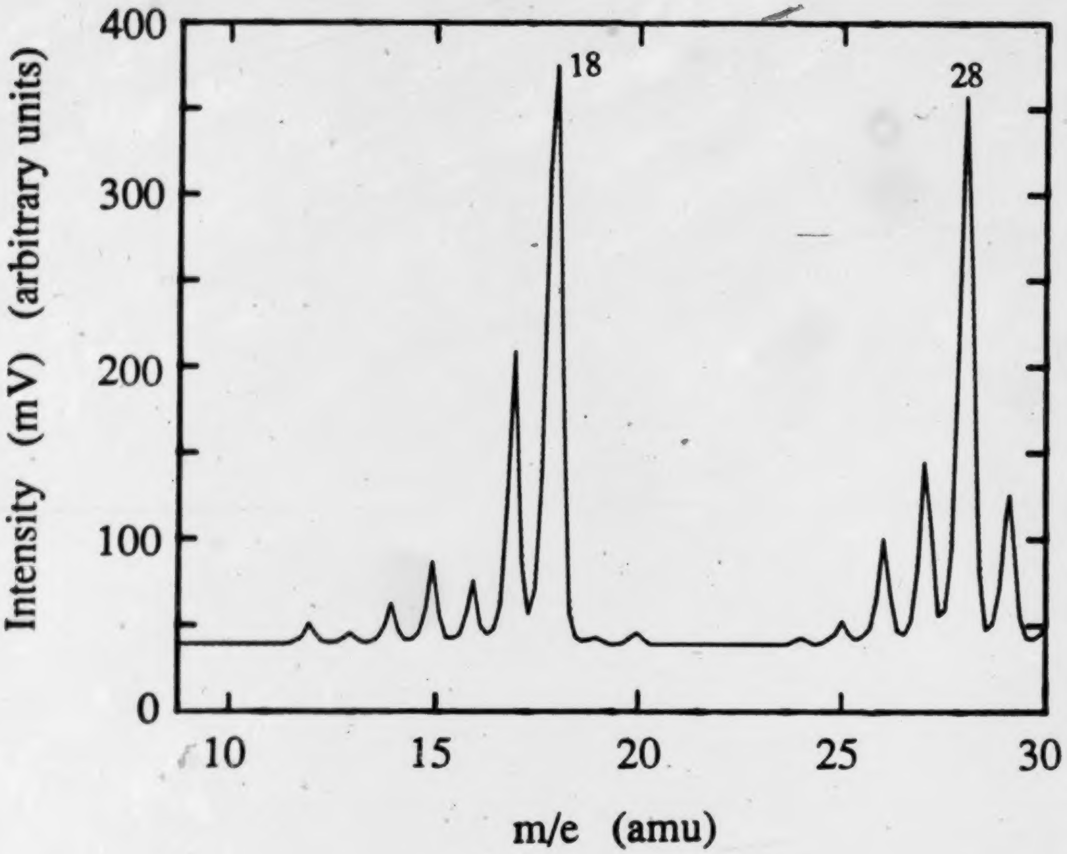

Figure A.8

Mass spectrum for OCS beam from m/e ~ 9 amu to m/e ~ 30 amu. Mass spectrometer background (solid curve) and OCS beam + background (dotted curve) are given. Labelled peaks correspond to H_2O^+, m/e = 18 amu, and N_2^+, m/e = 28 amu.

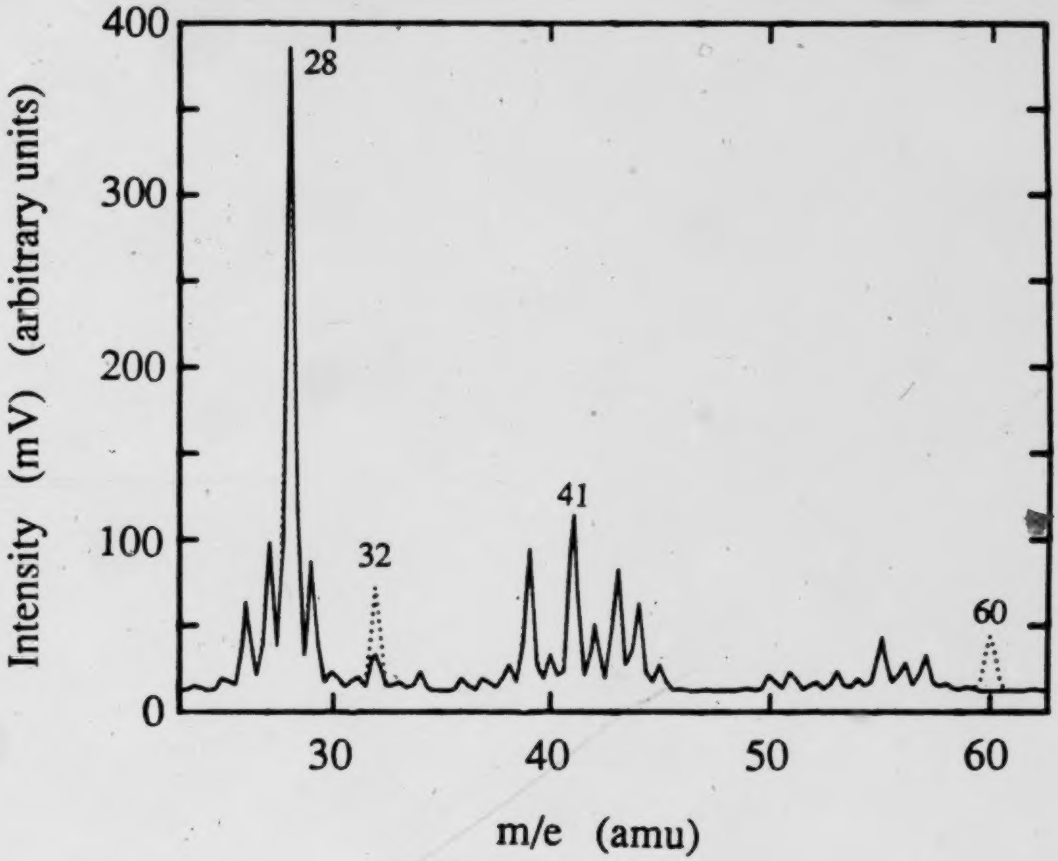

Figure A.9

Mass spectrum for OCS beam from m/e ~ 24 amu to m/e ~ 62 amu. Line types as for Fig. A.8. The labelled peaks correspond to S^+, m/e = 32 amu, and OCS^+, m/e = 60 amu. The cluster of peaks around m/e = 41 amu originate from hydrocarbon fragments in the diffusion pump oil.

measuring the time difference between when the choppper blade "flagged" the beam and when the OCS arrived at the mass spectrometer detector. This plot is shown in Fig. A.10, where the flight time was determined as 1.026 msec. Using the narrow slots in the TOF chopper blades to allow a short pulse of gas to emmanate from the chopper, we determined the time width of the pulse which, as discussed above is affected by the TOF chopper freqency (operated at 70 Hz physical freqency), the mass spectrometer aperture (used the 1.0 mm aperture), and the electronics and trigger delays. This plot is given in Fig. A.11 for OCS. The full-width-at-half-maximum (FWHM) value of this peak was found to be 0.174 msec. Using these numbers in equation (A-5) above, leads to a t_{true} value of 982.7 μsec. The velocity distribution is then simply (for narrow velocity distributions) the peak width over the t_{true}, giving $\Delta v/v = 17.7\%$ which is the value reported for our OCS molecular beam.[13]

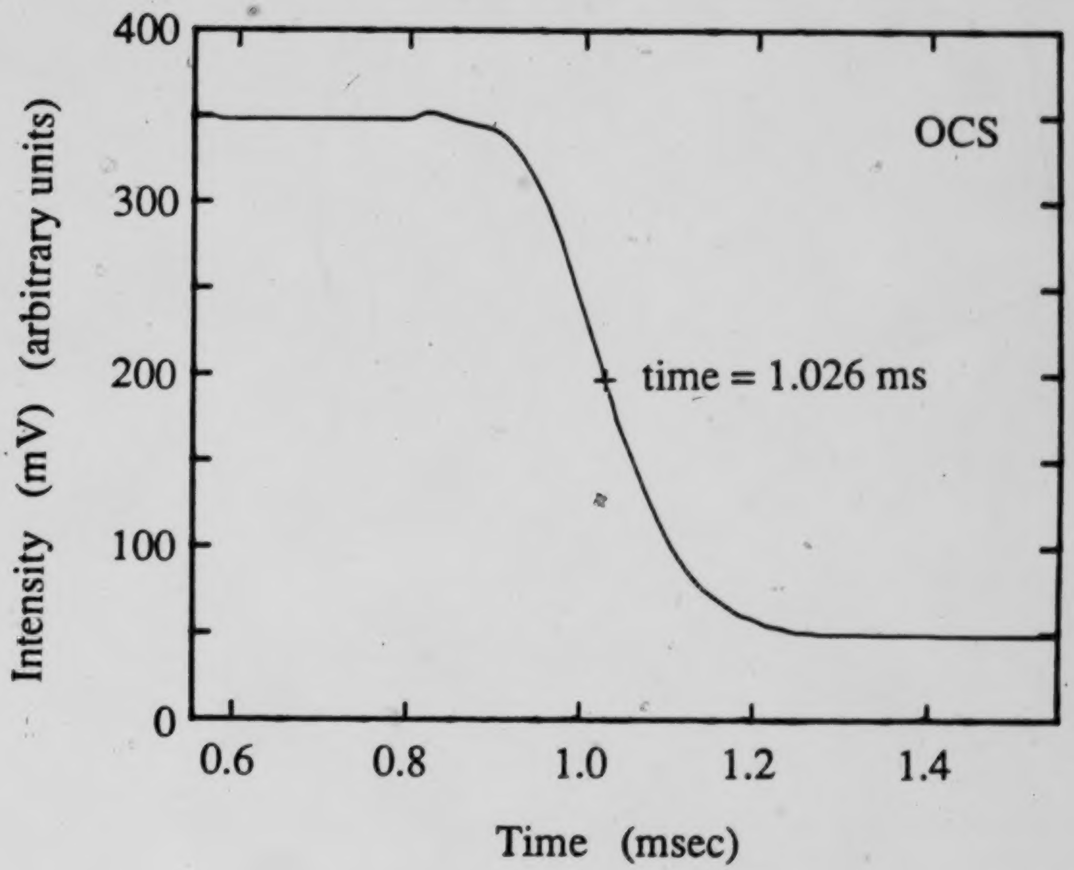

Figure A.10

Flight time for the OCS beam. The solid curve represents the "falling" edge of the TOF chopper. The midpoint of this curve corresponds to the OCS beam being flagged off by the TOF chopper.

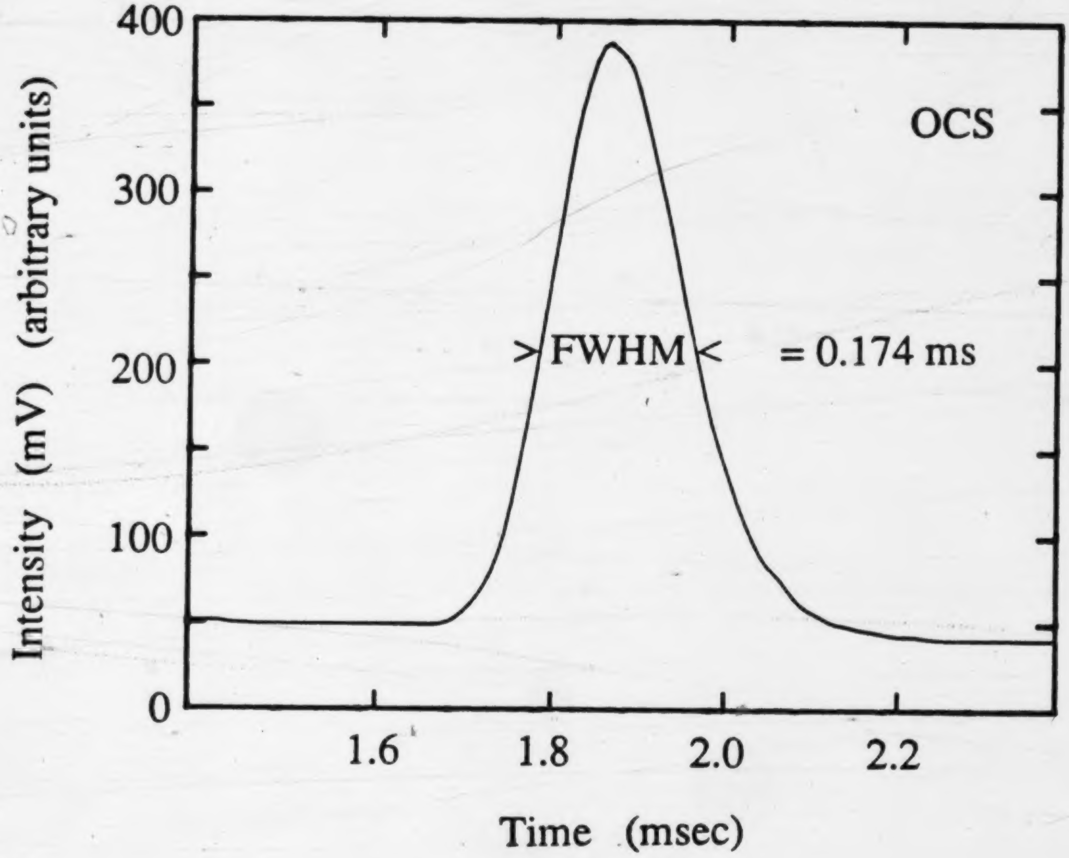

Figure A.11

Velocity breadth of the OCS beam. The solid curve corresponds to the width in velocity of a short pulse of OCS gas from the narrow slots in the TOF chopper.

A.4. SCATTERING CHAMBER AND DETECTOR

The scattering chamber and detector have, for the most part, been discussed in Secs. 2.2.B and A.1.B. This section will provide further details and discuss some experimental problems encountered with these components of the apparatus. The scattering chamber houses the beam flags, choppers and collimators, as well as the bolometer detector and the TOF chopper. The bolometer detector rotates about the scattering center on a $\sim$ 47 cm diameter rotating flange which is centered on the scattering center. The center of the bolometer assembly is located $\sim$ 9 cm off of the center of the rotating flange. This flange is $\sim$ 8 cm high (sitting on the top plate of the scattering chamber) and has a large gear on it to facilitate rotation. A Superior Electric Slow-Syn stepping motor (type M093-FD07E) and controller (Model ST101A) is used to drive a Boston Gear 300 Series Model 01 gear reducer which, in turn rotates the rotating flange. The gear reducer and rotating flange are connected with a Uniroyal Powergrip belt (# 800H100). The stepping motor has 200 steps/revolution and, via the gear reducer, 100 steps corresponds to 1.00° of rotation on the rotating flange. Thererfore, the angular scale on the rotating flange can be positioned and read to ±0.02° (i.e. ±1 step). The angular scale is just a metal tape measure glued and bolted to the rotating flange where 1° of rotation corresponds very precisely to 4 mm on the tape measure.

The stepping motor is driven under computer control (IBM PC-AT) via a parallel output port. For large changes in the desired angle however, positioning of the rotating flange cannot be done reliably under computer control, with the current arrangement. Therefore, manual intervention is necessary to ensure that the desired angle has been reached before data collection begins. To remove the uncertainty in positioning the rotating flange, a 0.64 cm thick by $\sim$ 2 cm long piece of plexiglass is mounted (on a movable mount) about 3-4 mm away from the tape measure angular scale. The plexiglass has a line scratched into it, with a scribe, on either face directly opposite one another. These scratches are darkened with black ink and can then be used to position the rotating flange. Lining up the two lines on the plexiglass (positioned to read 340.0 mm when the bolometer detector is directly opposite the He beam; i.e. at 0.00°) and the appropriate line on the tape measure ensures that the desired angle has been reached ±0.02°. The tape measure has a line every millimeter, corresponding to a 0.25° change in the angle (also corresponds to 25 steps on the stepping motor).

A.4.A. The Bolometer Detector

The detector is a windowless composite Ge bolometer (Infrared Laboratories) operated at 1.5 K by pumping on a liquid helium reservoir. It consists of a 3 mm wide x 9 mm high sapphire heat absorber with a thin $\sim$ 1 mm x $\sim$ 1 mm Ge block epoxied to its center. The heat absorber is thermally and electrically isolated from its copper mount ($\sim$ 4.3 cm long x $\sim$ 2 cm wide x $\sim$ 0.5 cm thick) with small glass support tubes which hold the composite bolometer into a rectangular recess in the copper mount. The Ge block has two gold leads (one from each side) which provide the connections for the input bias voltage and the measured output voltage (dc amplified by an LN-6C amplifier from Infrared Laboratories). Since the device is a semiconductor, its resistance will increase as its temperature decreases. The bias voltage is provided by a 2.72 V mercury battery through a 10 MΩ resistor mounted on the bottom of the liquid He dewar to reduce thermal noise caused by the resistor. The device has a room temperature resistance of 13 Ω and a 1.5 K resistance of $\sim$ 8 MΩ, giving a noise equivalent power (NEP) of 10^{-14} W/$\sqrt{\text{Hz}}$.

The detector is mounted to a modified Model HD-3 liquid He dewar system (Infrared Laboratories). This dewar system has an outer vacuum jacket which is ~ 17.8 cm in diameter and ~ 25 cm high. Inside the vacuum jacket, is a liquid nitrogen dewar (liquid capacity of ~ 0.9 ℓ) with a liquid He dewar directly below it. The liquid He dewar, originally ~ 13 cm in diamter and ~ 8 cm high, was modified (for previous use) by increasing its length and liquid capacity (from ~ 1 ℓ to ~ 1.7 ℓ) with the addition of a 5.1 cm o.d. x 33.0 cm long extension. A right-angle, gold-plated, oxygen free, high conductivity copper bolometer mounting bracket (Fig. 2.2) is bolted to the bottom of the 33 cm long extension. Thus the liquid He dewar assembly is ~ 41 cm long supported by its neck (~ 1 cm in diameter) at the top of the liquid nitrogen dewar. Further, to position the detector at the correct height to view the scattering center, the outer vacuum jacket had to be extended by ~ 10 cm.

In order to ensure that the liquid He (particularly at 1.5 K) lasts a reasonable length of time (~ 10 hours), it is necessary to reduce the thermal radiation load onto the liquid He dewar by means of a liquid nitrogen cooled radiation shield. In the Model HD-3 dewar system, a ~ 14.3 cm o.d. x ~ 14.1 cm i.d. x ~ 14.3 cm long aluminum radiation shield is bolted to the bottom of the liquid nitrogen dewar and therefore surrounds the original liquid He dewar. Due to the 33 cm long extension of the liquid He dewar, the radiation shielding also had to be extended. A ~ 10 cm o.d. x ~ 9.5 cm i.d. x ~ 30 cm long alloy grade aluminum 1100 tube was bolted to the bottom of the original radiation shield. A removable cup ~ 9.5 cm long (positioned with alignment pins), of the same material, was added to the bottom of this tube (Fig. 2.2) to surround the bolometer detector. This entire length of radiation shielding cools to ~ 100 K (near the detector) by way of thermal conduction from the liquid nitrogen dewar in ~ 3 hours. The bolometer assembly is therefore very long (~ 41 cm for the liquid He dewar and ~ 54 cm for the radiation shielding).

Owing to the long length of the modified dewar system, there were many problems with the proper positioning of apertures for the bolometer detector. First, the thermal contraction plus pump down motion of the liquid nitrogen radiation shield was measured with a travelling telescope and found to be 1.96 ±0.05 mm. However, a horizontal motion of up to ~ 0.4 mm was also noticed during these measurements. For the liquid He dewar, the thermal contraction was found to be 1.52 ±0.05 mm, again with a horizontal movement of up to ~ 0.4 mm. These measurements correspond to the difference in position of the apertures at 300 K and 1 atmosphere, to the evacuated and cooled down conditions averaged for several measurements. The entire assembly had to be made more rigid, at least to eliminate the horizontal motion. The liquid He dewar was therefore supported by two sets of three fiberglass standoffs to the radiation shielding. The first-stage standoffs (always there) are located near the bottom of the original radiation shielding. The second-stage standoffs (put in by us) are located at the bottom of the 33 cm long liquid He extension (Fig. 2.2). The standoffs are tightened concentrically (one standoff every 120°) to ensure that the liquid He dewar is not stressed in any particular direction, to avoid problems when the dewars are cooled down. Further, the radiation shielding was supported with three nylon standoffs, to the outer vacuum jacket, located near the bottom of the outer vacuum jacket extension.

These measures however, did not reduce the horizontal motion substantially. Therefore, since the horizontal motion of the liquid He dewar was not independent of the radiation shielding's horizontal motion, a horizontal support post was constructed for the radiation shielding. It is bolted to the outer vacuum jacket of the dewar assembly, and extends down to the bottom of the radiation cup. Vespel standoffs are used to peg the bottom of the radiation cup to the horizontal support post allowing thermal contraction to occur (Fig. 2.2). The horizontal movement was thus reduced to ~ 0.25 mm. This motion was not very reproducible however, and so had to be eliminated. We found, to our amazement, that upon evacuating the scattering chamber, the top plate (of the scattering chamber which is 2.54 cm thick with reinforcement struts) moved downward by ~ 0.25 mm near its center. This motion affected the horizontal motion of the dewar system. The contraction of the top plate due to pump down, was eliminated using a stainless steel support post inside the scattering chamber. This post was bolted to the bottom plate and then tightened onto the top plate using a bolt threaded into the top of the post. With this post in place, as well as the standoffs and support post (mentioned above), the horizontal movement of the radiation shielding was almost completely eliminated (measured to be $\tilde{<} 0.08$ mm). The entire bolometer dewar system was thus made quite rigid. The thermal contraction plus pump down motion of the radiation shield and the liquid He dewar had to be remeasured and were found to be 2.04 ±0.05 mm and 1.61 ±0.05 mm respectively.

To accomodate these vertical movements, the bolometer detector apertures (Fig. 2.2) had to be deliberately misaligned at room temperature. This was accomplished by drilling small dimples at 2.04 mm from the center of the apertures mounted on the radiation shielding, and at 1.61 mm from the center of the apertures mounted on the right-angle bracket. To ensure that the displacement of the apertures was by the correct amount, rotation of the apertures during misalignment had to be eliminated. Therefore, a portion of the aperture disk was lathed flat perpendicular to a line joining the center of the dimple and the aperture. Using a HeNe laser beam to define the beam path through the scattering chamber, the apertures were properly positioned. A height gauge (which has a vertically travelling level support arm) was used to prevent rotation of the apertures during their positioning. The dimples were thus postioned onto the beam path. This alignment procedure proved to be very reliable and reproducible.

Another problem with the initial bolometer dewar assembly was an inablilty to collect any liquid He. This problem plagued us for several months and was due to several simultaneous problems. First, the liquid He transfer line that we were using was not vacuum jacketed on the delivery end (the end going into the bolometer liquid He dewar). Consequently, the liquid He coming from the storage dewar was exposed to a 300 K radiation load near the top of the bolometer dewar assembly, and could not cool down enough to form liquid in the bolometer liquid He dewar. Second, the thermal contact between the bottom of the liquid He dewar and the right-angle bracket (Fig. 2.2) was found to be inadequate. This may have lead to a slow thermal leak onto the liquid He dewar preventing condensation of the incoming He liquid. Third, the fiberglass standoffs may have been too large in diameter providing too much thermal contact between the liquid He dewar and the $\sim$ 100 K radiation shield. These problems were overcome by borrowing a transfer line (from Dr. Bertie) which was properly vacuum jacketed, using an indium gasket between the right-angle copper mounting bracket and the bottom of the liquid He dewar, and reducing the size of the fiberglass standoffs. An indium gasket was also used between the copper bolometer mounting block and the right-angle bracket. The fiberglass standoffs are $\sim$ 4.5 cm long with a thread diameter of $\sim$ 2 mm. A central region of $\sim$ 2.3 cm in length was turned down to a diameter of $\sim$ 1 mm. After all of these problems were overcome, we were able to collect $\sim$ 1.1 ℓ of liquid He in the bolometer dewar (using $\sim$ 5 ℓ from the storage dewar) giving a pumped lifetime (at 1.5 K) of 10-11 hours.

This however, was not the end of our problems with the bolometer dewar. Once we were able to cool the device down to 1.5 K, we noticed a rather large ($\sim$ 100 mV peak-to-peak) 60 Hz component in the output signal of the bolometer amplifier, before the lockin amplifier. At that time, the bolometer was directly grounded to the apparatus and a single #35 teflon coated, constantan signal lead came from the detector to an Infrared Laboratories LN-6 amplifier. The problem was due to pickup, through the ground connection, of the 115 V line frequency in the laboratory. To reduce this problem, the bolometer was electrically islolated from the apparatus. A miniature coaxial cable was used to bring both the signal and ground connections up from the detector into the amplifier. After careful elimination of ground loops within the amplifier, the 60 Hz component was reduced to $\sim$ 2 mV peak-to-peak. Recall that this is prior to the lockin amplifier (Stanford Research SR510) which will reduce the 60 Hz component by another factor of $\sim$ 300 with a 60 Hz notch filter (Q of 10 and roll off of -50 dB) prior to lockin amplification. Subsequent to this problem, we began to observe $\sim$ 20-100 mV of noise near the chopping frequency of $\sim$ 26 Hz. Suspecting that this was due to some resonant vibration in the dewar assembly, amplified by the warm LN-6 amplifier, we replaced the LN-6 with an LN-6C amplifier.

The advantage of the LN-6C amplifier is that the first stage of amplification occurs at a JFET (maintained at $\sim$ 77 K) mounted at the bottom of the liquid He dewar. Thus, it is close to the generated signal from the bolometer detector, suppressing any vibration problems due to the signal leads, and is cooled, suppressing any Johnson noise problems. This amplifier allowed us to see the $\sim$ 29 Hz noise problem even better than the previous amplifier did, but did not reduce it at all. The solution to the problem followed the realization that upon cooling, the lower stage fiberglass standoffs were probably not as tight as they were at 300

K, allowing the liquid He dewar to vibrate with respect to the radiation shielding. Therefore, we spring-loaded them using spring steel, to the radiation shield. This appeared to solve the problem, reducing the ~ 29 Hz noise level to ~ 200-300 μV (after the lockin amplifier). The 60 Hz noise after the lockin amplifier was ~ 500 μV.

A further consideration in using the bolometer detector is its insensitivity to the source of the impinging energy. The bolometer is unable to distinguish modulated scattered He beam signals from modulated thermal radiation, modulated secondary beam signal, or modulated background signal. One therefore has to ensure that the measured signal corresponds to that of the scattered He only. This can, in principle, be accomplished by modulating the He beam and then flagging the secondary beam on and off. The difference between the secondary on and off signals should correspond to the scattered He signal. The problem with this arrangement of chopping and flagging however is that modulating the He beam generates a large modulated background signal for low scattering angles, due to the wings of the intense He beam. The seondary beam off signal, for this arrangement, is ~ 90% of the beam on signal at low scattering angles. In other words, one is taking the difference of two very similar large numbers, resulting in large uncertainties for the scattered signal. To get away from this problem, we modulate and flag the secondary beam. The on-off difference signal for this arrangement is usually 80-100% of the on signal. Thus, there is far less uncertainty in its determination.

Initially there was a thermal background problem which was strongly angular dependent. At ~ 4.5° for example (for He + Ar) the off signal was −0.84 mV while the on signal was 9.1 mV. At 5°, the off signal was ~ 0.05 mV with an on signal of ~ 6.3 mV. Consequently, the on-off difference signal was not a true reflection of the scattered He signal since the background signal depended on the scattering angle. We also noticed that the measured signal, even with no He beam gas flowing was strongly negative when the He beam flag was open and almost zero when it was closed. The modulated secondary beam may have been scattering off of the He beam flag into the detector causing a signal 180° out of phase with the detector. Further, the detector may have "seen" the 300 K choppers (the detector is at 1.5 K) generating an out of phase thermal background signal. This problem was corrected by carefully masking the choppers and flags with black electrical tape ensuring that the modulated gas passing through the scattering center must also have passed through the beam collimator. The background signal (secondary beam off signal) under these conditions was always positive and more or less constant at 0-10% of the on signal.

Secondary beam scattering can be eliminated kinematically, for well velocity and angularly collimated beams. Though the bolometer can be positioned between $-12°$ and $+102°$ (the secondary beam being detected at $+90°$), the angular range uncontaminated by scattered secondary particles can be determined from the kinematics and is $\tilde{<} 35°$ for the HeNe interaction. Detection beyond this angle results in an increase in the scattered signal (see Fig. A.12) due to the detection of scattered secondary and scattered primary beam molecules. The angular range of the detector is restricted by the source snouts (shown in Fig. 2.1) which protrude into the scattering chamber, and by the outer diameter of the radiation shield. At $\sim -12°$, the radiation shield is almost touching the secondary source snout. To prevent the bolometer dewar assembly from touching the snouts, electrical trip point switches are used to shut off the electrical power to the rotating flange stepping motor at preset angles. They are currently set at $-12°$ and $+98°$.

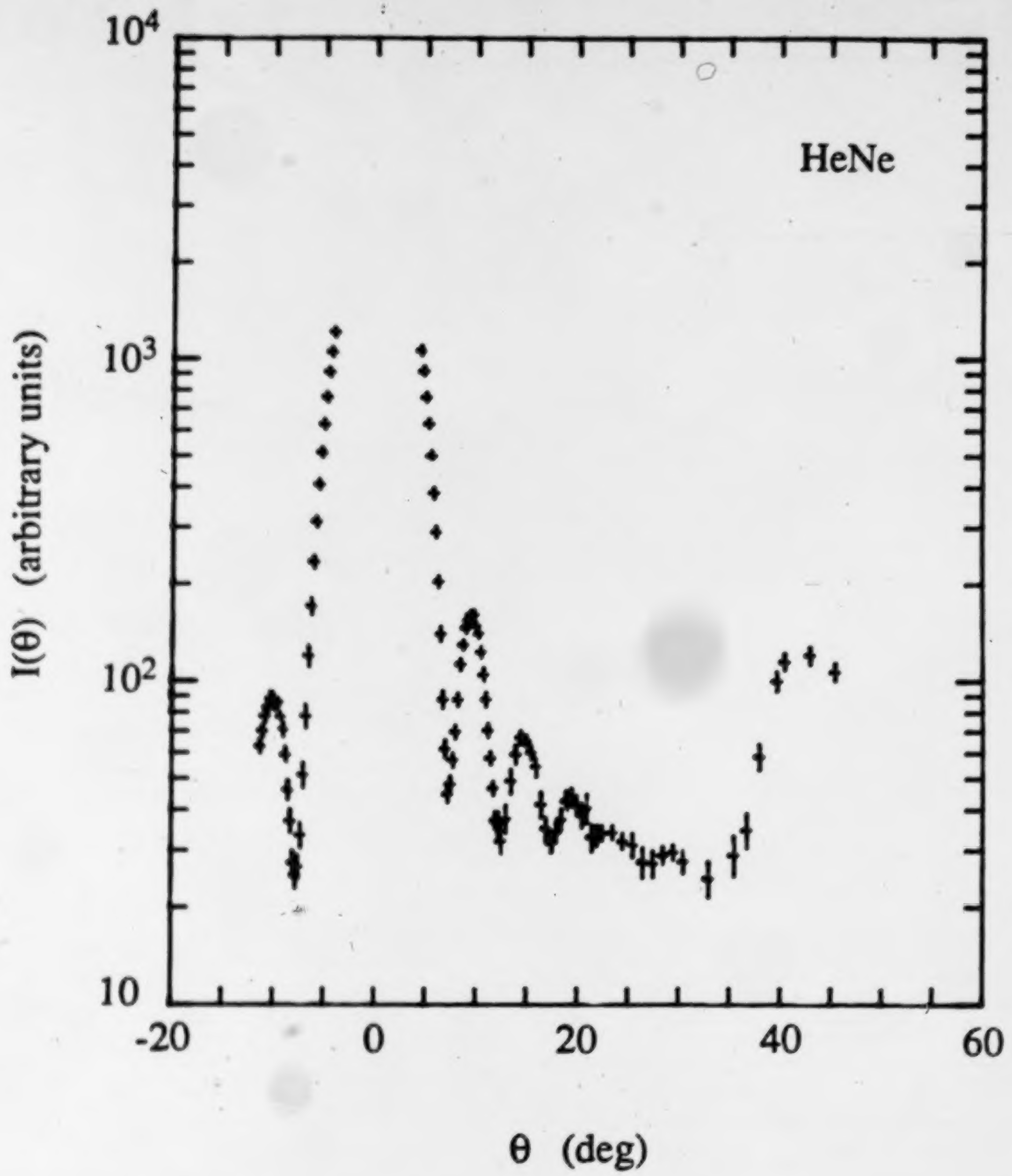

Figure A.12

Measured HeNe DCS showing data beyond the kinematically determined maximum detection angle ($\theta \sim 35°$). The ordinate scale is in arbitrary units, as measured by our bolometer detector.

A.4.B. Apparatus Angular Resolution

The apparatus angular resolution has been described in Secs. 2.2.B and 2.6.A. Figure A.13 depicts the apparatus angular resolution based on the angular divergences of the primary and secondary beams and on the viewing angle of the detector (positioned directly opposite the primary beam). As discussed in Sec. 2.2.B, the overall apparatus angular resolution may be estimated by considering the maximum possible deflection angle that a He atom may suffer and still be detected when the bolometer is positioned directly opposite the He beam.

In order to perform this calculation, we must know some pertinent data for the apparatus. We need to know the following apparatus constants for the primary beam: skimmer-to-collimator = 28.5 mm, skimmer-to-scattering center = 48.7 mm, nozzle-skimmer = 9.5 mm, skimmer diameter = 0.525 mm, and collimator diameter = 0.787 mm. For the detector we need to know: collimating aperture #1-to-scattering center = 33.4 mm, collimating aperture #2-to-scattering center = 66.7 mm, collimating aperture #1 diameter = 0.64 mm, and collimating aperture #2 diameter = 0.67 mm.

Treating the He nozzle as a point source, the skimmer diameter over the nozzle-skimmer distance leads to a beam angular divergence of 1.58° from the beam centerline. However, the collimator diameter over the nozzle-collimator distance (28.5 + 9.5 mm) gives a beam divergence of 0.59° from the beam centerline. It is the collimator therefore, that defines the He beam angular divergence in the scattering chamber. This angular divergence gives a beam radius of 0.6 mm at the scattering center. Now, the detector has two collimating apertures separated by 33.3 mm. From simple geometry, we can treat the detector as a point source originating at 49.7 mm from the scattering center. This gives us a detector viewing angle of 1.13° from the beam centerline. However, the He beam radius is only 0.6

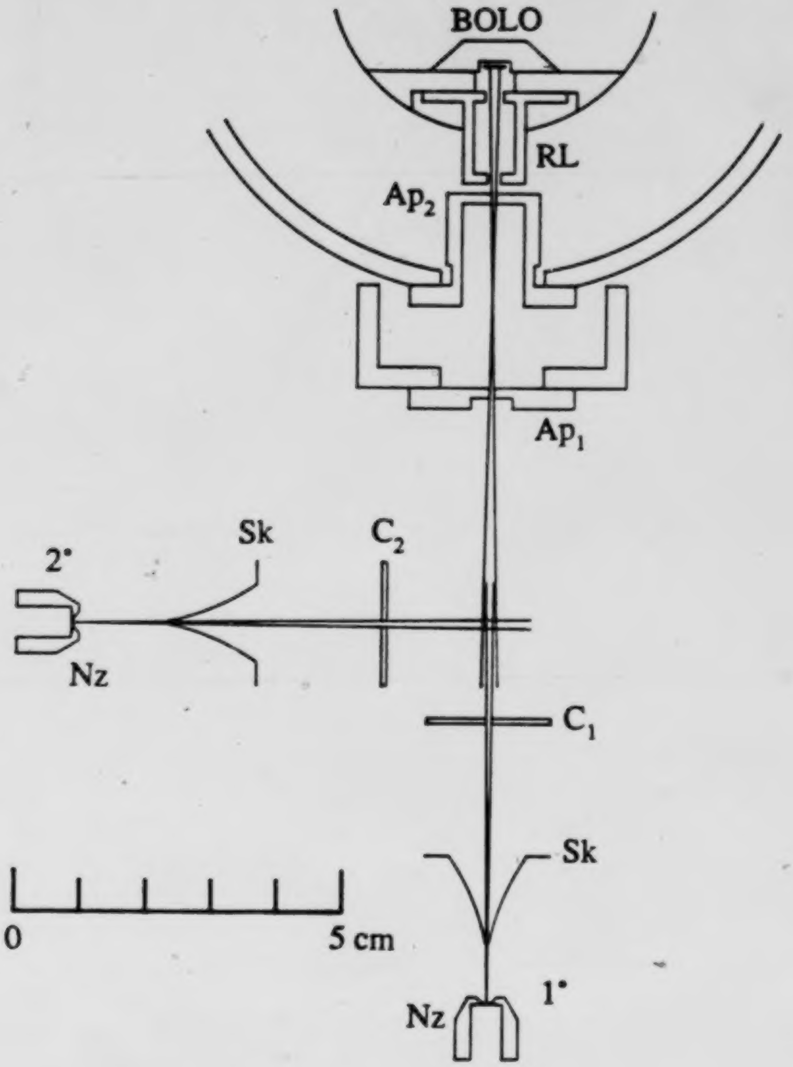

Figure A.13

Angular resolution of the apparatus. The beam divergences and detector viewing angle are shown as solid lines intersecting at the scattering center. Nz = nozzle, Sk = skimmer, C_1 = primary collimator, C_2= secondary collimator, AP_1 and AP_2 = 100 K collimating apertures for the detector, RL = 1.5 K radiation limiting apertures, BOLO = bolometer detector.

mm at the scattering center which, for the purposes of this calculation, restricts the detector viewing angle to 0.70°. That is, a scattered He atom cannot originate from outside of the He beam at the scattering center. A He beam traveling at 0.59° off the beam centerline may therefore be deflected by $\sim$ 1.29° (0.59 + 0.70°) and still be detected by the bolometer. This then is a crude estimate of the apparatus angular resolution (see Sec. 2.6.A).

For completeness sake, the corresponding apparatus constants for the secondary beam are: skimmer-to-collimator = 28.2 mm, skimmer-to-scattering center = 48.5 mm, skimmer diameter = 0.502 mm, and the collimator diameter = 0.978 mm. The apparatus constants given here (and those for the primary beam and the detector) arise from several important considerations. First, the primary beam divergence is critical to the apparatus angular resolution since it is the beam detected. Second, the bolometer detector must view the entire scattering volume at all scattering angles to avoid systematic errors arising from scattered He signals which are smaller than they should be, at some angles, due to the detector masking part of the scattering volume. Third, the secondary beam should not be any smaller than the primary beam at the scattering center to maximize the number of He atoms scattered out of the He beam. Fourth, the size of the scattering volume and of the detector collimating apertures determines the signal-to-noise ratio that will be observed (i.e. the smaller these are the smaller will be the observed scattered signal). Last, the overall apparatus angular resolution should be $\tilde{<}$ 2° to resolve the sharp oscillations in the He + rare gas DCS's (see Chapter 2). These considerations led us to the distances and sizes reported earlier. It is worth noting, that there are many possible combinations of collimator sizes and distances to the scattering center which would satisfy these conditions.

The computer controlled data acquisition has been described in detail in Secs. 2.2.C and 5.2.B.

A.5. EXPERIMENTAL PROCEDURE

This section will outline the general experimental procedure followed in our laboratory to collect the DCS data reported in this thesis. On the night before an experiment is conducted, the liquid nitrogen auto-fill system is set up to cool down the radiation shielding (which takes ~ 3 hours). A 50 ℓ liquid nitrogen dewar (Minnesota Valley Engineering) which maintains a pressure of ~ 3 psig is connected to an insulated transfer line. The transfer line contains an electric solenoid valve connected to a 24 hour timer. Further, the solenoid valve is regulated by the liquid level in the bolometer assembly liquid nitrogen dewar (monitored by two 100 kΩ carbon resistors). The timer is set to turn on the solenoid valve at ~ 4 a.m. Consequently, when one arrives at ~ 7 a.m. the radiation shielding will have cooled to ~ 100 K (measured in the region of the bolometer detector).

The liquid He transfer line is then blown out with He gas for ~ 10 minutes to ensure that there is no moisture or dirt in it. The He transfer line is first put into the bolometer assembly liquid He dewar, lowered to the bottom, and then raised by ~ 0.5 cm. The He return line is opened to allow the blow-off (gas generated in cooling the bolometer assembly liquid He dewar) to return to the He liquifier room in the Physics building. The other end of the transfer line is then slowly lowered into the 30 ℓ storage dewar (Minnesota Valley Engineering), with its 0.5 psi blow-off valve open, until it reaches the bottom where it is raised by ~ 0.5 cm.

The voltage across the bolometer detector is monitored and should read ~ 1.635 V at this stage. The liquid He storage dewar is pressurized with He gas, keeping the 0.5 psi blow-off valve open, and liquid He is transfered to the bolometer assembly at this pressure for 15 minutes. The 0.5 psi blow-off valve is then closed and the storage dewar pressurized to ~ 1 psi. The transfer precedes at this pressure for a total of 13 minutes. After a few minutes, the voltage across the bolometer will decrease to ~ 1.629 V. After ~ 7 minutes at 1 psi, the He gas entering the bolometer dewar assembly will begin to condense and the voltage across the bolometer will increase to ~ 1.640 V. The 1 psi transfer pressure should be maintained for an additional 6 minutes after condensation occurs.

At the end of the transfer, to prevent the liquid He in the bolometer dewar assembly from being sucked back into the storage dewar, the He pressure (the He gas used to pressurize the dewar is shut off) is vented on the bolometer dewar side. Once the pressure has decreased to ~ 0.5 psi, the transfer line can be removed from the bolometer dewar (usually have to heat up this side of the transfer line with a heat gun due to frost build up) and the storage dewar. Again, this should be done by breaking the seal on the bolometer dewar side first. The liquid level in the bolometer dewar can then be measured (with a "whistle stick") and should be ~ 1.1 ℓ.

At this point, the bolometer detector will be at 4 K, where the beam angular scans are conducted. First, a 400 sccm He beam is inlet to the secondary source chamber. He is used to avoid secondary beam condensation on the bolometer detector. With the LN-6C amplifier on the x200 amplification, this beam is scanned from ~ 87° to ~ 93° (see Fig. A.5). Note, the beam is modulated and the signal input to the lockin amplifier. The output signal of the lockin amplifier is input to a strip chart recorder (Linear Model 1200) to allow us to check the beam profile. Typically the lockin amplifier signal is ~ 100 mV at 90° for these conditions. Any asymmetry or double-peaking of the angular profile requires re-optimization of the nozzle alignment through the skimmer and collimator onto the detector. Recall that this can be achieved with the external tilt-platform controls. The detector is positioned at 90° and the tilt-platform controls adjusted to maximize the observed signal. The angular profile is then remeasured to make sure that any problem has been corrected. Once satisfied with the secondary beam alignment, the He gas input to this chamber is shut off. An ~ 800 sccm He beam is then input to the primary source chamber and its angular profile measured from ~ −3° to +3° (see Fig. A.5). As with the secondary beam, this beam is optimized for alignment if necessary. While at 4 K, one can also measure the attenuation of the He beam by the crossed beam. The detector is positioned at 0° and the He beam intensity is measured. The crossed beam is then turned on and the decrease in the He beam intensity measured.

The liquid He is then pumped on with a Welch Duo Seal (Model 1397) mechanical pump. It takes about 30 minutes to reach the operating pressure of ~ 4.5 torr over the liquid He bath. The primary beam (He) should be left on during this time as it takes a long time for it to stabalize its mass flow. The secondary beam can then be turned on and data collection can begin. The amplification switch on the LN-6C should be on the x1000 position for DCS measurements.

From here on, almost everything is handled by the IBM PC-AT. Executing the program CMBSCAT will initialize the lockin amplifier, set up the flag status for the experiment (secondary beam is modulated and flagged), and ask for the current rotating flange angle (which should be manually adjusted to +5° approached from the clockwise direction). This program will either read (from a disk file) the lockin parameters required for each angle, or allow the user to input them as the experiment is conducted. For most of the DCS measurements, +5° is chosen as the arbitrary reference angle. Typical signal levels at this angle range from ~ 0.16 mV for HeC_2H_6 to ~ 1.75 mV for HeNe. The computer integrates the scattered signal for 10 to 200 seconds and then closes the secondary beam flag repeating the measurement for the background signal. The "flag:off" signal subtracted from the "flag:on" signal was taken to be proportional to the intensity of He atoms scattered by the crossed beam. This difference signal was measured four times, and then averaged, for each laboratory scattering angle.

The signal level determines the integration time and the time constant used for the lockin amplifier at each angle. For He + Ar, the scattered He signal ranges from ~ 2.5 mV at 4.5° to ~ 0.05 mV at 45°. For signal levels $\tilde{>}$ 1.0 mV, the time constant, τ, is set to 0.1 sec and a 2 sec integration time is used. For scattered signal levels between ~ 0.3 mV and 1.0 mV, τ is set to 0.1 sec and a 5 sec integration time is used. With signals between ~ 0.1 mV and 0.3 mV, τ is set to 0.3 sec, and the integration time is increased to 10 sec. At signal levels between 0.03 mV and 0.1 mV, τ remains at 0.3 sec, and the integration time is increased to 20 sec. For very low signal levels $\tilde{<}$ 0.03 mV (encountered in the $HeCHF_3$ system), τ is again 0.3 sec, and the integration time increases to 50 sec. These values are chosen to provide reasonable error bars ($\tilde{<}$ 20% for the wide angle scattering) on the measured signals.

For low scattering angles ($\tilde{<}$ 3.5°), the wing of the intense He beam caused the detector to heat up substantially resulting in scattered signals which were artificially lowered. To avoid this, at the low angles, the He beam was flagged on and off a few times. If this resulted in overloads on the lockin amplifier, the temperature of the bolometer detector was changing too rapidly. In other words, the wing of the He beam was saturating the detector at 1.5 K and causing it to heat up. This could be observed directly by monitoring the voltage across the bolometer which would decrease by up to 10% for scattering angles $\tilde{<}$ 3.5°. Therefore, no measurements are reported closer than 4° to the He beam centerline to avoid this problem.

Data were collected and archived onto a disk file until the liquid He ran out. To prepare the apparatus for another experiment, the liquid He and liquid nitrogen dewars, in the bolometer assembly, are blown out with dry nitrogen gas overnight. This ensures that they warm up to room temperature and that any gas condensed on the detector is removed. If one wants to run an experiment on the following day, it is still necessary to warm up the detector. Failure to do this, will result in decreased sensitivity of the detector and therefore a poorer signal-to-noise ratio.

The reference angle (usually 5°) was remeasured at least once every 30 minutes during an experiment. This allowed the data collected between references to be time normalized (assuming a linear change in the reference signal with time) by executing the program ARCNORM. This normalization corrected the data for long term drifts in the reference angle scattered signal. An experiment lasts 10-12 hours during which time the reference signal may vary by up to 5-10%. One generally observes a decrease in the reference signal over time, probably due to the background gas forming solid layers on the 1.5 K surface of the detector. Once the data are normalized, ARCNORM collates them in terms of scattering angle and determines the average signal and error for each scattering angle (if there is more than a single measurement). The entire DCS is measured at least three or four times to improve the signal-to-noise ratio and to establish the statistical uncertainty of the measurements.

The program ERRBAR, takes these averaged quantities and 5-point smooths the error bars over scattering angles. This prevents an error bar which, for some reason, is very different from those of the two angles on either side of it. It also convolutes the angular scale uncertainty with the statistical measurement uncertainty at each angle to give the appropriate overall error bars for each data point. A minimum error bar of 3% is imposed at this stage (particularly for the low angle measurements) to avoid excessive weighting of any particular data point in the data reduction program. The program ERRBAR also allows, if wanted, one to reject individual data points at a particular angle (provided there are more than 3 measurements at this angle) by way of a Q-test.[14] The Q-test was used for all of the He + Rg DCS's reported in this work and also for the He + C_2H_6 DCS. This procedure rejected no more than 1% of the data (typically 3 points out of $\sim$ 400 measured points), and did not therefore, significantly change any of the measured DCS's. The smoothed data generated by ERRBAR were then used in the data reduction program.

References

1. M.A.D. Fluendy and K.P. Lawley, Chemical Applications of Molecular Beam Scattering, (Chapman and Hall Ltd., 1973).
2. J.B. Anderson, R.P. Andres, and J.B. Fenn, *Supersonic Nozzle Beams* in Adv. Chem. Phys. **10** (Interscience, New York, 1966), Ch. 8.
3. L.J. Danielson and M. Keil, J. Chem. Phys. **88**, 851 (1988).
4. *Vacuum Technology its Foundations Formulae and Tables*, Leybold-Heraeus Vacuum Products Inc., 2300 Finch Avenue West, Unit 29, Weston, Ontario M9M 2Y3.
5. (a) D. Halliday and R. Resnick, *Physics: Parts I and II* (John Wiley & Sons, Inc., New York, 1966) pp. 1101-1114; (b) M. Mizushima, *Theoretical Physics: From Classical Mechanics to Group Theory of Microparticles* (John Wiley & Sons., Inc., New York, 1972) pp. 190-195.
6. H.V. Malmstadt, C.G. Enke, and S.R. Crouch, *Electronics and Instrumentation for Scientists* (The Benjamin/Cummings Publishing Company, Inc., London, 1981).
7. W.R. Gentry and C.F. Giese, Rev. Sci. Instrum. **46**, 104 (1975).
8. L.J. Danielson, M.Sc. Thesis, Waterloo, Ontario (1982).
9. J.B. Anderson and J.B. Fenn, Phys. Fluids **8**, 780 (1965).
10. J.P. Toennies and K. Winkelmann, J. Chem. Phys. **66**, 3965 (1977).
11. N.C. Blais, J.B. Cross, and G.H. Kwei, J. Chem. Phys. **66**, 2488 (1977).
12. *Atlas of Mass Spectral Data*, E. Stenhagen, S. Abrahamsson, and F.W. McLafferty editors, Vol. **1** (John Wiley and Sons Inc., 1969), p. 35.
13. L.J. Danielson, K.M. McLeod, and M. Keil, J. Chem. Phys. **87**, 239 (1987).
14. (a) R.B. Dean and W.J. Dixon, Anal. Chem. **23**, 636 (1951); (b) D.A. Skoog and D.M. West, *Analytical Chemistry: An Introduction* (Holt, Rinehard and

Winston, New York, 1965), p. 51; (c) W.J. Dixon and F.J. Massey, Jr., *Introduction to Statistical Analysis* (McGraw-Hill Book Company, New York, 1969), p. 328.

APPENDIX B

Experimental Data not yet Published

The $HeCO_2$ and HeOCS data reported in Chapter 5 are also given in Table B-1 and Fig. B.1. The tabular data, and the plotted data for $\theta > 20°$, have not been previously published.[1] Our experience with the He + Rg systems,[2] indicates that DCS data for scattering angles beyond $\sim 30°$ are sensitive to the repulsive wall of the interatomic potential. Therefore, the $HeCO_2$ and HeOCS earlier DCS data[1] were supplemented by five additional measurements from $\theta \sim 20°$ to $\theta \sim 45°$.

In particular, we are interested in determining an asymmetric intermolecular potential for HeOCS which would correctly reflect the $C_{\infty v}$ symmetry of OCS. Such a determination however, requires supplementary information on the angular asymmetry of the HeOCS potential. This work is ongoing,[3] and should provide us with SCF calculations for the repulsive wall of the HeOCS potential and perhaps some information on the asymmetry of the long range part of the potential. Further, recent line broadening data[4] can yield details on the asymmetry of this interaction. Measurements of the diffusion data near room temperature are also underway for this interaction.[5] Inclusion of all of this information in a multiproperty fit should yield an interatomic potential that is slightly more damped in the region of $\theta \sim 12°$ (see Fig. 5.2), and consequently properly reproduce the DCS measurements.

The $HeCO_2$ DCS results will be used in a multiproperty fit as previously[6] to determine an anisotropic intermolecular potential. This new potential should provide a better description of recent incompletely resolved rotationally inelastic DCS's for $HeCO_2$[7] than did the previous Keil and Parker[6] potential.

Table B-1. Measured DCS data for $HeCO_2$ and HeOCS

$HeCO_2$			HeOCS		
θ(°)	I(θ)	ΔI(θ)%	θ(°)	I(θ)	ΔI(θ)%
−8.55	126.97	6.5			
−8.05	134.44	5.4	−8.20	147.78	3.0
−7.77	139.17	5.1	−7.70	176.39	3.5
−7.05	139.66	5.3	−7.20	199.25	4.4
−6.55	175.56	4.4	−6.70	200.89	4.3
−6.05	250.73	3.1	−6.20	228.18	3.4
−5.55	397.98	3.0	−5.70	316.16	3.0
−5.05	624.05	3.0	−5.20	472.50	3.0
−4.55	834.97	3.0	−4.70	706.37	3.0
−4.05	1091.96	3.0	−4.20	993.44	3.0
4.45	974.58	3.0	4.30	1040.87	3.0
4.95	724.78	3.4	4.80	755.19	3.1
5.45	500.00[a]	5.0	5.30	500.00[a]	3.4
5.95	329.30	6.0	5.80	356.40	3.3
6.45	242.77	6.0	6.30	292.94	3.5
6.95	217.46	5.3	6.80	281.48	4.3
7.45	229.85	4.3	7.30	262.89	4.9
7.95	222.33	4.6	7.80	219.97	4.5
8.45	205.29	5.9	8.30	176.43	3.9
8.95	169.50	6.8	8.80	142.14	3.7
9.45	126.20	8.0	9.30	105.49	3.7
9.95	97.49	10.1	9.80	91.62	4.2
10.45	86.74	11.7	10.30	86.62	5.4
10.95	66.54	12.0	10.80	81.87	6.5
11.45	68.62	11.1	11.30	77.55	6.8
11.95	70.28	11.0	11.80	68.03	6.6
12.45	67.53	11.4	12.30	60.26	6.0
12.95	67.45	10.2	12.80	59.74	5.8
13.45	62.73	8.2	13.30	52.29	7.0
13.95	58.00	8.1	13.80	41.62	9.7
14.45	41.44	10.4	14.30	43.38	12.9
14.95	39.83	13.4	14.80	38.71	14.8
15.45	37.14	15.8	15.30	40.54	15.5
15.95	42.02	18.2	15.80	40.08	15.7
16.45	45.58	20.8	16.30	35.63	14.0
16.95	34.62	20.6	16.80	34.60	10.9
17.45	39.58	16.3	17.30	28.08	9.7
17.95	45.32	12.9	17.80	35.45	10.0
18.45	33.58	13.6	18.30	31.04	11.1

··· continued on the next page ···

Table B-1 continued ···

HeCO$_2$			HeOCS		
θ(°)	I(θ)	ΔI(θ)%	θ(°)	I(θ)	ΔI(θ)%
19.45	24.39	14.6	19.30	31.45	14.8
20.45	34.97	13.1	20.30	25.34	19.2
25.45	29.88	11.6	25.30	21.46	21.3
30.45	24.48	12.8	30.30	21.66	22.4
35.45	26.42	15.3	35.30	22.44	23.0
40.45	23.50	16.3	40.30	17.52	21.6
45.45	21.59	15.5	45.30	15.47	19.1

[a] Reference angle used for periodic normalization.

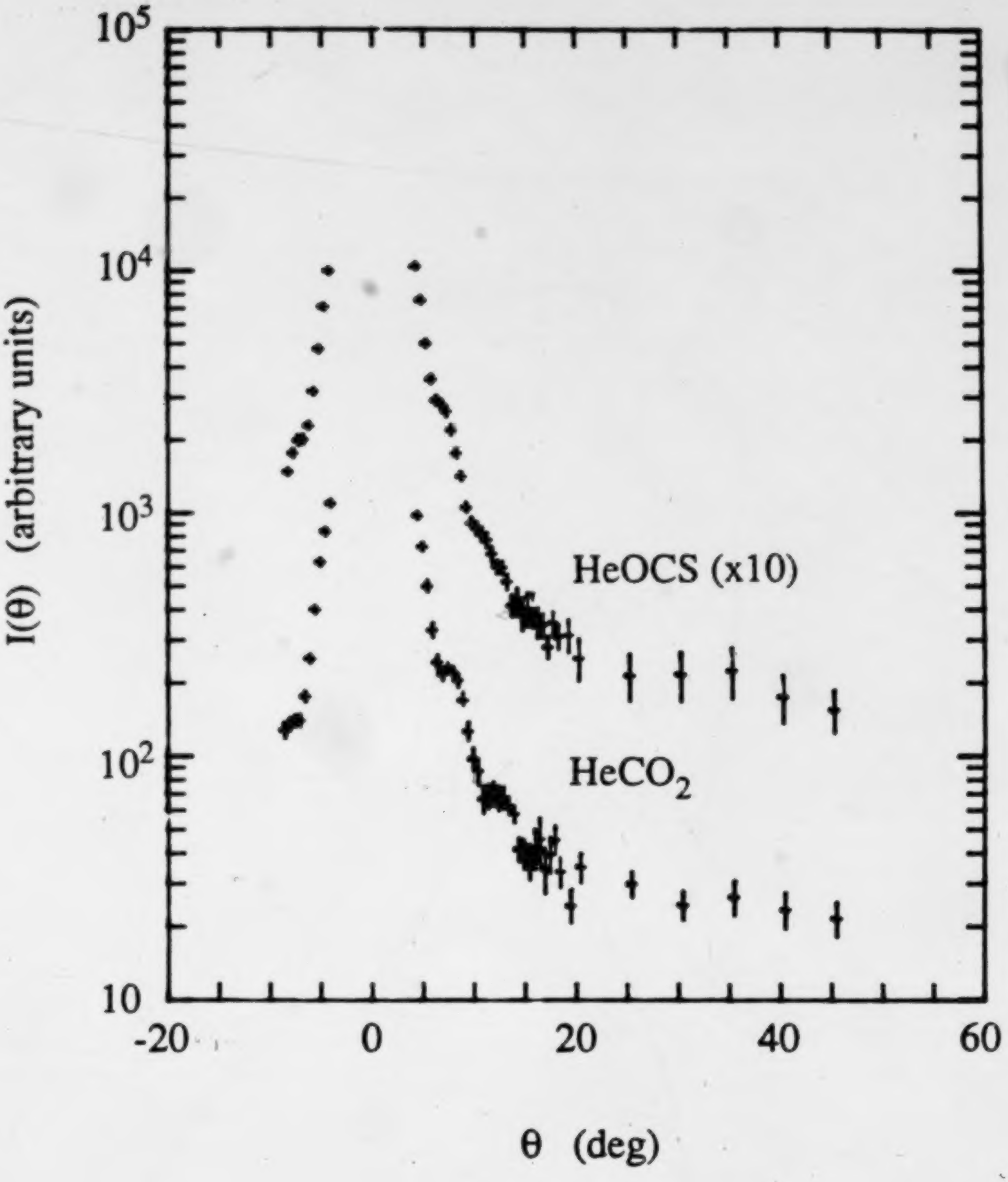

Figure B.1

Measured $HeCO_2$ and HeOCS DCS's. The HeOCS data has been multiplied by 10 for clarity of display. The data show the supplemental measurements from $\theta = 20°$ to $\theta = 45°$.

References

1. L.J. Danielson, K.M. McLeod, and M. Keil, J. Chem. Phys. **87**, 239 (1987).
2. L.J. Danielson and M. Keil, J. Chem. Phys **88**, 851 (1988).
3. L.J. Danielson, T. Dingle, P.J. Dunlop, and M. Keil (in preparation).
4. (a) A. Picard-Bersellini and B.J. Whitaker, J. Mol. Struc. **115**, 347 (1984); (b) M. Broquier, A. Picard-Bersellini, B.J. Whitaker, and S. Green, J. Chem. Phys. **84**, 2104 (1986).
5. P.J. Dunlop, private communication to L.J.D.
6. M. Keil and G.A. Parker, J. Chem. Phys. **82**, 1947 (1985).
7. U. Buck, H. Meyer, M. Tolle, and R. Schinke, Chem. Phys. **104**, 345 (1986).